Veli-Jussi Laurila

Structure and Properties of Nickel Based Braze Surface with Diamond Grits - Interaction Phenomena between Brazing Alloy and Diamond Grits

Julkaisu 1510 • Publication 1510

Tampere 2017

Veli-Jussi Laurila

Structure and Properties of Nickel Based Braze Surface with Diamond Grits - Interaction Phenomena between Brazing Alloy and Diamond Grits

Thesis for the degree of Doctor of Science in Technology to be presented with due permission for public examination and criticism in Konetalo Building, Auditorium K1702, at Tampere University of Technology, on the 24th of November 2017, at 12 noon.

Doctoral candidate: Veli-Jussi Laurila
                       Materials Science
                       Engineering Sciences
                       Tampere University of Technology
                       Finland

Supervisor: Petri Vuoristo, professor
                       Materials Science
                       Engineering Sciences
                       Tampere University of Technology
                       Finland

Pre-examiners: Uta Klement, professor
                       Department of Industrial and Materials Science
                       Chalmers University of Technology
                       Sweden

                       Veli Kujanpää, professor
                       Technical Research Centre of Finland
                       Finland

Opponents: Wolfgang Tillmann, professor
                       Institute of Materials Engineering
                       University of Dortmund
                       Germany

                       Veli Kujanpää, professor
                       Technical Research Centre of Finland
                       Finland

Abstract

Diamond is known as the hardest material in the world. However, the diamond crystals found in nature are expensive and are mostly used for jewellery. In the middle of the last century, man learned how to produce single diamond crystals artificially on an industrial scale, which has dramatically reduced the cost of diamonds used in tool manufacturing. However, the size of these crystals is limited and if they are to be used as components in tools, they somehow have to be fixed to the tool body.

One popular way to affix diamonds to tools is to use brazing. Several types of brazing filler materials are used for this purpose. One group of these materials consists of low cost, nickel-based brazing materials to which chromium has been added to improve the mechanical strength and, especially, the corrosion resistance of the joint. Unfortunately the brazing temperature of these nickel-based alloys is high compared to the other brazing materials, and because of the high temperature and the effects of the chromium, the braze material reacts with the diamond, thus reducing the strength of the diamond crystals. Carbon also dissolves into the surrounding braze. Here it has to be remembered that the carbon also compose chromium carbides between the braze and the diamond crystals. These are needed to lower the contact angle between the braze and the diamond, and also to form a good mechanical bond between the diamond and the braze. This greatly improves the mechanical bond between the braze filler material and the diamond grit.

In this work, the reaction layers between the diamond and the nickel based braze filler material are studied in detail. The dilution of the carbon affects the construction and properties of the braze material. The degradation of the diamond single crystals roughens the facets of the crystals and thus reduces their mechanical properties and also their efficiency as tools. On the other hand, the carbide layers which form on the diamond surface between the braze filler material and diamond smooth out the difference in the thermal expansion coefficient between the diamond and the braze filler material.

Two different kinds of nickel-based braze material were chosen for the studies to see what effects their composition has on the final structure existing between the braze and the diamond. The effect of the carbide formation when boron and silicon containing Ni-Cr-Si-B was used as the braze material was found to be slight compared to the Ni-Cr-P braze, despite the fact that the brazing temperature is clearly higher for the Ni-Cr-Si-B material. The reasons for this are not only the lower chromium content, but also the formation of chromium borides in the Ni-Cr-Si-B braze matrix. The chromium in the alloy does give good corrosion resistance but it has also been shown to decrease the mechanical strength of the diamonds because of the excess carbide formation. The braze filler materials studied here have been developed mainly for joining stainless materials and super alloys, such as those used in corrosive applications and at high temperatures.

In this study, it was found that the degradation mechanism for different types of diamond facets varies, which in turn affects the mechanical strength of the diamond when it is strained in different directions. According to the results of this work, it is clear that the higher the available chromium content, the thicker the carbide layer on the diamond surface, and thus there is considerable degradation of the diamond surface.

The cross-sections of the carbide layers between the diamond and braze were studied using Scanning Electron Microscopy (SEM) and Backscattered Electron (BSE) analysis. BSE-imaging together with the image analysis program used to measure the grey levels of the phases proved to be very efficient tools

for characterizing the phases of the structure. This method is especially useful for identifying the different phases for the kinds of multiphase materials in which some of the components are electrically insulating.

The BSE-imaging confirmed that two different layers of carbides are formed between the diamond and the braze filler material, seen as contrasting lighter and darker phases, indicating the difference in the compositions of these carbides. There was no evidence of graphite formation, even though the braze materials contained nickel. The results of the research indicate that the deterioration of mechanical properties of the diamond composite may in part be caused by the degradation of the surfaces of the single diamond crystals.

The internal structure of the diamond crystals was also studied. According to these results, the reactions, which occur on a single diamond crystal's surface do not degrade the crystal internally. This suggests that although the carbon may diffuse into the brazing material, the components of the braze cannot diffuse into the diamond itself at the brazing temperature used.

Preface

Table of contents

Abstract

Preface

Author's contribution

List of terms and abbreviations

AUTHOR'S CONTRIBUTION

The author designed and performed all measurements and calculations included in the experimental part of this work, except for the XRD curves, where the measurements were taken with the help of Mr. Leo Hyvärinen. The manuscript was written by the author and commented by the supervisor, Professor Petri Vuoristo.

List of abbreviations and symbols

α	Ferrite
a_0	Side Length of the unit cell
AISI	American iron and steel institute
AMS	American material standard
ASTM	American Society for Testing and Materials
AWS	American Welding Society
BCC	Body centred cubic phase
BIB	Broad Ion Beam
BSE	Backscattered electron
c	Mass fraction
C^D	Concentration of carbon, in diamond $C^D=1$
CFS	Compressive fracture strength
CTE	Coefficient of thermal expansion
CVD	Chemical vapour deposition
d	Distance between crystal planes
ΔF	Standard free energy
DIN	Deutsches Institut für Normung
ε	Elongation
E	Young's modulus
E_e	Primary electron energy
E_f	Young's modulus of film
E_{corr}	Corrosion potential
EDX	Energy dispersive X-ray analyser, spectrometer for chemical analysis
E_{OCP}	Open circuit potential
E_s	Young's modulus of substrate
FCC	Face centred cubic
FEM	Finite element method
FM	Filler metal
$F_\%$	Percentage fraction
γ	Austenite
γ'	Ordered FCC phase
g-vector	Reciprocal lattice vector defining diffraction conditions
Gx	Fraction of information coming from the depth x from the specimen surface
h	Measured bend of specimen
HV	Vickers hardness
I_{corr}	Corrosion speed
λ	Thermal conductivity
l	Length of the specimen
LVDT	Linear voltage displacement transducer
μ	Mass absorption coefficient
m	Mass
MBC	Maximum brazing clearance
MBF	Metallic brazing filler
m_c	Mass of the coating
m_d	Mass of the diluted layer
Me	Metal atom
n	Order of reflection
η	Backscattering coefficient
η_i	Backscattering coefficient for an element

$N_C^{Me(C)}$	Carbon concentration
P_c	Phosphorous content
P_o	Original content of phosphorous
P_{Ni2P}	Content of phosphorous in $(Ni, Cr)_2P$ phase
ρ	Density of the component
r	Radius of curvature
R_a	Roughness average
ρ_d	Density of the diluted material
R_m	Tensile strength
R_q	Root mean square
ρ_s	Density of the coating material
R_t	Maximum height
R_z	Mean maximum height
σ	Stress level
SE	Secondary electron
SEM	Scanning electron microscope
sp2	Spinel of electrons
STDEV	Standard deviation
Θ	Bragg angle
t	Time
Θ_C	Contact angle
t_c	Thickness of the coating layer without dilution
t_d	Thickness of dilution layer
TEM	Transmission electron microscope
t_f	Film thickness
TI	Toughness index
t_s	Substrate thickness
TTI	Thermal toughness index
V	Volume
W	Wettability
w_i	Weight fraction of a component in the solid material
x	Depth from the specimen surface
X^D	Specific diamond dimension at times t=0 and t=t
X^{Me}	Metal in contact dimension at t=0 and t=t
XRD	X-ray diffraction
Y_f	Distance from neutral plane to a point in the film
Y_s	Distance from neutral plane to a point in the substrate
Z	Atomic number of element
ZAF	Correction calculation for EDX-analyses

1. Introduction

Since the beginning of our civilization, materials with high mechanical strength and superior hardness have been associated with human achievements. Hard stones were first used not only as simple implements such as hammers and anvils, but also as more sophisticated tools for shaping and sharpening other suitable materials. This was probably the most important technology developed by early man, the technology needed to break, chip, splinter, shape and finish less softer stones and other natural materials such as wood, bone and horn in order to produce tools for work, hunting and defence. [1]

The stone age, i.e. the age of using stones as tools, was succeeded by the bronze age, and metals such as bronze replaced stones as the most efficient material for producing tools [1]. Later, around 5000 years ago, bronze was replaced by iron, and later still, steel, and these metals dominated tool manufacturing technology and industry until industrial diamonds, hard ceramics and cermets (composites of ceramic materials and metals) have been developed. Also since that time, ceramic materials have become industrially available. Although steel is still an important basic industrial material, modern ceramic materials (such as silicon carbide) are increasingly available and utilised for industry [1].

Among the many hard materials currently used in industrial applications such as turning, cutting, drilling, boring and grinding, diamond still holds its place as the hardest. Indeed the use of synthetic diamonds is today a commercial and relatively low-cost solution for many technological applications such as low cost everyman's tools for cutting stone and grinding hard ceramics and glass. As long ago as the beginning of the 20th century, it was already known that diamond was an allotropic form of carbon [1, 2, 3, 4].

Some crystallographic data of diamond and values for the hardness of abrasive materials are presented below in Tables 1 and 2. In addition to hardness, diamond also has the highest Youngs modulus (E) and thermal conductivity (λ) of all the hard materials presented in Table 2.

Table 1. Crystallographic data of diamond crystal [5].

Side Length, a_0	3.567Å (0.3567nm)
C - C Bond Length	1.54Å
Atomic Density	1.76 x 10^{29} atoms/m^3
Packing Fraction	0.34

Table 2. Summary of physical properties of super abrasive and some conventional abrasive materials. [6]

Property	Diamond	Cubic boron nitride	Silicon carbide	Alumina	Tungsten carbide
Knoop Hardness[†] (GPa)	70-100	50	25	22	20
Young's Modulus[†] (GPa)	1143	909	410	366	570
Poisson's ratio[†]	0.07	0.12	0.14	0.22	0.22
Density (g/cm^3)	3.52	3.48	3.21	3.92	15.0
Thermal Conductivity (W/m-K)	2100	1400	380	40	105
Coefficient of Thermal Expansion (10^{-6} $^\circ$C^{-1})	4.8	5.6	4.5	8.6	4.5

[†] Orientational average

High quality, low cost, commercially-produced diamond single crystals are still quite small in size, and partly therefore they have to be fixed to a suitable tool body if they are to be used as effective and economically viable tools. Attaching diamond single crystals to a stainless steel tool body with mechanically strong and corrosion-resistant brazing filler alloys is of great importance to many manufacturing industries, and is the central issue in this work. The primary motivation for this study came from the development of mechanical wood-pulping devices used in the Galileo concept by the Valmet Corporation in Finland [8], but the applications of this research are significant for many other manufacturing processes and industries. However, the success of the Valmet Galileo concept should be emphasised here. The experience gained from using the Galileo concept in grinders all around the world has shown that it has enabled a reduction in specific energy consumption of about 25-35 %. This is because the conventional ceramic stone surfaces of the mechanical wood-pulping grinders have been replaced with steel coated with industrial diamonds. According to reference [8] diamond grits are set in specific, precise patterns depending on the wood species to be ground, the processing conditions and the desired pulp quality. The Galileo concept not only reduces production costs, it also increases pulp production and provides more uniform end-product quality. [8]

1.1 Motivation for the research work

The manufacturing method of brazing is used to join diamonds (or other suitable super-abrasives) to a particular material's surface as part of the tool-manufacturing process. There are several types of brazing filler material used in tools for this purpose; these include copper, nickel, palladium, gold and silver based brazing filler alloys [2]. Most of these materials have adequate mechanical strength but do not perform well in elevated temperatures or under severely corrosive conditions. This research work focuses on *nickel-based* brazing filler materials due to their mechanical strength, relatively low cost, strong performance in elevated temperatures and high corrosion resistance when compared to the other brazing filler materials. When grinding pulp and wood using the Galileo concept [8], these particular properties are favoured for the tools, leading nickel to be the most appropriate choice as the brazing material to join single crystal diamonds on to stainless steel substrates in a vacuum furnace.

For the study two types of commercial chromium-alloyed braze filler materials were selected to braze the single diamond crystals to a stainless steel based surface material. The selected nickel-based braze materials were phosphorus containing a Ni-Cr-P alloy and boron and silicon containing a Ni-Cr-Si-B alloy. These materials were selected because of their differences: there are slightly different brazing conditions, a totally different final structure, differing interaction with the diamond single crystals, and a varying corrosion resistance and mechanical behaviour between the materials. It is also pertinent to note that studying the differences in composition and final structure of these nickel-based materials would lead to a greater understanding of their behaviour under industrial conditions.

Research questions to be answered with this study:

1. What are the reactions between the braze material and diamond crystals: the structure of the formed connecting layers and effect of the brazing process to the diamond single crystal structure and surface? Furthermore, how does the brazing process affect the diamond single crystal surface and what is the possible degradation mechanism? How can the structure be characterized and what kind of analysing techniques can be used and developed? What is the final structure of the brazing material? What kind of dilution of the base material is observed?
2. To elaborate: how does the dilution of carbon from diamond crystals and the elemental components from the tested base material affect the final structure of the braze joint?
3. What kind of residual stresses are formed on the diamond surface during the manufacturing process and what is the mechanical strength of the single diamond crystals after the brazing process?
4. How does corrosion affect the structure of the final braze layer and diamond crystals and how does the corrosion resistance differ between the study materials?

These questions will be answered according to the literature review and test results and analysis.

1.2 Structure and properties of diamond single crystals

During the 20th century it was discovered that, with the application of certain pressures and temperatures, Figure 1, it was possible to convert the soft hexagonal structure of graphite material into the hard cubic structure of diamond, as illustrated in Figure 2. In the United States in 1955, General Electric research group were the first to successfully produce synthetic diamonds, therefore helping bring about a reduction in the price of commercial diamond grits. Nowadays, therefore, the cost of diamond tools is compatible with other hard abrasive materials [1]. Table 1, above, presents basic crystallographic data for diamond crystals. Table 2 (also above) presents a summary and comparison of the physical properties of super-abrasive and conventional abrasive materials.
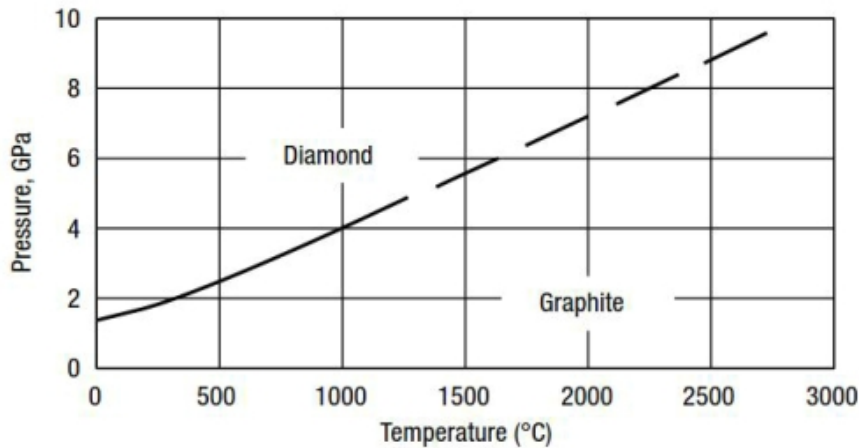
Figure 1. Pressure vs. temperature diagrams for carbon. [1]
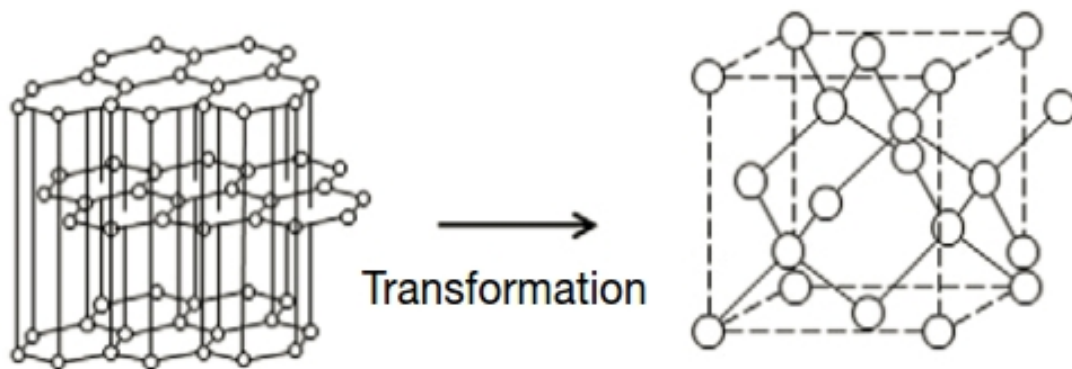
Figure 2. Structural transformation at high pressure and high temperature from the hexagonal structure of graphite to a hard cubic diamond structure. [1]

Contrary to the well-known saying, 'diamonds are *not* forever'. In spite of their remarkable properties, there are some applications of use where - as a carbon-based material - diamonds have serious technological limitations. For example machining of certain iron-based alloys induce working temperature restrictions, in turn leading to degradation of the diamond material. [1]

It is important to note here that in the high temperatures needed for the brazing process, the oxidation of diamond initiates as low as 600°C and conversion to graphite takes place above 900°C, the temperature being below the typical brazing temperature for nickel-based brazing materials [2]. Machining or tooling of a ferrous alloy or a nickel-based super-alloy with diamond deteriorates its properties. As a consequence of these limitations, tools containing diamonds are used at moderate temperatures where their application is restricted to non-metallic materials and a range of non-ferrous alloys. There are still important applications and scope for diamond-based tools within this field. [1]

The crystal structure of diamond is a Face-Centred Cubic (FCC) lattice, with a basis of two identical carbon atoms associated with each lattice point: one at (0, 0, 0) and the other at (1/4, 1/4, 1/4). This

is the same as two interpenetrating FCC lattices, each with atoms at only the lattice points, offset from one another along a diagonal body by one quarter of its length [5]. Single crystal diamonds are presented in Figures 3 and 4 below. Figure 3 demonstrates the low index crystal planes or facets of an FCC crystal. As seen in Figure 4, the type of diamond facet can be identified from the shape of the facet and the shape of the single diamond crystal. The final shape of the diamond crystal produced is dependent on requirements, with specific crystal shapes used in different applications and manufacturing conditions. [5]

Figure 3. Three-dimensional cubic single crystal with {100}, {110} and {111} type facets of diamond structure. [6]
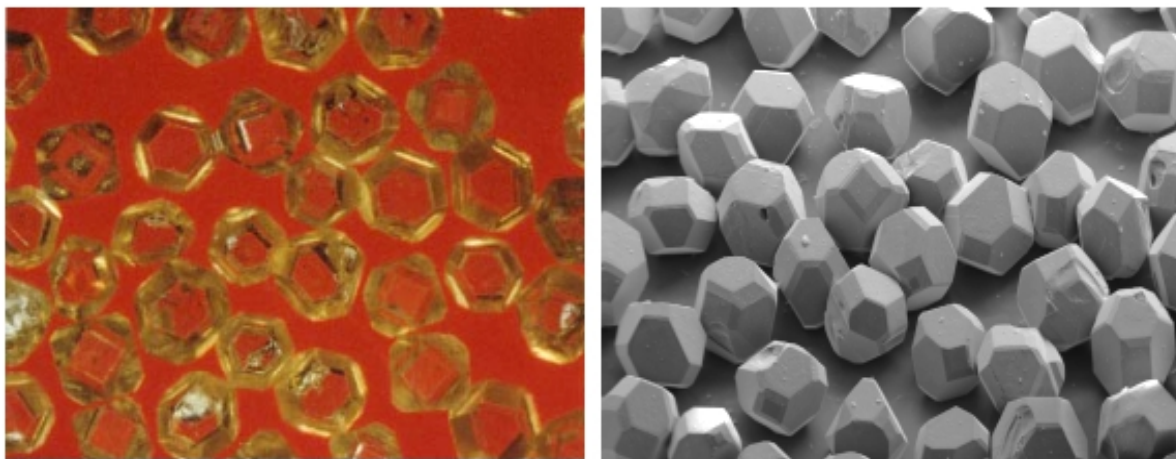
a)   b)

Figure 4. Well-crystallized and tough diamond crystals, (a) optical and (b) Scanning Electron Microscope (SEM) micrographs. Note the clear facets of the crystals and the edge angles important when diamonds are used for machining – angles are over 90 degrees. [6]

The shape of a single diamond crystal has been found to be critical to its strength, toughness and ease of retention in a bond [6]. Shapes range from octahedral to cubo-octahedral to cubic, as illustrated in Figure 5 and the eccentricity (ratio of maximum and minimum diameters) can deviate significantly from one crystal shape to another [6]. According to the shape of the single crystal and the angle value of the corners of the facets it is possible to separate and identify the facet types of the diamond single crystal.
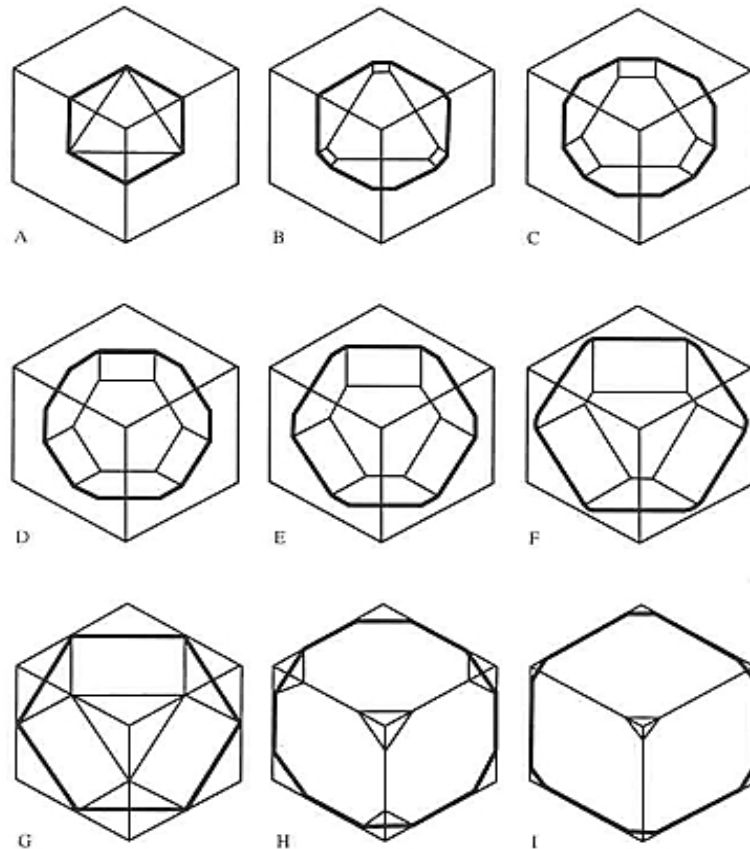
Figure 5. Shapes of cubo-octahedral diamond crystals. [6]

As mentioned previously, diamond manufacturers have long been aware that the single diamond crystal shape is sensitive to its growth conditions, with higher temperatures generally producing a more octahedral crystal; therefore manufacturers have found temperature control to be an important tool in controlling the crystal shape. [6, 7]

Fabrication of abrasive tools containing mesh diamonds grits, particularly with metal bonds, involves processing at temperatures of up to 900°C or even higher if a nickel-based braze filler material is utilized [2]. The thermal stability of the crystals is therefore very important for such applications. The most common way to characterize thermal stability is to perform a toughness test after exposure to high temperatures. A toughness test could involve exposure for 10 minutes at 1100°C in an inert atmosphere, yielding a Thermal Toughness Index (TTI). The thermal stability of diamonds is mainly determined by the internal concentration of inclusions, catalyst metal and other impurities. Back-conversion of diamond to graphite around the inclusion may occur upon heating and, in addition, the thermal expansion coefficient of most inclusions is higher than that of diamond. This induces further

internal stresses inside the single diamond crystals. These effects contribute to the generation of internal stresses that weaken the crystals. [6, 7]

As previously stated, the shape of a single diamond crystal has been found to be critical to its strength, toughness and ease of retention in a bond. The highly irregular shape of resin grade crystals contributes to their high friability as well as improving bond retention. Even with well-faceted saw grade diamond crystals presented in Figure 3, the shape can range from octahedral to cubo-octahedral to cubic, as illustrated in Figure 5, and the eccentricity (ratio of maximum and minimum diameters) can deviate significantly from one. [6, 7]

Although more difficult to quantify, the fracture characteristics of diamond crystals can greatly affect overall performance of the final product. The fracture characteristics may be assessed by examination of fractured crystals. This will include the debris produced by toughness or strength tests, including the size and shape of the fragments. Tough (high-strength) diamonds break down via splintering of the crystal edges, producing large and medium fragments and splinters. Many blocky crystals with smooth facets remain. Friable diamonds, by contrast, fracture more completely, producing few large fragments and many small pieces with a rough, irregular texture. The fracture characteristics are affected by many factors: crystal morphology, shape and the type, content, and distribution of inclusions [6].

1.3 Microstructure of nickel based brazing materials

Nickel-based materials such as Ni-Cr-P and Ni-Cr-B-Si are widely-used brazing alloys in several applications [2]. The reason for the high bonding strength between diamond and the Ni–Cr-based brazing alloy is the reaction and formation of carbides at the diamond/braze filler material interface during the brazing process. Carbides such as Cr_3C_2 and Cr_7C_3 have been reported to form on the diamond surface [16]. It has also been reported that there is no graphite formation when chromium is present in the braze material, but that graphite forms when pure nickel braze materials are used [16].

As is widely acknowledged, diamond is the hardest known material, making it ideal for many types of tool manufacture. Commercial synthetic diamond crystals are relatively small in size and the brazing process by which the crystals are fitted on to the tool body is made in a controlled atmosphere or vacuum. Table 3 below presents the brazing filler metal groups, of which at least nickel, copper, gold, silver and palladium-based materials can be used to braze diamonds. In general, the chosen braze filler material has to have high mechanical strength to hold up the stress of the tool in use. In this work only nickel-based braze materials are under examination because of their good corrosion resistance and high mechanical strength [9, 10, 11].

Table 3. Brazing filler metal groups. [2]

| Brazing filler-metal groups	Joining temperature °C
Ni, Co, and Pd alloys	≥1100
Cu, Ni, and Au alloys	≥1100
Cu-Zn, Cu-Sn, Ni-P, Ni-Cr-P, Pd-Ag-Cu	≥900
Cu-P, Cu-Ag-P	600–800
Ag-Cu-Zn, Ag-Cu-Zn-Cd	600–800
Al-Si	580–600
Mg-Al-Zn	585–615

The braze filler materials Ni-Cr-P and Ni-Cr-Si-B contain phosphorous or boron and silicon respectively – these act to reduce the melting temperature and improve the flux of the alloy for brazing. Silicon can be added to the alloy for this same purpose, as it is in the Ni-Cr-Si-B type brazing alloy as presented in Table 4 below. Table 4 presents most of the common commercial nickel-based brazing materials with varying compositions for different applications. It can be said that these alloys contain phosphorous or boron and silicon to reduce the melting temperature of the brazing alloy; note the relatively high silicon and chromium content of alloys BNi-1, BNi-1a and BNi-5.

Important information about the melting temperatures and phase compositions of Ni-P, Ni-B, Cr-P, Cr-B, Ni-Si and Cr-Si binary systems is given in Figures 6 - 9, where the binary phase diagrams of the components involved in this work are presented together with the phases formed during solidification [12]. The results are used further on during the analysis of the formed braze structures.

Table 4. Composition (American Welding Society AWS standard) presented together with the brazing temperature range of some commercial grades of nickel-based brazing materials including Ni-Cr-Si-B (BNi-2) and Ni-Cr-P (BNi-7), brazing filler materials. [2]

	Cr	B	Si	Fe	C	P	S	Al	Ti	Mn	Cu	Zr	Ni	Brazing T/°C
BNi-1	13.0–15.0	2.75–3.50	4.0–5.0	4.0–5.0	0.6–0.9	0.02	0.02	0.05	0.05	...	...	0.05	bal	1065–1205
BNi-1a	13.0–15.0	2.75–3.50	4.0–5.0	4.0–5.0	0.06	0.02	0.02	0.05	0.05	...	...	0.05	bal	1075–1205
BNi-2	6.0–8.0	2.75–3.50	4.0–5.0	2.5–3.5	0.06	0.02	0.02	0.05	0.05	...	...	0.05	bal	1010–1175
BNi-3	...	2.75–3.50	4.0–5.0	0.5	0.06	0.02	0.02	0.05	0.05	...	...	0.5	bal	1010–1175
BNi-4	...	1.5–2.2	3.0–4.0	1.5	0.06	0.02	0.02	0.05	0.05	...	...	0.05	bal	1010–1175
BNi-5	18.5–19.5	0.03	9.75–10.50	...	0.1	0.02	0.02	0.05	0.05	...	...	0.05	bal	1150–1205
BNi-6	...	...	...	...	0.1	10.0–12.0	0.02	0.05	0.05	...	...	0.05	bal	925–1095
BNi-7	13.0–15.0	0.01	0.1	0.2	0.08	9.7–10.5	0.02	0.05	0.05	0.04	...	0.05	bal	925–1095
BNi-8	...	...	6.0–8.0	...	0.1	0.02	0.02	0.05	0.05	21.5–24.5	4.0–5.0	0.05	bal	1010–1095
BNi-9	13.5–16.5	3.25–4.0	...	1.5	0.06	0.02	0.02	0.05	0.05	...	...	0.05	bal	1065–1205

Figure 6 presents the binary phase diagram of the nickel - phosphorous system. According to the phase diagram the melting point of the binary alloy with 11 wt.-% of phosphorous is about 870°C. Figure 7 presents a similar phase diagram for the binary chromium - phosphorous system. According to the information it is possible that when chromium is dissolved into the braze material it slightly increases the brazing temperature. These two phase diagrams also show that the solidified braze forms two different phases with this phosphorous content: a face-centred cubic (FCC) nickel-based phase with about 0.17 wt.-% of phosphorous in it and X_3P phase where X can be nickel and chromium. The crystal structure of the Ni_3P phase is tetragonal, space group I$\overline{4}$, the dimensions for the unit cell being a=8.954 Å and c=4.386 Å. The Cr_3P phase has the same crystal structure I$\overline{4}$ with unit cell dimensions a=9.185 Å and c=4.560 Å. [6, 14, 15]
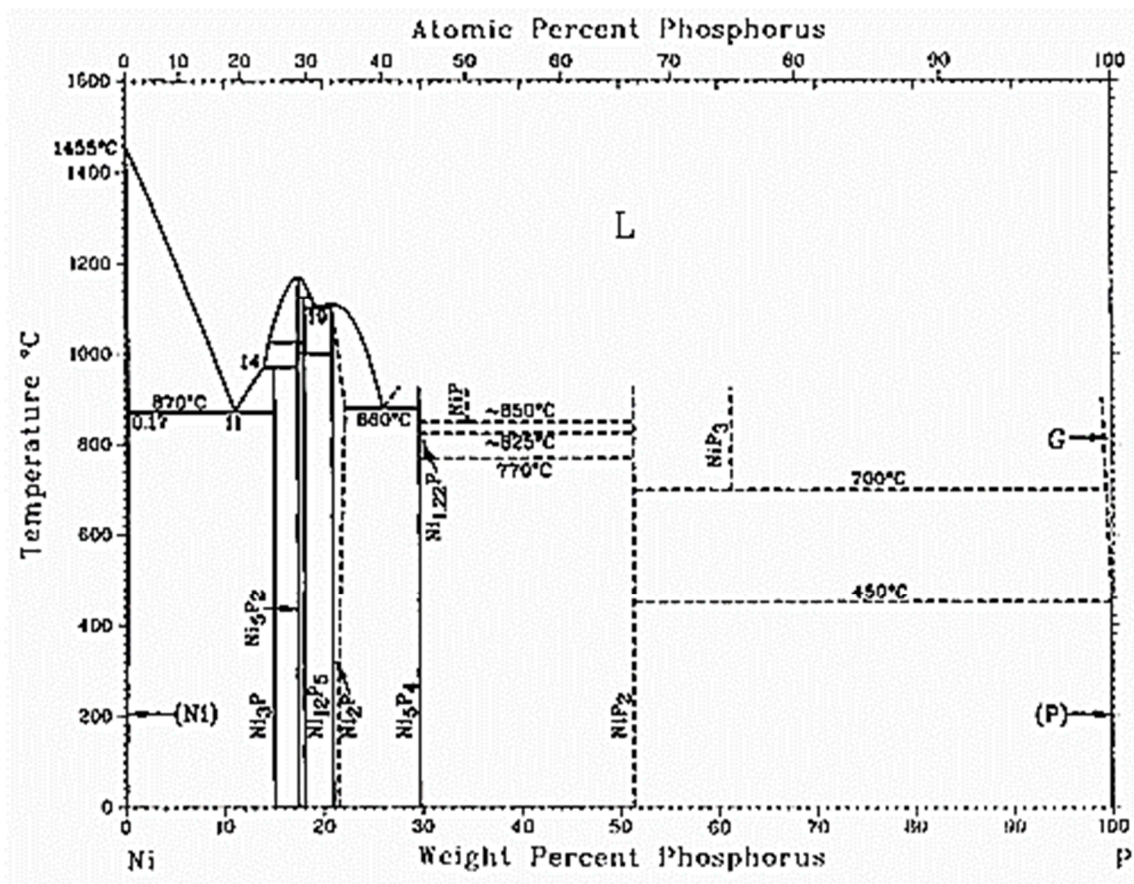
Phase	Composition, wt% P	Pearson symbol	Space group
(Ni)	0 to 0.17	cF 4	Fm $\overline{3}$m
Ni_3P	15	tI 32	I $\overline{4}$
βNi_5P_2	17.5	...	...

Figure 6. Nickel - phosphorous binary phase diagram and table of phases present and structural information of the phases. [12]
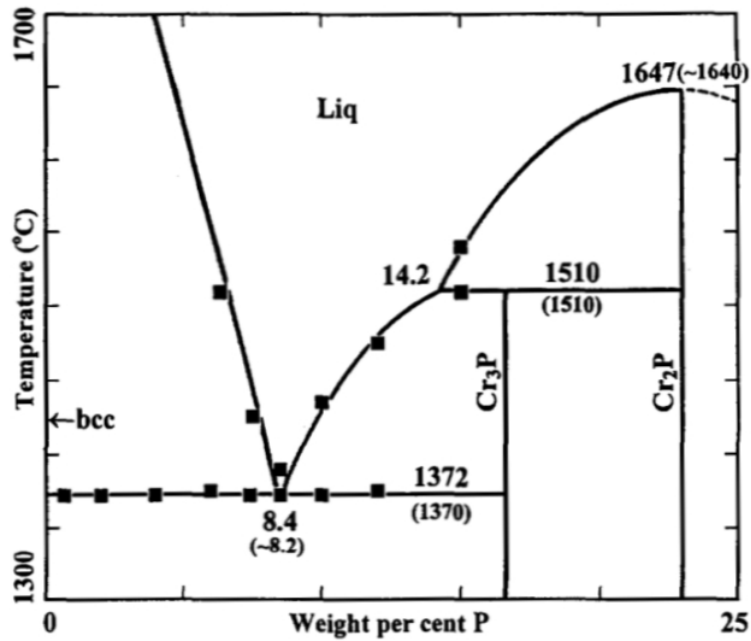
Figure 7. Binary phase diagram for chromium - phosphorous systems. [13]

Figure 8 presents the binary phase diagram of the nickel - boron system. According to the phase diagram the melting point of the binary nickel - boron alloy with 3.1 wt.-% of boron is slightly under 1100°C. Figure 9 presents a similar phase diagram for the chromium - boron system, where it can be seen that the melting point of this alloy is high: 1630°C with a boron content of 3.1 wt.-%. The high melting point indicates the increased brazing temperature when the nickel-based brazing filler material is significantly alloyed with chromium. The formed phases together with nickel or chromium rich phase in this case are Ni_3B for binary nickel - boron system and for chromium - boron binary system Cr_2B phase. Furthermore, because of the high melting point, Ni-Cr-B brazing alloys are also typically alloyed with silicon.
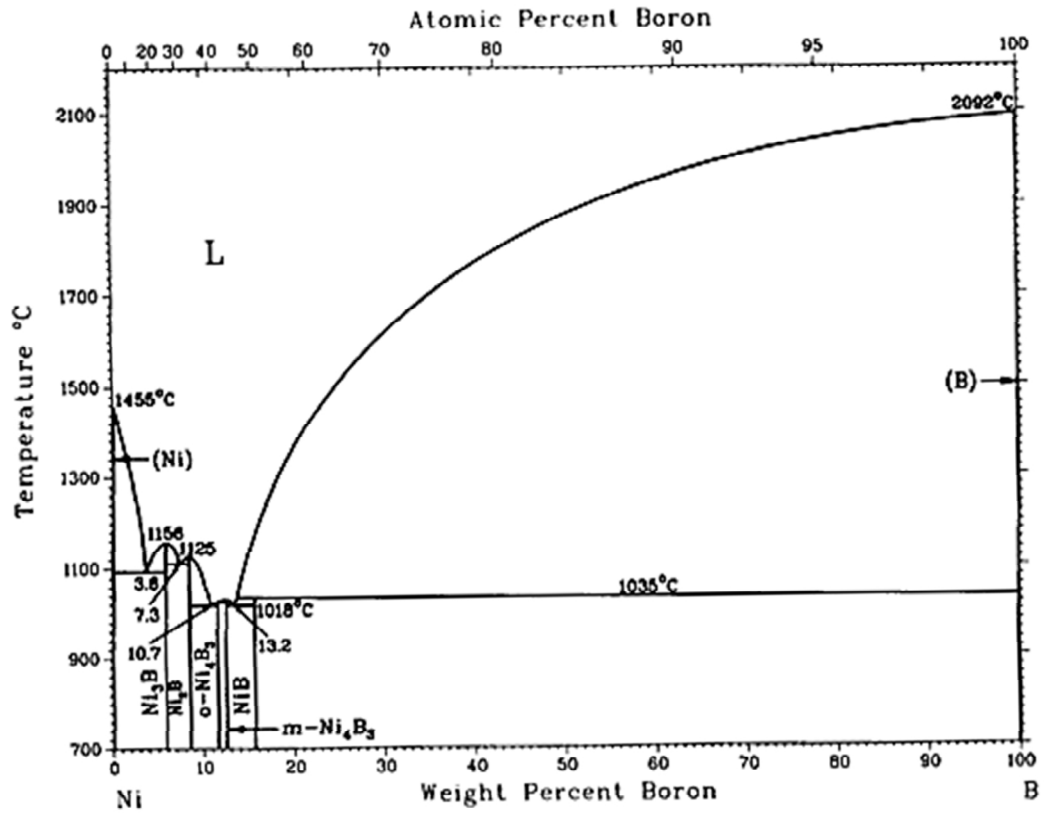
Phase	Composition, wt% B	Pearson symbol	Space group
(Ni)	0	cF 4	Fm $\overline{3}$ m
Ni$_3$B	6	oP 6	Pnma
Ni$_2$B	8.4	tI 12	I 4/mcm

Figure 8. Nickel - boron binary phase diagram with a table of phases and their structural information. [12]
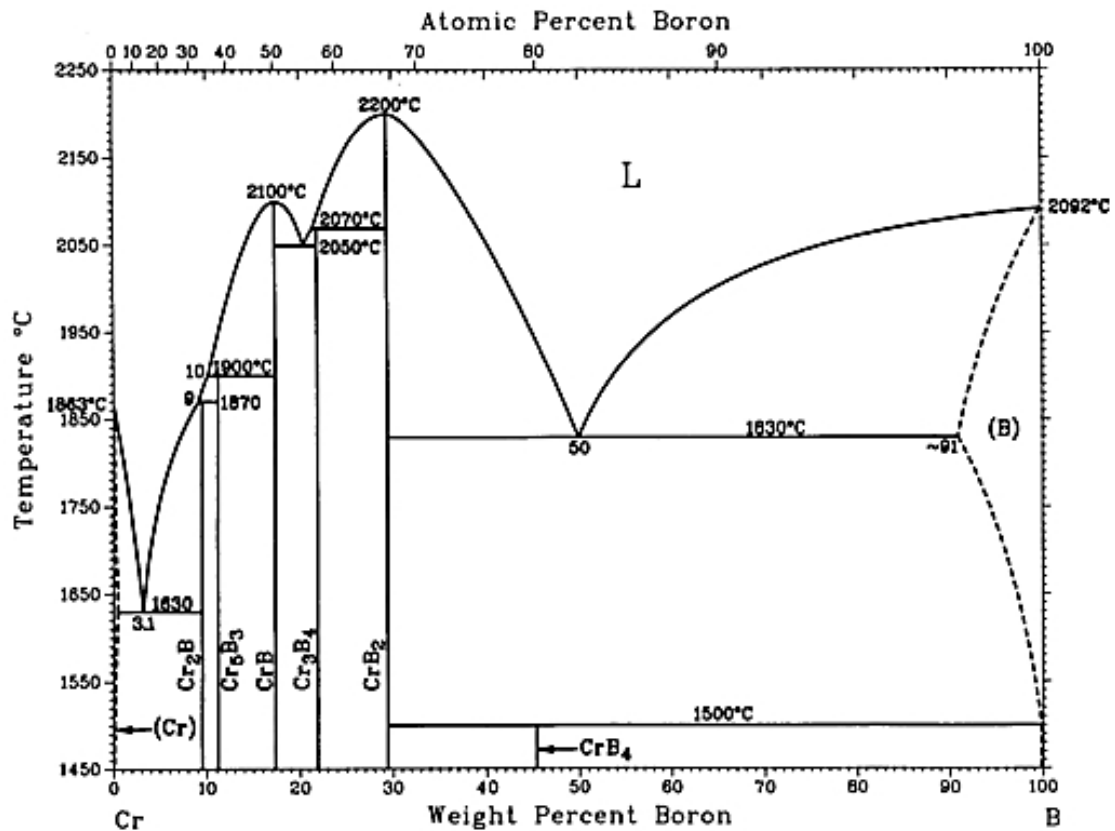
Phase	Composition, wt% B	Pearson symbol	Space group
(αCr)	0 to ~ 0.2	cI 2	Im $3n$
Cr4B(a)	5	oF 40	Fddd
Cr$_2$B	9.4	oF 40	Fddd

Figure 9. Chromium - boron binary phase diagram with a table of phases and their structural information [12]

Nickel-based brazing materials are frequently used filler metals for stainless steel and super alloys when a high strength material with good corrosion resistance is necessary. Nickel-based brazing filler metals provide joints that have excellent corrosion resistance, mechanical strength and mechanical strength at high temperature. These filler metals are typically supplied in the form of powders mixed with an organic binder. A limited number of filler metals are also available as sintered rods, preforms, and foils [2].

However, the brazing filler metals may react with stainless steel based materials, forming intermetallic phases with two undesirable characteristics. First, the phases are considerably less ductile than either the base metal or the filler metal, even at elevated temperatures, and are therefore a potential source of rupture. Secondly, the alloys formed with stainless steel have a higher melting point and are likely to freeze during the brazing process, where temperatures block further brazing filler metal flow into the joint. Because of the relatively high brazing temperatures required for the nickel brazing filler

12

metals, their use is generally limited to furnace brazing in a controlled atmosphere. This includes vacuum furnaces and is also the case when the single diamond crystals are brazed. [2, 12]

The data in Figure 10 presents X-ray diffraction (XRD) curves of the rapidly solidified amorphous or semi-amorphous foil of boron containing Ni-Cr-Si-B brazing filler alloy – this is shown through the low and wide diffraction peaks and a similar curve for the same crystallized alloy after its heat treatment at 930°C. Crystallization of the nearly amorphous foil is carried out during the heat treatment procedure. The FCC nickel-based phase is formed together with the Ni_3B phase. One diffraction peak coming from silicon is also identified in the Figure 10, but in this case it is not very probable that the braze material contains pure silicon after the heat treatment procedure, silicon should be dissolved into nickel based matrix as the binary phase diagram presented in Figure 11 presents. Referring back to Figure 8, the heat-treated structure represents the structure seen in the binary phase diagram, consisting mainly of a face-centred cubic FCC nickel phase and Ni_3B phase. The diffracted intensity peaks from the Ni_3B phase are relatively low compared to the intensity peaks of pure nickel. This makes the identification of the diffraction peaks considerably more difficult.
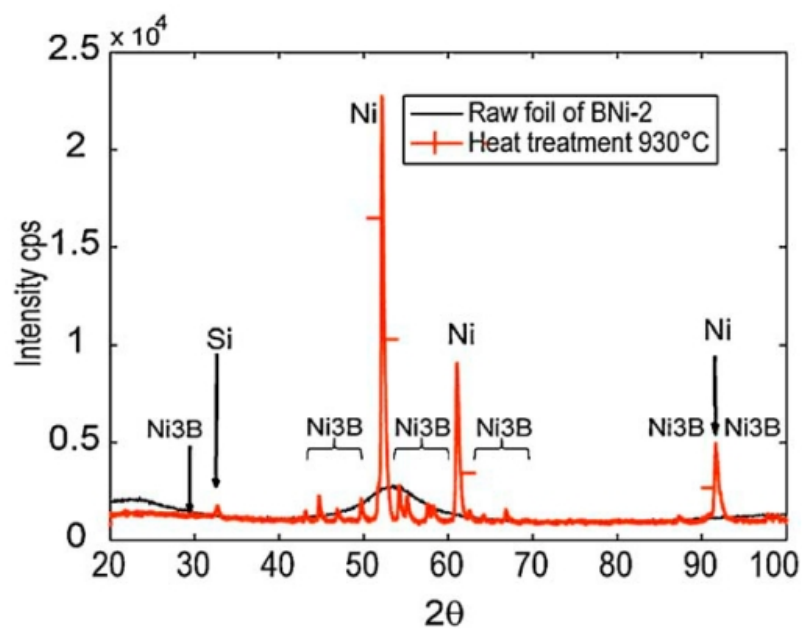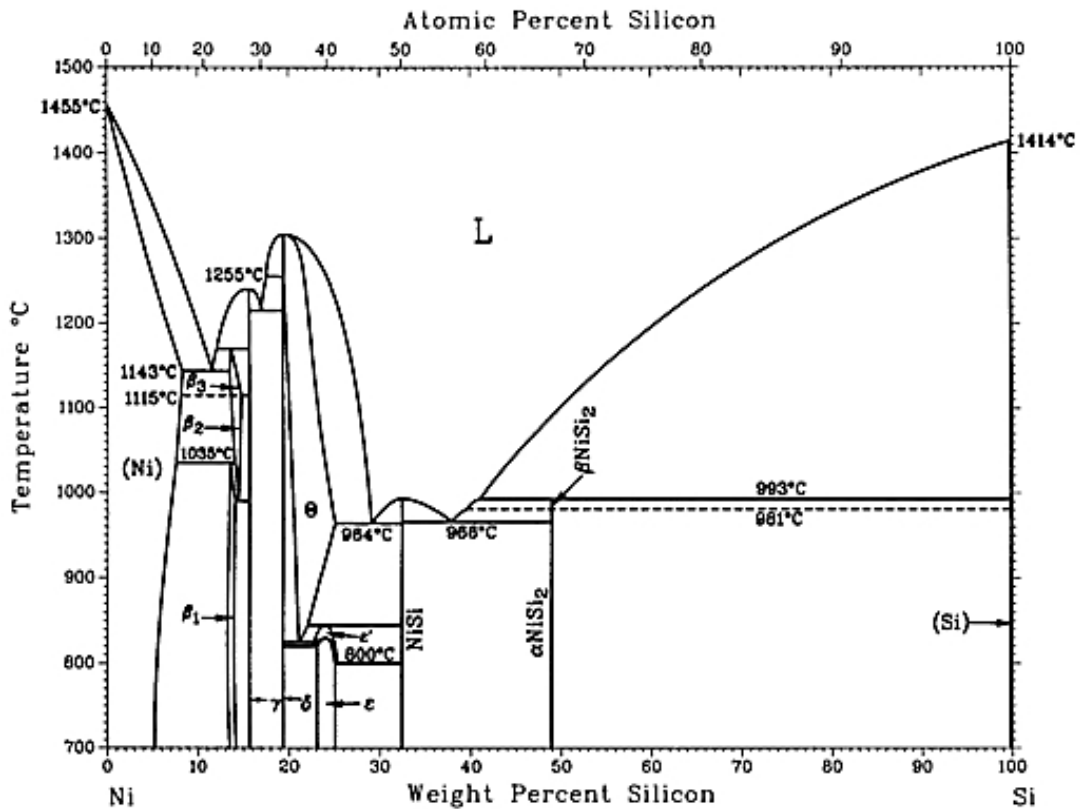

Figure 10. X-ray diffraction (XRD) diagrams of the as received rapidly solidified Ni-Cr-Si-B foil and the material after heating up to 930°C [18].

Phase	Composition, wt% Si	Pearson symbol	Space group
(Ni)	0 to 8.2	cF 4	$Fm\overline{3}m$
β_1 (Ni$_4$Si)	12.4 to 13.4	cP 4	$Pm\overline{3}m$
β_3 (Ni$_3$Si)	~13.4 to 14.1	mC 16	...
β_2 (Ni$_3$Si)	~13.4 to 14.1	mC 16	...

Figure 11. Nickel - silicon binary phase diagram, the table of phases and their structural information. [12]

Figure 12 shows the typical microstructure of a re-solidified Ni-Cr-Si-B brazing filler alloy, Ruiz-Vargas et al. [18]. Figure 12 c) depicts the related chemical maps measured with the Energy Dispersive X-ray (EDX) analyser for the same specimen area. Below Figure 12 is Table 5, reporting the mean chemical compositions measured across the different components of the microstructure. Four main components can be detected: rod-like chromium borides (type Cr_2B with low Si content) and shown as the pink phases in Figure 12 c); nickel borides (type Ni_3B, with addition of Fe and Cr and a low Si content) as shown in the blue phases; a FCC Ni-based component with a Si addition (green phase), containing cuboidal precipitates, which are likely the ordered FCC Ni_3Si-based ϒ' phase; and a multi-phase component rich in Si and B (the blue/green regions of Figure 12 c) [18]. A question arises when looking at these results: why are the crystalline chromium borides not identified in the X-ray diffraction curve shown in Figure 10?
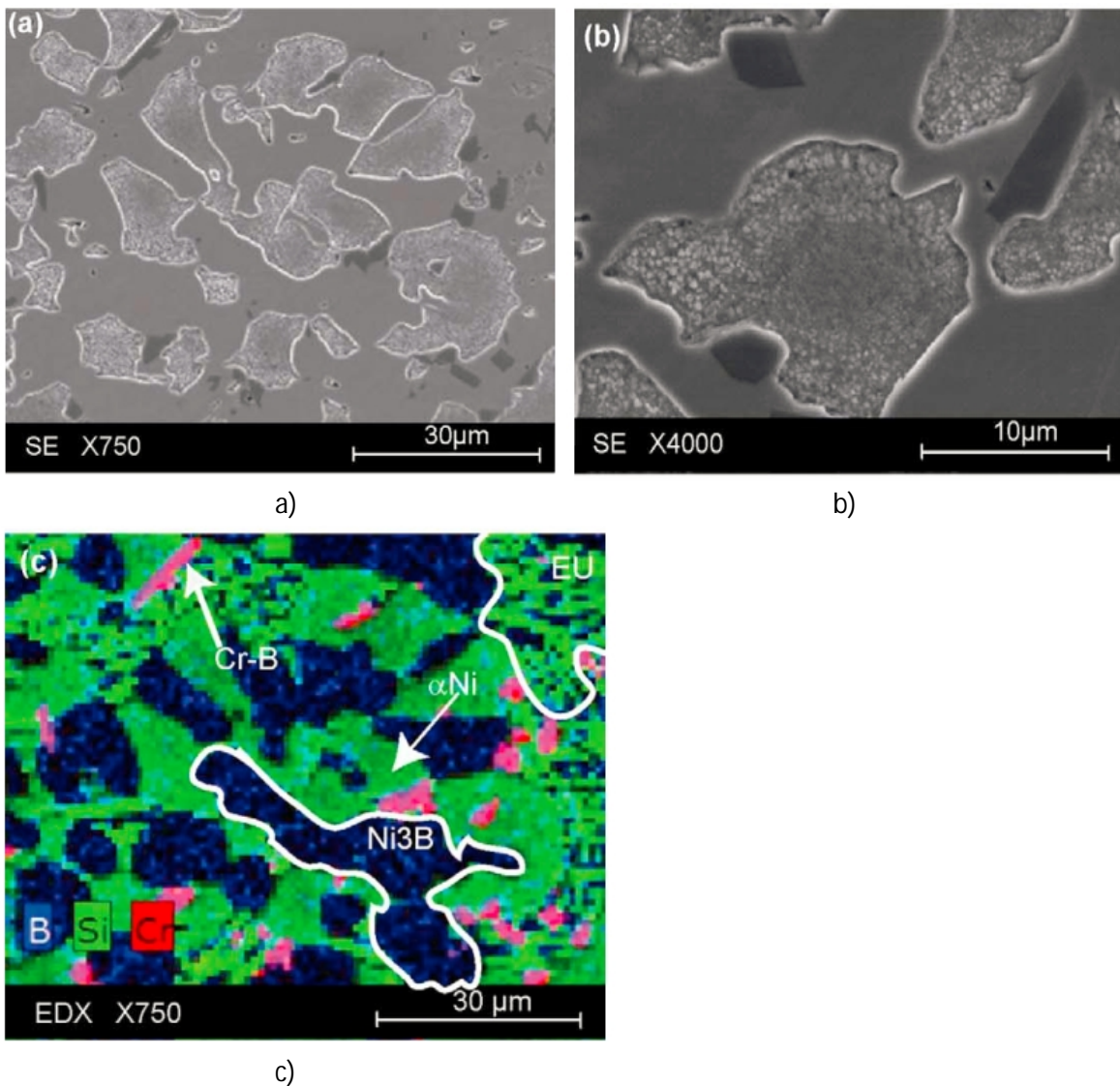
Figure 12. Scanning Electron Microscope (SEM) images of typical microstructure of a re-solidified Ni-Cr-Si-B alloy. Micrographs taken with two magnifications are shown in (a) and (b), and (c) presents an Energy Dispersive (EDX) elementary map of boron, silicon and chromium obtained through the same zone as in (a). [18]

The volume fractions of Cr-B, bulky Ni_3B, Ni, Υ' (Ni_3Si) and eutectic phase mixture were estimated to 7 %, 36 %, 40 % and 17 %, respectively [18]. It can be noted that the XRD analysis on the crystalized state (in Figure 10) and the microstructure characterization on the re-solidified state (presented in Figure 12 and Table 5) agree significantly. Indeed, the two main components Ni_3B and FCC Ni/Υ' are detected in both cases with comparable amount ratios. Ni_3Si-based Υ' phase cannot be well differentiated from Ni by XRD since they have similar crystal structure. The Cr_2B phase was observed with a low-volume fraction after solidification, which could explain why it was not detected on the XRD patterns. However, it is also possible that Cr_2B and Ni_3Si-based Υ' phases were not present after crystallization from the amorphous state, due to an energy barrier for their solid-state nucleation [18]. Table 6 below depicts the phases of equilibrium, the composition and amount for the Ni-Cr-Si-B alloy at temperatures of 1050°C and 650°C. [18]

15

Table 5. Composition and amount of phases present in the re-solidified Ni-Cr-Si-B alloy. The vol.-% was calculated using 3.3 g/cm^3 density for chromium boride, 8.2 g/cm^3 for Ni$_3$B and the estimated density value of 8.9 g/cm^3 for the other nickel-based constituents, temperature 20°C. [18]

Phase	Amount (vol%)	Amount (wt.%)	Chemical composition (wt.%)				
			Ni	B	Si	Fe	Cr
CrB	7	2.6	3.6	19.1	0.2	0.6	76.5
Ni$_3$B	36	35.8	85.4	8.2	0.2	2.3	3.9
αNi + γ'Ni$_3$Si	40	43.3	82.0	2.1	5.5	4.5	5.9
Eutectic	17	18.3	85.7	1.6	8.6	1.6	2.4

Table 6. Equilibrium phases (composition and amount) predicted by 'ThermoCalc' calculation program with TTNI7 database for Ni-Cr-Si-B alloy at 1050°C and 650°C. [18]

Temperature	Phase	Amount (wt.%)	Chemical composition (wt.%)				
			Ni	B	Si	Fe	Cr
1050°C	CrB type boride	7.9	1.64	17.11	0.00	5.37	75.88
	Ni$_3$B type boride	13.5	87.48	5.81	0.00	6.15	0.56
	αNi phase	55.4	91.43	0.04	6.60	1.29	0.64
	Liquid	23.2	85.56	4.02	3.66	4.43	2.33
650°C	CrB type boride	8.2	0.13	17.17	0.00	2.94	79.76
	Ni$_3$B type boride	29.1	88.51	5.80	0.00	5.55	0.14
	αNi phase	43.9	92.05	0.00	5.19	2.46	0.30
	γ'Ni$_3$Si phase	18.8	86.38	0.00	11.82	0.35	1.45

1.4 Interaction between diamond single crystals and elemental metals and alloys

According to Chen et al. [43] the brazing of the diamond grits using the Ag-Cu-Ti and Ni-Cr brazing filler alloys produced interesting results. Variations in the morphology of the brazed diamond grits, such as graphitization, erosion, micro-cracking and fracturing are observed. The compressive strength and Thermal Toughness Index (TTI) of the brazed diamond single crystals were evaluated. The results obtained show that the morphologies of the original, unaltered diamond grits are similar to those of the brazed diamond grits. When the diamond grits were brazed using the Ag-Cu-Ti-alloy disadvantageous phenomena, i.e., graphitization, erosion, micro-cracking and fracturing were not observed and the compressive strength and the TTI values of the brazed diamond grits only slightly decreased. However, when the diamond grits were brazed with the Ni-Cr alloy, surface graphitization, erosion, micro-cracking and fracturing of the brazed diamond grits resulted. There was also a significant reduction in the mechanical strength of the brazed diamond grits [43]. Following conclusions on the morphologies and mechanical properties of diamond can be reached [43]:

1. The Ag-Cu-Ti alloy has little effect on the morphologies and mechanical properties of diamond grits. The morphologies of the resulting brazed diamond grits are similar to that of the unaltered diamond grits, while the compressive strength and the TTI-values of the brazed diamond grits were decreased by 6 % and 5 %, respectively.

2. The Ni-Cr alloy results in graphitization, erosion, micro-cracking and fracturing of the brazed diamond crystals. However, the graphitization only occurs on the surface of the diamond grits. The erosion of brazed diamond grits is readily apparent and significant. Additionally, micro-cracking of the diamond grits appears near interfaces. Meanwhile, the compressive strength and the TTI-values of brazed diamond grits are decreased by almost 40 % and 84 %, respectively.

3. Because a decrease in the mechanical strength of diamond crystals would undesirably affect the grinding performance of brazed diamond tools, the Ag-Cu-Ti-alloy is a more suitable choice for use in these tools than a Ni-Cr alloy, if the difference in corrosion resistance of these alloys is not taken into account.

A question arises here concerning the mechanism of the degradation of diamonds when nickel-based chromium containing braze materials are used: how does the brazing process really affect the single diamond crystal surface? Another question arises when thinking about the results presented: How does high residual stress on the surfaces of single diamond crystals occur, if there is graphitization observed on the diamond surface? This mechanically weak graphite layer should relax the tension between the diamond and the nickel-chromium braze filler material.

Images of diamond grits brazed with both braze alloys Ag-Cu-Ti and Ni-Cr presented above are shown in Figure 13, in Figure 13 a) there is a diamond brazed with the Ni-Cr alloy and in Figure 13 b) diamond brazed with the Ag-Cu-Ti alloy. These micrographs demonstrate that each brazed diamond single crystal is supported by the corresponding underlying brazing filler metal. Additionally, the attachment of the diamond grits is further reinforced by chemical bonding between braze and the single diamond crystal [43].
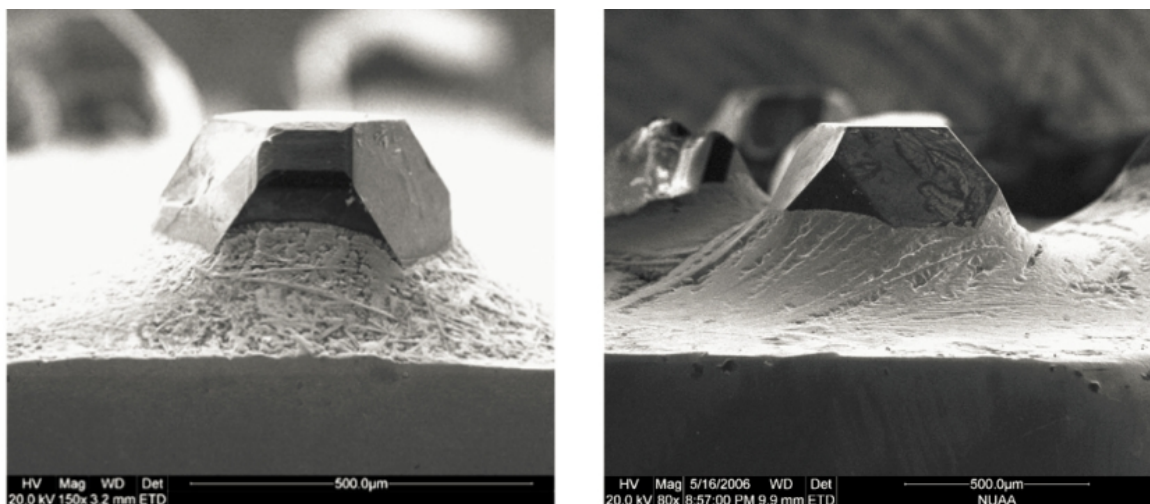
a)   b)

Figure 13. Images of diamond single crystals brazed with the different brazing filler metal: (a) diamond brazed with the Ni-Cr alloy and (b) diamond brazed with the Ag-Cu-Ti alloy [43]. There are only slight differences in wettability and also in the surface structure between these braze filler materials.

Additionally, a Scanning Electron Microscope (SEM) image and Energy Dispersive X-ray analysis (EDX) line scan along the indicated line of interface between brazed diamond single crystal and Ni-Cr alloy

are shown in Figure 14 a) and b). Nickel is a catalyst that can promote the transformation of diamond to graphite under normal pressure and high temperatures (above 800°C), and it can also dissolve the carbon element. Furthermore, chromium is a carbide forming element. Both of the elements mentioned above can result in a significant reduction of the carbon on the surface of the single diamond crystals, as well as in pit formation. Hence, the erosion is mainly caused by the change of the structure of the carbon element from diamond to graphite, the reaction between the Ni-Cr alloy and carbon, and the dissolution of carbon into the liquid brazing filler metal at high temperatures. [43] The location of silicon, chromium and carbon given by the line analysis demonstrate that chromium forms carbides but silicon does not. The uneven polished specimen surface is seen as a reduced carbon content in the line analysis just inside the diamond crystal.
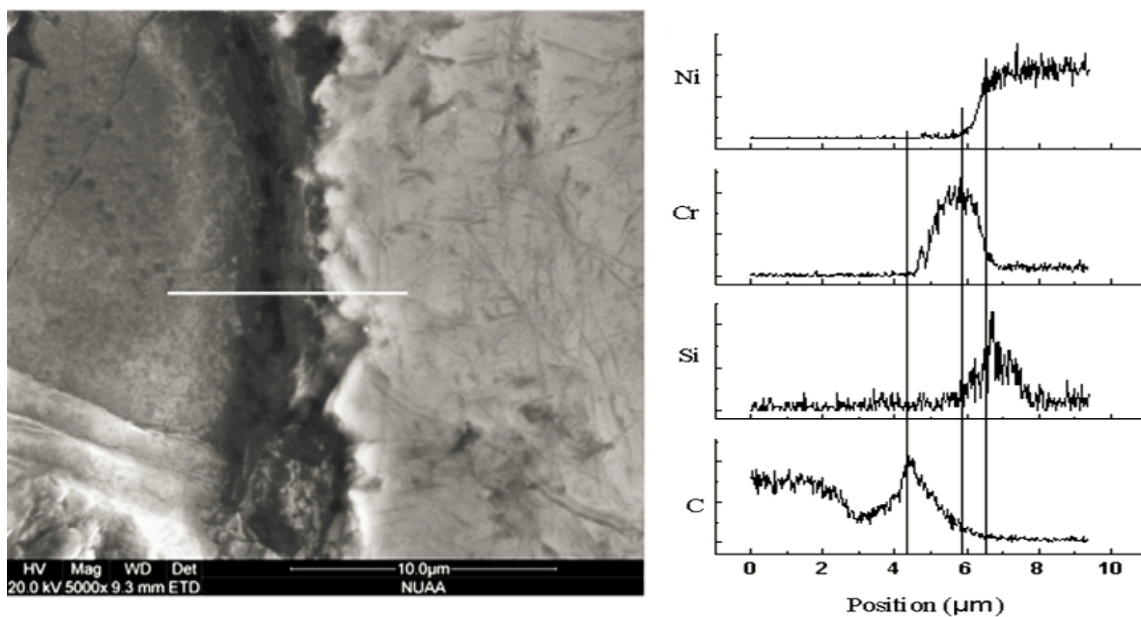
a)   b)

Figure 14. SEM image and EDX line analysis along the indicated line of interface between brazed single diamond crystals and the Ni-Cr alloy: (a) SEM image, (b) EDX line analysis scan along the indicated line [43].

When analysing the results presented above one has to remember that EDX-analysis is not a very accurate method when the measured surface is not perfectly polished and especially when light elements such as carbon are analysed together with heavy ones such as nickel and chromium [44]. This is the reason why in the experimental part of this work the intermediate layers between the braze material and diamond were analysed using Backscattered Electron Images (BSE) instead of EDX-microanalysis.

When comparing the erosion of single diamond crystals brazed with the Ag-Cu-Ti alloy or the Ni-Cr alloy there is a significant difference, as presented in Figure 15. The morphology of the brazed diamond grits is like that of the unaltered single crystals, although the edges of the single crystals are not as sharp as the unaltered diamond grits; additionally, many small pits are present on the surface of crystals. This can be seen in Figure 15 b) below, which has been brazed with the Ni-Cr alloy. The

presence of the pits on the surface indicate that the diamond grits have been corroded during the brazing process. [43]

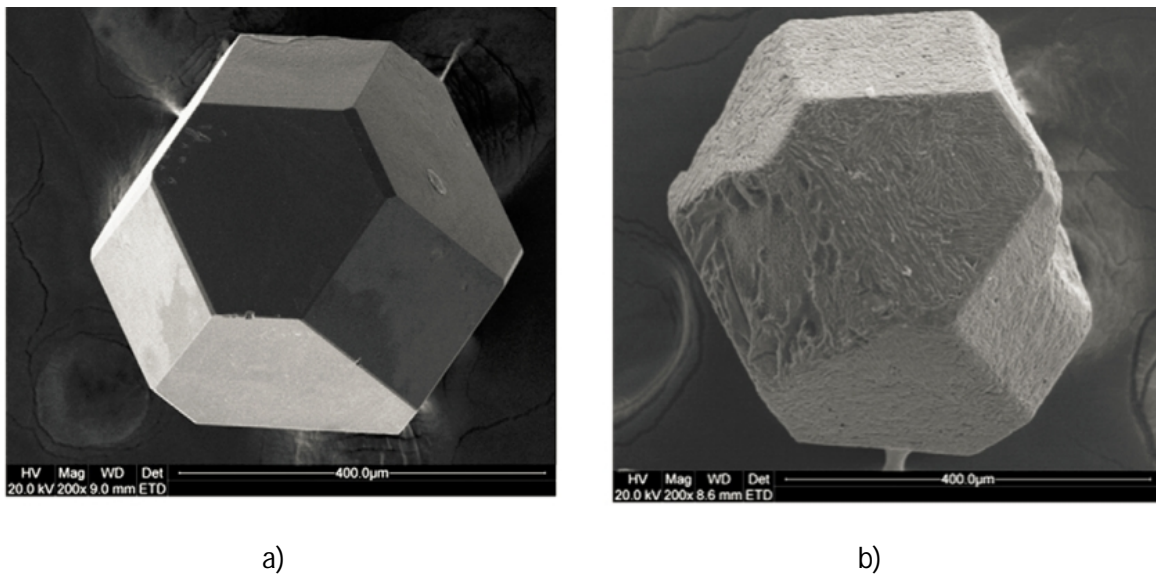a)   b)

Figure 15. Damage on brazed single diamond crystals after removal of the brazing filler metal: (a) Surfaces of a diamond grit brazed with the Ag-Cu-Ti alloy; (b) Surfaces of a diamond grit brazed with the Ni-Cr alloy. [43] Note the significant difference of the surface morphology between these grits.

To evaluate the effect of a particular brazing filler metal selection on the mechanical properties of single diamond crystal grits, the compressive strength and thermal toughness index (TTI) of diamond grits were investigated, Chen et al. [43]. The compressive strength and TTI of diamond grits treated in a vacuum at different temperatures were measured to clearly distinguish between the effects of high temperatures versus on the brazing filler metal. The results are shown in Table 7. The compressive strength of the diamond grits decreases with increasing treatment temperature and is further reduced because of the brazing process. The brazing process using the Ag-Cu-Ti alloy has a minor effect on the compressive strength of the diamond grits; that is, the compressive strength of the brazed diamond grits decreases by 6 % compared to the diamond grits brazed with the Ni-Cr alloy, where the compressive strength decreases by nearly 40 %. In contrast, the temperature of the vacuum heat treatment has a small effect on the TTI value of the diamond grits. Similarly, the TTI value of diamond grits is also reduced because of the brazing process. The TTI value of the diamond grits brazed with the Ag-Cu-Ti alloy is decreased by 5 %, while the diamond grits brazed with the Ni-Cr alloy decreases their TTI value by nearly 84 %. [43]

Due to the use of a high brazing temperature and the significant differences in the material properties between the single diamond crystals and brazing filler materials, interfacial stress between the steel substrate and brazing filler metal is induced. To investigate the resulting interfacial stress, an axial symmetric model was established along the central line of symmetry by Chen et al. [43]. In the Finite Element Model (FEM), the development of interfacial-stress in the brazed joint specimen was computed to simulate cooling from the brazing temperature down to room temperature. The results of FEM analysis are shown in Figure 16. [43]
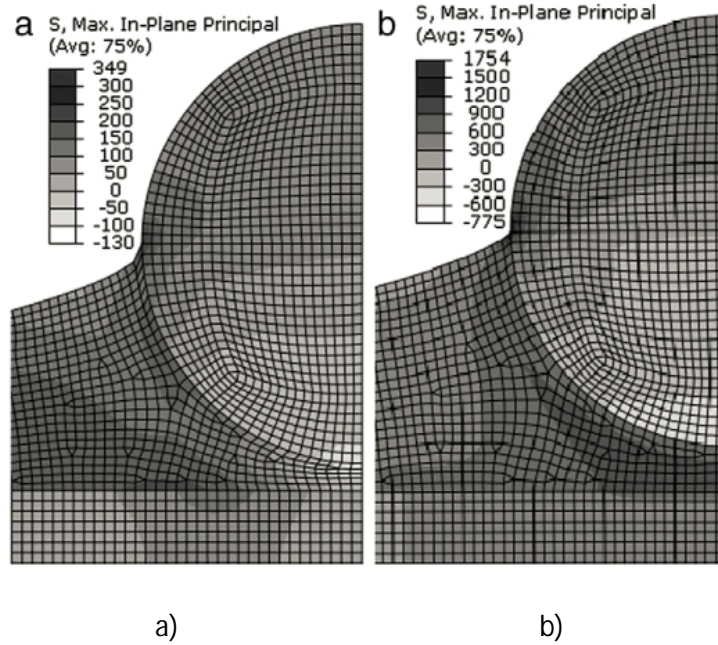
Figure 16. The distribution of interfacial stress in a brazed joint, (a) the maximum principal stress when using the Ag-Cu-Ti-alloy, (b) the maximum principal stress when using the Ni-Cr alloy. [43]

According to the results presented in Figure 16, the highest thermal stress exists near the interface between the diamond grits and brazing filler metal. The value of the maximum tensile residual stress reaches 349 MPa for the Ag-Cu-Ti alloy and as high as 1.754 GPa for the Ni-Cr alloy, i.e., the interfacial stress in the joint brazed with the Ag-Cu-Ti alloy is significantly lower than that of the Ni-Cr alloy. Such significant residual tensile stress in the joint brazed with the Ni-Cr alloy can exceed the tensile strength of the diamond grits (1.32–2.5 GPa) [43] and initiate cracking near the interface of the diamond grits. Here, the modelled maximum stress for the Ni-Cr system is showing overly high values: the stress should, in this case, be relaxed by yielding the braze material matrix. Useful information in Figure 16 is the location of the maximum stresses near the diamond crystals.

Table 7. A comparison of the parameters of diamond single crystals treated under different conditions. [43]

Treatment type	Compressive strength (N)	TTI (%)
Unaltered	166.700	75
Vacuum heat treatment (920 °C)	162.167	75.5
Vacuum heat treatment (1050 °C)	157.167	74.5
Vacuum brazing with Ag–Cu–Ti alloy	156.683	71.2
Vacuum brazing with Ni–Cr alloy	103.300	11.8

1.5 Wetting of diamond single crystals by metals and alloys

In order to use brazing to join different materials together, wetting and low contact angle between the brazed materials is determining the quality of the joint [2]. Naidich et al. (1988) [39, 40] found that wetting between diamond and other elements and contact angles Θ_c are determined directly by the nature of the components involved, which correlates well with the work of adhesion of atoms on a diamond surface. They also proved that wettability or work of adhesion, W, correlates well with the enthalpy of formation of the highest carbide existing in any particular metal-carbon system. Therefore, the following order of wettability may be postulated on the basis of thermodynamic data for the enthalpy of carbide formation for the important metals shown in Table 8: Ni, Co, Fe, Cr, Nb, Ta, Ti and Zr. Here nickel has the minimum work of adhesion whereas zirconium should have the maximum value. It is important to underline that nickel and cobalt do not wet diamond under any of the temperature, pressure and environmental conditions applied [39]. Non-transitional elements from group IIB of the periodic table interact with diamond in the liquid state only via physical interaction and thus have very large contact angles. For example, Cu, Ag, Au, Ga, Sn and their alloys have Θ_c about 120-150°. In the case of the carbide-forming transition metals, wetting of diamond occurs with the creation of a carbide film. This is because metal atoms have a tendency to build strong chemical bonds at the interface. Therefore, metallic layers that are in contact with diamond have a different nature and structure from that of the matrix. Thus, use of the term 'wetting' in the case of transition metals is rather conditional because of the practically instantaneous diamond/metal chemical bonding. It is worth mentioning that the larger the similarity between the diamond crystal's carbon atomic pattern and the forming carbide, the better the wetting and lower the contact angle. This has been confirmed by observation of a lower contact angle on a {111} type diamond plane than that on {100} type plane. [16]

The wetting of diamond by solid metals during the annealing process of diamond/metal composites is important since metal-diamond bonds can exist only on the joint interface. This wetting occurs via metal vapour condensation, which when solidification process begins, form small metal droplets that then grow into complete films, Rabinkin, 1982 [41]. It was also noticed that many alloys containing carbide-forming elements start to wet at much lower temperatures than corresponding elemental metals. An interesting phenomenon was also observed [41], when considering diamond wetting by chromium containing alloys and pure chromium. Thus, at low temperatures (about 900°C) chromium carbides appear on the socket surface like small drops of liquid, with a high surface tension (see Figure 17 below). Wetting or carbide formation on diamond occurs only at 1000°C, as demonstrated in Figure 18. When used as an annealing atmosphere, nitrogen contributes to the wetting by iron starting from 900°C; however, in the cases of niobium, zirconium and Inconel-type nickel-based super-alloys it reduces wetting and carbide formation substantially. According to the reference [16] stainless steel grade AISI 316L also wets diamond like a liquid with high tension – this is similar to pure chromium, as presented in Figure 17 b).
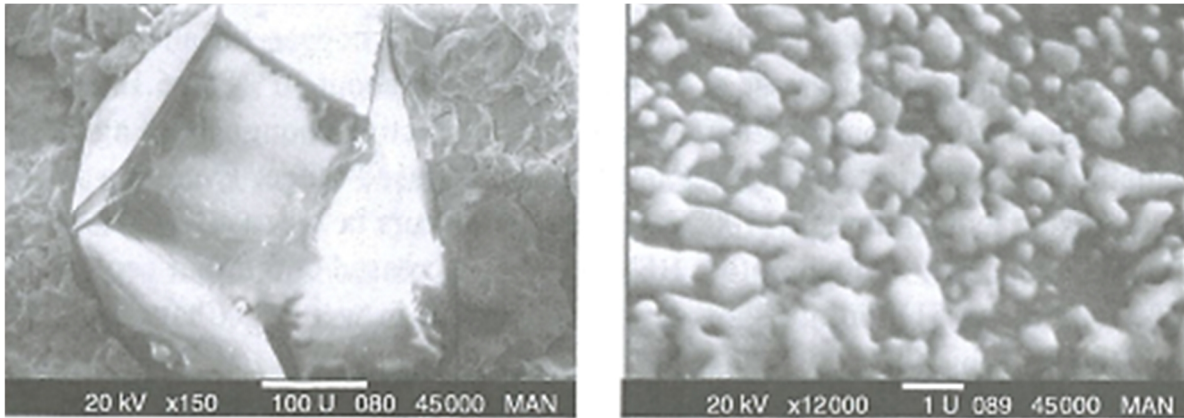
a)   b)

Figure 17. Wetting of diamond single crystal surface, (a) diamond-chromium interaction in a vacuum at 900°C for 5 hours. Carbide formation starts on a socket surface (b), carbides appear as frozen droplets of a liquid with high surface tension seen using higher magnification. [16]
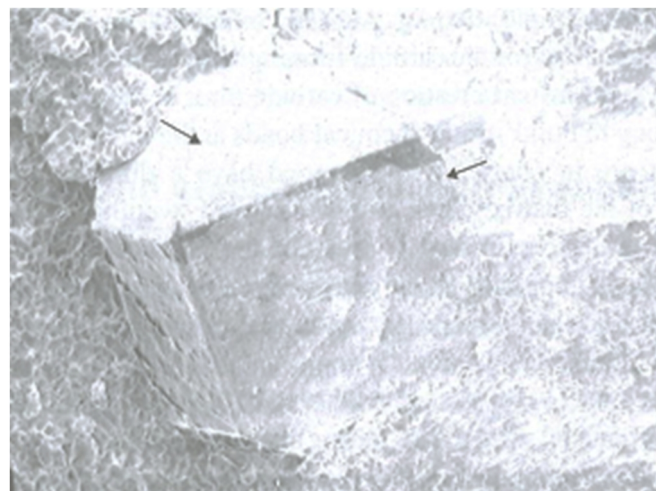

Figure 18. Diamond/stainless steel, grade AISI 316L composite sintered at 1000°C for 5 hours. Good formation and attachment of the even chromium carbide film occurs on all crystallographic planes marked with arrows. [16]

1.6 Interface between diamond single crystals and braze material: Basic nature of the interactions

Especially when brazed using nickel-based chromium-alloyed brazing filler materials, single diamond crystals are affected by the aggressive brazing material at high brazing temperatures [37, 38]. Both the diamond-metal interaction and the structure of the diamond/metal joint interface depend on the nature of the atomic bonding between the carbon and metal atoms [37, 38]. This in turn is also determined by the crystallographic orientation of the diamond crystal lattice surface on which the carbon atoms are positioned when reacting with metals and metal compounds, mostly forming carbides in the process. One of the important effects of crystal orientation is the different wettability of diamond planes with different crystal indexes [16]. Detailed analyses of such interactions are given

22

by Naidich et al. (1988) [39, 40] and Rabinkin (1981) [41]. Alloy phase diagrams containing carbon as one of the elements under consideration are well-constructed and reliably express what may be formed from these interactions, not only at the diamond/filler metal (FM) interface, but also in the metal volume outside the interface. They also help to predict what kind of carbon/metal compounds should be expected in the interface area. Practically all aspects of the interaction of any particular metal or alloy with diamond depend on whether or not it forms stable carbide. Important transition metals have rather diverse free energies of carbide formation, as is presented in Table 8.

Table 8. Standard free energy ΔF of formation of some metal carbides per atom in kcal/g-atom= ΔF kcal/mol/(x+y), where x and y are taken from carbide formula Me_xC_y. [16].

	Metal							
	Ni	Co	Fe	Cr	Nb	Ta	Ti	Zr
Highest carbide	Ni_3C	Co_2C	FeC	CrC	NbC	TaC	TiC	ZrC
ΔF at:								
1200 K	1.525	0.5	−0.09	−5.34	n/d	−18.45	−20.15	−20.35
1300 K	1.475	0.4	−1.62	−5.32		−18.4	−20.00	−20.15
Sign of $\partial (\Delta F)/\partial T$	<0	<0	>0	<0	n/d	~0	<0	<0

The second important factor is the solubility or diffusion of carbon in the liquid brazing filler metal and in the base metal's solid state. This solubility depends on the temperature and pressure applied. Selected elements of the periodic table can be separated into three different batches according to the type of diamond-element interaction. Batch 1 consists of elements, such as Ag, Au, Cu, Zn, Al and others, which normally do not form any compounds with carbon. Most of the IIB-group elements have relatively low energy for atomic bonding with diamond and, therefore, dissolve carbon in minuscule quantities in both their liquid and solid states. The corresponding phase diagrams in these cases have no areas with any noticeable carbon solubility in the solid state of these metals. Batch 2 consists of transition-metals forming carbides, such as V, Ta, Cr and others, whereas batch 3 contains transition metals, which include for example Ni and Co. The elements dissolve diamond in its liquid phase but do not form carbides. [16]

1.7 Formation of carbides on a diamond single crystal surface during the brazing process at high temperatures

According to Naidich et al. [39, 40], transition elements of IV-VI groups of the periodic table and silicon and boron have very strong chemical bonds with carbon, forming carbide layers with a rather permanent composition. The Me-C binary phase diagrams for Body Centred Cubic BCC elements Zr, Ti, Ta and Nb systems demonstrate the existence of the $(Me)_xC_y$ carbides [12]. Figure 19 a) shows a schematic diagram of carbide formation in the Ti-C and Zr-C systems, while Figure 19 b) presents the general outline of the carbon concentration profile at the diamond/metal interface during diamond-metal interaction at temperatures higher than 1000°C.
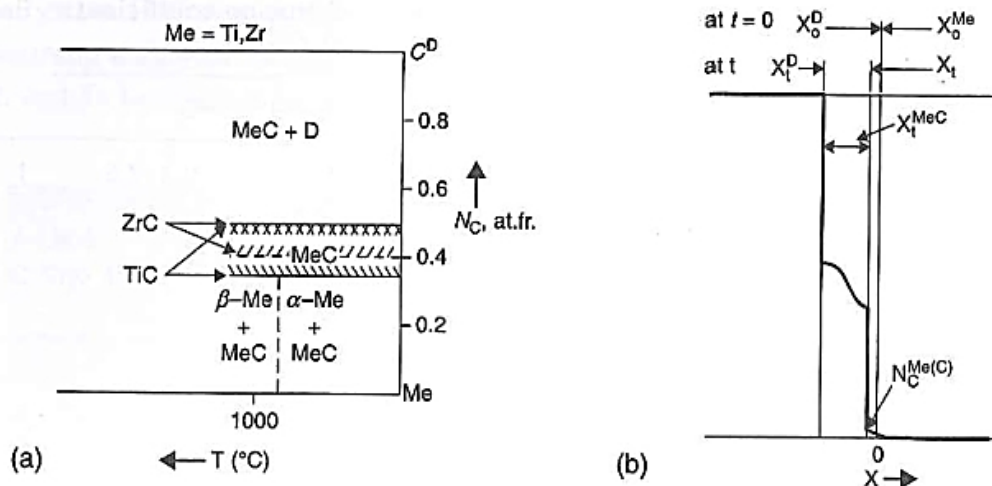
Figure 19. Formation of carbides according to Ti- and Zr-C partial phase diagrams (a) and general outline of the carbon-concentration profile at the diamond-metal interface during diamond-metal interaction at temperatures higher than 1000°C. Here t is the time, X^D is the diamond dimension at times t=0 and t=t; X^{Me} is the metal in contact dimension at t=0 and t=t; $N_C^{Me(C)}$ is the carbon concentration; and C^D is the concentration of carbon in diamond, $C^D = 1$. Figure (b) presents the general outline of the carbon concentration profile at the diamond-metal interface. [16]

Carbide-formation in joints occurs via the reactive diffusion process. The morphology of the carbide layer formed by Zr, Ta and Nb on a diamond surface is the same as the morphology of the diamond surface [40]. These layers are very even and uniformly cover all crystal diamond facets, as is presented in Figure 20. In the case of titanium the attachment is not as good as that in Zr, Ta or Nb. The strength of the interface between the diamond and any formed carbide keenly depends on the close epitaxial relationships of their crystal lattice parameters. The closeness is determined by any misfit between atomic positions in both crystal lattices. The strength of the diamond-carbide bond will be at its maximum when the misfit is at a minimum. Moreover, due to differences in the atomic dimensions on different atomic planes, this strength is not constant on crystal planes with different indexes. [16]
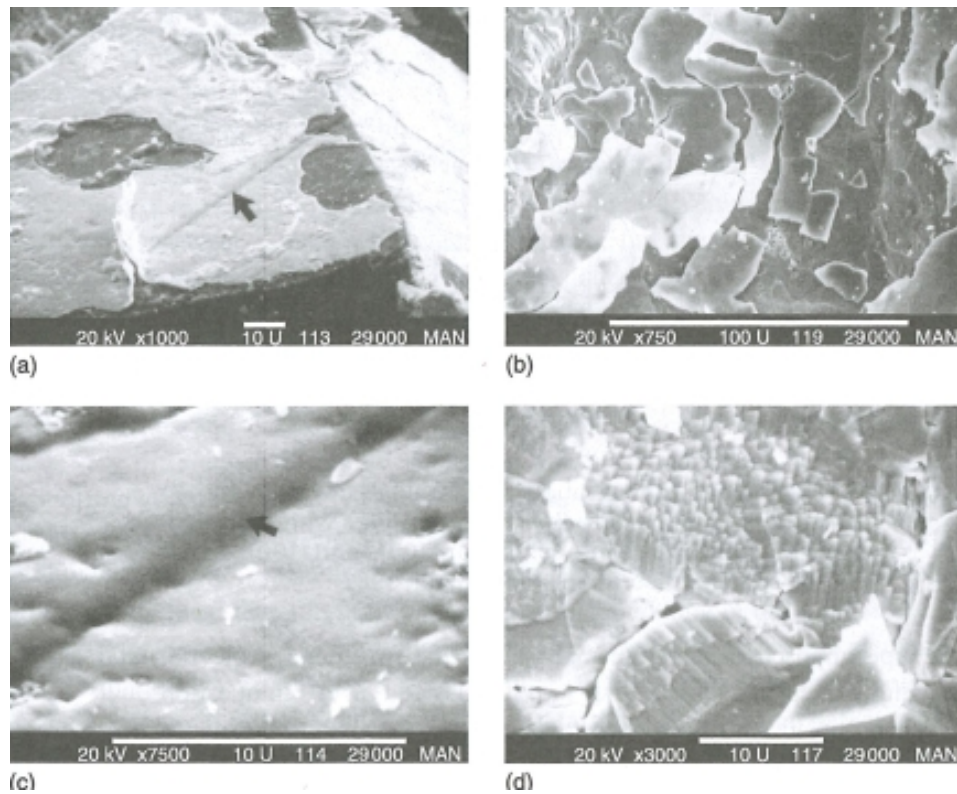
Figure 20. A thin epitaxial carbide film formed on the diamond surface during sintering of diamond in zirconium powder at 1000°C for 5 hours in a vacuum. The film is uniform and covers all crystal facets and even the original crystal growth steps, arrows on (a) and (c). The longer sintering time results in overgrowth, which leads to loss of bonding with both the diamond (b) and the matrix, (d) fracture occurs on both D/ZrC and ZrC/Zr interfaces. [16]

To understand the possible reasons for this, it is worth considering the structural patterns and lattice constants of diamond and the highest carbides (MeC) of Ti, Nb, Ta and Zr with the structure. Figure 21 shows $(100)_{MeC}$ and $(110)_{MeC}$ projections of MeC (B1) carbide on which $(100)_D$ and $(110)_D$ diamond projections are superimposed. Figure 21 also shows $(110)_{Me}$ metal projection and lattice-spacing discrepancies for four of the carbides and metals in question. When considering these structural patterns and lattice constants, there are notable similarities between the $(100)_D$ and $(111)_{MeC}$ planar nets of diamond D and carbides when $(100)_D$ II $(110)_{MeC}$. Specifically, the closest proximity and the strongest atomic bonds calculated were found by Yamazaki et al. (2009) [17] between diamond and V_4C_3 carbide lattices in the case of the interface with $(111)_D$ and $(111)[111]_{V4C3}$ indexes. [16]

The difference *V*, in Figure 21 below, between the lattice spacing of diamond and carbides is in the range favourable for epitaxy: that is, -7 % for ZrC and up to 14 % for TiC. Therefore, formation of the thin carbide epitaxial layer on a diamond surface might be expected on the sites where carbon atoms dissolve. On the other hand, in the case of graphite, *V* is substantially higher and there is no convenient orientation relationship. These circumstances might be the reasons for the different contact behaviours of various forms of carbon. It is worthwhile mentioning that for titanium the difference *V* has the highest value of the four carbides. This could explain why titanium carbide has the worst attachment to diamond among all carbide-forming elements. Therefore, the use of a titanium coating before brazing for diamond grit may not be the best choice.

25

There are important details of the carbide-formation process worth noting at this point. First of all, the volume changes during formation of metal carbides by various metals and diamond are negative. Moreover, carbon and metal atoms have very different diffusivities. Therefore, the mass transfer is not capable of supporting volume-continuity. This results in porosity of the carbide film with the interface area. Epitaxial formation of thin carbide films on the diamond surface might be expected during annealing in the solid state not only with Zr, Ta, Nb and Ti, but also with powders of alloys containing these elements. [16]
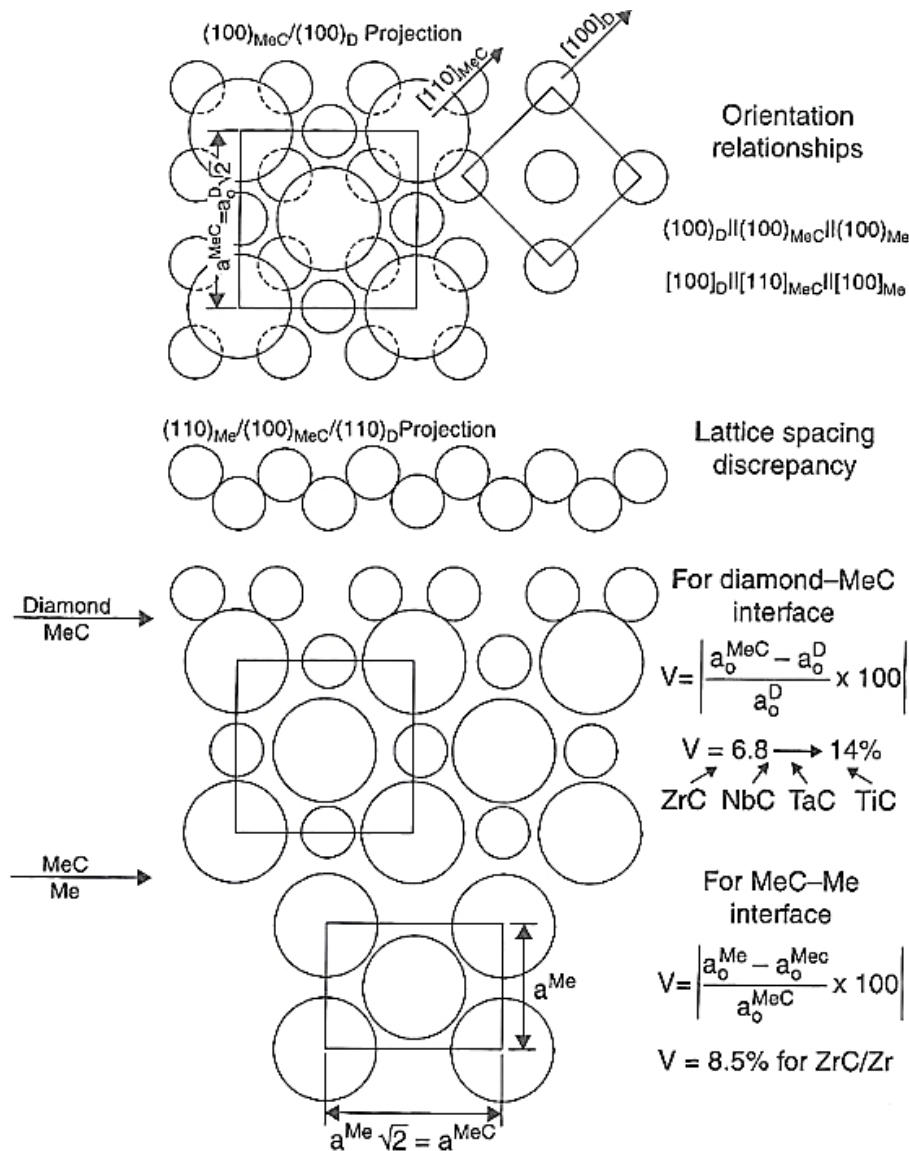

Figure 21. Schematic presentation of crystal lattices of diamond D, some body centred cubic BCC transitional metals, and their (Me)C carbides. Possible epitaxial relationships for (100)$_D$ and (100)$_{Mec}$ planes and lattice spacing discrepancy. [16]

This formation is very important for sintering diamond/metal composite tools. Nevertheless, any crystal defects, such as edges or corners of crystals, dislocations, crystal growth steps, etc., occur where the diamond-metal interaction starts. The most interesting phenomenon found is the decrease

of the selective sensitivity of the diamond-metal interaction with an increase in the metal affinity with carbon. Specifically, in diamond crystal-metal composites made via sintering with Ni, Co or Fe, the reaction starts and develops first at defects or on very uneven surfaces with numerous steps, pits, etc. In interactions involving Zr, Nb and Ta, uniform and complete carbide films appear on all kinds of crystal facets, regardless of the presence of similar diamond defects. Therefore, dissolution proceeds uniformly, so that the majority of the crystals preserve their original shape during joining. Carbide films formed by alloys are very different from those formed by their elemental constituents. Their formation starts at much lower temperatures. [16]

Strong and regular atomic bonds formed on the diamond/carbide interface result in good attachment of the carbides to diamond when the carbide thickness is small (0.1-0.5 μm). The appearance of fine and regular porosity in joint components after annealing and brazing in both vacuum and a nitrogen atmosphere might be an additional source of carbide film brittleness. For elements which do not form carbides on diamond surface due to low affinity to carbon (Ni, Co, Fe), wetting hardly occurs.

1.8 Graphitization of diamond surface during annealing and brazing treatments

The diamond graphitization process starts at high temperatures in a vacuum or other medium that *does not assist* graphitization. For pure natural diamond grit this temperature is 1500°C or higher [16]. Graphitization of the diamond-metal composites 'nickel + diamond', 'cobalt + diamond' and 'iron + diamond' was observed in a vacuum at 1000°C, Rabinkin [41]. The retention of graphitized diamond is poor and, therefore, should be avoided during diamond joining. It was also shown that the use of nitrogen as an annealing atmosphere retards this process. [16]

Since the activation energy of graphitization for different diamond crystal planes is different, one would expect that if diffusion proceeds via graphitization, then the rate of diffusion would be strongly dependent on the crystallographic directions. The microstructures observed in sintered diamond-metal composites clearly display spherically-shaped regions enriched by a carbon 'halo' that surround single crystals with various crystallographic planes in contact with the matrix. Furthermore, strong carbide-forming elements yield uniform carbide films on different crystallographic planes. The same behaviour was confirmed by direct measurements of the carbon concentration along different crystallographic directions by Rabinkin [41]. These results suggest that the dissolution and diffusion rates on a macro level are affected weakly by the diamond crystal plane crystallographic indexes. [16]

The reaction mechanism of the interface between diamond, commercial Ni-Cr-P alloy and steel substrate was studied using optical microscopy, a scanning electron microscope (SEM), X-ray diffraction (XRD) and Raman spectroscopy by Tillmann et al. [45] and Wang et al. [46]. The reaction layers formed between diamond, the brazing alloy and steel substrate produced good wettability of diamond grits. The reaction layer between diamond and the brazing alloy comprised separate reaction layers of brazing alloy and diamond. Cr_7C_3 and Cr_3C_2 carbides formed in the reaction layer of brazing alloy was the main reason for improving the bonding strength of the Ni-Cr alloy to the diamond grits. A reaction layer of diamond may be a graphitization layer formed on the surface of diamond under high temperature brazing. The life and sharpness of the brazed diamond boring drill-bit fabricated was superior to the electroplated one already on the market, owing to its high protrusion and bonding strength. [45, 46]

The microstructure, phases and carbides that formed between diamond, the brazing alloy and steel substrate were studied in a commercial Ni-Cr-P alloy. The reaction layer at the interface produced good wettability of diamond grits (essential for achieving better quality tools). Two chemical reaction layers between brazing alloy and diamond and between brazing alloy and steel substrate improved the high bonding strength of the brazed diamond grits. Separate reaction layers of brazing alloy and diamond were found within the reaction layer of brazing alloy and diamond.

1.9 Thermal properties of diamond – braze composites

The Coefficients of Thermal Expansion (CTE) in the range of cooling temperatures are presented in Figure 22 below for the Ag-Cu braze material, TiC, AISI 316L base material and natural diamond [47]. As presented in Figure 22 the thermal expansion of TiC is nearly the same as the value of diamond while the other materials have clearly higher values.

One important property of diamond is that it cannot substantially dissolve any element. Conversely, however, carbon atoms of diamond dissolve and react with metals, forming a variety of metal carbides. In this respect, the diamond-metal interaction is literally one-directional: all joint formation, including morphology, phase composition and joint stresses arising from joining, occurs outside the diamond surface in the metal or alloy volume. Rabinkin [41] has shown that the dissolution of both diamond and graphite happen at almost the same rate being slightly faster in diamond's case. It is very likely that the diffusion of carbon from the diamond into the metal matrix at moderate temperatures occurs via direct diamond dissolution without the intermediate conversion to a graphite stage [16]. This dissolution starts at the diamond crystal corners, edges, crystallization defects, dislocations, etc. For Ni, Co and Fe matrixes, the dissolution process occurs step by step along the planes of the diamond crystals. However, the selectivity of dissolution strongly decreases as the carbide-forming ability of the matrix metal increases. Thus, carbide formed by Zr, Nb and Ta have equal thickness for all facets and edges, as Figure 23 presents below. [16]
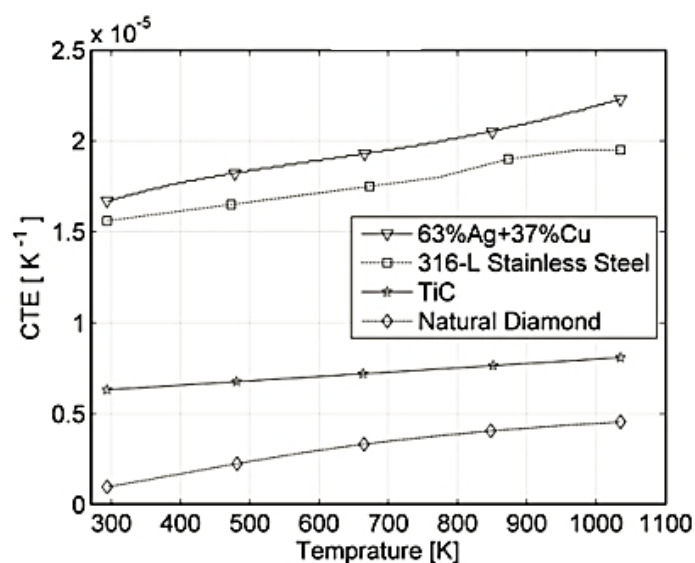

Figure 22. Coefficient of Thermal Expansion (CTE) of four materials in the range of cooling temperature in the brazing procedure [47].
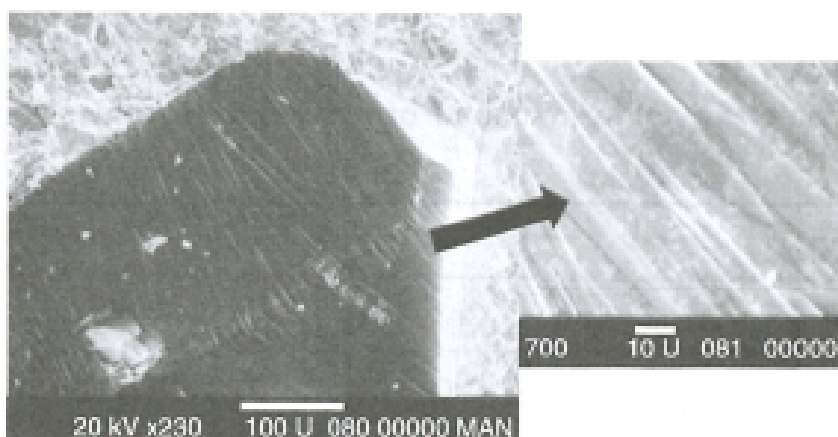
Figure 23. Carbide film formed on diamond surface sintered with niobium at 800°C, with a sintering time of 5 hours in a vacuum furnace. Film morphology depends neither on the metal matrix morphology nor on the crystal plane indexes. Niobium carbides bands spread around the crystal, which appears as if it is completely wetted. [16]

Relative to the rate of diamond dissolution, all metals can be divided into two categories: carbide forming and non-carbide forming. The solubility in non-carbide forming metals depends on the limit of carbon solubility in the metal at a given temperature and pressure. It can be stated that the higher the solubility, the higher the rate of carbon diffusion and therefore the higher the rate of diamond dissolution. [16]

For carbide forming elements, if the carbon solubility is low, the rate of dissolution is nearly equal to the rate of carbide formation at the diamond-metal interface. Therefore, as was mentioned, the formed carbide protects the diamond because the carbon diffusion rate through a carbide film is extremely low. When the solubility is high, the rate of dissolution is a compromise between the carbide build-up and the carbon diffusion from the carbide-metal interface into the Me-C solid solution. Since the solubility of diamond depends on diffusion processes and capillarity effects occurring in the metal and carbide, it is worthwhile considering some of the parameters of diffusion for some metals and carbon in metals and carbides, as presented in Table 9. This data clearly demonstrates an enormous difference in the rate of diffusion of carbides and metals by both metals and carbon. The coefficients of diffusion in carbides are of the order of 10^{-4} to 10^{-5} times smaller than those in metals. In all the various cases of diamond dissolution the two factors determining when it occurs are the diffusion processes between components of all virgin phases in base metals' newly formed phases, and their comparative rates. Dissolving carbon may precipitate in the metal matrix, forming small carbide particles. Usually this process is accompanied by strong dispersion hardening, which was observed in most of the metals and metal matrixes. Brazing and annealing diamond/metal composites in nitrogen during sintering decrease the diamond dissolution rate in both cases, for it decreases carbon activity in Υ-Fe, as was proven by direct measurements in the samples annealed in a vacuum and in a nitrogen atmosphere. [16]

Table 9. Parameters of carbon and metal diffusion in various metals and carbides. [16]

Material	Temperature (°C)	Activation energy for diffusion, Q (kJ/mol)		Diffusion coefficient, D_0 (cm²/sec)	
		Metal*	C	Metal*	C
Ni	700–1365	267–280 (Ni)	167	0.4–1.3 (Ni)	0.9–2.5
Fe					
α	900–1050	249 (Fe)	80.3	5.8 (Fe)	0.167–0.006
γ		280 (Fe)	135	1.3	0.1
Nb			139		0.004–0.015
			113		
NbC		531 (Nb)	393	0.11 (Nb)	0.11
Ti					
α			182		5.06
β			203		1.08
TiC		737 (Ti)	399	4×10^{-4} (Ti) (!)	7
ZrC		720 (Zr)	460	1×10^{-3} (Zr)	14

*Metals being referred to are given in parentheses.

1.10 Mechanical strength of diamond single crystals and nickel based brazing materials

Mechanical strength of the braze-diamond construction commonly defines the life span of the tool. This makes the mechanical testing of the tool a very important issue. The strength of diamond to diamond joints and diamond to metal-brazed joints cannot be measured using standard testing methods for mechanical properties due to the small size of the brazed diamond particles or inserts. The average diameter of the synthetic diamonds is typically well under 0.5 mm when they are brazed on the tool base. Therefore, indirect methods are developed and used for the mechanical characterization and quality assessment of brazed joints. For example, the three-point bending test of a steel plate coated with brazed diamond grains gives statistically proven characteristics of the mechanical behaviour of brazed joints made at different temperatures in a vacuum by different filler metals, such as Ni-Cr-Si-B, BNi-3 and BNi-6 presented in Table 4. According to Tillmann et al. [19] specimens for the bending test were manufactured on chromium-nickel steel plates, brazed on 300-400 µm diamond grits, situated in the region expected to have the biggest deformation during the test. The number of diamond grits still remaining in the brazed metal coating after the test would indicate joint strength, dependent on brazing temperature, holding time and bending angle. [19]

According to the studies of Tillmann et al. [19] brazed joints made with boron containing a Ni-Cr-Si-B braze material exhibited good results. At brazing temperatures in the range of 1005-1080°C with a holding time of 10 to 15 minutes - almost 100 % of the diamond grits were intact, while lower brazing temperatures were associated with only 50 % intact diamonds. The phosphorous containing BNi-6 filler metal demonstrated the opposite behaviour: an increase in the brazing temperature of over 1000°C resulted in worsening quality, to 55 % intact diamonds at 1100°C. BNi-6 containing 3-5 % of chromium demonstrated good, high quality wetting when brazing the diamond, with 96 % of the

diamond grits being intact after being subjected to joining at 950-1000°C with only 5 minutes of holding time. Results of the studies give good guidelines for choosing brazing parameters. [19]

Interfacial bonding strength between various brazing filler metals and chemical vapour deposition (CVD)-formed diamond is tested by Y-C. Hsien et al. [20]. Nine nickel-based alloys, including the most interesting alloys Ni-Cr-Si-B and Ni-Cr-P, together with frequently used Cu- and Ag-based alloys, were tested. The best bonding strength, about 280-400 MPa, was achieved for joints prepared using Cu-10Sn-15Ti and particularly with silver-based brazing materials. According to these results the brazed interface was stronger than the bulk of the joints [20]. Notable is that the popular BNi-series (AWS) alloys presented in Table 4 containing B or P as the melting point depressants caused the catalytic degradation of diamond into $sp2$-bonded carbon because of the presence of Ni in the filler metal base. As a result of this transformation to graphite structure, the joints had a much lower strength of 80-120 MPa [16]. It can be noticed that strength is lower but obviously the corrosion resistance is better with nickel-based chromium alloyed brazing alloys. Additionally, the strength of Ni-based brazing alloys is also decreased due to the higher brazing temperatures.

The results of the bonding test provide only limited information about the mechanical behaviour of diamond grinding tools in real-life application. In order to check the grinding ability of a diamond-steel or diamond-cemented carbide tool, specimens can be subjected to the pin-on-disk test [19]. In this test the specimen, fixed in a grip and loaded in the vertical direction, is brought into contact with rotating steel or an abrasive counter-body. The test is interrupted after a certain running time or at path intervals. The loss of counter-body mass is measured, as well as the number of diamond grits that are removed or destroyed. This test provides information about the removal rate, indicating the wear resistance of diamond-steel brazed joints. Three-point bending and pin-on-disk allow a confident evaluation of the quality of diamond grit brazed joints from a functional point of view. They show that the specimens brazed with nickel-based filler metals exhibit a substantially higher removal rate of diamond grits and higher masses of the counter body than in specimens brazed with silver-based filler metals [19]. The amount of material removed from ceramics is greater with grinding tools brazed with phosphorous containing BNi-6 in comparison with tools brazed with the Ni-Cr-Si-B alloy. However the Ni-Cr-Si-B filler metal has better abrasion ability due to higher micro-hardness than of BNi-6. [16]

Perhaps one of the most important properties of mesh diamond is toughness or, conversely, friability [6]. In the most commonly applied test, crystals of a fixed mesh size are placed within a steel capsule along with a single ball bearing. The capsule is then vigorously shaken, at a controlled amplitude and frequency for a specified period of time. The diamonds are then removed, placed on a sieve that is one size smaller than their nominal size and weight fraction so that whatever does not pass through the mesh grid is measured. Some manufacturers report this weight fraction of essentially unbroken crystals as the Toughness Index (TI), while other manufacturers report the length of time required to break down a fixed fraction of the crystals. In the most aggressive saw-blade applications, tougher crystals perform better, but in many other applications there is an optimum level of toughness, i.e., a significant degree of friability. The toughness test has the advantage of being able to test a large number of crystals quickly and cost-effectively, but has the disadvantage of only testing or breaking down the weakest crystals in a distribution. No quantitative information is gained about the strength of the stronger crystals, only that they survived the treatment [6]. Another limitation of the testing method is that brazed diamond crystals have to be removed from the braze to gain information about the brazing process on the mechanical strength of the crystals.

Some manufacturers report the results of single crystal crush tests, in which a crystal is placed between two plates and the load or weight is increased until the crystal breaks. A certain amount crystals are tested in this way, and the mean and standard deviation of the crush strength are reported. This test is rather tedious and does not mimic the type of loading of the diamond crystals that occurs in actual applications. [6]

General Electric company developed a strength test denoting Compressive Fracture Strength (CFS), that cost-effectively measures the strength of each crystal and also simulates the dynamic impact loading conditions that are experienced by crystals in an abrasive tool [6]. The test is illustrated schematically in Figure 24. To perform this test crystals are dropped one-by-one into the narrow region between two spring-loaded, counter-rotating tungsten carbide wheels. As each crystal "catches" the wheels move apart to accommodate its diameter, increasing the force on the crystal until it breaks. The maximum force on each crystal, measured by a Linear Voltage Displacement Transducer (LVDT), is recorded electronically, so that the mean, standard deviation, or entire histogram of crystal strengths can be reported. [6]
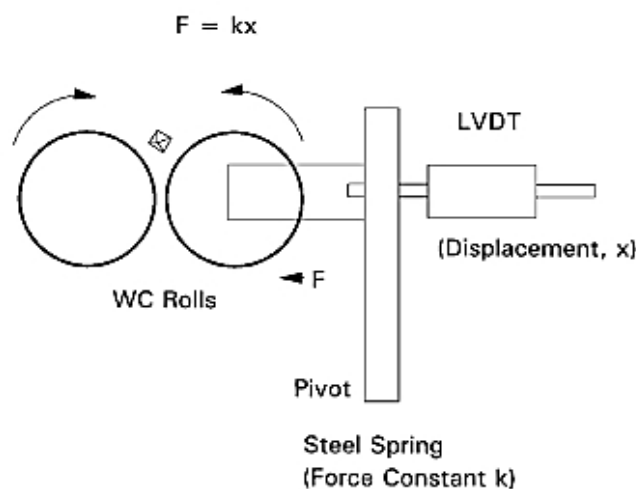

Figure 24. A schematic of roll-crusher apparatus developed by General Electric Inc. for measuring the compressive fracture strength of super abrasive crystals with linear voltage displacement transducer (LVDT). [6]

A tensile test specimen according to the testing standard DIN EN 12797 with all the requisite dimensions is presented in Figure 25 [21, 22]. For the Ni-Cr-P braze material the value of the tensile strength of the brazed specimens depends on the brazing temperature as is presented further on in Figure 26 a). If this alloy is brazed at 1030°C, the tensile strength reaches only 60 % of the base metal yield strength. To increase the tensile strength of the joints, it is necessary to braze at higher temperatures or to increase the holding time at brazing temperature, Figure 26 b). Samples joined at 1040°C for 10 minutes reached strength values in the range of the base metal yield strength, as is presented in Figure 27. However, inverse to the improvement of the mechanical strength, the corrosion resistance of Ni-Cr-P degrades dramatically under higher brazing temperatures. These

specific characteristics of Ni-Cr-P joints are probably caused by the diffusion of the constituent elements [21]. In addition, the increased brazing temperature generates higher degrees of base metal dilution, which leads to a higher content of diluted iron into the joint. This could also explain the variation of joint properties as described above. For information about the compositions of the tested braze joints see also Table 10. [21]
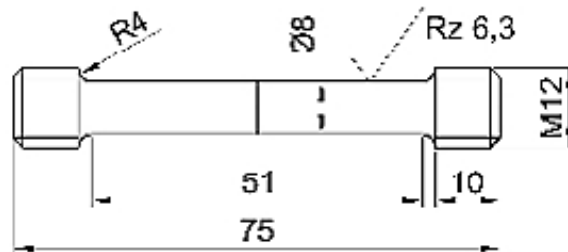

Figure 25. Butt brazed tensile test specimen according to DIN EN 12797 testing standard [21].

Table 10. Chemical compositions and melting ranges of selected brazing filler materials used in the mechanical tests presented in Figure 26 [21]. There are both boron and phosphorous containing nickel based braze materials involved. Note also the high chromium content of the materials.

Alloy System	Alloy	Composition [wt.%]							Melting Range [°C]		Form*
		Ni	Fe	Cr	Mo	P	Si	B	Tl	Ts	
Ni-Cr-Si-B-X	VZ 2120 (BNi-2 / NI 102)	82.4	3	7	-	-	4.5	3.1	1025	970	F
	Alloy #1	80.5	-	9	1.5	-	7	2	1050	980	F
Ni-Cr-P-X	VZ 2170	70	-	21	-	8	0.5	0.5	925	880	F
	BNi-7 / NI 107	76	-	14	-	10	-	-	890	890	F
	FP-613	61	-	29	-	6	4	-	1030	965	P

*): F = amorphous foil, P = Powder/Paste product
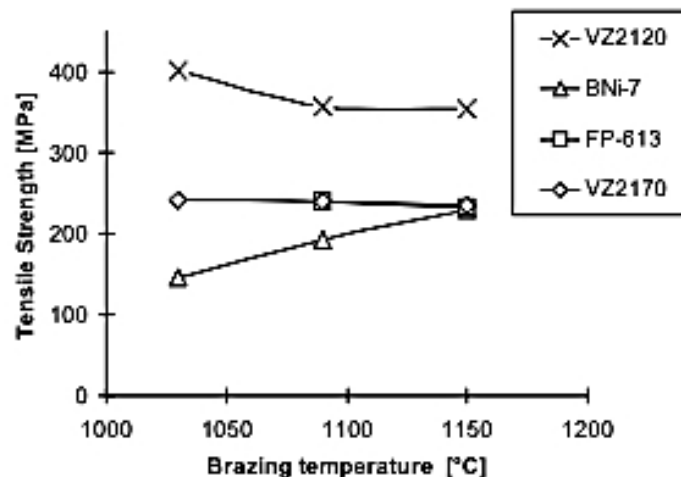
a)
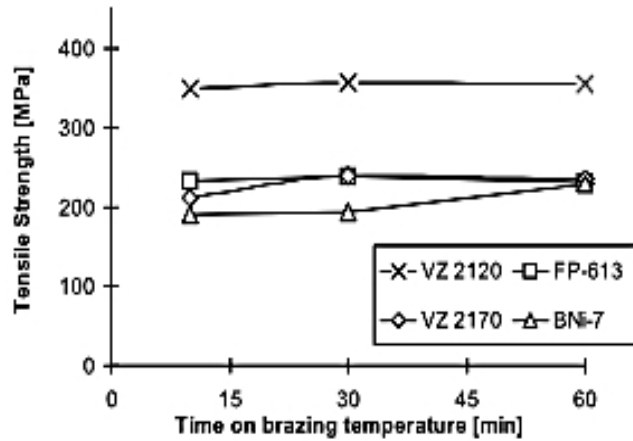
b)

Figure 26. Joint strength of butt brazed AISI 316L type stainless steel specimens brazed with various filler metals (see also Table 10) at varying brazing parameters, (a) effect of brazing temperature on tensile strength, brazing time 30 minutes and (b) effect of brazing time on tensile strength brazing at temperature 1090°C [21].
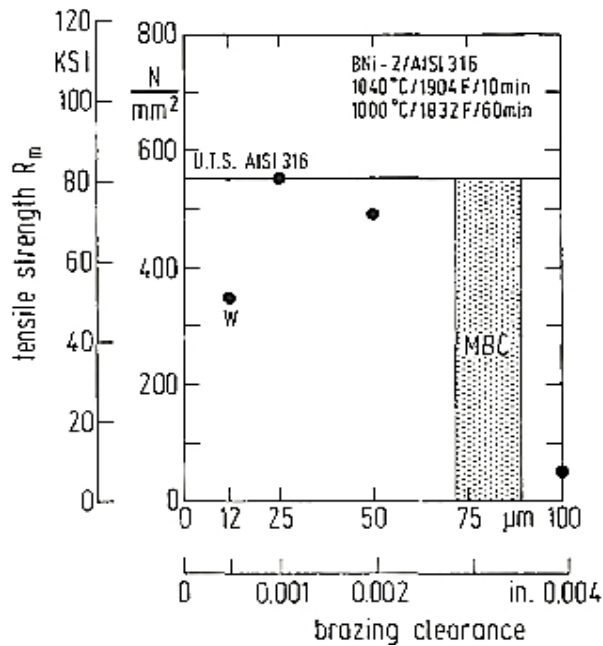

Figure 27. Tensile strength test results obtained with the Ni-Cr-Si-B filler metal on AISI 316-type stainless steel butt joint specimen brazed at 1040°C for 10 minutes and followed by heat treatment for 60 minutes at 1000°C. Marking W denotes wetting defect and MBC is the Maximum Brazing Clearance. [14]

Lugscheider et al. [14]. tested brazed butt joint tensile specimens with parallel brazing clearances were to verify metallurgical findings by. Tensile testing was carried out using the specimen illustrated in Figure 25, and the tensile strengths of brazed butt joint specimens with parallel gaps of various brazing

34

clearances are shown in Figures 27 and 28. Also shown in these Figures 27 and 28 is the ultimate tensile strength of AISI 316 stainless steel after different brazing heat treatments and the corresponding Maximum Brazing Clearance (MBC) in a range of ±10 µm. A dotted area in Figure 27 depicts a MBC of about 80 µm for two conditions: brazing at 1040°C for 10 minutes and heat treatment at 1000°C for 60 minutes. The tensile strength test results shown in Figure 27 indicate that joints brazed using the same brazing and heat treatment conditions with a clearance below the MBC have a joint strength close to the ultimate tensile strength of the base metal. Higher brazing clearances than the MBC lead to low load resistance because of the hard phases contained in the braze material. Figure 28 shows that low tensile strengths were obtained when brazing stainless steel joints with Ni-Cr-P filler metal. In the latter case the strength is clearly lower because the brazing is performed over the maximum brazing clearance.
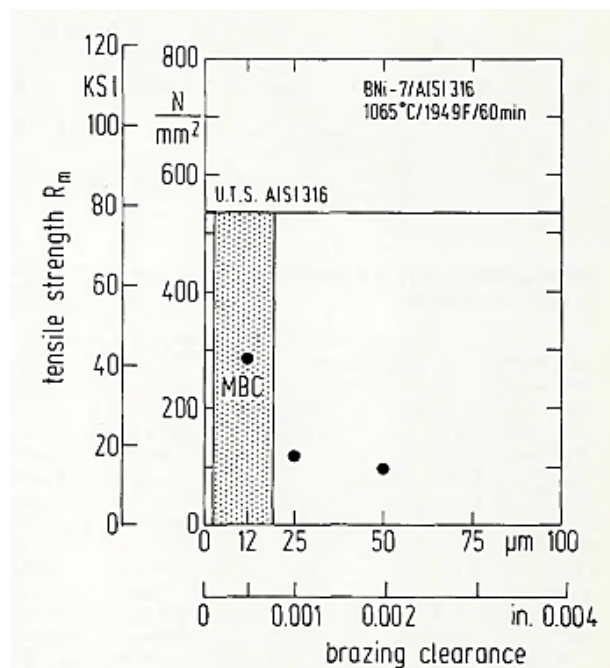

Figure 28. Tensile strength test results obtained with Ni-Cr-P filler metal and AISI 316-type stainless steel butt joint specimen brazed at 1065°C for 60 minutes [14].

Leinenbach et al. [23, 24, 25, 26] and also Bojiang et al. [27] have studied the mechanical strength of brazed single crystal diamonds. In their studies they have used Cu-Sn [23] and Ag–35 wt.-% Cu–1.75 wt.-% Ti brazing filler materials, but not any nickel-based alloys, to join the single crystal diamonds on their substrates [26]. Interesting in these studies [23, 24, 25, 26] are the methods they have used: Figures 29 and 30 show photographs of a specimen pin and a schematic experimental setup used to study the mechanical strength of the joint of one single crystal diamond. The test has been used to detect differences in the mechanical strength when brazing parameters such as temperature and holding time are adjusted [23].
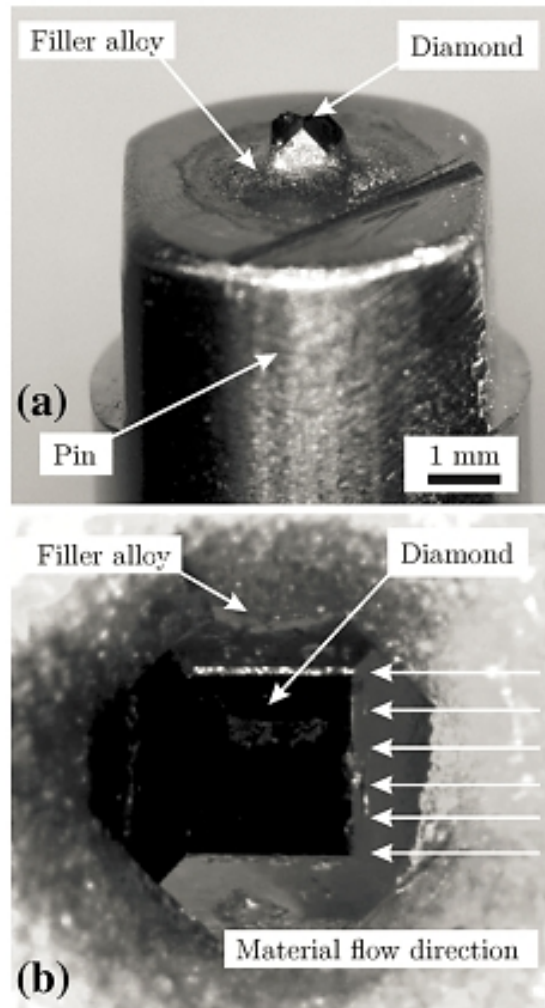
Figure 29. (a) Pin with a brazed single crystal diamond (b) squared facet of a brazed single diamond [25].
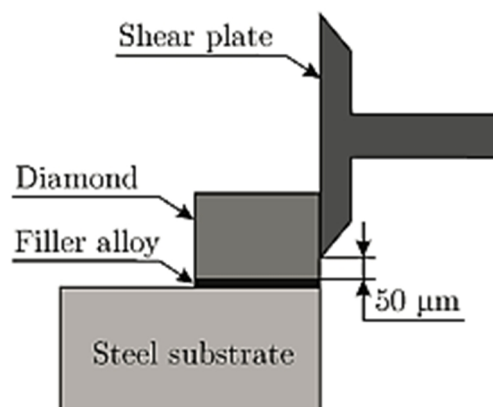

Figure 30. Schematic experimental setup for the shear tests [25].

1.11 Corrosion resistance of nickel based braze materials

Nickel based brazing filler materials are normally used to join diamonds on the tool surface when good mechanical strength and corrosion resistance is needed, but still only a few joint corrosion tests have been performed and reported so far although standard low melting brazing alloys are susceptible to interface or crevice corrosion by water or humid atmosphere [31]. There are some publications made about the corrosion resistance of stainless steel joints brazed with nickel based braze material [14, 28, 29, 30, 32, 33], but in these publications diamonds are not brazed.

Rabinkin et al. [35] tested the corrosion resistance of joints manufactured of AISI 316L type stainless steel and high chromium containing Ni-Cr-Si brazing alloy grades (a) and (b), see Table 11. These materials are alloyed with silicon and 15 to 19 wt.-% of chromium.

Table 11. Compositions of corrosion tested BNi-5 (a) and (b) grade nickel based brazing alloys [35].

| MBF | AWS & AMS classifications | Nominal composition, wt-% | | | | | | | | | Melting temp., °C (°F) | | |
		Cr	Fe	Si	C^a	B	P	W	Co	Ni	Solidus	Liquidus	Braze temp. (approx.), °C (°F)
50	AWS BNi5a	19·0	–	7·3	0·08	1·5	–	–	–	Bal.	1052 (1924)	1144 (2091)	1170 (2138)
51	AWS BNi5b	15·0		7·25	0·06	1·4	–	–		Bal.	1030 (1886)	1126 (2058)	1195 (2183)

Four different corrosive media such as a standard sea water solution, a highly alkaline 30 % $NH_4(OH)$ solution, a 25 % phosphoric acid solution, and mixed 0.5 % NaCl and 0.3 % $(NH_4)_2S$ solution were applied in the case of MBF-51 joints. Only two of these solutions, the standard sea water solution and 25 % phosphoric acid water solution were used for testing MBF-50. The results of these studies are shown in Table 12 and also in Figure 31 below. [35]

As presented in Table 12, the BNi-5a type test specimens experienced low weight loss in both seawater and 25% phosphoric acid solution media. Only seawater caused some visual sign of a corrosive pitting attack seen mostly at the joint fillet 'beach line' separating the wetted and un-wetted areas of the base metal part. This pitting occurred on all of the specimens tested in seawater, with some large pockets of attack on specimens after 648 hours and 864 hours of exposure time. [35]

In the case of joints brazed with BNi-5b foil under conditions giving the highest strength, the weight losses of the test specimens were also low, as presented in Table 12. Some corrosion was detected in specimens immersed in seawater and 25 % phosphoric acid, but amounted to little, if any, corrosion attack. SEM examination of specimen surfaces and cross-sections is reported to show little, if any, corrosion or pitting attack after exposure. [35]

Some traces of attack were also seen in the base metal on the specimens subjected to the phosphoric acid solution, but generally, according to the results all the specimens had an excellent visual appearance after the corrosion testing. Therefore, it can be concluded that the corrosion resistance of joints brazed with the mentioned brazing alloys is high. In both cases, the test results showed that it was as good as the AISI 316L base metal corrosion resistance. It is interesting to note that there was more pronounced pitting corrosion in the BNi-5a joints, in spite of the fact that chromium concentration in this foil is higher being 19 wt.-% versus 15 wt.-% in the BNi-5b grade brazing alloy.

One explanation for the increased corrosion is the short conventional brazing cycle time for BNi-5a alloy. [35]
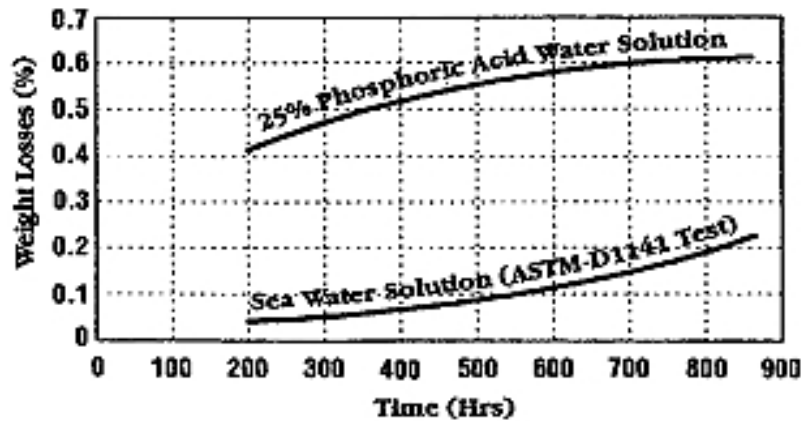

Figure 31. Weight losses of stainless steel AISI 316/BNi-5b/AISI 316 joint construction in 25 % solution of phosphoric acid with water and in seawater [35].

Table 12. Total weight loss and appearance of stainless steel AISI 316L/MBF-50 (BNi-5a) and MBF-51 (BNi-5b) braze joints subjected to corrosion testing [35].

Corrosion medium	Percent weight losses after exposure for 864 h		Visual appearance of traces of joint corrosion	
	MBF-51	MBF-50	MBF-51	MBF-50
Standard sea water solution (ASTM-D114 Standard Procedure)	0·21	0·019	Minor pitting	Yes
30% NH₄OH water solution	None	N/A	None	N/A
25% H₃PO₄ water solution	0·62	0·088	Minor pitting	None
0·5% NaCl & 0·3% (NH₄)₂S water solution	None	N/A	None	N/A

Tested samples were composed of two overlapping $2·5 \times 3·75 \times 0·317$ cm 316L plates brazed with MBF-51 brazing foil with 50 μm (2 mil) thickness. The brazed overlap is 1·25 cm. Samples were completely immersed in corrosive solutions at 50°C (120°F) under 1 atm for up to 864 h.

Studies concerning corrosion resistance of such brazing joints will typically be conducted electrochemically using polarization-measurements [36]. According to Hartmann et al. [36] it can be said that practical conditions should generally be favoured, because the corrosion behaviour of a component will be affected from a complex interaction of different conditions between the component and its environment [36, 34]. Hartmann et al. [36] tested samples of the base material AISI 316L joined with different brazing foils. Samples were conducted in a quantitative immersion corrosion test. In this testing method the corrosion resistance is affected by compositions of the base material and the brazing filler metal, but also by the volume of the brazing filler metal applied compared to the base material volume.

The corrosion media was a synthetic exhaust condensate [36] with a low pH-value of 1.6. In the solution there was sulphate-, nitrate- and chloride ions and the tests were carried out at 70°C temperature. After exposure, the weight loss of the brazed samples was measured.

The major founding in the studies [36] was that brazing filler metal alloyed by iron, copper and molybdenum had higher corrosion resistance in environments of synthetic exhaust condensate even with lower chromium contents. Another benefit of these elements is the quite rapid passivation in the corrosion test. So the alloying of the brazing filler material if affecting to the corrosion resistance of the brazed structure. This result is underlining the need of brazing filler material development work in the future.

2. Experimental work

2.1 Brazing procedure

Nickel-based braze materials are used to join single crystal diamonds on the molybdenum-alloyed stainless steel surface where high strength and good corrosion resistance are important properties of the final product. As seen in the binary phase diagrams presented earlier in Figures 6 - 9, these braze materials are dissolved at high temperatures and therefore need to be produced under a high vacuum to prevent oxidation of the braze material and also, in this case, oxidation of the diamond single crystals. Diamond as one crystalline form of carbon will oxidise and perish in air at temperatures over 600ºC [43]. To produce the needed composite materials for the experiments the brazing process was carried out in a furnace under a high vacuum to avoid oxidation of the diamond and the brazing filler metal. All the studied specimens were manufactured and brazed by Valmet Technologies Inc. locating in Tampere, Finland.

Before the brazing process, the surfaces of the base materials were cleaned of any oil remainders by wiping them with pure acetone. The high vacuum level used for brazing was found to be reducing the oxide layers from base material surfaces during the brazing process, because no oxide layers between the braze layer and the base material were found from none of the studied cross-sectional specimens.

The diamond single crystals were placed on the base material surface and the brazing filler metal was sprayed as a layer on the surface. All the studied materials were brazed in the same Schmetz vacuum furnace (Menden, Germany) with a load volume of 90x120x70 cm^3. The raising speed of the temperature of the furnace was set to be 3ºC/min and holding time at brazing temperature from five to eight minutes. Cooling speed after brazing was 2ºC/min, the specimens were cooled down with the furnace in vacuum. Vacuum level during the brazing was measured to be between $2*10^{-6}$ and $6*10^{-6}$ mbar. The brazing temperatures were between 950ºC and 1055ºC depending on the braze filler material used.

The studies were used to get information about the diamond surface, the diffusion of carbon from the diamond and also diffusion of the brazing filler metal components into the diamond crystals during the brazing process.

The angularity of the diamond crystals is essential for the functionality of the construction as an abrasive tool. An important factor in the diamond's mechanical strength is the remaining stress in the diamonds after brazing has occurred. The final properties of the diamond braze material composite will also be affected by the dissolution of carbon into it.

2.2 Materials involved

The compositions of the materials involved in this study are presented in Table 13. To make the results easy to compare with each other all the experiments were done using commercial Ni-Cr-Si-B and Ni-Cr-P type braze filler materials onto the same grade of stainless steel or, in a few special cases, on a graphite substrate. The reason for focusing on these two brazing materials was the interesting and differing microstructures, high chromium content, good corrosion resistance and high mechanical strength. The filler materials have rather high brazing temperatures, 950ºC [47] for Ni-Cr-P compared

to the boron and silicon containing braze material Ni-Cr-Si-B which had a typical brazing temperature of 1055°C [47]. In the Ni-Cr-P braze material the slightly lower brazing temperature is achieved by alloying it with phosphorous while Ni-Cr-Si-B material is alloyed with boron and silicon. The compositions are presented in Table 13. Note the difference in chromium content between these two test materials.

The phosphorous content of the Ni-Cr-P type braze material is near to the eutectic point (see Fig. 6) of the solution, being about 10 wt.-%. This is to have a low melting point, a narrow melting temperature range and to improve the fluxing and wetting behaviour of the braze filler material on the surfaces involved. The brazing temperature in these studies was from 950°C to 1055°C, and the temperature was higher when Ni-Cr-Si-B braze was used. Before brazing the braze material was spread on the substrate over the diamond single crystals. Two different substrates were involved, the molybdenum alloyed stainless steel, and for residual stress measurements also porous graphite substrate, see the composition of the stainless steel base material in Table 13.

Table 13. Compositions of materials involved in the study [2, 48].

	Cr	B	Si	Fe	C	P	S	Al	Ti	Mn	Zr	Ni
Ni-Cr-Si-B (BNi-2)	6.0–8.0	2.75–3.50	4.0–5.0	2.5–3.5	0.06	0.02	0.02	0.05	0.05	...	0.05	bal
Ni-Cr-P (BNi-7)	13.0–15.0	0.01	0.1	0.2	0.08	9.7–10.5	0.02	0.05	0.05	0.04	0.05	bal

	Cr	Si	Fe	C	P	S	Mn	Ni	Mo	N
Substrate AISI 316L	16.0-18.0	0.75 max	bal.	0.03 max	0.045 max	0.03 max	2 max	10.0-14.0	2.0-3.0	0.10 max

2.3 Characterization methods

The research work of the brazed materials was concentrating on the structure and consistency studies of diamond – braze composites brazed on the stainless steel base material surface. The evaluation of the diamond surfaces and the structural studies of the cross-sectional specimens were found to be important parts of the work. Several specimen preparation methods and a large body of research methods and equipment were used during the experimental work.

2.3.1 Specimen preparation procedure for SEM studies

The specimen preparation for the surface studies using Scanning Electron Microscopy (SEM) was normally started by washing the surfaces and in some cases with coating them with either thin gold or a carbon layer to produce high quality images. This is because the diamond, unlike the other crystalline form of carbon, graphite, is not electrically conductive and charges in Secondary Electron (SE) imaging. Microanalyses were measured mainly from polished cross-sections without any coating layer on the specimen surface. The Backscattering Electron (BSE) measurements were all done without coating the specimen, because any extra layers on the specimen surface could affect to the grey levels measured.

Specimens for cross-sectional microstructure observations were prepared by cutting and moulding them into an electrically conductive resin. The specimens were then mechanically ground and, finally,

polished with a fine diamond paste. A Broad Ion Beam (BIB) specimen preparation technique was also used to give detailed information of the layer between the braze material and the diamond single crystal. These specimens were prepared by Top Analytica Oy Ab locating in Turku Finland. This technique cut the specimen cross-section gently with the broad ion beam hitting the specimen. All the studied specimens (prepared using both preparation techniques) were studied uncoated.

In the diamond – braze filler material interaction studies the interesting aspects were the brazing material and diamond interactions during the high temperature brazing procedure. In order to see the single diamond crystal surface the braze layer had to be removed from the diamond surface. To do this a special specimen preparation method was developed based on electro-polishing. The diamonds were either polished totally off from the substrate for TEM analysis and fracture surface studies or the thin covering braze layer was singularly removed from the diamond top surface. The layer thickness of removed braze material was adjusted by changing the duration time of the electro-polishing procedure. It was noted that the electro-polishing removed also the electrically conductive carbide layers from the diamond surface.

The electro-polishing procedure was carried out at low temperatures between minus 30ºC and minus 40ºC. The electrolyte was installed into an alcohol bath, which was continuously cooled with liquid nitrogen to keep the temperature of the electrolyte within the desired temperature range. The electro-polishing solution was a mixture of 60 vol.-% nitric acid and of pure cooled methanol, at a ratio of 1:2. The polishing voltage was adjusted to between 7.5-8.0 V and the current between 0.3-0.6 A/cm^2, depending on the surface area of the specimen. The voltage adjustment was to ensure that the polished material operated at a certain polishing plateau typical for the polished material. When operating at the plateau the polishing current is not significantly increasing when the polishing voltage is increased. A special lacquer was used to crop the desired polishing area on the surface of each specimen.

The polishing time could be from 5 to 20 minutes, depending on how much of the brazing filler metal was to be removed and how high the polishing voltage was. After polishing the specimens were carefully cleaned by washing in an ultrasonic washer consisting of alcohol and warm water. After a final pure alcohol bath they were left to air-dry. The final step of the specimen preparation was to remove the layers of lacquer.

2.3.2 SEM studies with contrast measurements using SE- and BSE-detectors and EDX- analyses

The diamond - braze filler material interaction was studied with a Scanning Electron Microscope (SEM) Philips XL30 (Amsterdam, Netherlands) equipped with an EDAX Energy Dispersive X-ray analyser (EDX) (NJ, USA) and also with a Zeiss Ultra Plus (Wetzlar, Germany) high resolution field-emission scanning electron microscope. The first SEM was useful for backscattering electron (BSE) imaging and microanalysis while the Zeiss microscope had a significantly better resolution for Secondary Electron (SE) imaging especially with low accelerating voltages. For BSE-imaging a semi-conducting detector was used. The diameter of the detector was 16 mm. It was divided into two sections, and the information has been summarized and used in this study. During the microstructural analyses the BSE-detector situated above the flat, polished specimen and the distance between the specimen and the detector was set between 5 and 9 mm. This means that the collecting angle of the BSE detector from

the analysed area of the sample surface is between 85 and 116 degrees with measurements of mostly over 110 degrees. A wide collecting angle minimises the effect of orientation contrast during the measurements.

EDX-analyses were measured with a silicon-lithium detector equipped with an ultra-thin window. The accuracy of the analyses was ensured by simultaneously analysing known elements or phases together with the unknown components. Particular known phases were the stainless steel substrate material far under the braze layer and also the $(Ni, Cr)_2P$ and $(Ni, Cr)_3P$ phases formed inside the braze layer during the brazing process, the phosphorous content of these phases being 33.3 and 25 at.-% respectively. The total count level of the maximum peak of the analyses curves, used in composition calculations, was well over 10.000 counts. It must be noted here that the ZAF-correction calculation (corresponding to the atomic number (Z), absorption (A) and fluorescence (F) corrections) used gives only *approximate* values of the content of individual elements.

With SEM the studied specimens were characterized with SE and BSE and EDX-microanalysis. BSE-detector in scanning electron microscopy is very useful when phases of differing composition have to be separated and characterized through high magnification. The best results in these studies are achieved if polished and flat specimens are used. This method could be applied, for example, when different types of carbides are involved. Is it possible to also get information about the diffusion of carbon with this kind of imaging? Or can we make assumptions about the composition of a particular phase of the material by analysing the grey levels of the BSE images?

To answer these questions the polished cross-sectional specimens were examined, looking at the structure of the brazing filler metal and the carbide layers formed at the diamond - braze filler material interface. Backscattered electrons contrast more acutely for the areas with different mass fractions of the atomic elements. The backscattering coefficient η is approximately independent of the primary electron energy E_e in the range of 10-100 keV and therefore the level of the acceleration voltage used in these studies does not have greatly influence the result [53, 54]. However, in the studies presented here the accelerating voltage used was consistently 20 kV.

The grey levels of different phases of taken BSE images were measured and analysed using 'Image J' (National Institute of health, Bethesda, MD, USA) image analysing program.

The measured backscattering coefficient of multicomponent targets can be fitted to the formula [53]:

$$\eta = \Sigma_i c_i \eta_i \qquad\qquad\qquad \text{(Eq. 1)}$$

In Eq. 1 factors η_i are the backscattering coefficients of the pure elements and values c_i are their mass fractions in the measured material. Factor η_i for the elements can be calculated using equation [53]:

$$\eta_i = -0.025 + 0.016Z - 1.86 \times 10^{-4}Z^2 + 8.3 \times 10^{-7}Z^3 \qquad\qquad \text{(Eq. 2)}$$

In Eq. 2 Z is the atomic number of the element [53].

Calculated (using Eq. 2) backscattering coefficient η_i-values and coefficient values found from the literature for the elements analysed in this study are presented in Table 14. These values are also plotted in Figure 32 with the calculated η_i coefficient curve for all the elements up to Z = 80. It can be concluded that the difference between the calculated coefficients and those found in the literature is

not significant in most cases, meaning the calculated values can be used as the basis for observations made in this study.

Table 14. The density, atomic weight and the values of the backscattering coefficients η_i for the elements relevant to this study. The calculated (using Eq. 2) values presented in this table were used in further calculations below. [53, 55, 58]

Z	Component	Density g/cm3	Atomic weight	η_i ref /10/	η_i/calculated
5	B	2.34	10.8110	0.041	0.050054
6	C	2.27	12.0112	0.061, 0.064, 0.049	0.064083
7	N	0.81	14.0067		0.077771
8	O	1.14	15.9990		0.091121
14	Si	2.33	28.0860	0.159, 0.194, 0.169, 0.164	0.164422
15	P	2.34	30.9740		0.175551
24	Cr	7.15	52.0100	0.259, 0.268,	0.262938
25	Mn	7.21	54.9380	0.286	0.271319
26	Fe	7,86	55.8500	0.276, 0.287, 0.294,	0.279452
28	Ni	8.91	58.6900	0.30, 0.301	0.294996
42	Mo	10.2	95.9400	0.387, 0.382	0.379989
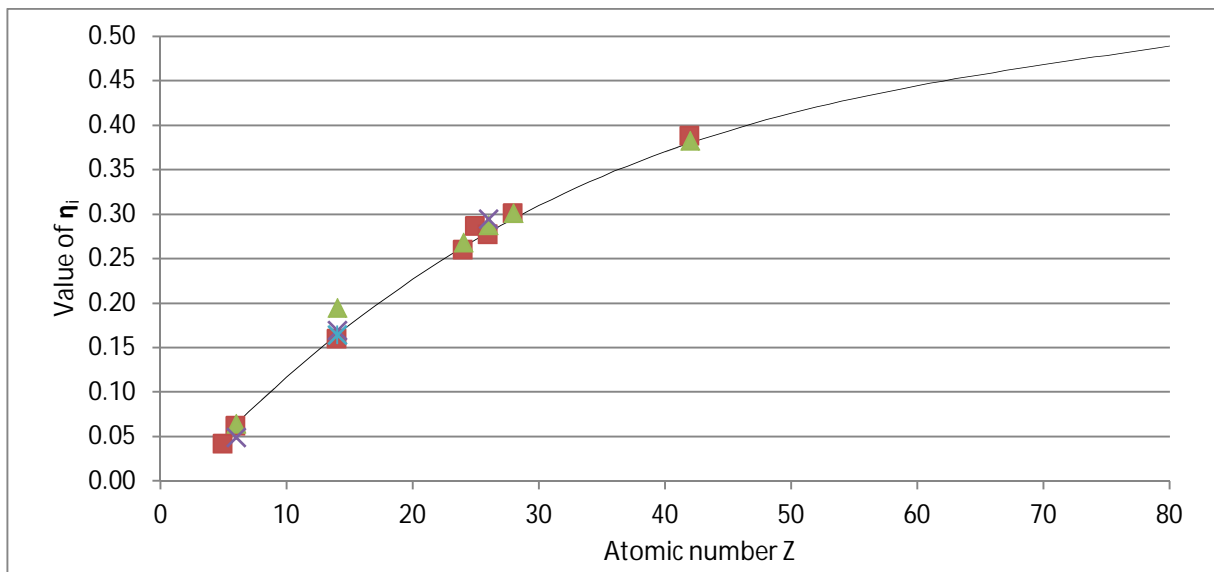
Figure 32. Calculated backscattering coefficients η_i (curve) and reference coefficients η_i given in Table 14 presented in same plot: the difference between calculated coefficients and those found from literature is not significant.

2.3.3 Micro-hardness measurements

Vickers micro-hardness measurements were done using an Anton Paar micro-hardness tester (Graz, Austria), which was coupled to the Philips XL30 microscope. In these analyses 5 g, 10 g and 20 g loads were used. The heaviness of the load determined the hit within the required phase so as to make a

reliable symmetrical mark to measure intention. Because it was noticed that there was some deviation between the results measured with Anton Paar equipment and the real hardness values of the standard specimens, the results were calibrated using the standard specimens. The calibration used the base material as a standard and the hardness values of the base and reference samples were measured with optical Shimadzu hardness tester (Tokyo, Japan) with higher 100 g and 300 g loads.

Measurements were done on the cross-sectional specimens made on stainless steel with brazed diamonds and also on specimens brazed on graphite base material without diamonds present. To ensure the reliability of the measurements three reference samples were used to confirm the hardness values. The reference samples used were a 695-715 HV0.3 sample, uniform hard chromium coated cross-section with hardness of 870-890 HV0.3 and austenite stainless steel base material with hardness of 190 HV0.3. These reference samples were measured with loads of 20 g, 10 g and 5 g using the Anton Paar tester and the same loads were also used in the braze material measurements. The results of the reference measurements are displayed in Table 15. The number of measurements of the reference samples for the Shimadzu hardness tester was 10 measurements per specimen, with the Anton Paar tester using 5 measurements per standard specimen.

As can be seen from the results presented in Table 15 and also in Figure 33, the Anton Paar micro-hardness tester gives approximate values for the micro-hardness level of the materials' phases. Although some linear correction was made using these calibration results, it seems that harder phases than the reference hard chromium measured with the Anton Paar tester give too high values for the measured phase. Still the measured results are valuable because individual phases of the braze materials can be compared and the hard and soft phases of the structure can still be characterised.

Table 15. Vickers micro-hardness reference measurements with results for Shimatzu and the Anton Paar hardness tester instruments.

Measured with:	Shimatzu		Anton Paar					
	HV0.3	STDev	HV0.02	STDev	HV0.01	STDev	HV0.005	
Base material	189	12	217	13				
HV695-715 reference	707	8	583	10	599		593	
Hard chromium coating	879	21	621	18	674	6	756	22

The following linear correction relations (Eq. 3-5) were created according to the reference measurements presented in Table 15 to extrapolate the hardness values (measured using the Anton Paar micro-hardness tester) from braze material cross-sections:

- for 20 g load $Y = 1.6X - 162$ (Eq. 3)
- for 10 g load $Y = 1.6X - 223$ (Eq. 4)
- for 5 g load $Y = 1.3X - 74$ (Eq. 5)

Results of the correction measurements together with the created correction lines based on the created formulas are presented in Figure 33.
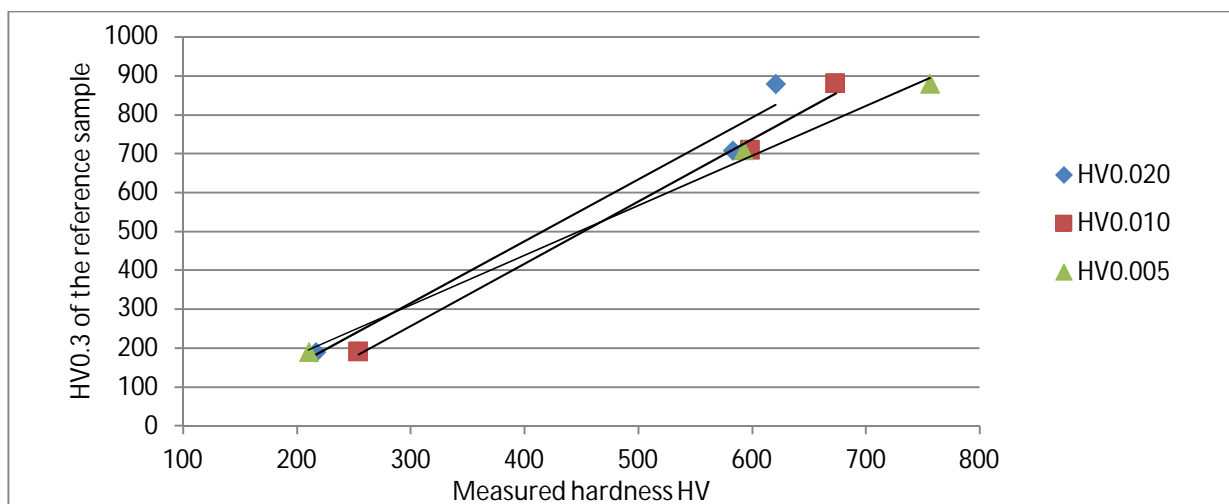
Figure 33. Measured hardness values and the hardness values of the reference samples.

2.3.4 Transmission electron microscopy

The Transmission Electron Microscope (TEM) studies were done with the JEOL 2010 (Tokyo, Japan) microscope operating with a 200 kV acceleration voltage. The results were photographed as Bright Field (BF) transmission images tilted at two-beam condition and as Selected-Area Diffraction (SAD) images. This kind of tilted two beam BF-imaging gives information of defects on the crystal plains such as precipitates, stacking faults, dislocations and inclusions inside the single diamond crystal structure.

The diamonds, which were electro-polished off from the substrate surface, were crushed mechanically especially for the TEM observations to get thin electron transparent cross-section specimens from the vicinity of the diamond surfaces degraded during the brazing process. The surface morphology of these fractured surfaces was also studied with an SEM microscope. For SEM examination the specimens were glued (after crushing) onto the specimen support stub and vacuum coated with a thin layer of evaporated amorphous carbon. Crushed specimens studied with a TEM were placed on copper grid support coated with a thin amorphous carbon layer (full of holes). Specimen areas over the holes were studied with electron beam.

2.3.5 Surface studies with optical profilometer

The surfaces of the diamond facets are eroded during brazing at high temperatures. The surfaces were photographed using the SEM, but in order to get numeric information about the surface characteristics and topography of different types of diamond facets, the surfaces of the brazed and electro-polished diamonds were characterized with an Alicona optical profilometer (Graz, Austria). The optical profilometer was also used to evaluate the surfaces of mechanically-tested samples before and after the tests. This method was also used in the radius of curvature measurements taken during the residual stress studies. Before taking the profilometer measurements the specimen surfaces were washed or cleaned using compressed air.

2.3.6 X-ray diffraction studies

X-ray Diffraction (XRD) curves were measured from the cleaned braze surfaces. The purpose of these studies was to identify the phases present in the braze layers. For these studies the Panalytical Empyrean Multipurpose Diffractometer (Almelo, Netherlands) was used. All measurements were done using copper K-α radiation with a wavelength of 1.54178 Å [49]. The specimens were mainly measured between 20-80 degrees of 2Θ and the measured diffraction peaks were analysed using the Bragg law Eq. 6 [49]:

$$n\lambda = 2d\sin\theta \tag{Eq. 6}$$

In Eq. 6 λ is the wave length of the radiation, n is the order of reflection, d is the distance between the crystal planes and θ is the diffraction angle [49].

The X-ray diffraction curves were measured from the surface of the Ni-Cr-Si-B and Ni-Cr-P brazing materials with diamonds made on stainless steel. Before analysing the results, it was essential to find out the depth of penetration of the x-rays through each material, as well as the depth of the layer of measured information coming from each specimen. This depth can be calculated using Eq. 7 [49]:

$$Gx = 1 - e^{-2\mu x/\sin\theta} \tag{Eq. 7}$$

In the Eq. 7 Gx represents the fraction of information from depth x within the specimen surface, Θ is the diffraction angle and μ is the mass absorption coefficient for each component of the studied material. Values for μ for the alloys can be calculated using Eq. 8 [49]:

$$\frac{\mu}{\rho} = w_1 \left(\frac{\mu}{\rho}\right)_1 + w_2 \left(\frac{\mu}{\rho}\right)_2 + \cdots \tag{Eq. 8}$$

Where ρ is the density of the component and w_i is the weight fraction of the component in the solid material.

As Table 16 presents, the mass absorption coefficient μ is very high for iron and chromium when copper radiation is used for the X-ray measurements – this is because of the absorption edge of the components near the wave length of copper K-α radiation. This is the same for chromium when a cobalt tube is used, as this was the alternative tube available when these measurements were taken. Because of the high absorption coefficients the penetration depths for different phases present in the two studied braze materials were calculated using the equation above. The results are presented in graphic form in Figures 34 and 35 as a function of the Bragg angle 2Θ for 50 % and 95 % information depth coming from the surface of the specimen.

47

Table 16. Mass absorption coefficient/density (µ/ρ) values in cm^2/gm for elements present in this study for copper and in comparison for cobalt x-ray tubes, µ is the mass absorption coefficient and ρ is the density of the element. [49]

	Cu tube	Co tube
	µ/ρ	µ/ρ
Si	60.3	94.1
P	73	113
Cr	259	392
Fe	324	59.5
Ni	49.3	75.1
B	3.06	4.67
C/Diamond	5.5	8.5

According to the results it can be said that the information measured from both braze material layers comes from the braze material and not the base material beneath it. When looking at Ni-Cr-Si-B braze in Figure 35, can be seen that the penetration depth into the dark chromium boride phase is generally thinner than into the other phases. This means that in the areas where the concentration of the dark boron-rich phase is high the penetration depth is low. The penetration depth into the Ni-Cr-P braze material is lower, at about 60 % of the value for Ni-Cr-Si-B braze material, mainly because of the lower silicon content and higher chromium content of the brazing filler material.

It can be noted that the X-ray penetration inside diamond is high over 500 µm at the Bragg angle value of 60 degrees indicating strong diffraction peaks within the diamond crystal structure.
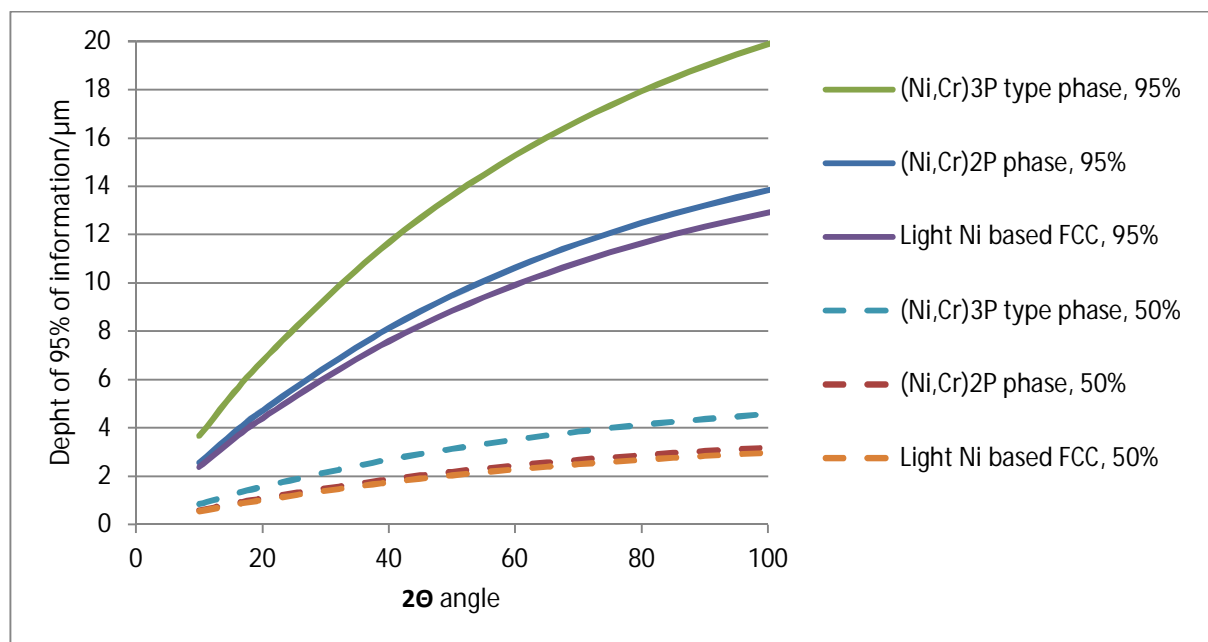
Figure 34. Layer thickness depth of 50 % and 95 % of coming information for copper K-α radiation within the present phases of the Ni-Cr-P braze material.
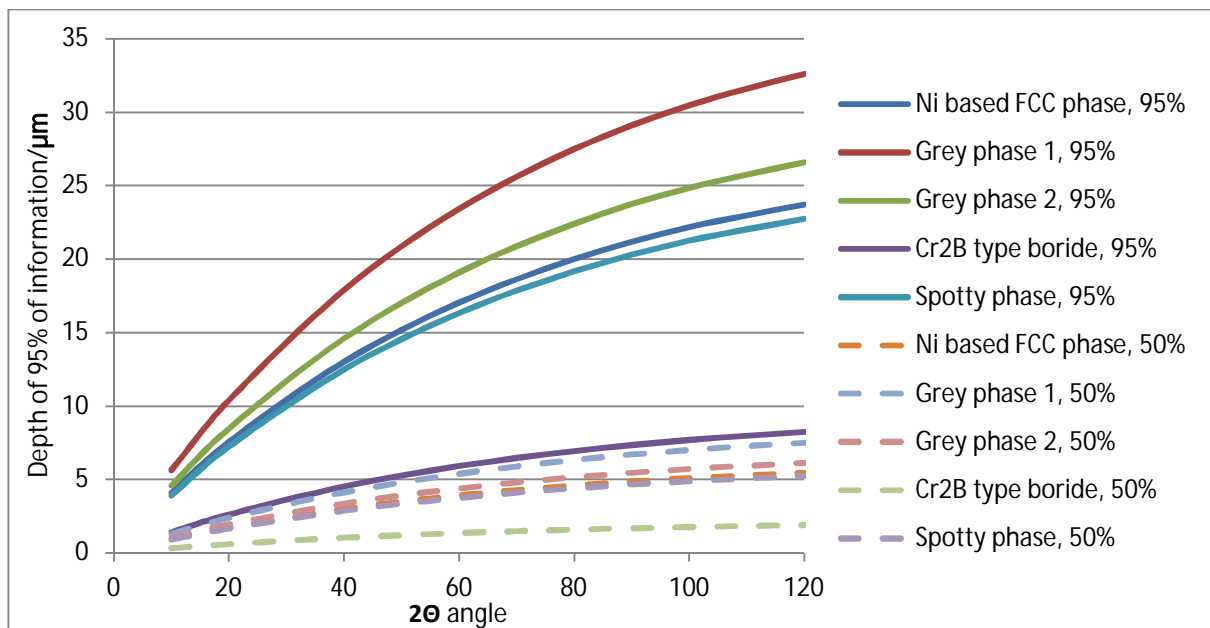
Figure 35. Layer thickness depth of 50 % and 95 % of coming information for copper K-α radiation within the phases of the Ni-Cr-Si-B braze material.

2.3.7 Mechanical testing of diamond – braze composites

Brazed diamonds are used in tools and other applications where they are to be stressed and carry mechanical loads. For example, when tooling or grinding hard ceramics it is important that the diamond is properly fixed to the tool body and that the individual crystals do not fracture when stressed.

To discover the stress-bearing ability of the diamond–braze composites it was necessary to test the breaking loads of individual single crystal diamonds. For the purpose a mechanical testing method suitable for the single diamond crystal testing was developed, using the base information given by Leinenbach et al. [25] presented in Figure 30.

For mechanical testing diamonds were brazed in rows on flat stainless steel plate surface with the nickel-based chromium alloyed braze material Ni-Cr-P. The distance between individual diamonds was set to 1 mm and the diameter of single diamond crystal grits was selected to be between 250-300 µm.

The tests were carried out with a hydraulic Instron 8800 heavy mechanical testing machine (Norwood, MA, USA). A simplified graph of the testing set-up is presented in Figure 36. Such a heavy instrument for mechanical testing was used to avoid the yield of the test set up during testing. Samples were tested using 50 kN and 5 kN load cells. With 5 kN cell it was found that the set-up was less unyielding than with a heavy cell. However, both cells were successfully used when testing the single diamond crystals.
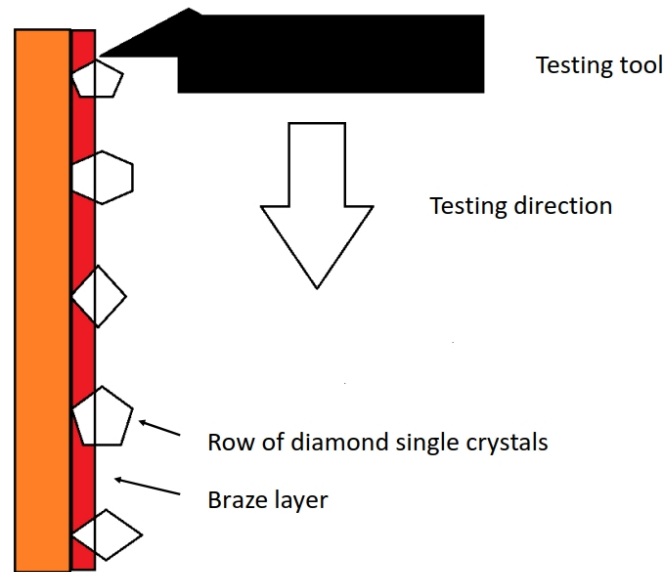
Figure 36. Configuration of the set-up for mechanical testing. An optical scope was used to position the diamond rows under the testing tool.

Testing speed for the tests was selected to be 2 mm/min and testing distance per test was 20 mm, so with one test performed the breaking load of 20 diamonds was measured. The position of the testing tool and the level of the load was measured 100 times per second. Because of noise detected both in detected position and load signals the averages of 5 measurements were calculated and used in following measurements and calculations. For each diamond tested the peak height of the force to break up the diamond single crystal was measured and the background was subtracted from the measured height of the peak.

2.3.8 Residual Stresses of diamond – braze composites

Differences in the Coefficients of Thermal Expansion (CTE) and remaining residual stresses of braze filler material vs. graphite were studied. Graphite was used because there were no large diamonds or diamond surfaces available to use for these particular studies and the CTE of diamond and graphite are at the same level being 2.0-4.8 $x10^{-6}$/K [16, 58] at room temperature. On the other hand, the carbon is diluted from graphite in the same manner it is diluted from the diamond surface, and forms carbides in the boundary between the graphite and brazing filler metal. Part of the diluted carbon does not form carbides and can be soldered into the other brazing filler metal phases.

For the studies on thermal expansion, braze samples were utilized on 30x50 mm graphite substrates. On the substrates carbon reacted with braze creating carbide layers between the braze filler material and the graphite base. Carbon was also diffused inside the braze, affecting its characteristics such as the thermal expansion coefficient. The brazing temperature for Ni-Cr-P braze material was 950°C and for Ni-Cr-Si-B it was higher, at 1032°C. Specimens were prepared in a vacuum furnace.

After brazing it was noticed that there were cracks in the braze layers of both specimen types. This was expected because of the different thermal expansion coefficients of the base material and braze

50

filler metal. The number and the width of the cracks were measured with the SEM. For this, a sharp line was scratched in the middle of each specimen and the width and angle of individual cracks crossing that line was measured. The vector component of the crack width to the line direction was calculated. During the observations the accuracy of the SEM was determined using a calibration standard [56] with the same magnifications and working distance values used to measure the cracks. It became evident that there was 1.2 % microscope error in the horizontal direction and this was corrected for the final results.

It was found that the brazed graphite specimens were bent after cooling to room temperature. This meant that residual stresses remained in the structure and that stress is not totally relaxed by fracturing. To calculate the stress level in the braze layer one must first measure the radius of curvature r of the specimen, which can be calculated from Eq. 9:

$$r = \frac{(l^2 + h^2)}{2h} \qquad \text{(Eq. 9)}$$

In Eq. 9 *l* is the length of the specimen and *h* is the measured bend of the specimen presented in Figure 37.
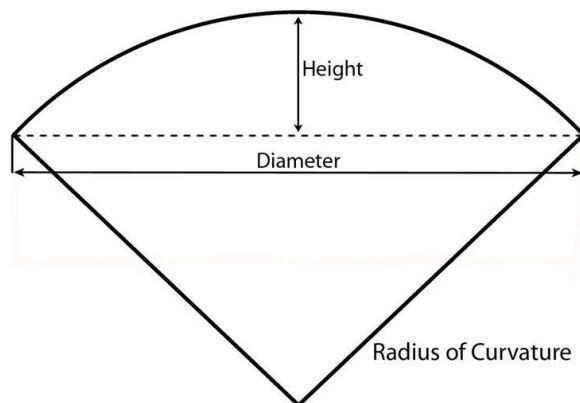
Figure 37. The radius of curvature

The radius of curvature r of the brazed specimen can also be measured using the optical profilometer, as presented in Figure 38. The blue curve is the measured profile of the backside of the porous graphite base material and the red curve is plotted according to the calculated curvature. In the studies presented here, the radius was measured using the optical profilometer.
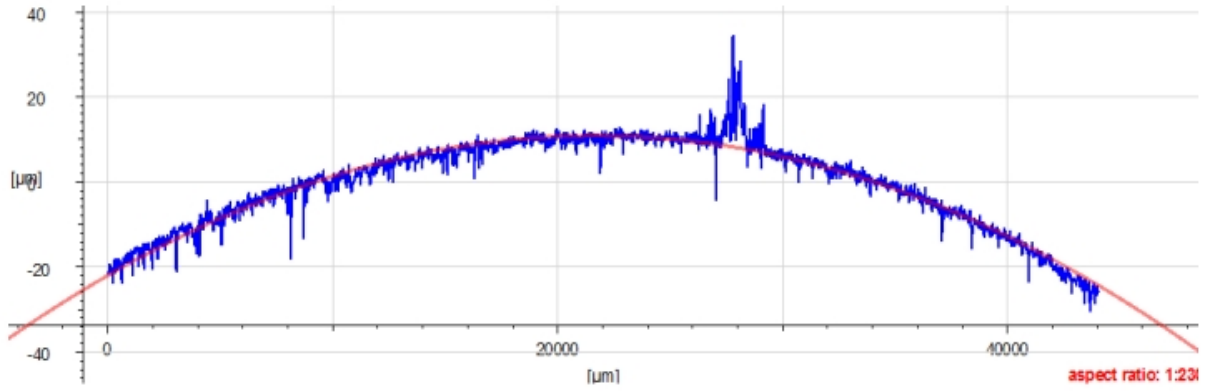
Figure 38. The blue curve is the measured profile of the graphite base material and the red curve is plotted using the calculations of the radius of curvature r of the specimen. Curve is measured from the backside of the test specimen.

The film stress can be calculated using Eq. 10 [57, 74]:

$$\sigma_f = \frac{t_f E_s}{6r}\left[\left(\frac{t_s}{t_f}\right)^2 + 6\frac{E_f}{E_s}\frac{Y_f}{t_f}\right] \; in \; where \; \frac{-1}{2} \leq \frac{Y_f}{t_f} \leq \frac{1}{2} \qquad (Eq. 10)$$

In the Eq. 10 t_f is the film thickness, t_s is the substrate thickness, r is the radius of curvature, Y_s is distance from the neutral plane to a point in the substrate, Y_f is the distance from neutral plane to a point in the film, E_s is Young's modulus of the substrate and E_f is the Young's modulus of the film. [57, 74]. Parameters used in calculations are presented in Table 17.

Table 17. Parameters used in residual stress calculations [57, 74].

Braze material	Ni-Cr-Si-B		Ni-Cr-P:	
t_f:	0.1	mm	0.1	mm
t_s:	6	mm	6.4	mm
r:	2281.817	mm	3715.345	mm
Y_f: Middle line	3.05	mm	3.25	mm
E_s: [58] (for porous graphite)	2.0682	GPa	2.0682	GPa
E_f: [48]	200	Gpa	200	GPa

Once the total width of the cracks has been measured and calculated and the residual stress levels remaining in the braze after the fracturing measured, it is possible to calculate the thermal expansion coefficients for these materials when brazed on the graphite substrate. The strain of the braze materials can be calculated from equation [59]:

$$\varepsilon = \sigma / E \qquad\qquad (Eq. 11)$$

In Eq. 11 ε is the elongation, σ the stress level and E the elastic modulus of the material. [59]

2.3.9 Corrosion testing of diamond – braze composites

Because the corrosion resistance is one of the key issues when using nickel-based brazing materials with chromium, two kinds of simple corrosion experiments were performed. Modified ASTM G48-00 corrosion test named as 'Standard test methods for pitting and crevice corrosion resistance of stainless steels and related alloys by use of a ferric-chloride solution' [70] was used first to compare the corrosion resistance of the braze material to the corrosion resistance of the stainless steel base material at low pH values. Another way to have information about the corrosion resistance was to measure the polarization curves of the materials.

To measure and compare the corrosion resistance of the coating materials with the AISI 316-type reference material, an ASTM G48-00 corrosion testing standard was utilized [70]. To prepare the corrosive chlorine solution for this experiment 100 g of $FeCl_3*6H_2O$ salt was dissolved with 900 ml of ion-exchanged pure water. The pH-value of the solution was measured to be 1.2 before the corrosion test and only slightly over 1.2 after the tests were performed. Approximately 60 ml of this solution was used in a polystyrene container for each specimen as depicted below in Figure 39. When the corrosion experiment was started, coating specimens were put under the container presented in Figure 39. A rubber seal between the tested braze filler layer and container prevented the corrosive solution from coming into contact with the blank base material.

Tests were carried out at a room temperature of 22°C. After the 3-day testing period the specimens were taken and washed carefully in warm water using ultrasonic washing equipment. Finally, the specimens were dewatered in pure alcohol and dried up for one day in dry air at 30°C temperature before scaling.
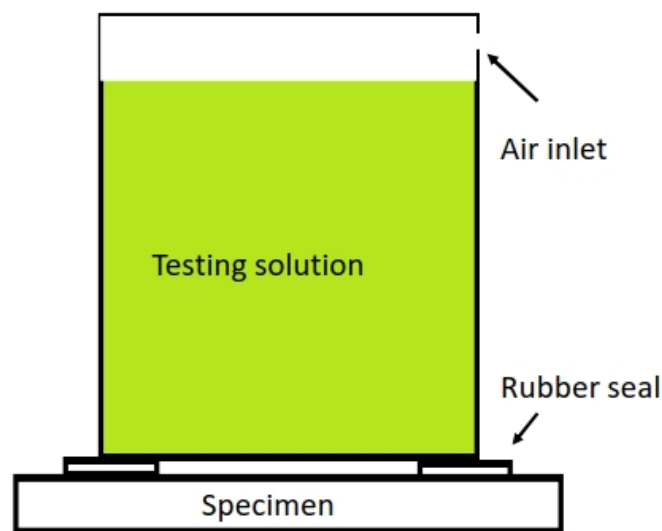
Figure 39. Corrosion test ASTM G48 [70] was utilized to test the braze materials. The specimen and the container was sealed with a rubber ring to prevent the corrosive solution from reacting with the base material.

The modified ASTM G48 test [70] was only a simple immersion test and was given only limited information about the corrosive behaviours within a particular environment. To get more information

about the corrosion behaviour of the materials polarization curves were also measured. In these measurements AISI 316-type stainless steel was used as a reference material where corrosive behaviours of the braze materials were compared. All of these measurements were performed at room temperature in 3.5 % ionized salt water and the potential of the specimen was measured against the reference electrode.

Electrochemical measurements of this study were performed with a computer-controlled Gamry Instruments potentiostat model G750 (Warminster, PA, USA). Open circuit potential and potentio-dynamic polarization measurements were carried out in a standard three-electrode cell. The test cell consisted of a nickel-based braze material – diamond composite as a working electrode, a silver - silver chloride (Ag/AgCl) reference electrode (+0.197 V with respect to the standard hydrogen electrode) and a platinum counter-electrode. Measurements were carried out at a room temperature of 22°C in a naturally aerated and unstirred 3.5 wt.-% NaCl solution (volume: 0.4 l).

Before each polarization scan the system was left to stabilize for 30 minutes with the open circuit potential (E_{OCP}) being measured. In potentio-dynamic polarization measurements, the potential was varied from -500 to +500 mV vs. E_{OCP} at the scan rate of 0.5 mV s^{-1}. The 'Gamry Echem Analyst' program was used to analyse the polarization curves, with Tafel-extrapolation to determine the corrosion potential and corrosion current densities. [71, 72, 73]

3. Results and discussion

3.1 Surface structure of brazed composites

Initial questions at the beginning of the experiments focused on how to evaluate the surface structures of the brazing filler material and the brazed diamonds and also how to analyse the structure inside the braze layer and the layers between the diamond single crystal and the braze filler material. Is the bond between diamond single crystals and braze material mechanically strong and load bearing? How is the diamond affected and eroded by the brazing procedure? It was also important to find out how the reaction between diamond and braze could be adjusted to upgrade the diamond tool performance and mechanical strength, in turn supporting further development of the braze filler materials.

To answer these questions surfaces of the specimens were at first studied using SEM from various viewing angles. Notable discoveries were the braze layer and diamond surface morphologies before and after the high temperature brazing treatment, where carbon from the diamond surface was dissolved and the surface damaged. It was interesting to see how effectively the brazing filler metal wet the single diamond crystals and what kinds of layers were formed on the surface. Together with these observations encouraging results came from the analysis of the morphology and structure of the brazing filler metal once alloyed with the base material and solving carbon of diamond.

Because of the chromium alloying in nickel-based braze materials studied, the brazing filler metal is effectively wetting the diamond surfaces during the brazing procedure. An example of this is presented in Figures 40 - 43 where single crystal diamonds are photographed from above after brazing with Ni-Cr-Si-B and Ni-Cr-P braze materials. Figures 41 and 43 taken with BSE detector show that the diamonds are almost totally covered by the brazing flux. In these images the visible pure diamond surface is seen as black or dark grey marked with circles in Figures 41 and 43. For both braze material types it is evident that the contact angle with the diamond is too low for use as an efficient tool because the braze covered the sharp diamond edges. What should also be noted here are the angular carbide crystals seen at the left-hand side edges of the diamond single crystal. Most of these carbides are formed from solving carbon of diamond.

The brazing was carried out at high temperatures. The difference in the thermal expansion coefficients of single diamond crystals and the brazing filler metal induced fracturing of the brazing filler metal as is presented in Figures 41 and 43. Notable here are the differences in the types of cracks: in Ni-Cr-Si-B braze the cracks are brittle like in glassy material while in Ni-Cr-P braze the cracks are tougher, which are presented in Figure 41 marked with arrows: here the cracks are locally closed and another crack is seen open near the first one. It was deduced from this result that at least part of the Ni-Cr-P braze was ductile.

Fractures were only discovered on the braze that covered the diamond surfaces: the braze surface on the base material was clean of fractures, indicating similar thermal expansion coefficients between the base and the braze materials. The difference between the brazing filler metal surface appearances dependent on the brazing filler metal should also be noted: when brazing with Ni-Cr-Si-B, rod-like chromium borides are formed, and examples can be seen in the BSE image Figure 43 below.
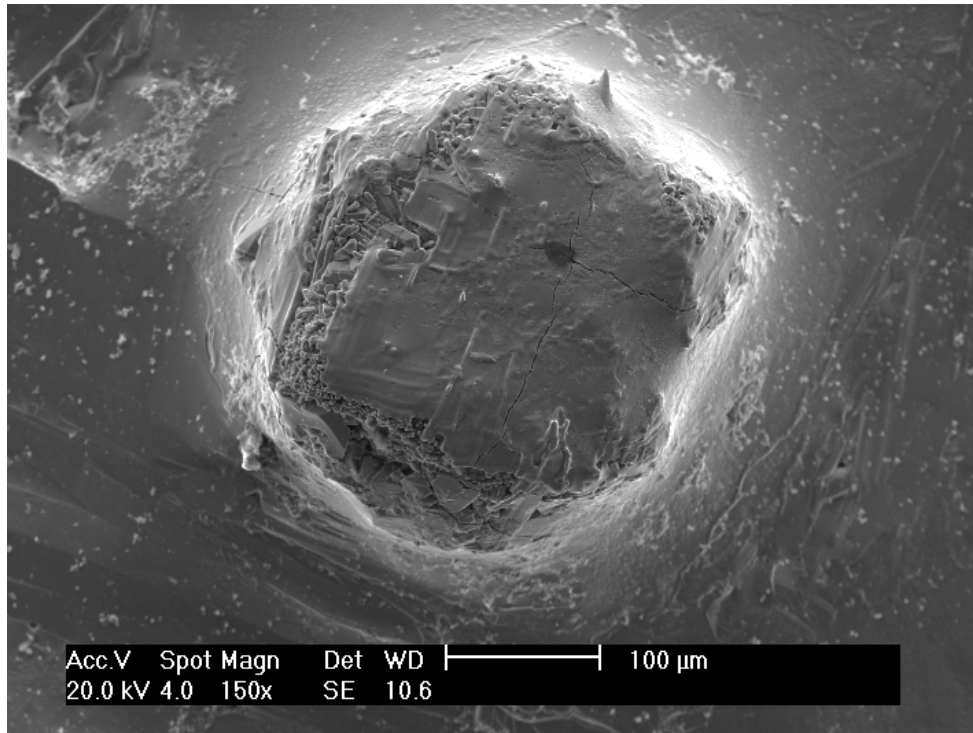
55

Figure 40. Top view of a brazed diamond single crystal brazed with Ni-Cr-P alloy, secondary electron (SE) image.
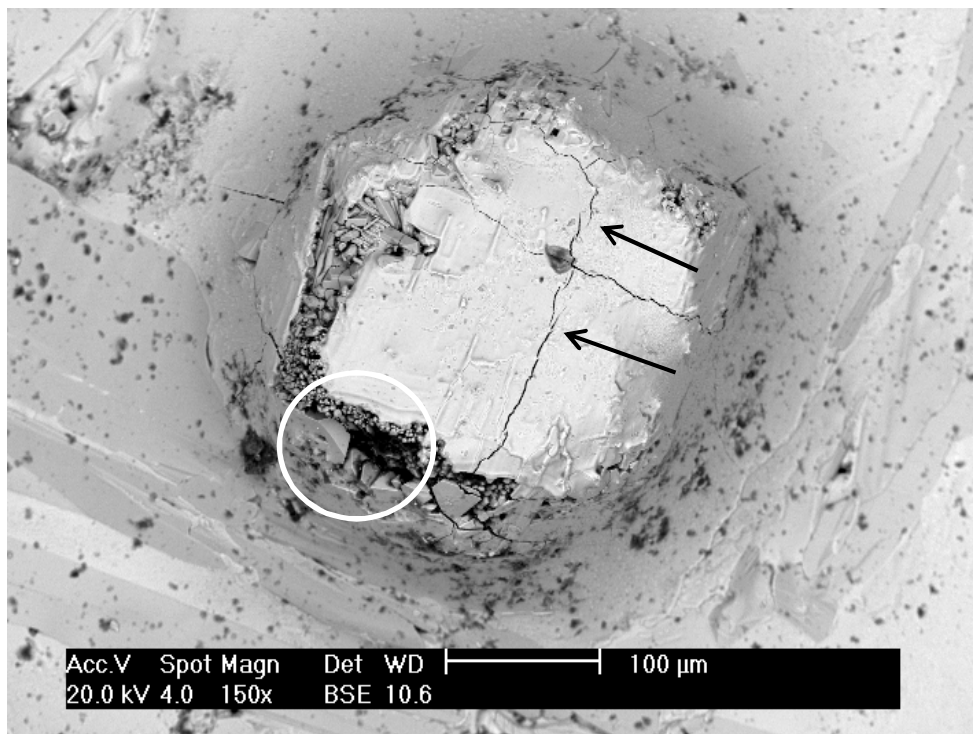

Figure 41. Top view of a brazed diamond single crystal brazed with Ni-Cr-P alloy, backscattered electron (BSE) image. Tough areas of the Ni-Cr-P braze layer are marked with black coloured arrows.
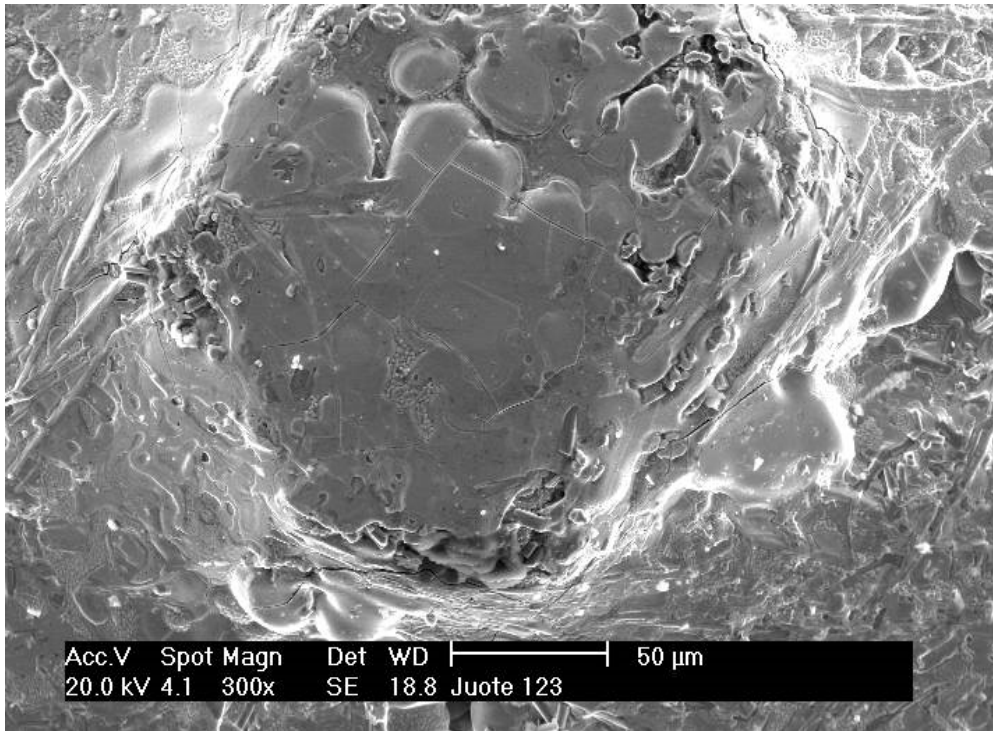
Figure 42. Top view of a brazed diamond single crystal brazed with Ni-Cr-Si-B alloy, secondary electron (SE) image.
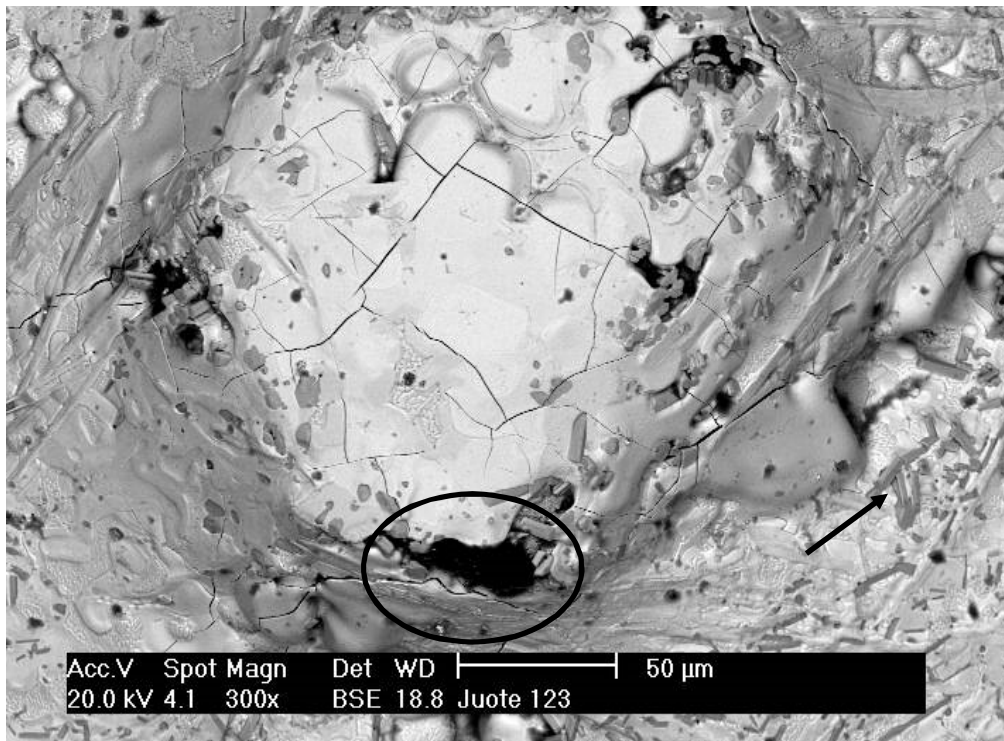

Figure 43 Top view of a brazed diamond single crystal brazed with Ni-Cr-Si-B alloy, backscattered electron (BSE) image. Note the rod like chromium borides (an arrow) visible on the braze surface and the brittle cracks in the thin braze layer on the top of the diamond.

3.2 Structure of diamond single crystal surfaces

The diamond single crystals are seen to be effectively covered by the active braze filler material after the brazing procedure. The braze materials efficiently wet the single diamond crystal surfaces, but how did the braze materials react with the diamond crystals at high brazing temperatures? How heavily were the diamond surfaces eroded? To find out the braze layer had to be removed from the diamond surface.

Figure 44 shows a single diamond crystal in its virgin state with {111} type crystal facet that had six corners facing the lens. The surface of the crystal was in a virgin condition because it has not been affected by the active brazing filler metal. Figure 45 presents a similar crystal after brazing with the Ni-Cr-P brazing filler metal. The surface of the diamond had been covered with the braze metal, but the brazing filler metal, including any carbides formed, had been removed from the surface by the electro-polishing treatment as described above in section 2.3.1.

Looking at Figure 44, the crystal corners had been rounded, especially at the lower part of the diamond facing towards the base material. This could be because of the easy diffusion path for carbon into the face centred cubic (FCC) stainless steel base material, or into the larger amount of braze material around the lower part of the diamond. The plane surfaces of diamond facets had also roughened. These features indicated that brazing affected the surface properties of the diamonds.
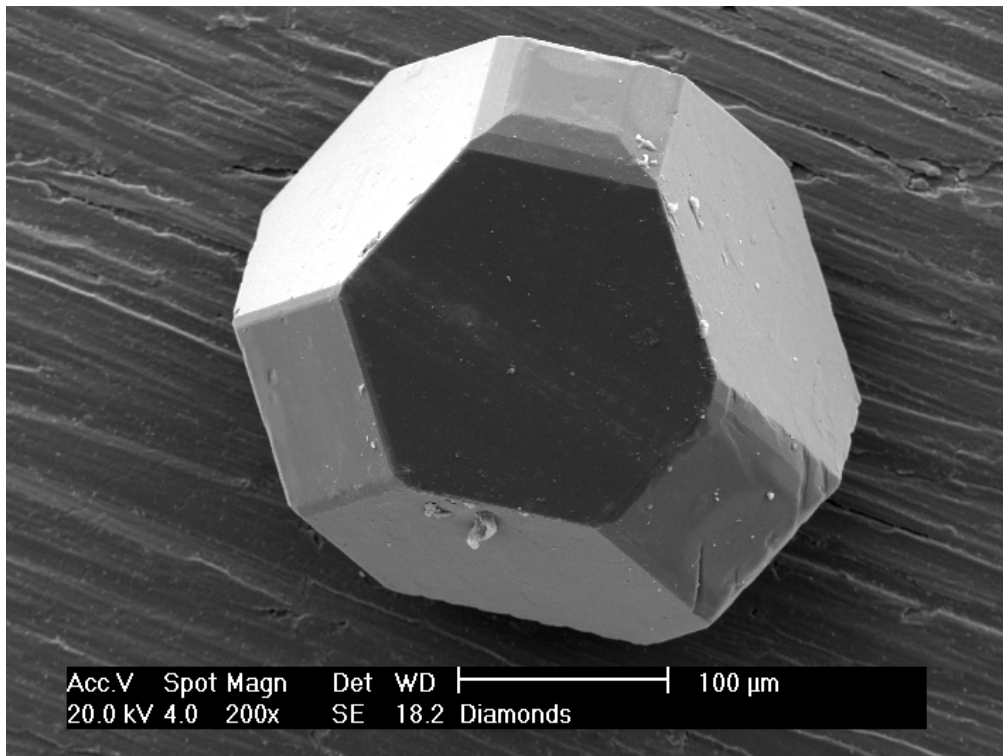
Figure 44. Diamond single crystal before the brazing procedure with {111} type crystal facet and six upward-facing corners.
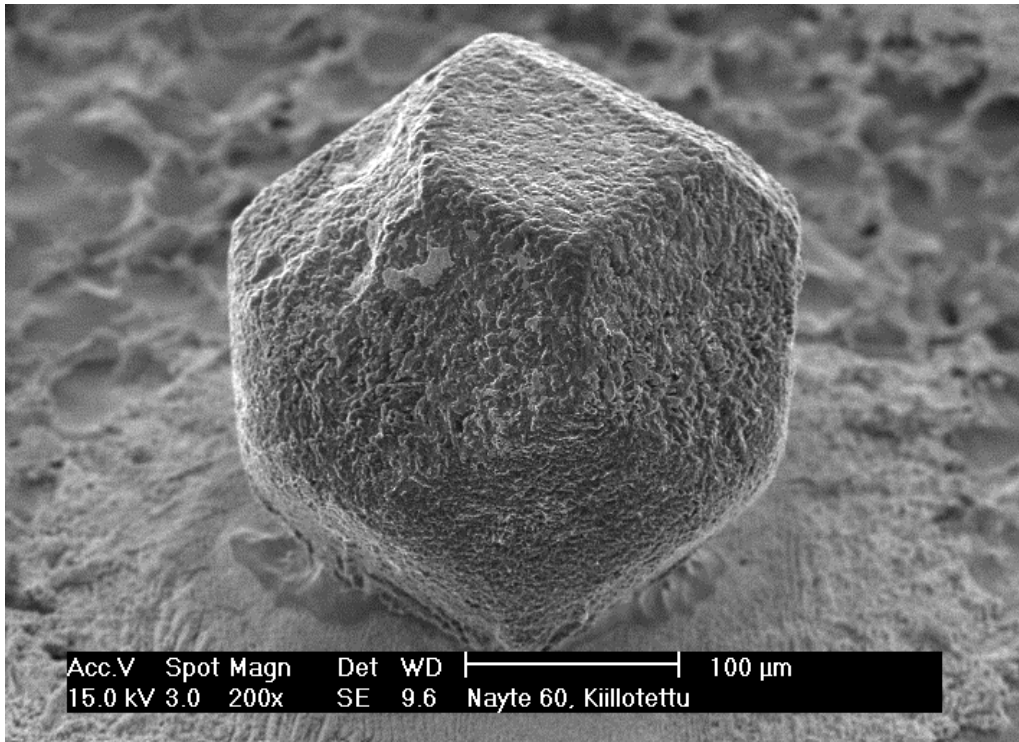
Figure 45. Diamond single crystal after brazing with Ni-Cr-P brazing filler metal {100} type facet facing upwards. The brazing filler metal and carbide layers was removed from the diamond surface by the electro-polishing method.
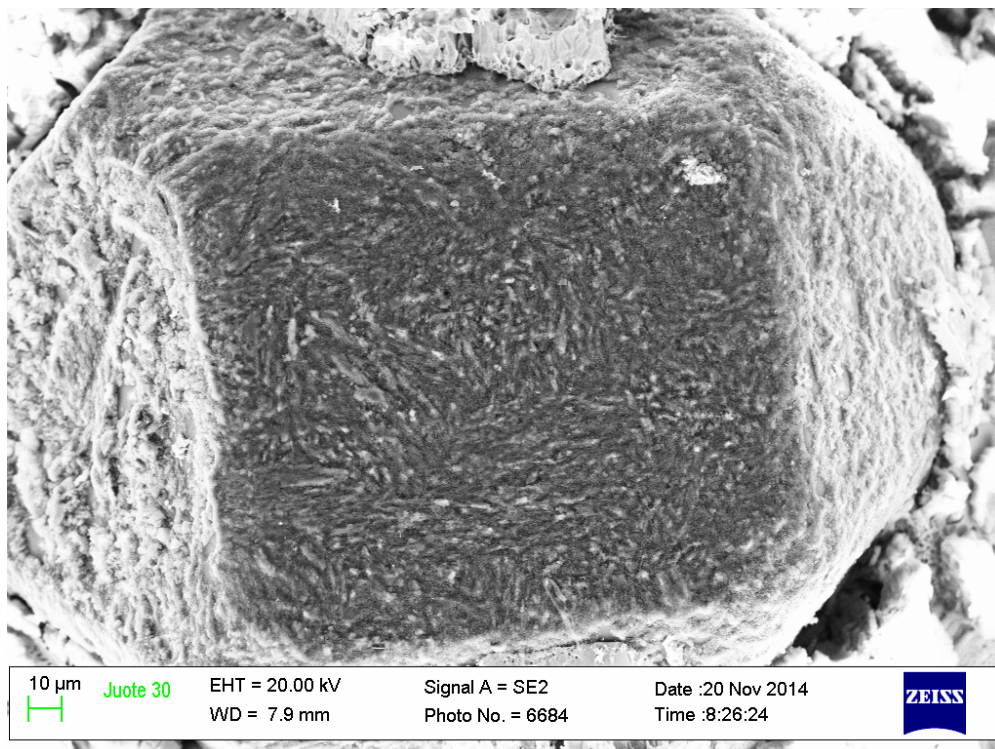
Figure 46. Details on the diamond surface brazed using the Ni-Cr-P type brazing filler metal: {100} type facet up towards the viewer.

In Figure 46 the {100} type facet of single diamond crystal faced upwards and the needle-like details are clearly visible on this electro-polished surface. This type of diamond facet is easily distinguishable from {111} type facets by its square appearance, whereas the {111} type facet has six corners. Carbon has dissolved into the braze filler material from the diamond surface, which explains the rough appearance.

In Figure 47, below, the surface structure of the diamond crystal is presented in more detail. The {100} type facet of diamond is on the left hand side of the image, the rounded corner between the facets is in the middle of the image and the {111} type facet on the right hand side. The image shows us that the surface morphologies of these facets are different: on {111} type facet surface there are clear plateaus between the more or less rough heights. This observation is confirmed in Figure 48, where the square {100} type facet is surrounded by three {111} type facets and once again the difference in the facets' surface morphology can clearly be seen. Further on, in Figure 49 the rounded corners between these facets are presented in more detail. Degradation of the diamond edges reduces the efficiency of diamond as a cutting tool.
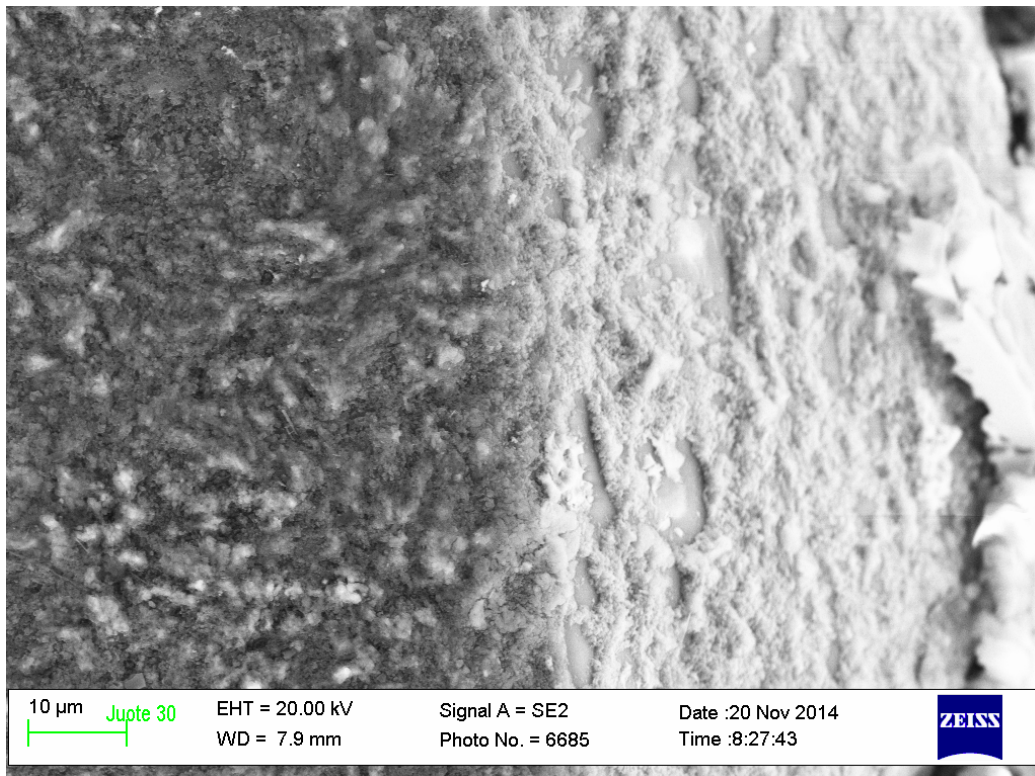
Figure 47. {111} and {100} facets of the diamond single crystal, note the difference in the surface topography.
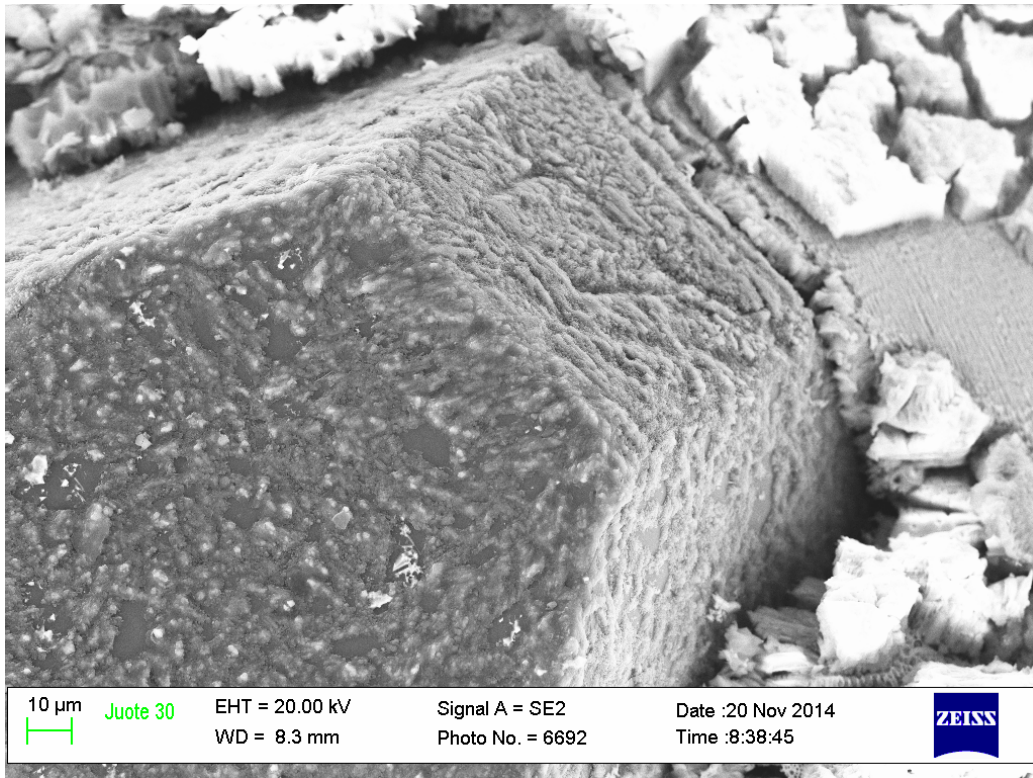
Figure 48. Diamond single crystal surface after removing the Ni-Cr-P type brazing filler material, square {100} and hexagon {111} type facets.
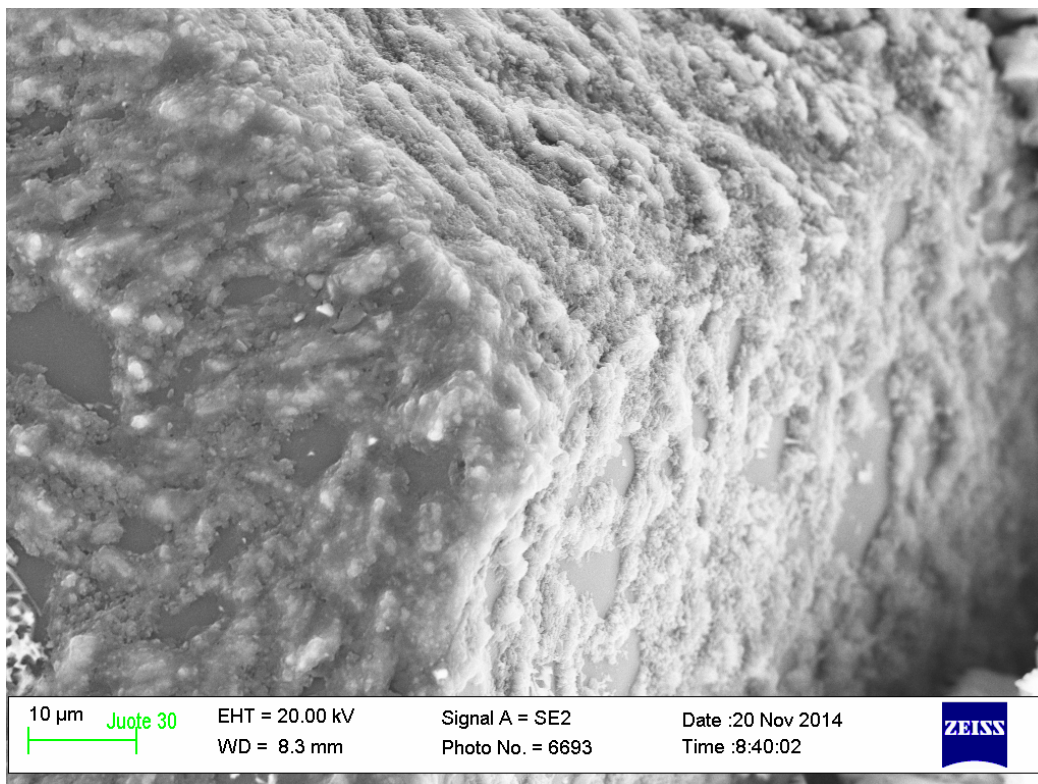
Figure 49. Details on the brazed diamond single crystal surface after removing the Ni-Cr-P type brazing filler material by electro-polishing.

From Figure 49, it was unclear if the surface of the diamond had carbides on it or not. To try to confirm this, the {111} type surface was photographed in higher magnification using SE and BSE with results presented in Figure 50. In Figure 50 a) we can see a detailed structure on the surface: the {111} type atomic layer has been dissolved into the braze material layer by layer, producing relatively plane-like plateaus and round heights between them. The BSE image in Figure 50 b) shows that at the site of view some of the braze material or carbides have remained on the diamond surface, the braze metal is white and the carbides light grey on the left-hand side of the image. To confirm that the surface of the diamond was totally clean an EDX-analysis curve (presented in Figure 50 c) was measured from the clean, dark area on the diamond surface (as marked with a circle on Figure 50 a). According to the curve showing only the huge K-α electron energy peak of carbon, the detail of the crystal planes in Figure 50 a) is part of the degradation structure of a clean diamond surface.
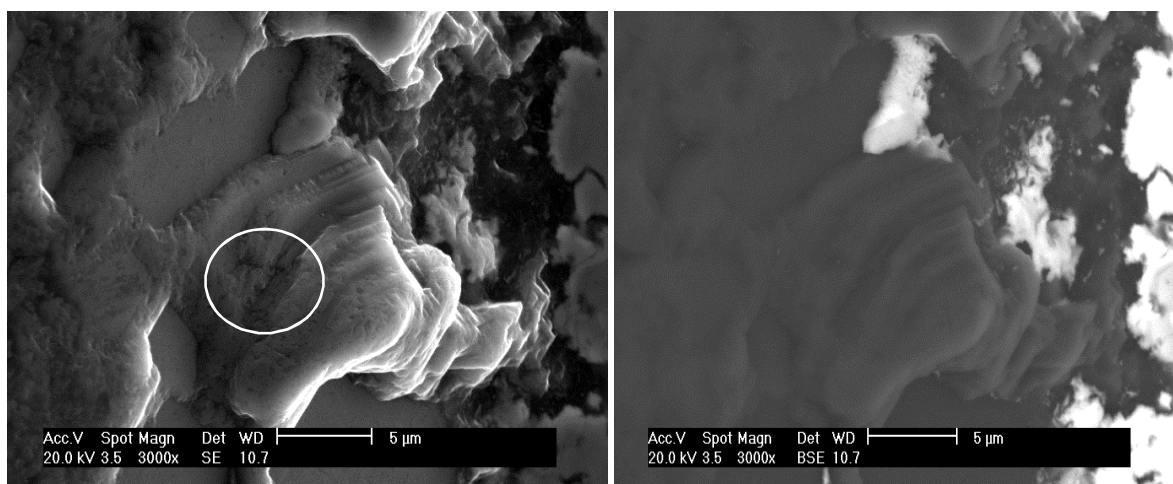
a)

b)
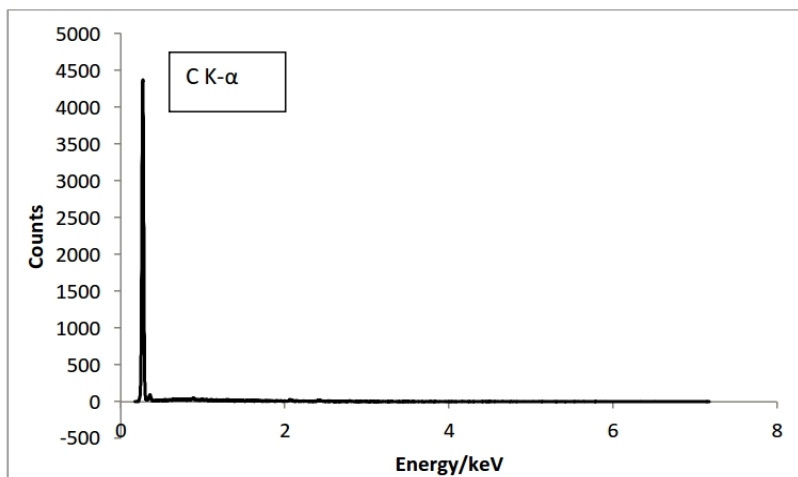
c)

Figure 50. Details on the brazed and electro-polished diamond {111} type facet, (a) secondary electron image and (b) backscatter electron image from the same area of the surface. Parts of the diamond crystal layers of type {111} have been destroyed and the carbon dissolved into the braze metal during

the brazing procedure. Figure (c) presents the EDX-analysis curve measured from the detail marked in Figure (a) with a white circle on the diamond surface showing only the characteristic energy peak of carbon with no traces of Ni-Cr-P type brazing filler material.

Observed differences in the morphology of the damaged diamond surface in directions <111> and <100> suggest that the removal of carbon atoms is dependent on the direction of the crystal. The observations and results indicate that carbon atoms are removed and diffused into braze from {111} type planes in a vertical direction vertical to <111> direction of the single diamond crystal.

 3.3 Differences in facet surface morphologies of pitted diamond single crystals after the brazing procedure

The above chapter presented SEM photographs taken from the specimen surface and from the diamond itself once the brazing filler metal layer was removed. Examination of the diamond surface showed it was affected differently dependent on the brazing material: different types of facet surfaces occurred, in different crystal directions of the single diamond crystal. To get numerical data for the single diamond crystal's facet surfaces it was necessary to use an optical profilometer.

For the measurements, layers brazed using Ni-Cr-P type brazing filler metal were removed from the diamond surfaces using the electro-polishing method as described earlier. The two types of facets, {111} and {100}, common with the diamond single crystals studied here were measured with the optical profilometer. In the following Figures 51 a) and b) the difference in the surface characteristics between the two facet types observed through the SEM can clearly be found: there are blank plateaus observed on the {111} type facet that cannot be seen on the {100} type facet surfaces.

To measure the surface statistical characteristics of the different facet types, clean upward facing facets were prepared and measured, with examples in Figure 51, where the square {100} type facet is presented in Figure 51 a) and {111} type facet (with six corners) in Figure 51 b). In Figure 51 b) some remainders of the braze material are present on the facet surface. These areas were excluded when the surface characteristics were measured.
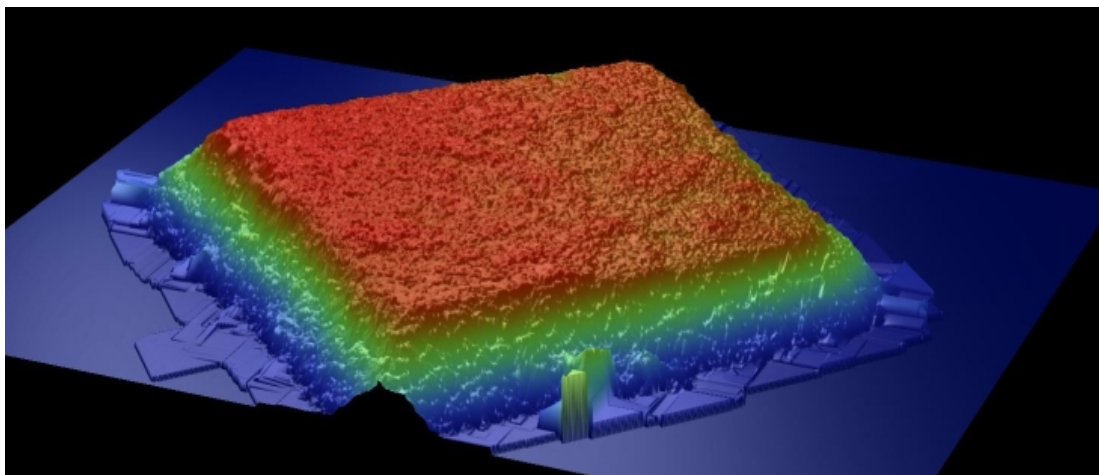
a)
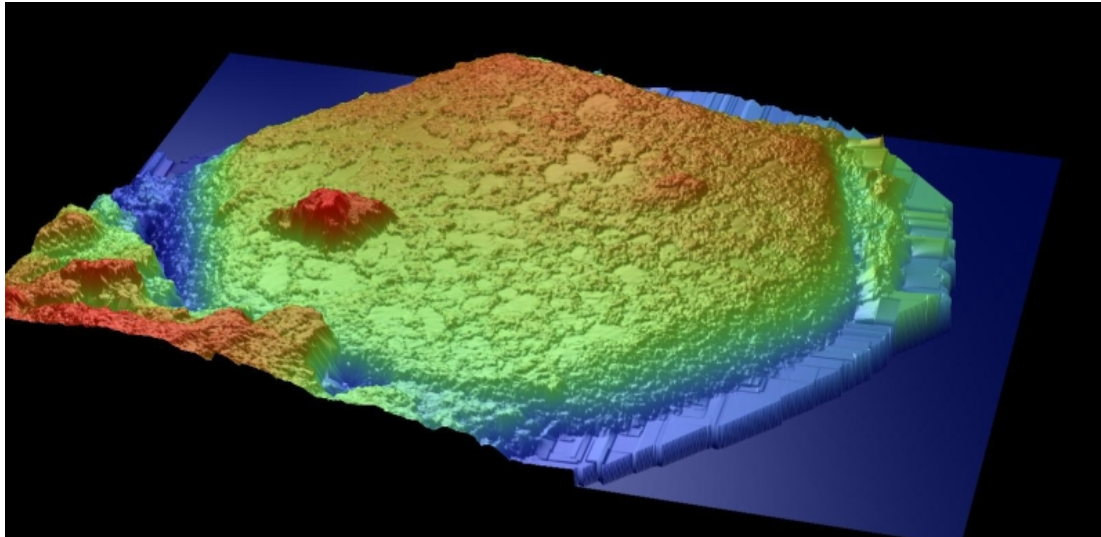
b)

Figure 51. Optical profilometer image measured from (a) {100} type diamond facet and (b) image from {111} type facet after removing the Ni-Cr-P type brazing filler material.

Table 18 presents the statistical surface values of roughness average R_a, maximum height R_t, mean maximum height R_z and root mean square R_q measured from the {111} and {100} type facet surfaces. Ten measurements were taken from the {100} type facet surfaces and fifteen measurements from the {111} type facet surfaces. Any possible tilt angles of the facets was corrected or compensated during the calculations. The numerical results presented in Table 18 are average values of these measurements and according to the results it is clear that the {100} type facets are smoother and finer in detail compared to the {111} type facets. All of the calculated surface roughness values presented in Table 18 are lower for the {100} type facet surfaces. This difference in appearance can of course affect the mechanical properties in the different directions of the single diamond crystals.

Table 18. Surface characteristics measured with the optical profilometer from {111} and {100} type diamond facets.

	{111}	{100}
Roughness average R_a/nm:	700	548
Root mean square R_q/nm:	879	692
Maximum height R_t/µm:	6.91	5.13
Mean maximum height R_z/µm:	5.60	4.21

3.4 Internal structure of diamond single crystals after the brazing process

If the diamond single crystal surfaces are defected during the brazing procedure and carbon diluted inside brazing material, is it also possible that diamond single crystals are defected inside by diffusion of carbon out of diamond crystal or by diffusion of braze metal atoms into the diamond single crystal? Answers to this question were found by focusing on the defects on the fractured diamond surfaces, and also from thin cross-sectional specimens especially prepared for TEM observations.

For these TEM studies single diamond crystals were brazed on the stainless steel surface with the Ni-Cr-P type brazing filler metal. The Ni-Cr-P brazing filler material was selected for these studies because in the earlier studies it found the destructive effect of this braze was harder for the diamond single crystal surfaces. The diamonds were first electro-polished off the surface, washed in alcohol, dried up and crushed between two toughened steel plates. These pieces of crushed single diamond crystals were collected on ultrathin carbon foil with holes in it, and finally studied using TEM operating with 200 kV accelerating voltage.

The focus of these studies was to examine the structure inside the diamond, near its surface. Using TEM it was possible to see if braze material diffusion inside the diamond single crystals or different thermal expansion coefficients or other remaining stresses had caused changes to the internal structure of the diamond crystal's internal planes. During the observations no evidence of this phenomena was observed. To prove this a bright field TEM image was taken with specimen tilted near two beam condition, as presented in Figure 52. Together with the bright field image is presented a selected area diffraction image taken from the area of interest found in the bright field image in Figure 52 a) showing the (111) type diffracted beam. Diffraction image is giving the g-vector direction for the given bright field image. Transmitted beam is marked with a circle in the Figure 52 b).

Some of the fine structure of the layers on the original pitted surface of the diamond are still visible on the right hand side of the Figure 52 a). Inside the diamond crystal there are dark thickness contours and some evidence of twinning due to crushing during the specimen preparation. No evidence of precipitate formation or weakening of the diamond crystal due to carbon atom diffusion from it or diffusion of braze material components into it was observed.

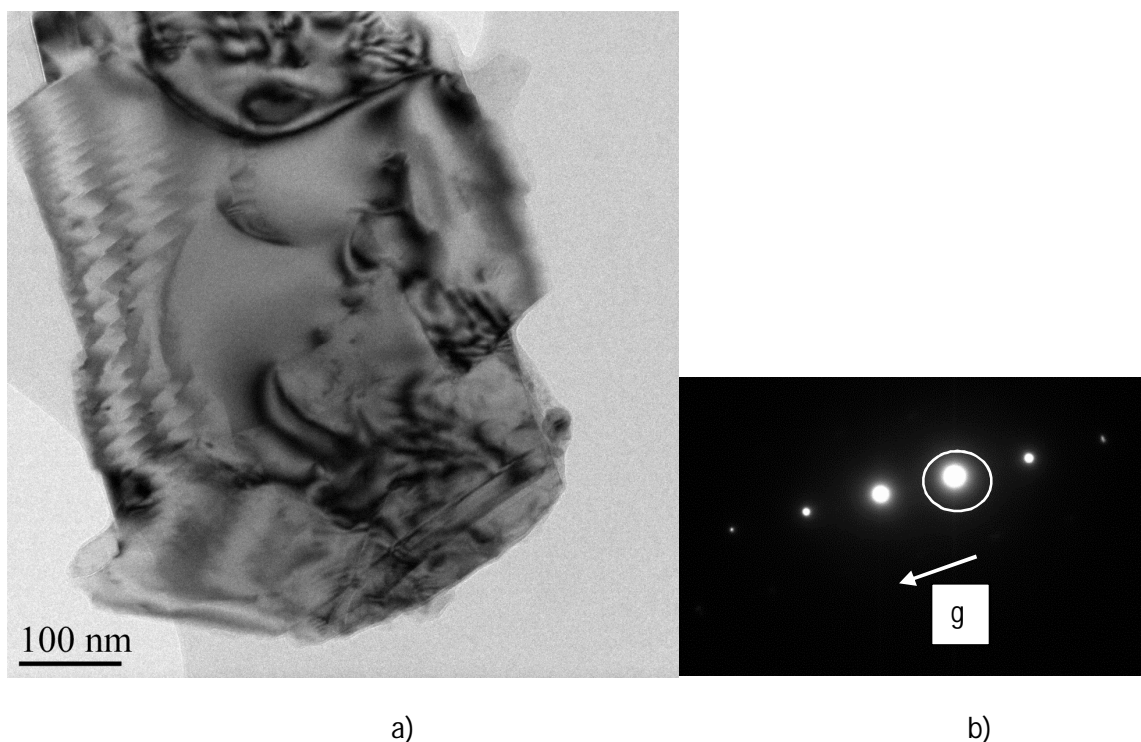a)   b)

Figure 52. TEM micrograph (a) of the diamond internal structure near its surface: bright field image in two beam condition with g-vector (111) in direction shown in the diffraction image (b).

3.5 Structure of the diamond crystal planes near the pitted surface

During the TEM studies no evidence of degradation of the structure inside the diamond single crystals was observed. This result was confirmed with larger volumes of specimen material, when the fracture surfaces were studied with the SEM microscope. These studies, together with hardness measurements and mechanical testing also aided better understanding about the mechanical properties and structure of the diamond crystals after brazing at high temperatures.

For these studies all diamonds brazed with the Ni-Cr-P type brazing filler metal were electro-polished off the surface. Diamonds were crushed between toughened steel plates, glued onto the specimen holder stub and finally coated under a vacuum with a thin amorphous carbon layer for electrical conductivity. If the diamond crystal structure is internally damaged, it should be well evident from the artificial fracture surfaces, which tend to seek out the weakest points and heterogeneity of structure - including the possible precipitates, pores and inclusions, which form stress fields around them.

Figures 53 and 54 show examples of an artificial brittle fracture surface near the original, degraded diamond surface. Looking at the surface, there are some small, light, loose particles attached to the surface during the preparation of the specimens, Figure 53. Even at a higher magnification of the image in Figure 54, it is not possible to detect that any inclusions were formed *inside* the diamond crystal structure.
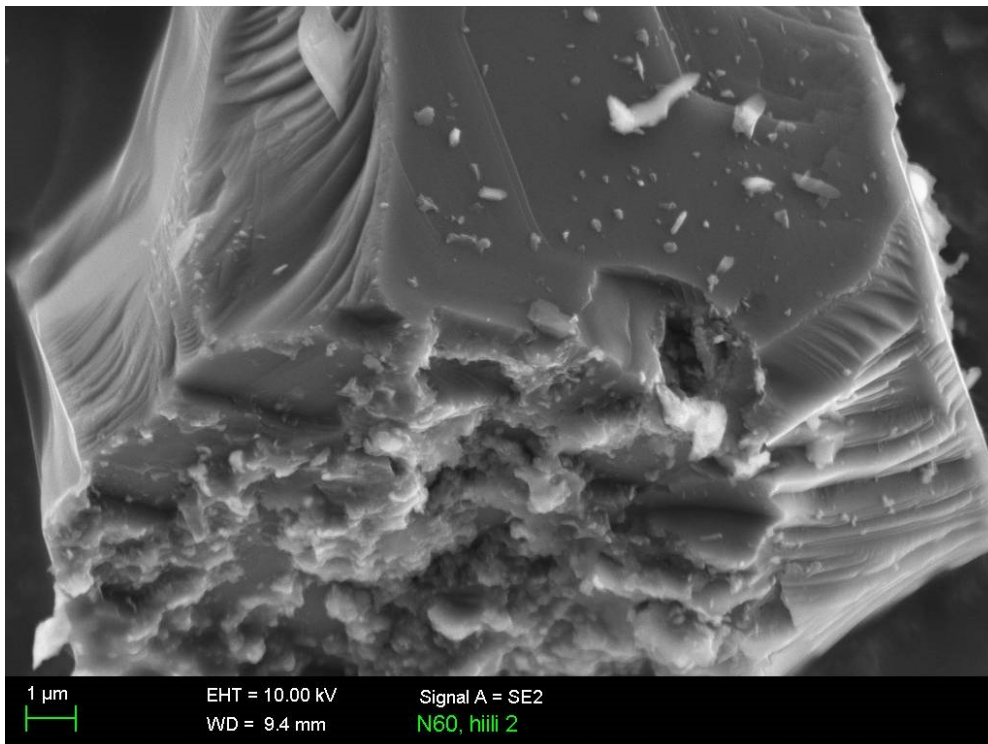
Figure 53. Fracture surfaces and original surface of a diamond single crystal, with the original pitted surface of the diamond facing down in the image. According to the surface morphology it is the {111} type diamond facet.
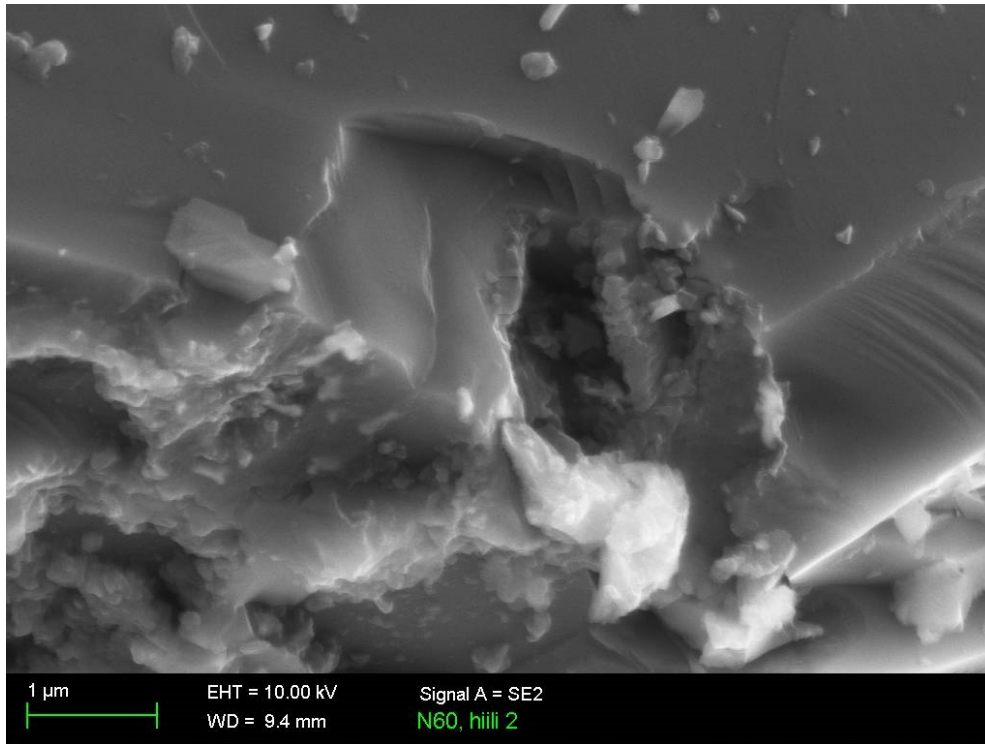
Figure 54. Details on the fracture surface crossing the pitted original {111} type facet surface of a diamond crystal.

Figure 55 depicts a {111} type diamond single crystal facet, from the details observed on the damaged diamond surface. These plateaus were similar to those found during the SEM and optical profilometer observations. The fracture presented in Figures 55 and 56 seems to propagate at the same diamond plane crossing the original diamond surface. The fracture crossing the rough height on the diamond surface on the right hand side of Figure 56 is also worthy of note: the fracture surface morphology is unaffected by the rough appearance of the diamond surface. No evidence of disturbance in fracture propagation is observed further out.

The results described above clearly show that carbon atoms are diffused to the braze material from the diamond surface, but not from inside the diamond. What must also be noted is that the brazing material does not seem to diffuse into the diamond during the brazing process. In this case a clear diffusion zone should be seen on the fracture surface near the diamond surface.
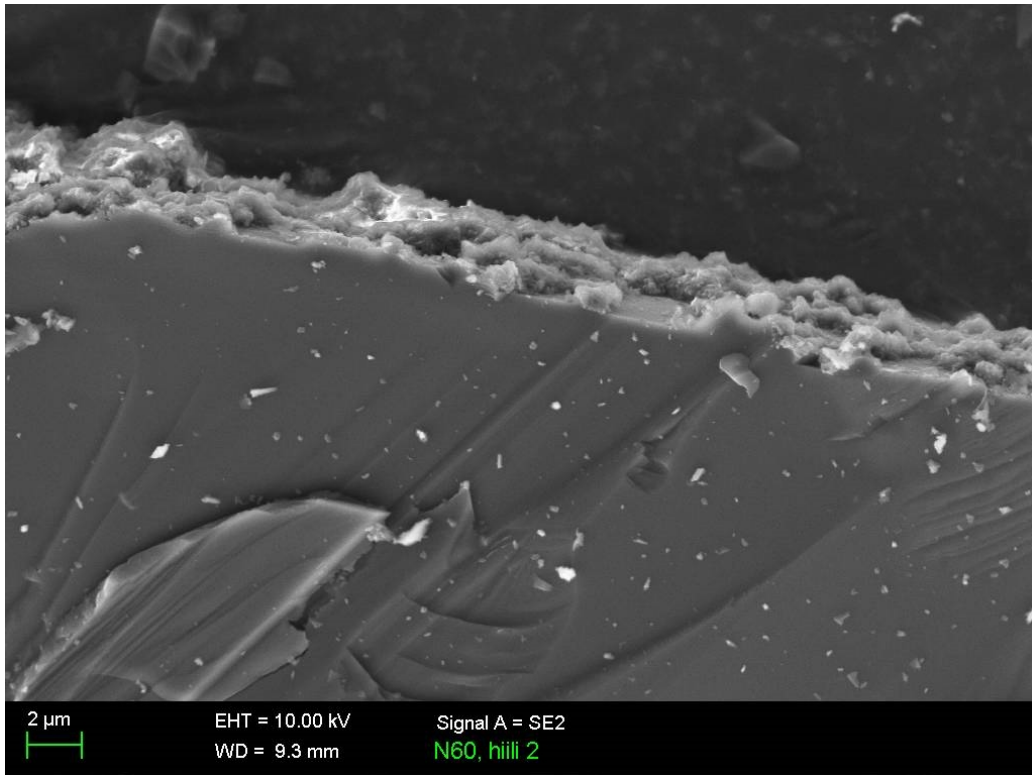
Figure 55. The original diamond surface is upward facing on the image. Some loose particles are attached on the fracture surface during the specimen preparation.
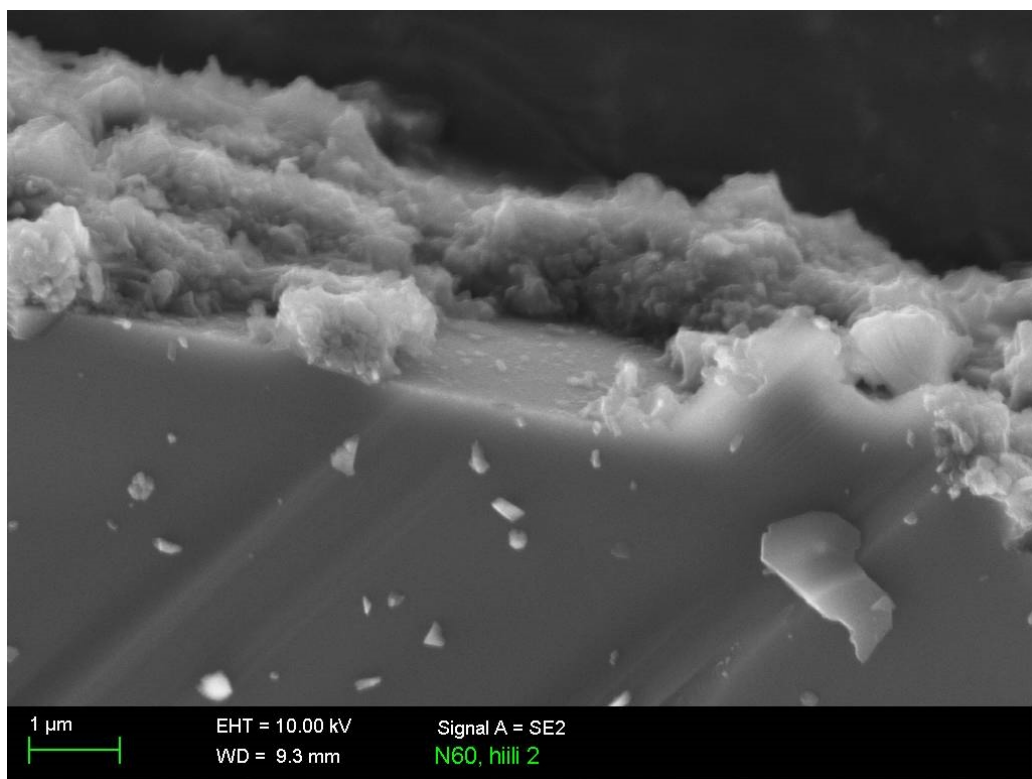
Figure 56. Fracture surface details near the original surface of the diamond. No evidence found of atomic diffusion inside the diamond single crystal.

3.6 Base material dissolution into the braze during the brazing process

The base material on which the braze layer is prepared dissolves into the braze filler material during the fabrication at high temperature, which affects the composition and structure by changing the phosphorous content. This is presented in the binary phase diagram from Figure 6. The amount that dissolves is of course dependent on the brazing temperature, braze material and holding time at the brazing temperature. Furthermore, is it possible to estimate the thickness of the dissolved layer or how much base material is dissolved in the braze filler material? Using BSE-imaging and simple image analysis methods it is possible to evaluate the dissolution from the images taken from the cross-sectional specimens.

Prepared and polished cross-sectional Ni-Cr-P specimens were studied with SEM using the BSE-detector, which gave a high atomic weight contrast from these polished but un-etched samples. Figure 57 presents the microstructure of the brazing filler material at a specimen area with no diamonds present. At this area it can be seen that the layer thickness of the brazing filler metal was between 40 μm and 50 μm. The brazing filler metal is built up of two major phases, according to the binary phase diagrams for Ni-P and Cr-P systems in Figures 6 and 7.
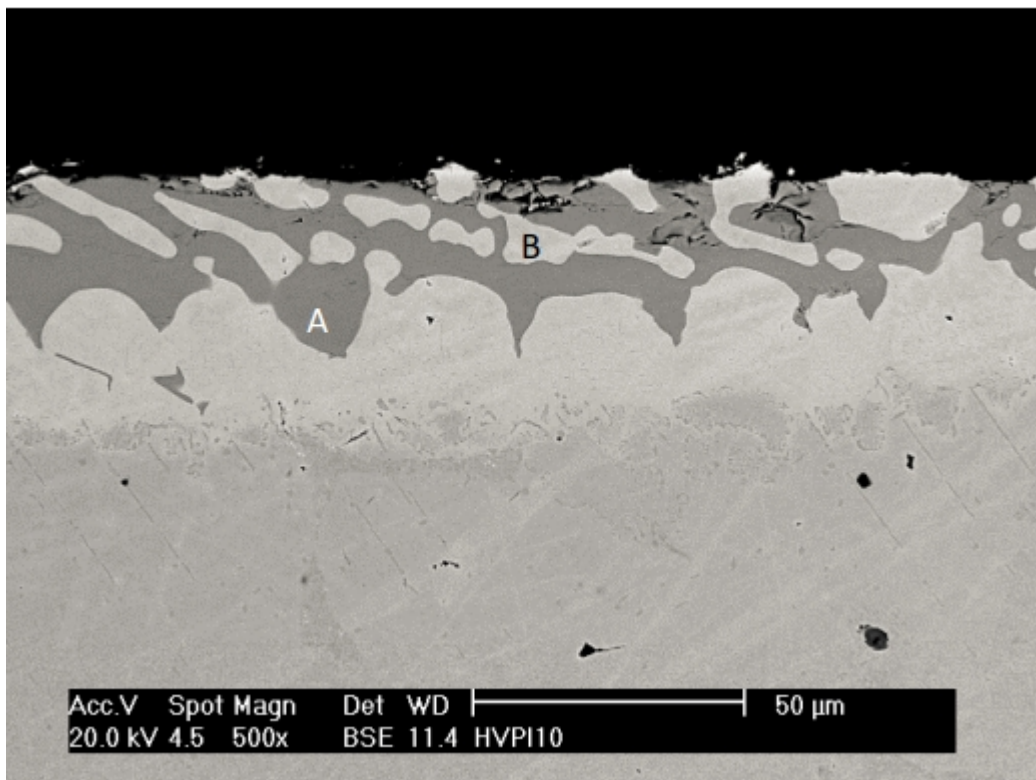
Figure 57. A cross-sectional BSE-image taken from the Ni-Cr-P type brazing filler layer structure. The two phases present are grey (Ni, Cr)$_2$P phase (A) and light Ni based FCC (B) phase, which are clearly separated.

The nickel rich lighter phase (B), with its face-centred cubic unit cell, contains mostly nickel but also has high levels of chromium and low levels of iron. This data is presented in Table 19 below, with approximate compositions of the phases measured by the EDX-analyser. According to the phase

diagrams (from Figures 5 and 6) together with this EDX-analysis the grey phase (A) is built up of 33.3 at.-% phosphorous, along with the chromium, iron and nickel. The imaging in Figure 57 also seems to indicate some brittleness in the grey phase.

Originally, there was approximately 0.2 wt.-% of iron (Table 13) in the brazing filler metal material–however, according to the EDX-analysis (Table 19) some iron dissolved from the austenite iron-based base material during the brazing process. The composition and structure of the brazing filler metal phases is presented in more detail later on.

According to Figure 57, there are only two phases present in the braze material in the area without any diamonds or carbon diffusion into the brazing filler metal. Figure 58 clearly shows the grey level peaks in the counts, which were then fractioned and the peak areas calculated. According to the histogram, the dark $(Ni, Cr)_2P$ type phase (A) is 36 % of the volume of the total braze area, with the rest of the layer made up of the nickel-rich light phase (B).
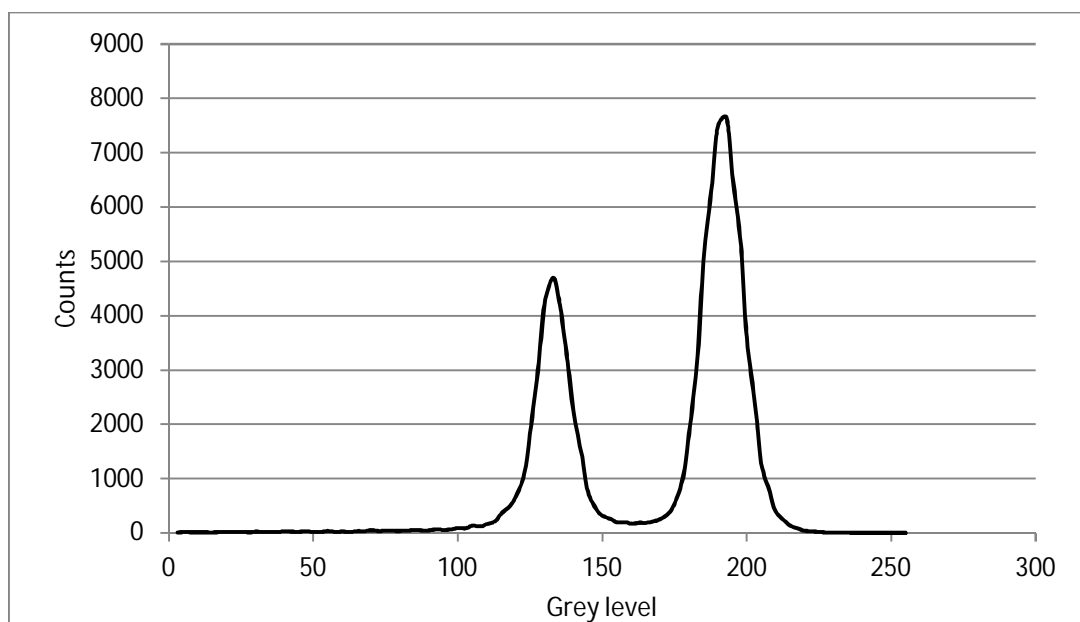
Figure 58. Histogram data taken from the binary structured braze layer presented in Figure 57 using the 'Image J' image-analysing program.

The composition of the phases within the brazing filler metal was measured using EDX-analysis and the ZAF correction calculation method and the results of the analyses are presented in Table 19. Using Table 19's data and the binary phase diagram (Figure 5) it can be calculated using the lever rule [50, 51] with 36 % of the volume of the brazing filler metal being $(Ni, Cr)_2P$ type phase and according to the binary phase diagrams presented in Figures 5 and 6, the content of phosphorous in the phase is 33.3 at.-% and the content of phosphorous in the light phase being near 0 at.-%, that total content of P in the brazing filler metal is 7.8 wt.-%. From this result we can calculate that there is 22 wt.-% of stainless steel dissolved into the braze material during the braze procedure. This means that, if the original density of the brazing filler metal is 8.17 kg/dm^3 [52] and the density of stainless steel is 7.8 kg/dm^3 [48] we can make an approximation that, at the Figure 57 area, where the brazing filler metal thickness

70

is 45 µm, the diluted thickness from the stainless steel surface into the brazing filler metal layer is about 10 µm.

Table 19. EDX-analyses taken from the binary structure of the Ni-Cr-P braze material presented in Figure 57. Approximate compositions of the phase are calculated using the ZAF-correction calculation method.

	A: Grey (Ni, Cr)$_2$P		B: Light Ni based FCC	
Element	wt.-%	at.-%	wt.-%	at.-%
P	21.2	32.6	0.7	1.2
Cr	30.6	28.0	10.4	11.4
Fe	6.7	5.7	20.7	21.1
Ni	41.6	33.8	68.3	66.3
Total	100.0	100.0	100.0	100.0

Figure 59, further on, presents a BSE image taken from the thinner brazing filler metal cross-section. For this thin braze layer the same calculation methods as used for the layer depicted in Figure 57 were employed. In the image the thickness of the layer was measured as just under 25 µm. This means the soldered stainless steel layer was probably more than 10 µm, as it was the case with the thicker coating above.

In this kind of simple binary-phase system it is possible to calculate the total dilution of the base material through combining the volume fraction of the (Ni, Cr)$_2$P phase with the layer thickness. In Figure 60 the diluted base material thickness is presented as a function of the (Ni, Cr)$_2$P volume fraction for the variations in the thickness of layers within the Ni-Cr-P brazing filler metal.

The relation of volume V and the mass m can be determined with a well known basic Eq. 12:

$$V = \frac{m}{\rho} \qquad \text{(Eq. 12)}$$

Here ρ is the density of the material. The phosphorous content P_c in wt.-% of the brazed layer can be expressed as Eq. 13:

$$P_c = P_0 \frac{m_c}{m_c + m_d} \qquad \text{(Eq. 13)}$$

Where P_o is the original content of phosphorous in wt.-%, m_c is the mass of the coating, m_d is the mass of the diluted layer. Using these two equations the next equation can be constructed if the volume is displaced with the thickness t for the coating and the diluted base material layer:

$$P_c = P_0 \frac{\rho_c t_c}{\rho_c t_c + \rho_d t_d} = \frac{P_o \rho_c (t_c - t_d)}{\rho_c (t_c - t_d) + \rho_d t_d} \qquad \text{(Eq. 14)}$$

In Eq. 14 t_c is the thickness of the coating layer without dilution, t_d is the thickness of dilution layer, ρ_s is the density of the coating material, ρ_d is the density of the diluted material.

Furthermore, using the above mentioned lever rule [50, 51] the percentage fraction $F_\%$ of the (Ni, Cr)$_2$P phase in in the braze can be calculated using equation:

$$F_\% = \frac{P_{pin}}{P_{Ni_2P}} = \frac{100P_o\rho_c(t_c-t_d)}{P_{Ni_2P}(\rho_c(t_c-t_d)+\rho_d t_d)} \qquad \text{(Eq. 15)}$$

In Eq. 15 P_{Ni2P} is the content of phosphorous in (Ni, Cr)$_2$P phase.

Results from these equations are presented in Figure 60, where the volume fraction of the (Ni, Cr)$_2$P phase is a function of coating thickness for the differing dilution values of the base material thickness. Using Figure 60, the volume fraction of the (Ni, Cr)$_2$P phase can be predicted and the dilution layer thickness defined when the volume fraction and coating thickness are measured from the cross-section image of the braze layer.
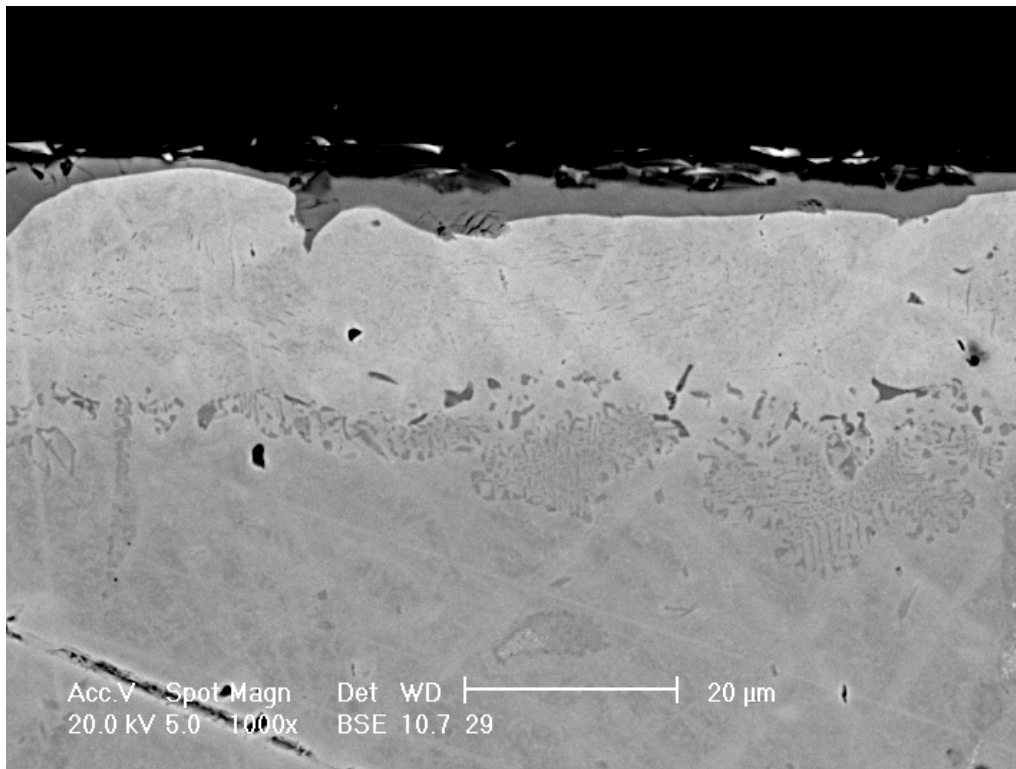
Figure 59. The cross-section of the Ni-Cr-P type brazing filler metal, the layer thickness is 25 μm.
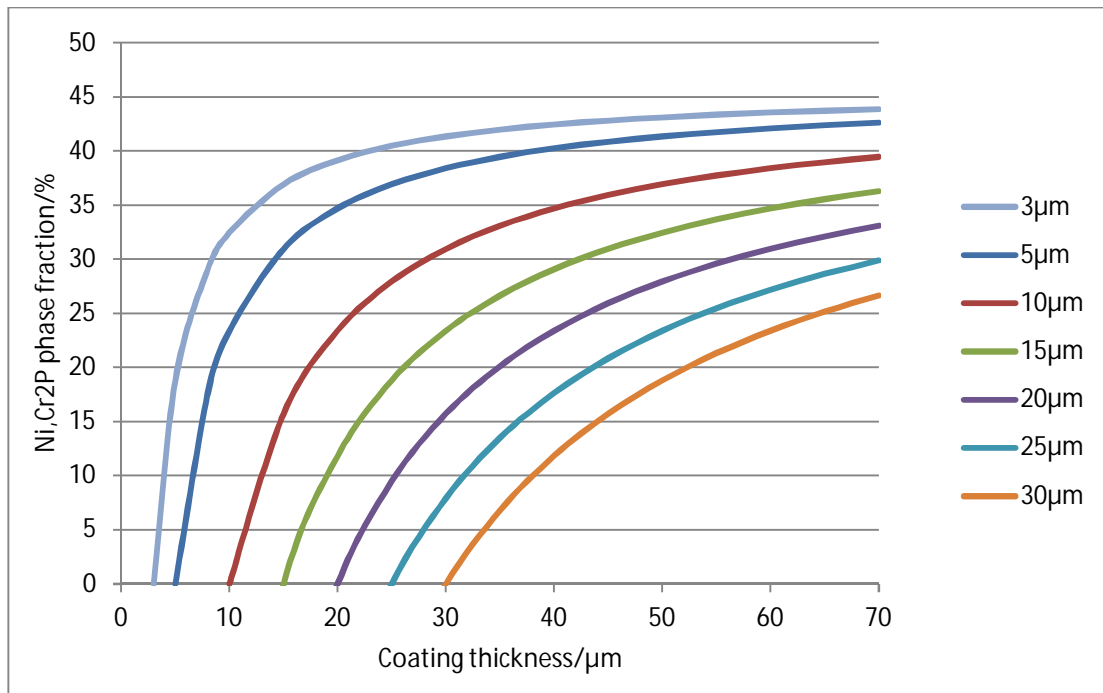
Figure 60. Volume fraction of the (Ni, Cr)$_2$P phase as a function of the braze coating thickness showing thickness measurements for each dilution layer of the base material.

3.7 Microstructure of the braze - diamond single crystal composites

The Back Scattered Electron (BSE-) detector in Scanning Electron Microscopy (SEM) is a powerful tool to get information about the composition differences of the flat, polished surfaces within the phases of the braze-diamond composite. Would the detector, therefore, be able to characterize the structure of braze–diamond single crystal composites? Is it possible to get information on the diffusion of carbon with this kind of imaging? Going further, can assumptions about the composition of various phases be made at a very detailed level of imagery, with micro-scale analysis of the grey levels within the BSE images? Answers to these questions are to be discussed with the next chapters.

The structure of the brazing filler metal and the carbide layers formed at the interface between the diamond and the braze material was studied from the polished cross-sectional specimens. Backscattered electrons gave contrast for the elements with different atomic mass fractions. The backscattering coefficient η is approximately independent of the primary electron energy E_e in the range of 10-100 keV and therefore the level of the acceleration voltage used in these studies does not have influence on the result [53]. However, in all these experiments the accelerating voltage was consistently kept at 20 kV.

3.7.1 Microstructure of the braze material in the Ni-Cr-P - diamond composite

In Figure 61 below (taken with the BSE-detector) a strong atomic contrast was found in the brazing filler metal cross-section. The single diamond crystal is the black section on the right hand side of the image and the plastic used to fix the cross-sectional specimen is the black parts above the braze layer

on the specimen cross-section. Adjacent to the diamond is an area where the braze structure is very fine compared to the structure on the image's left-hand side. This suggests that the braze material has solidified near the eutectic point.

From the specimen area presented in Figure 61, the compositions of the phases were measured using EDX-analyser. The calculated results are presented together with calculated backscattering coefficient values η in Tables 20 - 24 below. It can be noted that the measured compositions of the intermetallic (Ni, Cr)$_3$P and (Ni, Cr)$_2$P phases are relatively near the composition of the phosphorous content formulas (Me)$_3$P and (Me)$_2$P, so the compositions measured from other phases with the same elements can be predicted to be close to the exact composition of the phase.

In the ZAF-correction calculations performed to ascertain the phase compositions, light elements such as carbon were not taken into account because the calculation of the carbon content could not be done accurate enough with the EDX-analysis method used. This is because the low energy X-rays (energy for carbon Kα-peak is 282 eV) generated by carbon is making it difficult to get the information out inside the specimen volume containing heavier elements. Another reason is the carbon contamination that occurred on the specimen surface during the measurements. Contamination is a common phenomena, especially when porous specimens and those cast in plastics are examined. Even the very thin contamination film on the top of the specimen surface is seen in the EDX-analysis curve as a relatively high carbon peak.

The results brought out several phases: two different (Ni, Cr)$_x$P type phases factor *x* being 2 or 3. The chromium content of each phase clearly differed. Together with these two phases there was also a light-coloured nickel-rich FCC phase and an angular phase containing Cr-Ni-P and carbon. This phase was adjacent to the diamond. There were also layers of small carbides detected on the diamond surface.
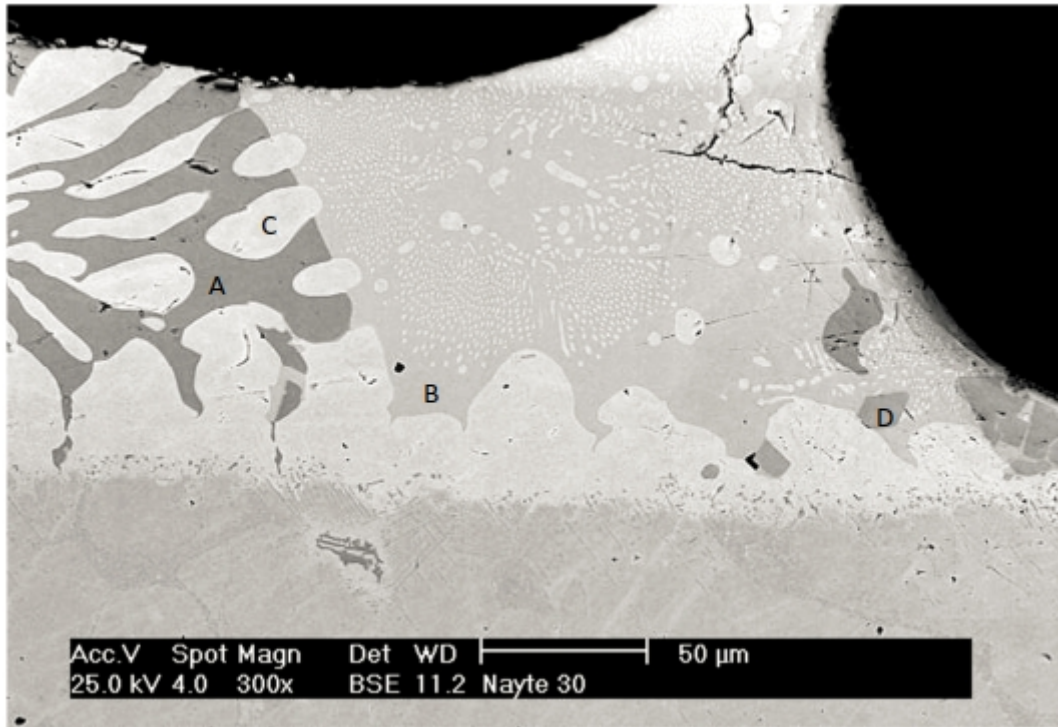
Figure 61. Microstructure of the Ni-Cr-P type brazing filler metal near the diamond single crystal seen in the right hand side of the image. Different phases are marked with letters A ((Ni, Cr)$_2$P phase), B ((Ni, Cr)$_3$P phase), C (Ni based FCC) and D (angular (Cr, Ni)-P-C phase).

Table 20. EDX-analysis measured from the dark grey (Ni, Cr)$_2$P type phase, which is marked with letter A in Figure 61. Given values of backscattering coefficient η_i were used to calculate the total η using the Eq. 1 above and the EDX-analysis data given in the table.

	Calc. η/EDX	Calc. by formula	Measured composition		
	η_i/elem.	Grey phase	Element	wt.-%	at.-%
Si	0.000395	Ni$_2$P	Si	0.2	0.4
P	0.037656		P	21.5	32.9
Cr	0.079644		Cr	30.3	27.6
Fe	0.017745		Fe	6.4	5.4
Ni	0.122925		Ni	41.7	33.7
η	0.258364	0.27006	Total	100.0	100.0

Table 21. EDX-analysis from the light grey $(Ni, Cr)_3P$ type phase, which is marked with letter B in Figure 61, and calculated η-values. Given values of backscattering coefficient $η_i$ were used to calculate the η using the Eq. 1 and the EDX-analysis data given in the table.

	Calc. η/EDX	Calc. by formula	Measured composition		
	$η_i$/elem.	Light grey phase	Element	wt.-%	at.-%
Si	0.000691	Ni_3P	Si	0.4	0.8
P	0.026526		P	15.1	24.8
Cr	0.019116		Cr	7.3	7.1
Fe	0.021015		Fe	7.5	6.9
Ni	0.205553		Ni	69.7	60.4
η	0.272900	0.27713	Total	100.0	100.0

Table 22. EDX-analysis from the white phase FCC nickel-rich phase, which is marked with letter C in Figure 61. Given values of backscattering coefficient $η_i$ were used to calculate the η using the Eq. 1 and the EDX-analysis data given in the table.

	Calc. η/EDX	Calc./formula	Measured composition		
	$η_i$/elem.	White phase	Element	wt.-%	at.-%
Si	0.001118	Ni based	Si	0.7	1.4
P	0.001756	FCC Phase	P	1.0	1.8
Cr	0.024006		Cr	9.1	9.9
Fe	0.058629		Fe	21.0	21.2
Ni	0.201217		Ni	68.2	65.7
η	0.286726		Total	100.0	100.0

Table 23. EDX-analysis measured from the base material and calculated η-values. Given values of backscattering coefficient $η_i$ were used to calculate the η using the Eq. 1 and the EDX-analysis data given in the table.

	Calc. η/EDX	Calc./formula	Measured composition		
	$η_i$/elem.	Base material	Element	wt.-%	at.-%
Si	0.001809	AISI 316L	Si	1.1	2.2
Mo	0.010450	Stainless	Mo	2.8	1.6
Cr	0.051720	steel	Cr	19.7	20.9
Mn	0.003147		Mn	1.2	1.2
Fe	0.180107		Fe	64.5	63.9
Ni	0.032096		Ni	10.9	10.3
η	0.279328		Total	100.0	100.0

Table 24. EDX-analysis from the angular (Cr, Ni)-P-C grey phase, which is marked with letter D in Figure 61 and calculated η-values. Given values of backscattering coefficient $η_i$ were used to calculate the η using the Eq. 1 and the η -analysis data given in the table.

	Calc. η/EDX	Calc./formula	Measured composition		
	$η_i$/elem		Element	wt.-%	at.-%
Si	0.002203	Angular (Cr, Ni)-P-C	Si	1.3	2.5
P	0.012780	phase	P	7.3	12.3
Mo	0.017707		Mo	4.7	2.5
Cr	0.121714		Cr	46.3	46.6
Fe	0.006623		Fe	2.4	2.2
Ni	0.112276		Ni	38.1	33.9
η	0.273303		Total	100.0	100.0

Table 25. Calculated η-values and measured phase brightness. The brightness of the phases was measured using the 'Image J' image-analysis program.

Phase	Calculated η	Brightness
$(Ni, Cr)_2P$	0.258364	150.0
$(Ni, Cr)_3P$	0.2729001	185.5
Ni based FCC	0.286726	202.9
Base material AISI 316L	0.279328	177.4
Angular (Ni, Cr)-P-C phase	0.273303	156.4

Together with the results of the EDX-analysis Tables 20 - 24 also present the calculated η-values for the analysed phases. In these calculations η-values presented in Table 14 were used for each element. In Tables 20 and 21 η-values for the Ni-P phase were calculated according to the formulas Me_2P and Me_3P, Me here being metal atom element Ni, Cr and Fe. The results are collated in Table 25 along with the results of the grey layer measurements. The grey level data was obtained using an image-analysing program 'Image J', which analysed ten areas of each phase from one cross-section image.

The results of these measurements are presented in Figures 62 and 63 below. Figure 62 presents the calculated η-values and measured grey level values for studied phases of the same image. The data shows that the angular phase in Figure 61 has lower grey levels than expected according to the EDX-analysis presented in Table 24. This is the case for both the austenite base material and also the light phase in the brazing filler metal. This can be explained through the soldering of light carbon element from diamond surface during the brazing process.

Figure 63 presents evidence of the soldering effect, where the grey level is presented as a function of η-value. Here the grey level data should form a straight line, but it can be seen that the grey levels of the angular (Cr, Ni)-P-C phase and the base material are far below the line, indicating the presence of carbon in this phase.
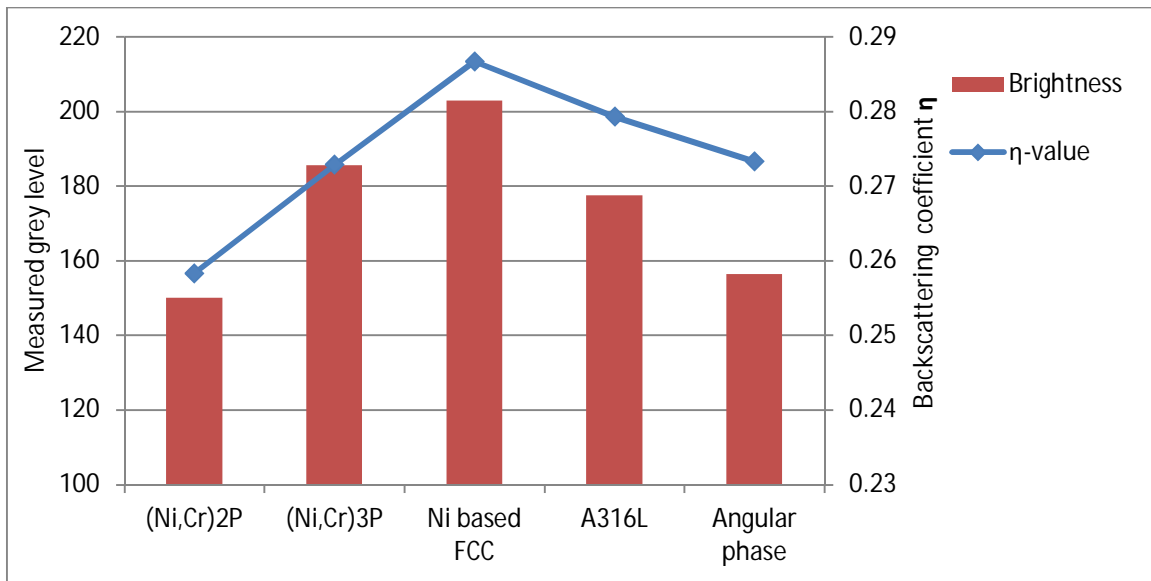
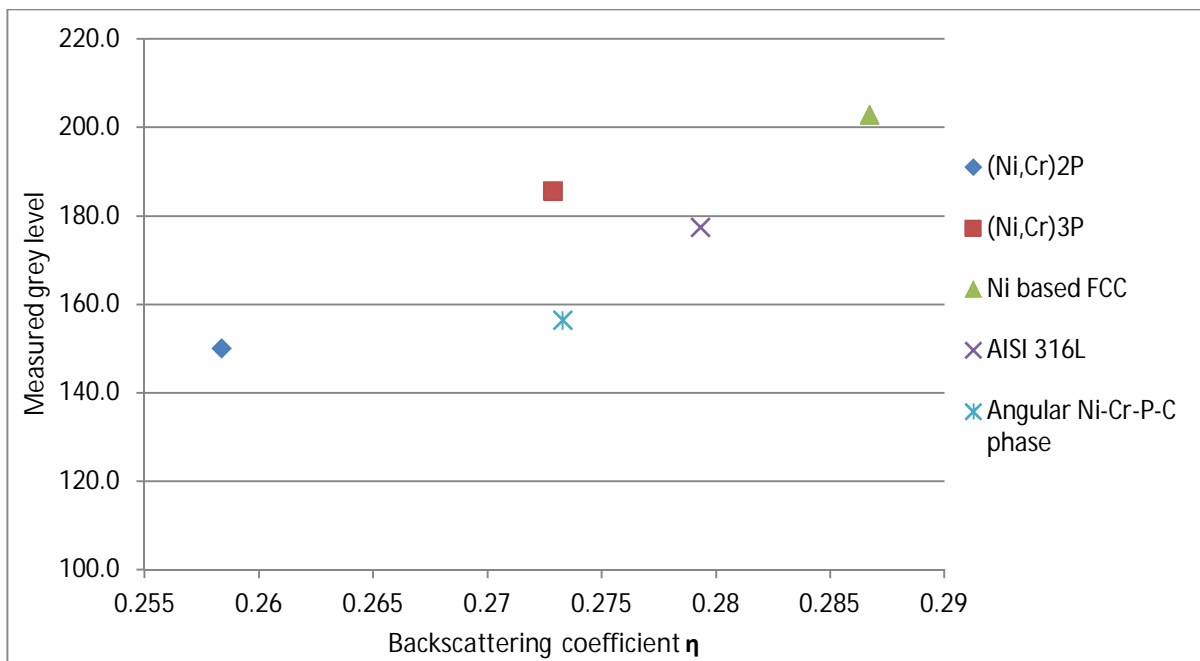Figure 62. Comparison of measured grey levels and calculated η-values

Figure 63. Grey level as a function of the backscattering coefficient η for the phases present.

Figure 64 presents a cross-section image of the grey-coloured carbide layers formed on the diamond single crystal surface (see the white arrows in the image). Analysing the diamond structure, the carbide layer is thicker above the diamond than under it, although Figure 61 shows that the edges of the diamond are more rounded due to more carbon dissolution under the diamond than on top of it. It is possible that the stainless steel base material dissolved the loose carbon more effectively into the matrix than the thin brazing filler metal layer above the diamond.

The thickness of the carbide layer over the diamond was measured to be between 20-30 μm and it was only a few micro-meters under the diamond.
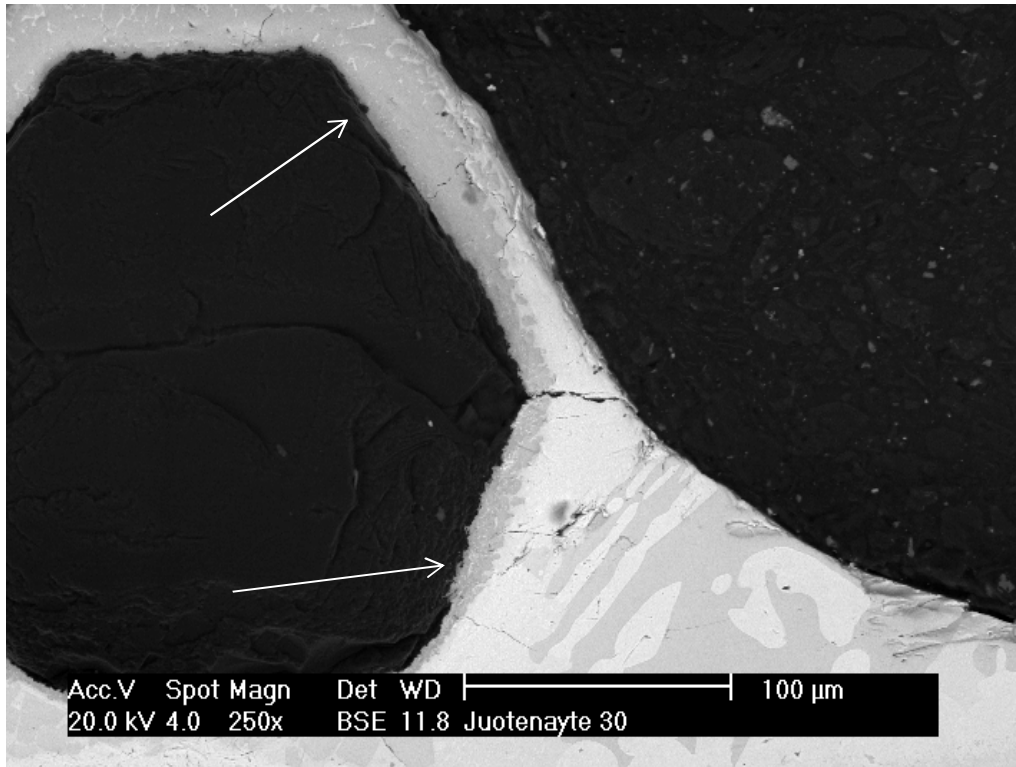
Figure 64. Carbide layers (arrows) formed on the diamond single crystal surface during the brazing process with Ni-Cr-P type brazing filler material.

Further analysis of the calculated η-values and measured brightness level from carbides on the diamond surface continued the characterization work. To do this, cross-sectional images were taken at the cross-section of the diamond and the brazing filler metal boundary. One of these areas is presented in Figure 65, where the black diamond is at the bottom of the image, with a thin dark grey layer of carbides on the surface of it, larger grey carbides in the middle of the image and light grey phosphorus containing braze matrix phase in the upper part of the image.

EDX-analysis confirmed that the layers are chromium carbides. The EDX-analysis curves are presented in Figure 66. As well as containing chromium, the dark grey carbide contains a small amount of molybdenum, shown in the low Mo-L peak in Figure 66 a). The higher peak of carbon measured from the darker carbide layer indicates a higher carbon content when compared to the other carbide's curve presented in Figure 66 b). This explains the variation in the grey levels of carbides presented in Figure 65. The point resolution of the EDX-analysis with used acceleration voltage of 20kV is only 2-3 µm within this material, so some of the data came from the adjacent diamond. The results show that the information from the BSE-imaging gives more detailed results, when compared to the EDX-analysis.

79
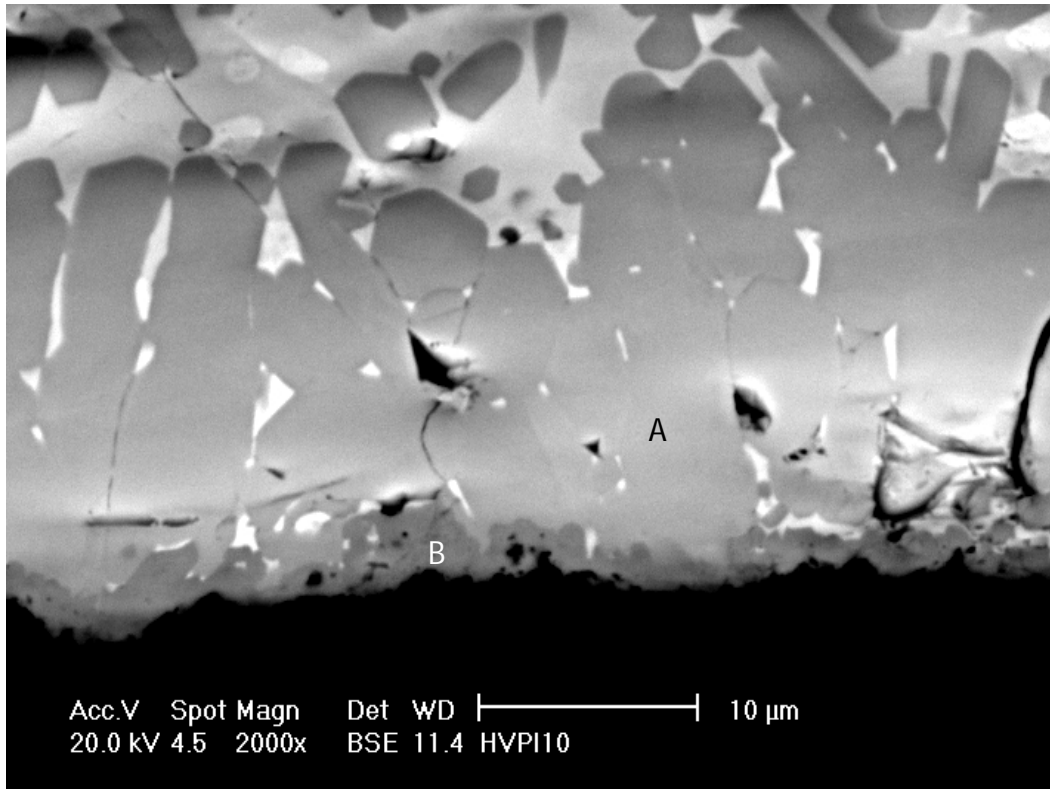
Figure 65. Carbide layers A (light) and B (dark) on the diamond single crystal top surface photographed using a BSE detector, brazing filler material is Ni-Cr-P.
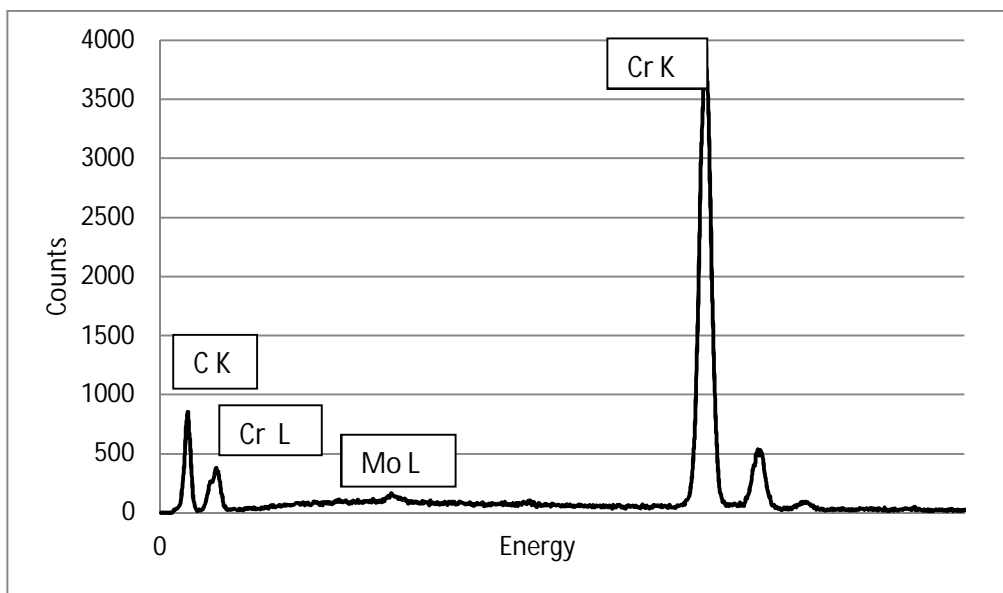
a)
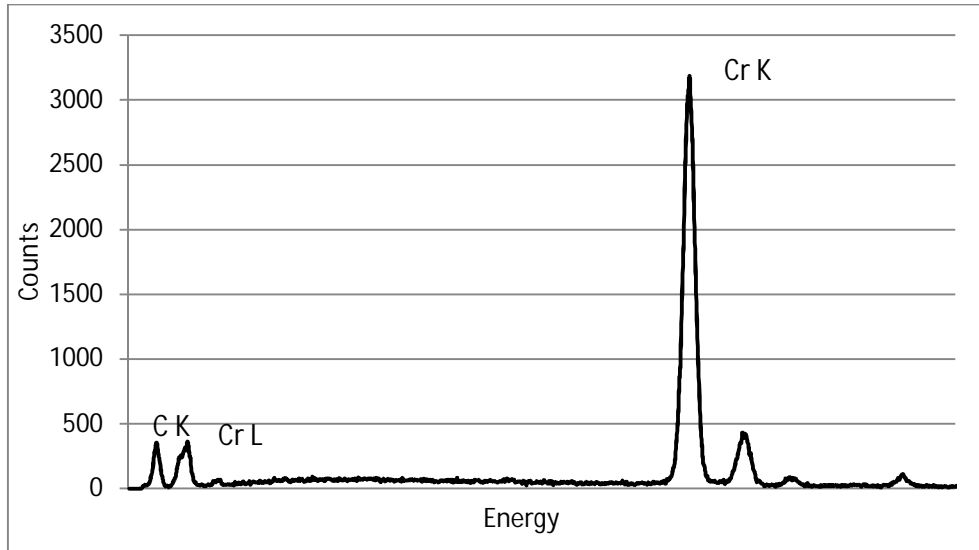
b)

Figure 66. EDX-analysis curve measured from (a) the dark carbide B and (b) the light carbide A presented in Figure 65.
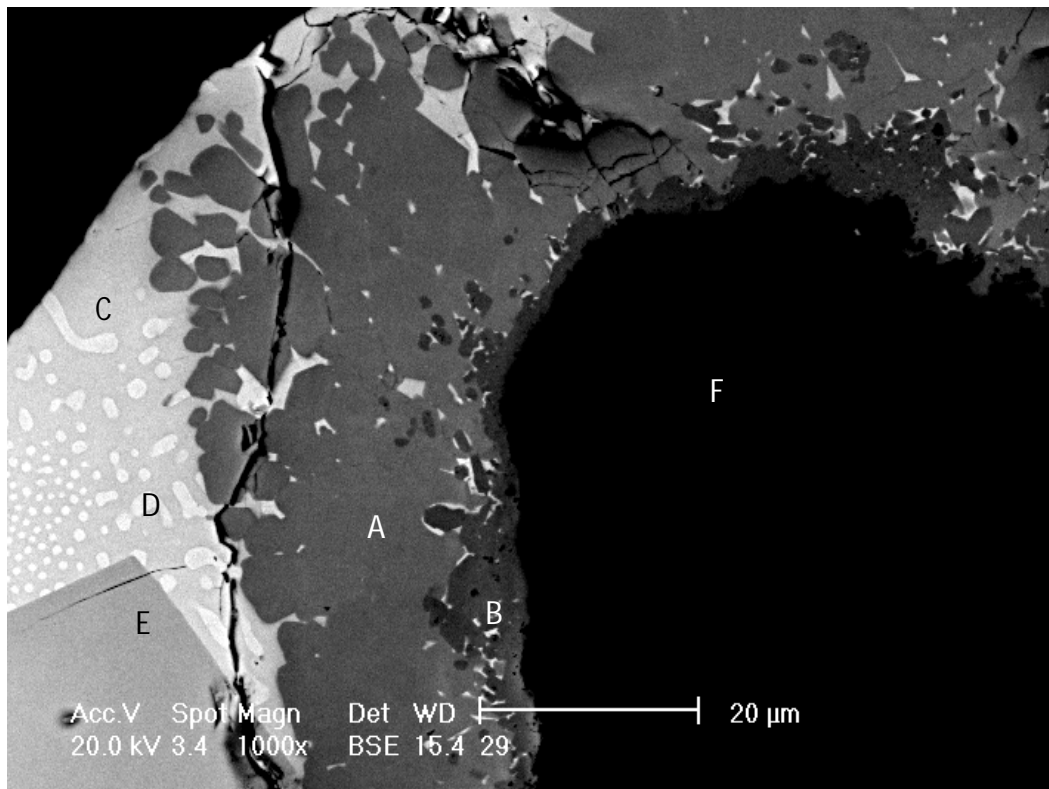
Figure 67. Two separate carbide layers A and B on the diamond single crystal surface (a BSE image). Brazing filler material is Ni-Cr-P.

The grey levels were measured with the 'Image J' image analysis program from the phases presented in Figure 67 above. A number of the areas measured, and the standard deviation of the results, are

presented in Table 24. The grey level of each phase was calculated as an average value of these measurements.

From data the grey level of the Cr_3C_2 carbide is seen as slightly lower than expected, the results are presented in Figures 68 and 69. It is also possible that some carbon has dissolved into (Cr, Ni)-P-C and Ni-based FCC phases because the grey levels of these phases have lower values than expected according to the η-values calculated.

Table 24. Measured grey levels and calculated η-values for the phases A-F present in Figure 67.

Formula	Grey level	η/ Calc.	Areas measured
A: Cr_7C_3	197.4	0.24508	3
E: (Cr, Ni)-C-P	224.2	0.273303	1
C: $(Ni, Cr)_3P$	235.4	0.2729	2
D: Ni based FCC	243.8	0.286726	2
B: Cr_3C_2	186.0	0.236452	4
F: Diamond	15.9	0.064083	1
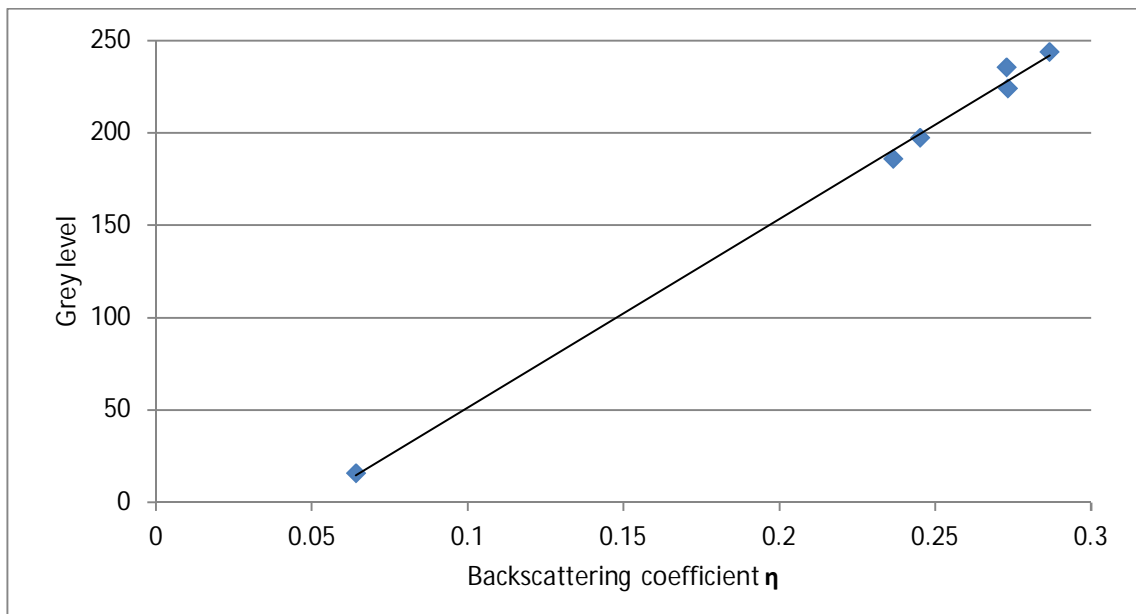
Figure 68. Grey level as a function of calculated η-values for the phases present in Figure 67 and Table 24.
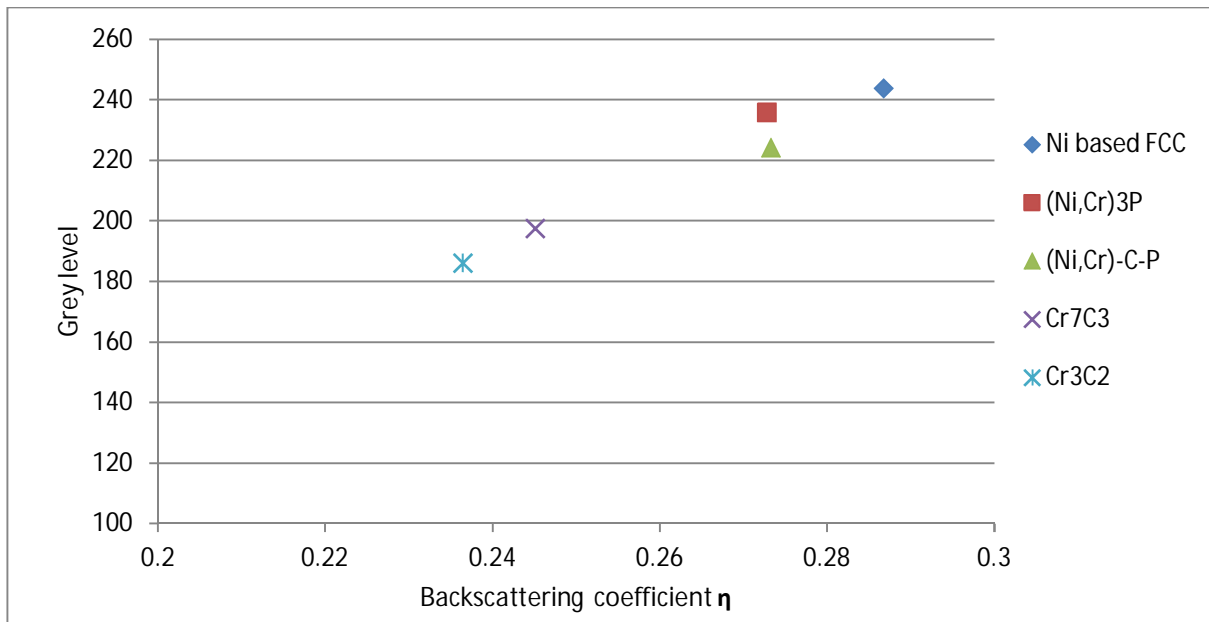
Figure 69. Grey level as a function of the backscattering coefficient η for the phases present in Figure 67.

3.7.2 Structure at the interface between the Ni-Cr-P braze material and the diamond single crystal

The Broad Ion Beam (BIB) specimen preparation technique was used to gain a detailed picture of the layer between the braze material and the diamond. There are two advantages to this technique against the mechanical grinding and polishing technique also used in the experiments: with BIB the diamond surround should not suffer any deformation during the specimen preparation; and the hard diamond will be cut also, showing the interface and the carbide layers in more detail.

Two images taken using BIB specimen preparation technique are included here in Figures 70 and 71. Note that in Figure 70 there are many fractures around the diamond, indicating residual stresses. This means that all the cracks found in specimens prepared by mechanical grinding and polishing are not due to specimen preparation. Figure 71 presents two carbide layers on the diamond surface similar to those found earlier in mechanically prepared specimens. The image shows two separate carbide layers appeared under the diamond, between it and the base material. This was not clear during examination of the mechanically prepared specimens. It can also be noted here that if there is a graphite layer between the diamond and the braze filler material it will relax the residual stresses and no cracking can occur in the braze filler material near the diamond crystal.

The finish achieved on the specimen surface from the ion-beam technique was not as flat and well-polished as by mechanical grinding and polishing. Figures 70 and 71 show the light ridges in the direction of the ion beam, which hindered the grey level measurements, making the BSE analyses somewhat more inaccurate than with mechanically finished specimens.
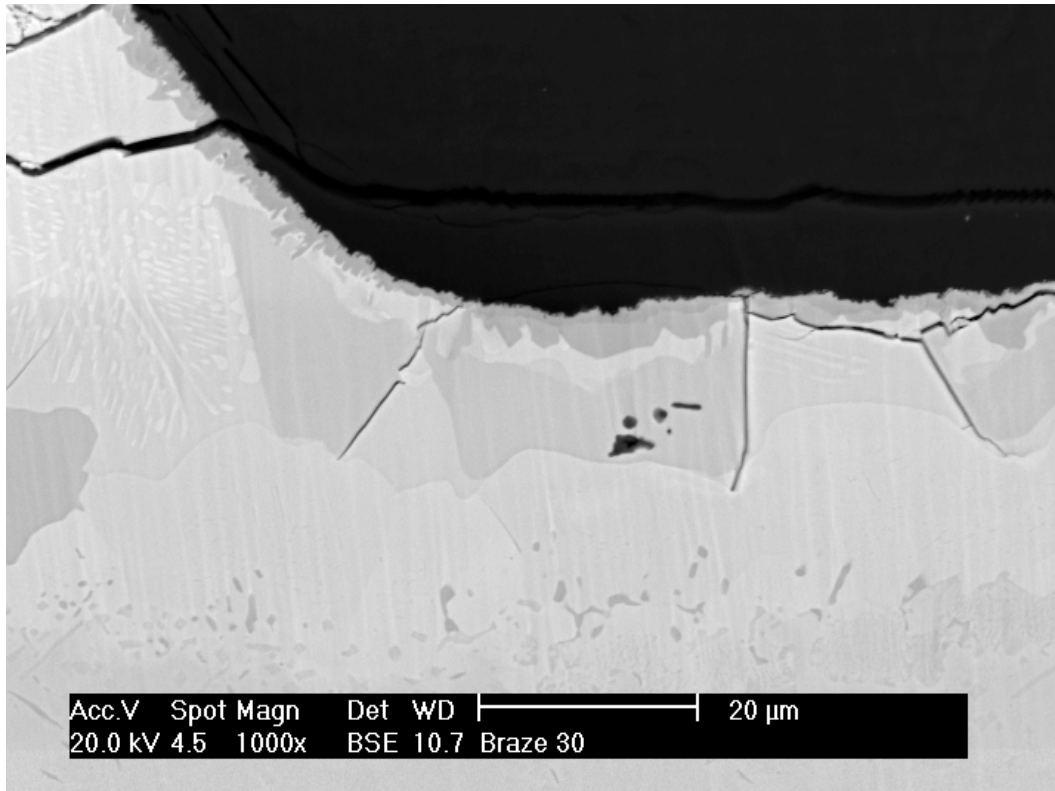
Figure 70. The Ni-Cr-P brazing filler material cross-section made with BIB-technique. The dark section in the upper part of the image is the diamond.
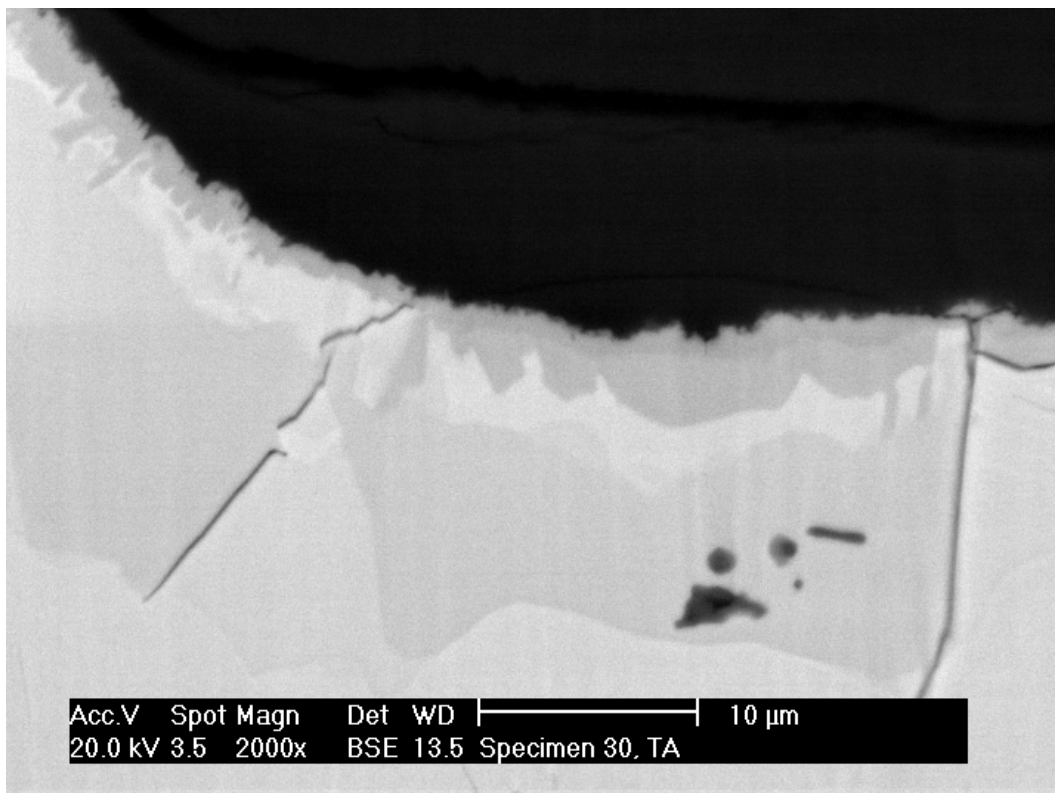

Figure 71. Two thin chromium carbide layers against the diamond single crystal surface.

3.7.3 Structure of the Ni-Cr-P brazing material on the graphite base material

Figures 41 and 43 show that the thermal expansion rate is different between the diamond and nickel-based brazing filler metal. Because of this difference residual stresses are formed after the brazing process. To study carbide formation and thermal expansion differences between the materials when carbon has diffused into the structure, the Ni-Cr-P brazing filler metal was introduced on the porous graphite plate. Specimens were prepared in a high vacuum furnace at 950°C. The braze layer thickness after the brazing process was measured to be 100 μm.

Cross-sectional specimens were prepared to get information about the structure of the brazing filler metal after carbon diffusion. Although fracturing was found on the braze layer surface, no fractures were found between the braze and the graphite base material, indicating a good bond between these materials. It was also noted that the studied brazing filer material structure was very similar to the filler used with single diamond crystals presented earlier. Three different phases were found and analysed with the EDX-analyser and the results presented in Table 25. As shown there, the chromium and iron content is low because there was no stainless steel base material to dissolve into the brazing filler metal. The grey matrix is the $(Ni, Cr)_3P$ type phase and chromium present was concentrated into the light nickel-based FCC phase. Here, as found near the single diamond crystals, a relatively large amount of the light grey (Ni, Cr)-P-C phase is present in Figures 72 and 73 (C). This phase can be distinguished from the carbide by the grey level as shown in Table 26. The difference between these phases was measured to be 17 grey level units.
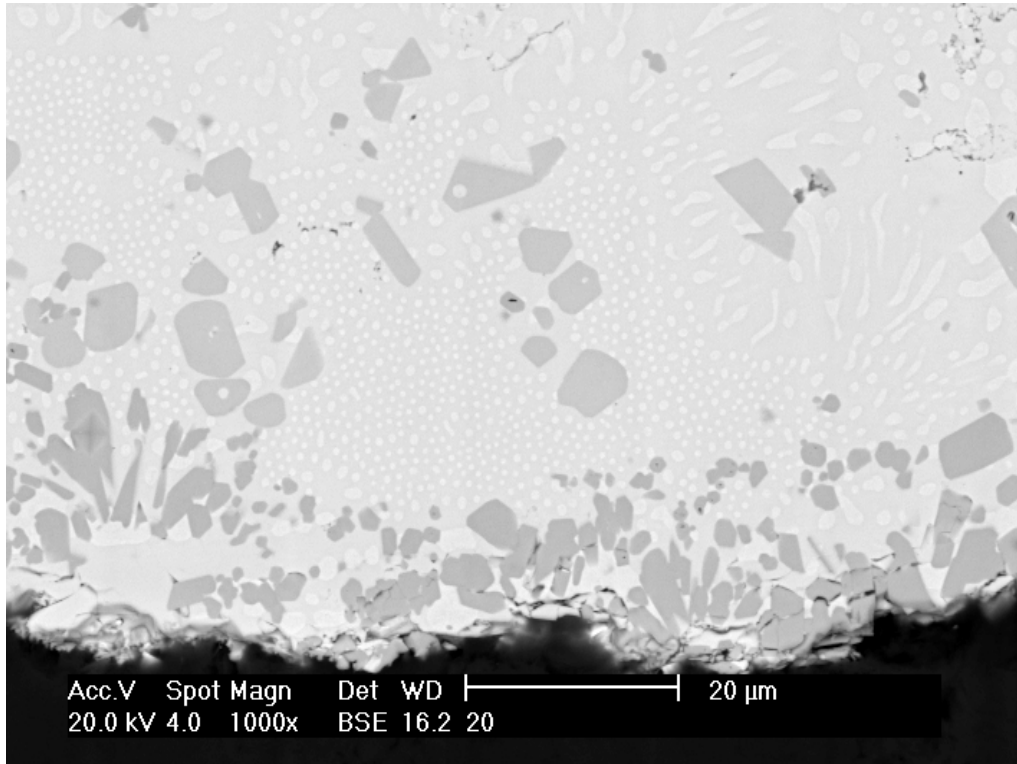

Figure 72. Structure of the Ni-Cr-P braze filler material near interface between the graphite base material, BSE-image.
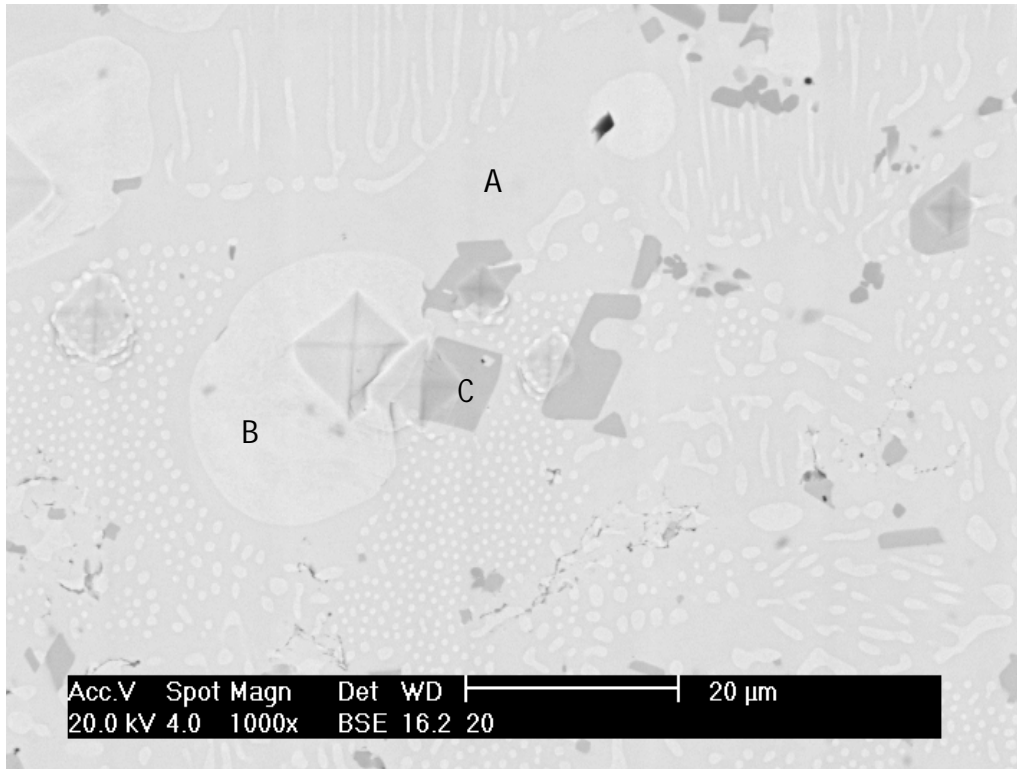
Figure 73. Shows the fine structure of the Ni-Cr-P type brazing filler material near braze surface, phases A, B and C.

Table 25. Compositions of the phases seen in varying grey levels in Figure 72.

	A: Grey matrix phase (Ni, Cr)$_3$P		C: Hard P containing phase (Ni, Cr)-P-C		B: Light Ni based FCC phase	
Element	wt.-%	at.-%	wt.-%	at.- %	wt.-%	at.-%
Si	0.4	0.8	0.6	1.0	0.0	0.0
P	15.1	25.0	10.4	17.0	0.8	1.4
Cr	4.1	4.0	46.0	44.8	12.1	13.4
Fe	0.3	0.3	0.3	0.3	0.8	0.8
Ni	80.1	69.9	42.7	36.9	86.3	84.4
Total	100.0	100.0	100.0	100.0	100.0	100.0

On the surface of the graphite base material there is a layer of carbides embedded in the (Ni, Cr)$_3$P-type matrix phase. The light FCC phase is very finely distributed, especially near the graphite surface, indicating that the solidification occurred near the eutectic point of the system.

The values of the backscattering coefficient η were calculated with Eq. 1 using the chemical information of EDX-analyses given in Table 25. These η-values are presented together with the measured brightness levels in Table 26. The brightness was measured from several areas of each phase and the given value in Table 26 is the average of these measurements. The results are presented in Figure 74 where the η-value is presented as a function of the grey level of the phases. The results form a good line and the grey levels measured far inside the brazing filler metal have a slightly lower

value. According to the results it seems that the grey level near the graphite boundary is the same or even higher as that far inside the braze indicating that the carbon content is at the same level in the braze layer.

If we look further into the results in Figure 75, we can see that the phosphorous containing hard phase and light FCC nickel-based phase both have a lower level of grey than expected. It is evident that carbon dissolved into these phases during the brazing process.

Table 26 The measured brightness level and calculated η-values for phases of the Ni-Cr-P metal brazed onto the graphite base material, with results presented in Figures 72 and 73.

The Interface		
Grey level	η	Name
204.0263	0.267033	C: Hard P containing phase (Ni, Cr)-P-C
186.9897	0.24508	Chromium carbide
226.4103	0.275048	A: Grey matrix phase Ni_3P
231.1805	0.290054	B: Light phase, FCC Ni based
6.499	0.064083	Graphite
Inside the braze		
227.9515	0.290054	B: Light phase, Ni based FCC
222.7765	0.275048	A: Grey matrix phase Ni_3P
198.3553	0.267033	C: Hard P containing phase, (Ni, Cr)-P-C
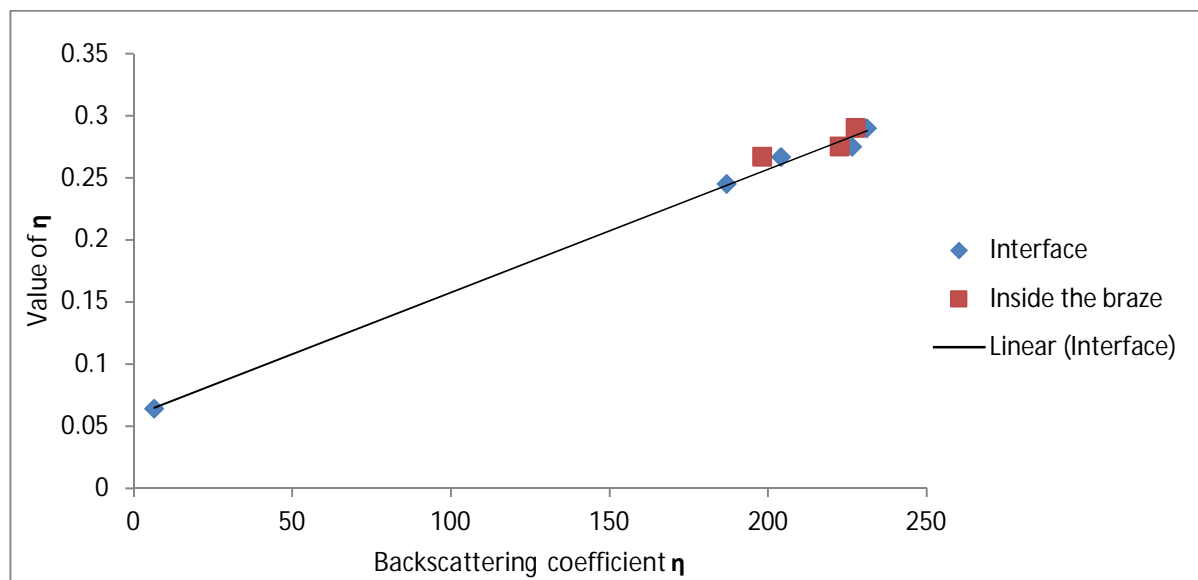
Figure 74. The backscattering coefficient η as a function of the grey level for the phases present in Figures 72 and 73.
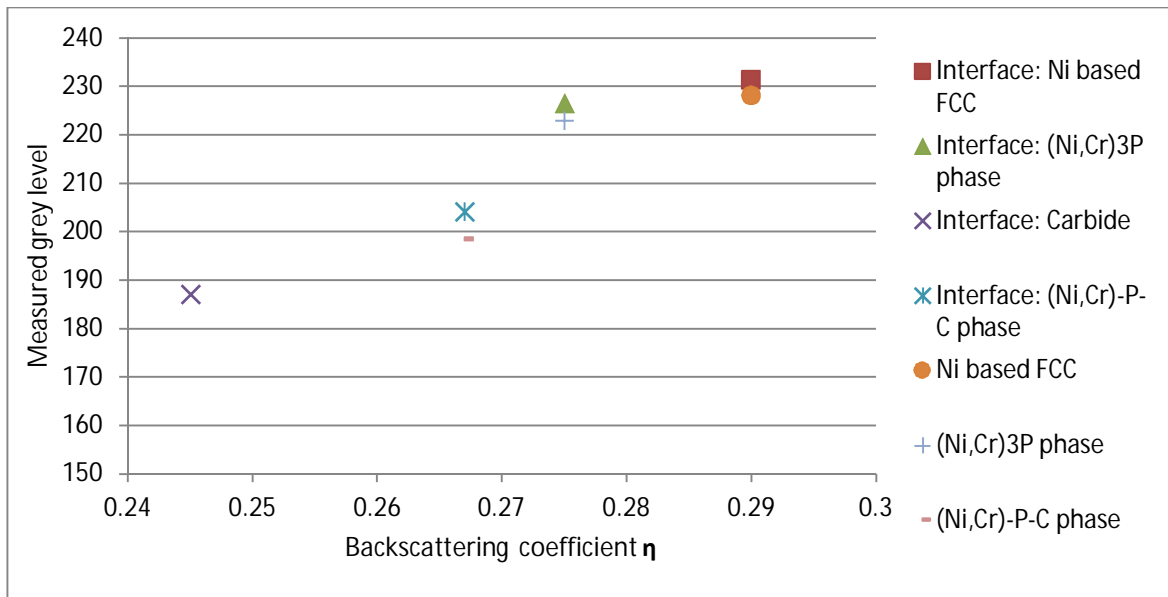
Figure 75. Grey level as a function of the backscattering coefficient η for the phases presented in Figures 72 and 73.

The boundary between graphite and the brazing filler metal was studied more in detail, see Figure 76. In this BSE-image the carbide layer and two slightly different grey levels of individual particles are evident. EDX-analysis curves were measured from these carbides and in Figure 77 the darker chromium carbide particles seem to contain more carbon when compared to the lighter carbides. Note the difference in the height of carbon K-α electron cell peaks compared to the peaks of chromium L-α. According to this result, the difference in the carbon content of these two carbides can be measured by EDX, where the analysed carbides are large enough.
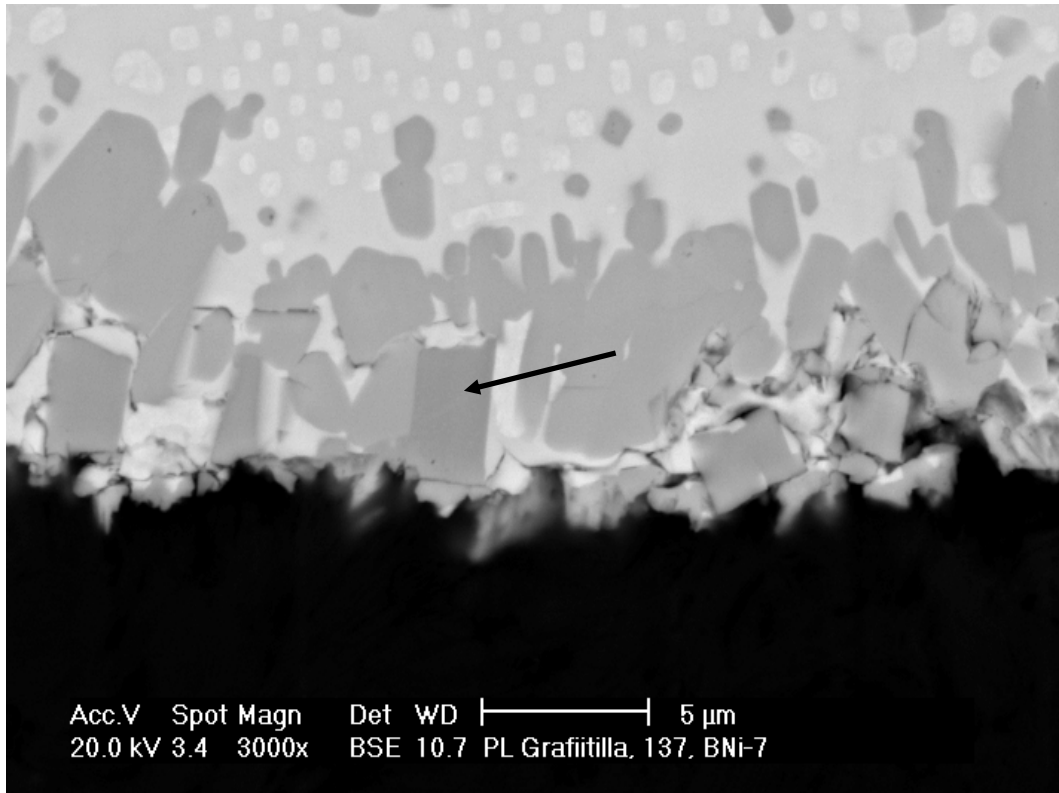
Figure 76. The layer of carbides formed at the Ni-Cr-P type brazing filler material - graphite interface. The dark grey carbide is marked with an arrow.
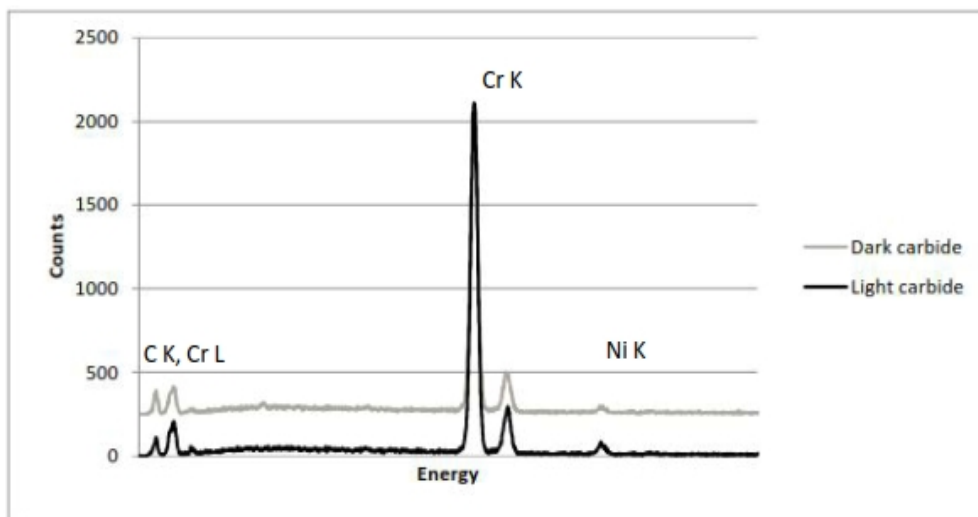
Figure 77. EDX-analyses taken from the different grey-level carbides presented in Figure 76 indicate a higher content of carbon in the dark carbide marked with an arrow in Fig 76.

 3.7.4 Microstructure of the braze material in Ni-Cr-Si-B - diamond composite

Earlier in the study the structure of the Ni-Cr-P type brazing filler metal was analysed in detail - it was found that the braze – diamond composite was formed of several phases, each with a different

composition. When the same analysis was performed on the Ni-Cr-Si-B brazing filler metal – diamond composite, it was found to have a remarkably different composition to the Ni-Cr-P type brazing material.

The microstructure of the Ni-Cr-Si-B brazing material is presented in Figure 78. The material solidified into five different phases, which were analysed using the EDX-analyser - their compositions are given in Table 27. The compositions were measured from the positions presented in Figure 79. The composition of the dark phase, i.e. chromium boride, is not measured by EDX-analysis because of the light boron element but it was assumed to be type Cr_2B according to the binary phase diagram presented in Figures 8 and 9.

The light phase presented in Figure 79 is nickel-based chromium and iron-containing FCC phase, although there were also two grey phases with discrepancies in their silicon, iron and chromium contents. The spotty phase formed last when the remainder of the brazing filler metal was solidified near the eutectic point of binary phase system, at the end of the brazing process.

With the earlier results in mind, is it possible to analyze the Ni-Cr-Si-B braze structure using the backscattering coefficient analysis in the same way as with Ni-Cr-P type brazing filler metal? For this work the backscattering coefficients η were calculated with Eq. 1 using the compositions measured with EDX-analysis in Table 27. The grey levels were measured from several areas for each phase and the results are presented in Table 28 together with the η coefficients and the names and/or formulas of the phases. The phases were identified using EDX-analyses.
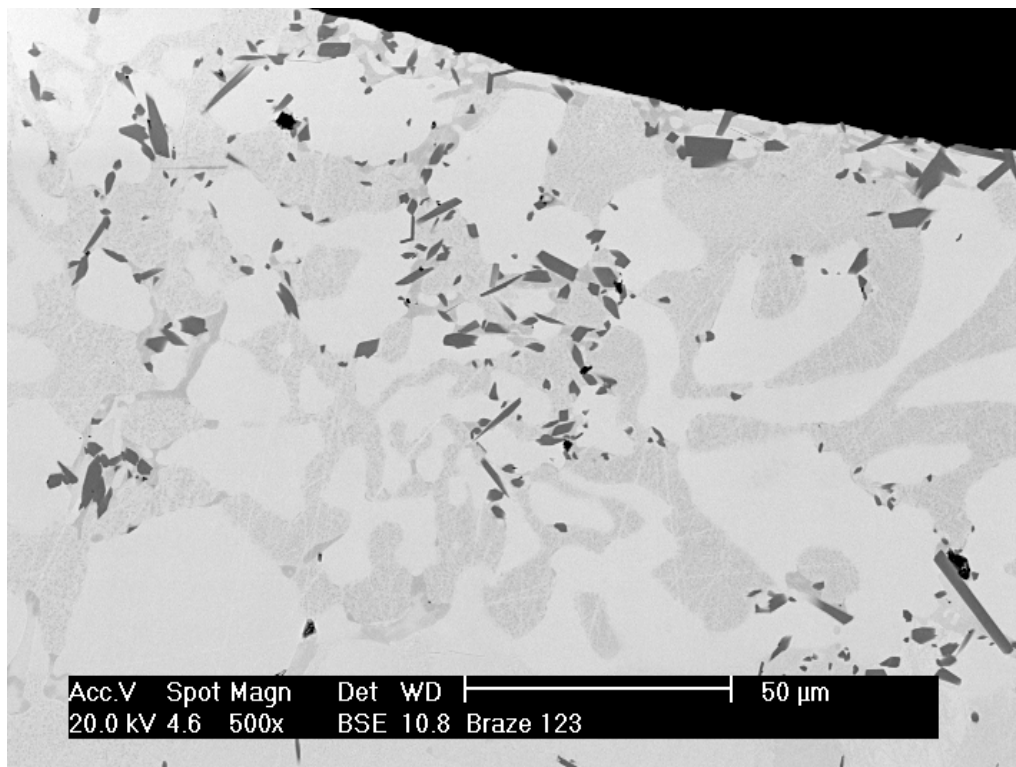

Figure 78. Microstructure on the Ni-Cr-Si-B brazing filler material (BSE image).
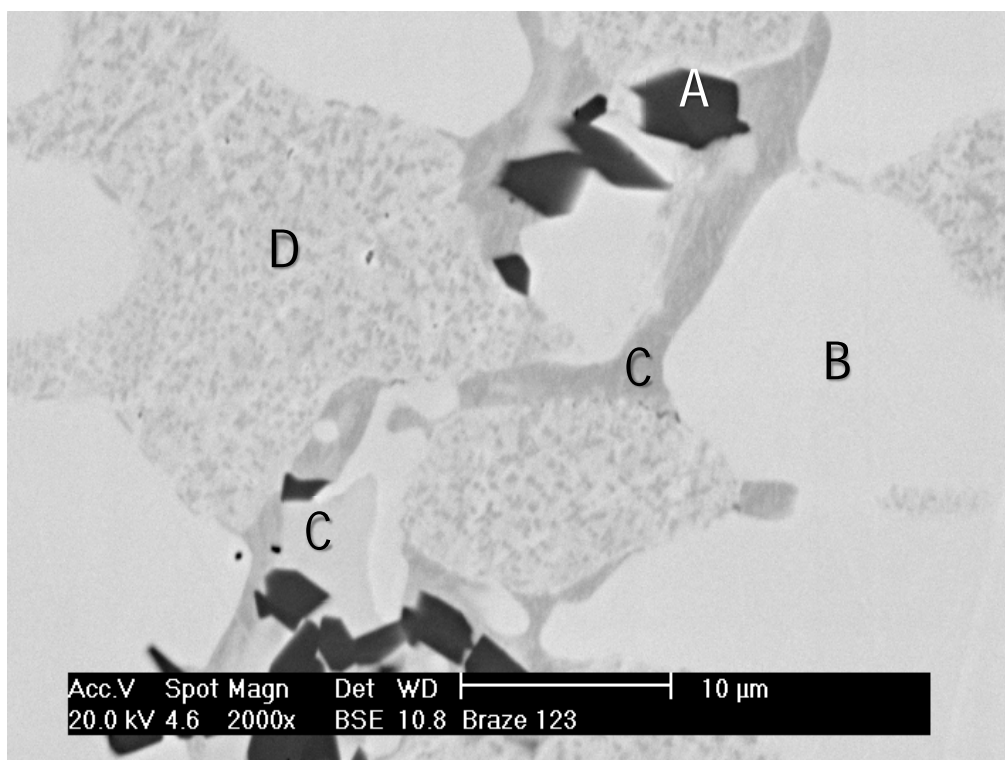
Figure 79. Phases in the Ni-Cr-Si-B brazing material: Cr_2B type boride (A), nickel-based chromium and the iron containing FCC phase (B), with two grey phases (C), that have discrepancies in silicon, iron and chromium contents and spotty phase (D).

Table 27 The five phases of Ni-Cr-Si-B brazing filler metal analysed using EDX-analysis. Boron is too light as an element to be measured accurately with this method. According to the (Ni, Cr)-B phase diagrams presented in Figures 6 and 7, the dark phase is assumed to be the Cr_2B type.

	B: Light phase		C: Light grey phase		C: Grey phase		A: Dark phase		D: Spotty phase	
Element	wt.-%	at.-%	wt.-%	at.-%	wt.-%	at.-%	wt.-%	at.-%	wt.-%	at.-%
B							8.4- 9.4	33.3		
Si	0.67	1.37	14.65	26.28	10.33	19.31			5.91	11.51
P	0.12	0.22	0.41	0.66						
Cr	4.91	5.46	1.34	1.29	2.71	2.73	90.6	66.7	4.54	4.78
Fe	3.8	3.92	0.64	0.58	3.62	3.41			5.96	5.84
Ni	90.51	89.0	82.96	71.18	83.34	74.55			83.59	77.88
Total	100	100	100	100	100	100			100	100

Table 28. The measured grey levels and calculated backscattering coefficient η values using EDX-analyses given in Table 27 for the phases of Ni-Cr-Si-B type brazing material.

	Grey level	η
B: Light phase: Ni based FCC	214	0.2918
C: Light grey phase: Ni_3Si	207	0.2748
C: Grey phase: $Ni_3(Si, B)$	176	0.2801
A: Dark phase: Cr_2B	60	0.2429
D: Spotty phase: Ni based FCC +$Ni_3(Si, B)$	199	0.2849

In Figure 80 the results are presented in graphical form. Results suggest that there is no boron dissolved in the light grey phase.

Figure 81 shows a cross-section of the brazing filler metal layer on the diamond surface. In here we can see only one thin carbide layer. Figures 82 and 83 presents the corresponding grey levels as a function of backscattering coefficients η. According to the Figure 83, the single carbide layer found from the diamond surface is rather formed of Cr_7C_3 type carbides than Cr_3C_2 type, because it is found from the line formed by the other analyzed phases in Figure 83.
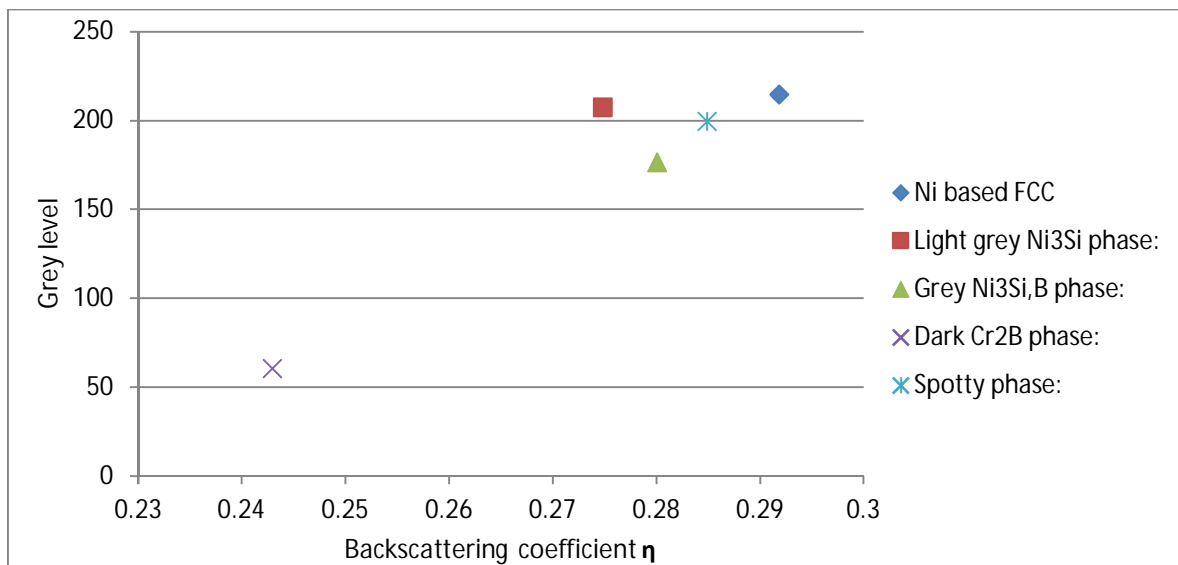
Figure 80. The grey levels as a function of the backscattering coefficient η for the phase of Ni-Cr-Si-B type brazing filler metal. See the compositions and formulas of the phases presented in Tables 27 and 28.
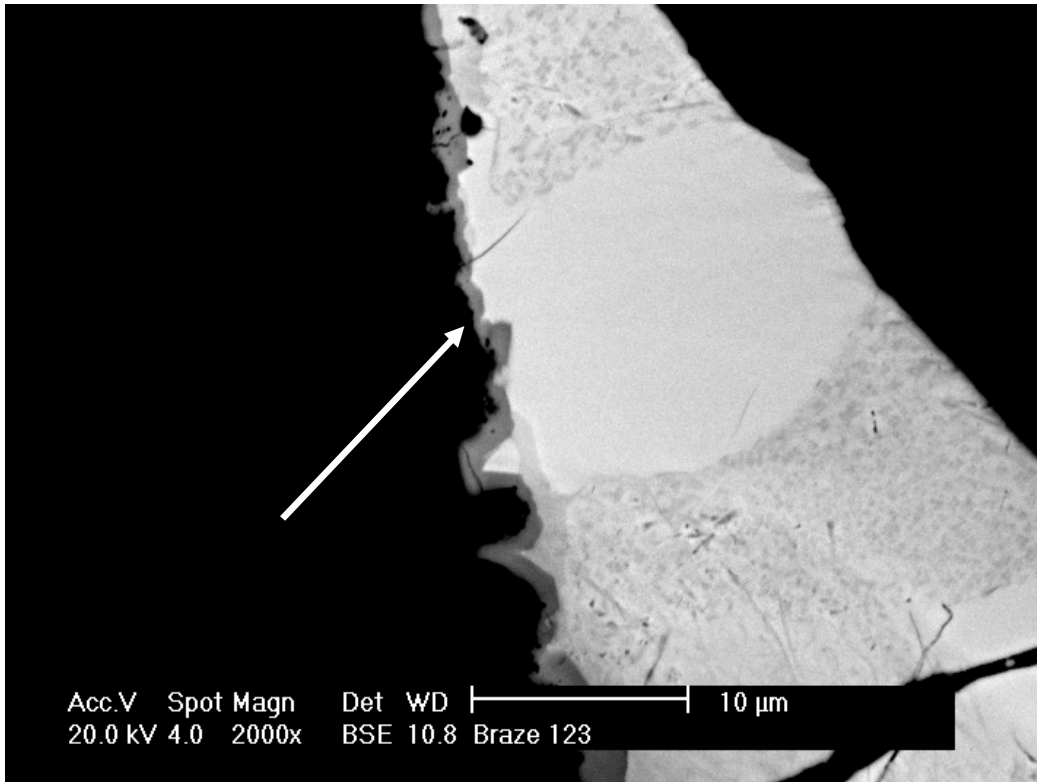
Figure 81. The brazing filler material Ni-Cr-Si-B has formed thin carbide layer marked with an arrow on the pitted diamond surface. Note the degradation of the diamond surface seen in the cross section at the middle of the image.
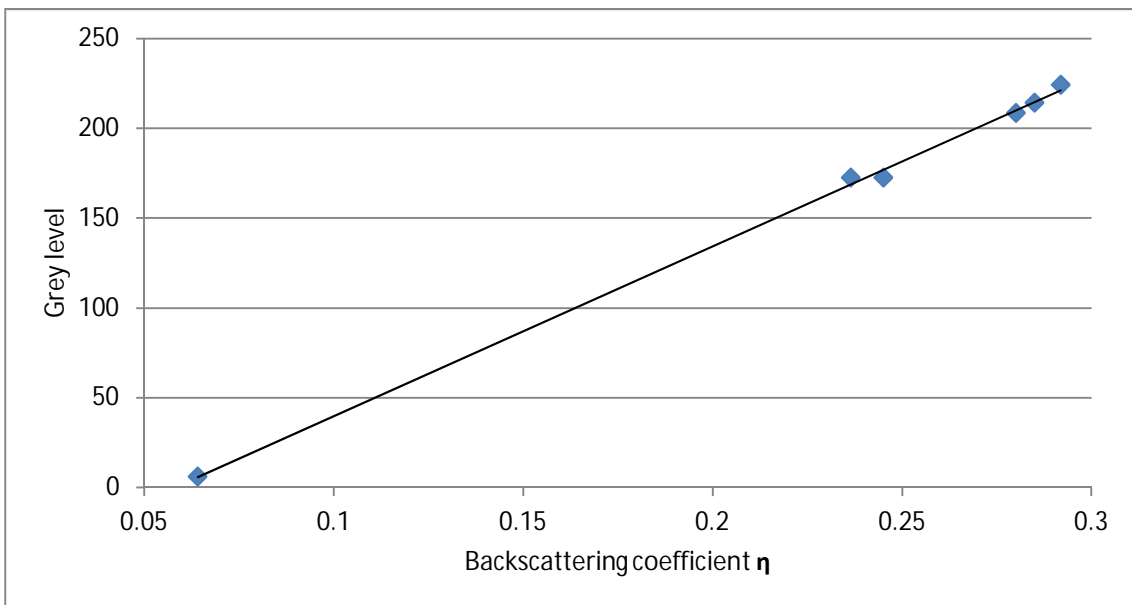

Figure 82. Grey level as a function of the backscattering coefficient η for the phase of the Ni-Cr-Si-B brazing material.
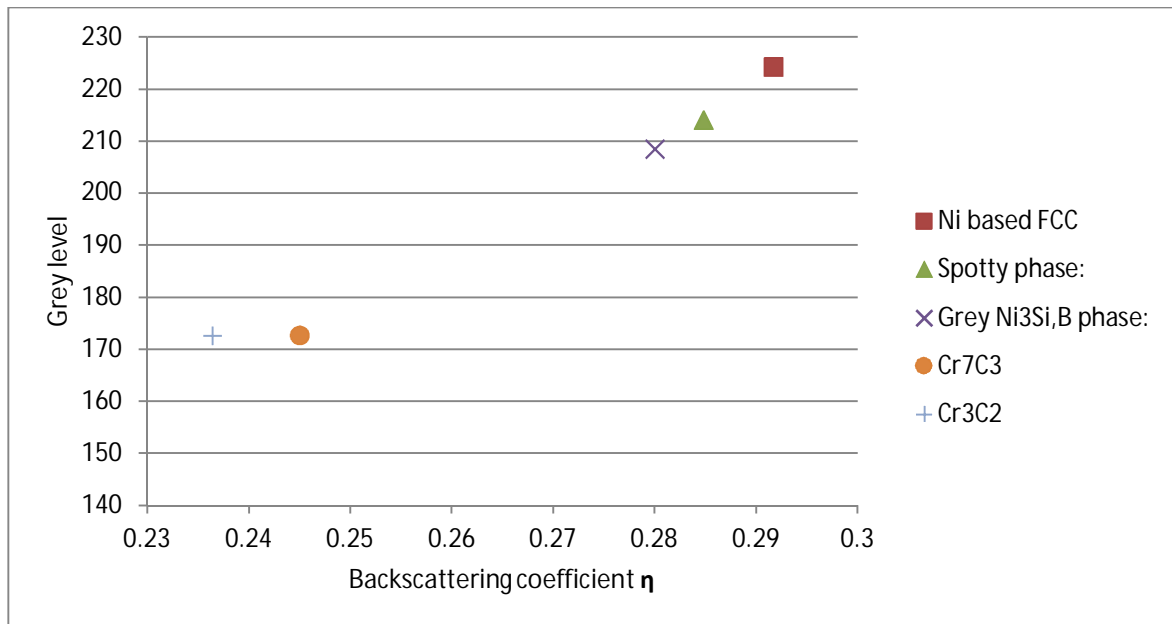
Figure 83. The grey level of the different phases present as a function of the backscattering coefficient η for the phases of the Ni-Cr-Si-B brazing filler material.

3.8 The phase structures of Ni-Cr-Si-B and Ni-Cr-P braze materials braze with diamond single crystals

Earlier in this study the structures of Ni-Cr-Si-B and Ni-Cr-P braze-diamond composite materials were studied from cross-sectional specimens using SEM imaging with SE- and BSE-detectors and EXD-analysis. Considerably small areas or volume of the samples with varying composition were then detected and analysed. To get further information about the crystal structure of the phases X-ray diffraction curves were measured from the surface of the Ni-Cr-Si-B and Ni-Cr-P brazing materials after they had been brazed with the single diamond crystals on the stainless steel substrate. Measurements were performed directly from cleaned specimen surfaces without any grinding or polishing.

X-ray diffraction measurement is giving information inside the studied material volume from certain depth. As it was calculated earlier when introducing the experimental methods of this work, copper radiation is suitable to use in these measurements, because it is giving information well inside the studied braze layer but not from the base material under the braze layer. Naturally the X-ray penetration onto the single diamond crystals was much deeper than into the braze material as it was presented earlier.

3.8.1 Phase structure of the Ni-Cr-P braze - diamond composite material

XRD measurements were carried out from the Ni-Cr-P braze layer, where the single diamond crystals were joined on the stainless steel base material surface. Figures 84 to 89 show the material's phases, its x-ray diffraction curve and possible compound candidates.

Figure 84 presents an XRD curve with nickel - chromium alloy reflections coming from lattice planes {111}, {200} and {220} marked with the blue bars in the image [60]. The shifted reflections marked with red bars indicate the presence of another similar phase with an FCC structure.

Diamond gives high-intensity reflections, as presented in Figure 85, where reflections from diamond {111}, {220}, {311} and {222} type lattice planes are identified [61]. The only phase found with a chemical formula of (Ni, Cr)P is identified in Figure 86. This phase has an orthorhombic crystal structure. Here, the peak at the 39.883° angle can be fitted with 100 % reflection of plane {112}. Some of the other minor peaks fit the XRD curve measured from the Ni-Cr-P braze material [62].
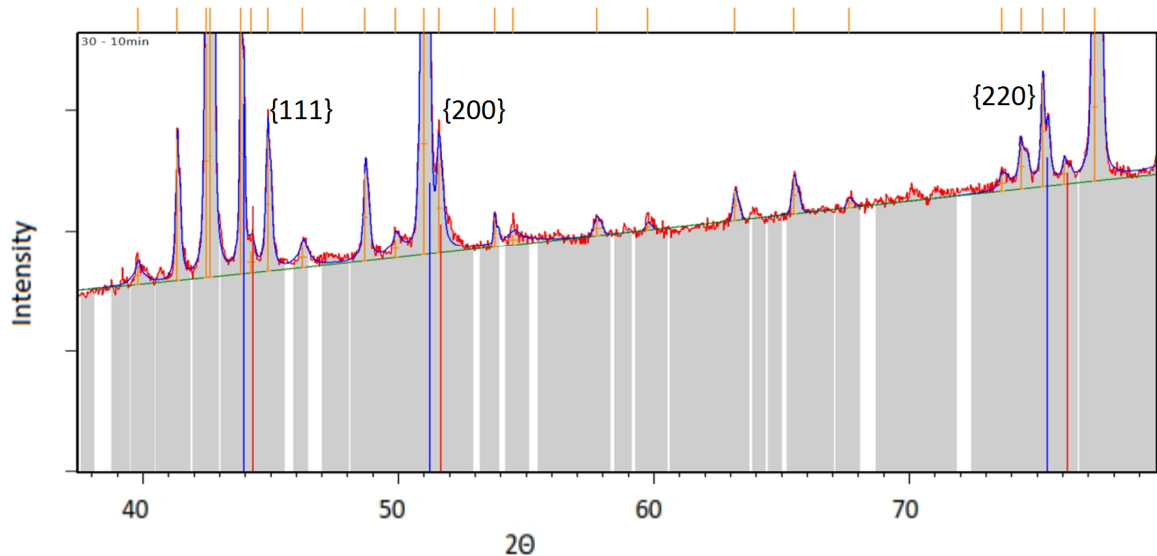
Figure 84. The braze of Ni-Cr-P, an XRD curve with the FCC type (Ni, Cr)-phase (shown as light-coloured during the SEM research earlier) identified, the reflections come from lattice planes {111}, {200} and {220} marked with blue bars. Note the slightly sifted reflections marked with red bars, which came from another phase such as pure FCC nickel. [60]
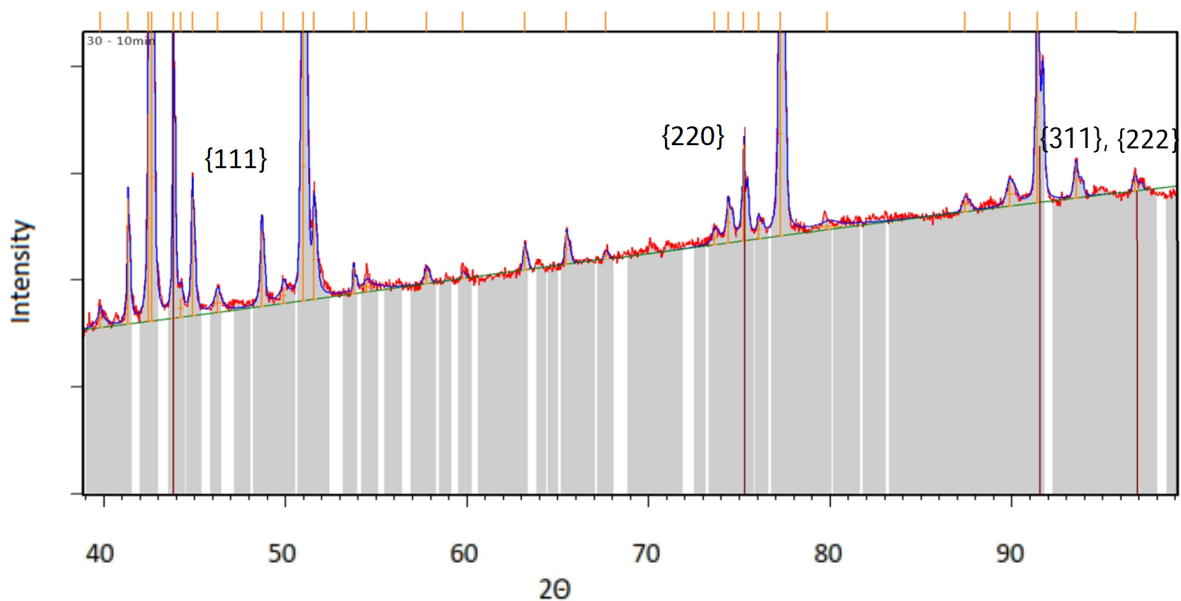

Figure 85. Clear diamond reflections from crystal planes type {111}, {220}, {311} and {222} marked with brown bars, Ni-Cr-P braze filler material. [61]

Figures 87 - 89 present the identification of carbides. The results show the best fit of peaks achieved were with Cr_3C_2 and Cr_7C_3 type carbides, although the peaks' intensity is too low to draw firm conclusions. The low intensity of the carbides is most probably due to their small volume fraction within the total volume of the structure. Carbides are normally well-crystalized and should give clear peaks to their diffraction curve.

Notable here is that large $(Ni, Cr)_3P$- and $(Ni, Cr)_2P$-type phases are not clearly visible in the XRD results despite their high prevalence within the braze structure, although the $(Ni, Cr)_2P$ phase can be identified according to Figure 86. This can indicate that the crystal structure of these phases is amorphous or near amorphous and clear peaks were not as clearly formed. The low amount of available data was not because of inadequate penetration of the copper radiation or a lack of material.
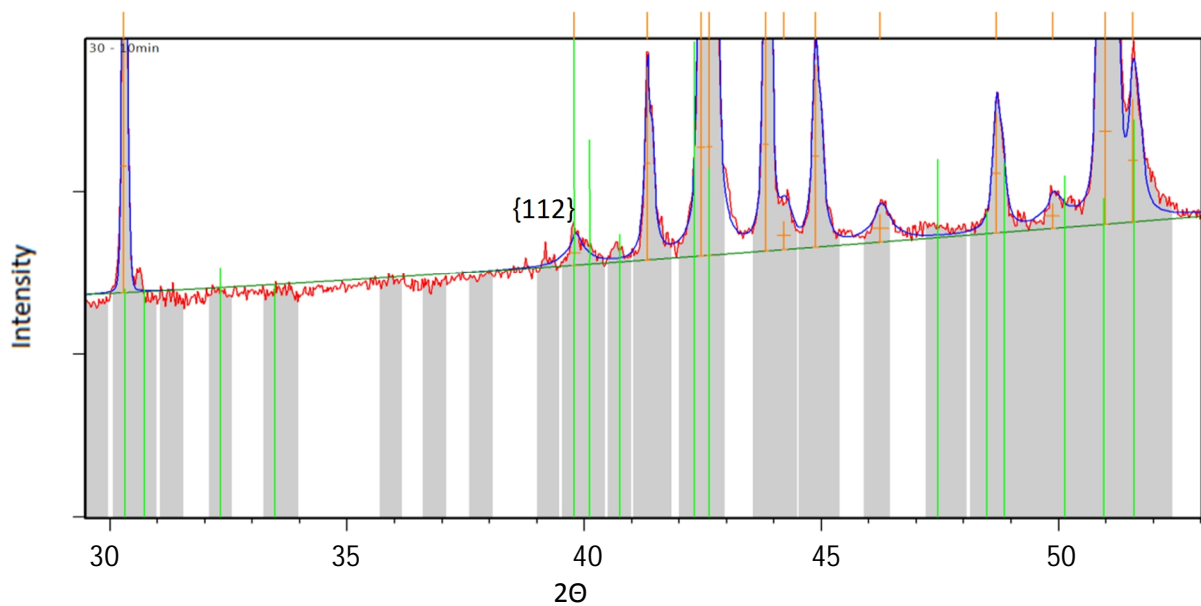

Figure 86. $(Cr, Ni)_2P$ phase reflections fitted in the XRD curve measured from the Ni-Cr-P braze material, fits at a 39.883° angle, 100% reflection of plane {112}. The second highest 75 % reflection is coming from {211} type planes at the 42.429° angle [62].

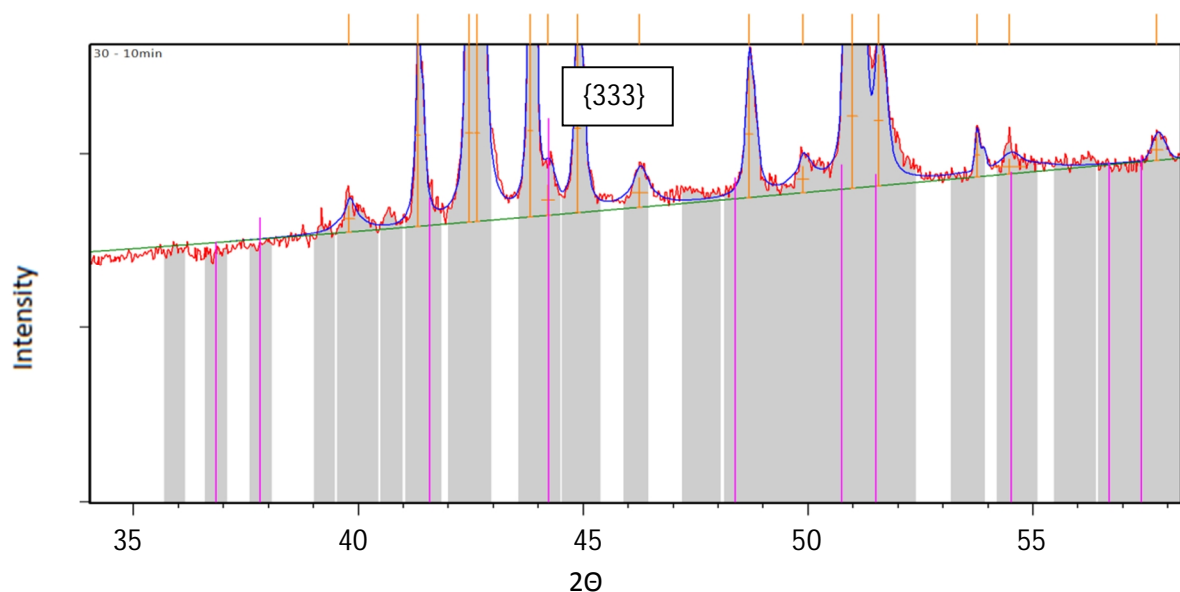Figure 87. A possible reflection of $Cr_{23}C_6$ carbide from planes type {333} with a 44.151° angle [63].
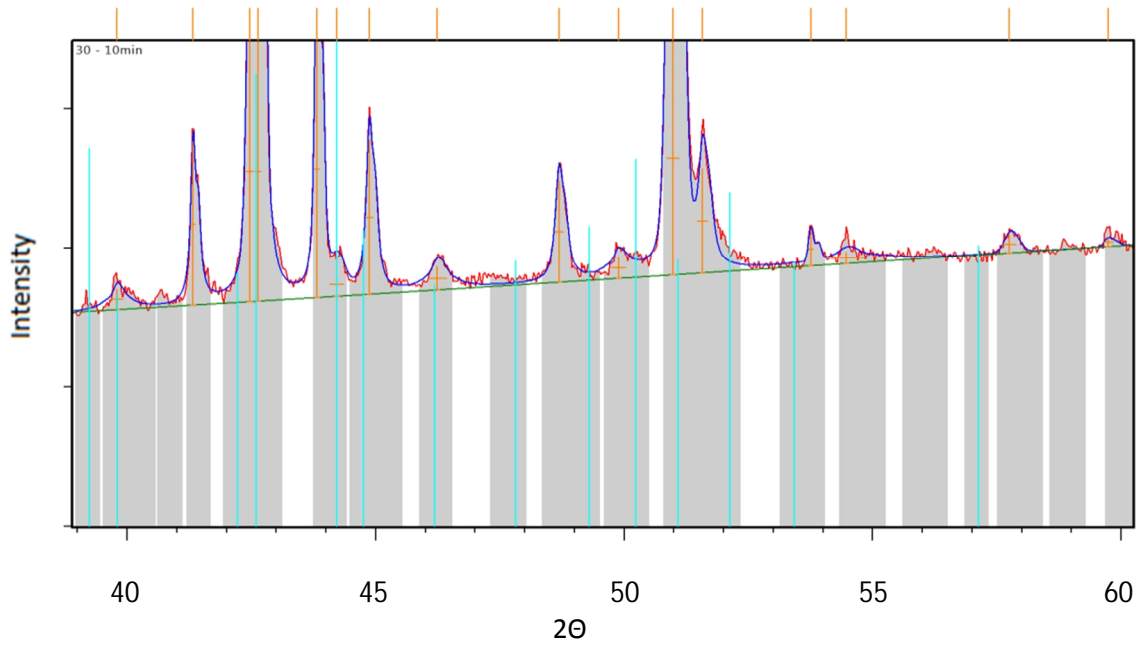
96

Figure 88. The Cr_7C_3 type carbide with 100 % reflection at a 44.167° angle; 46 % reflection at a 42.546° angle and 33 % reflection at a 39.189° angle, where a possible match can be identified [64]
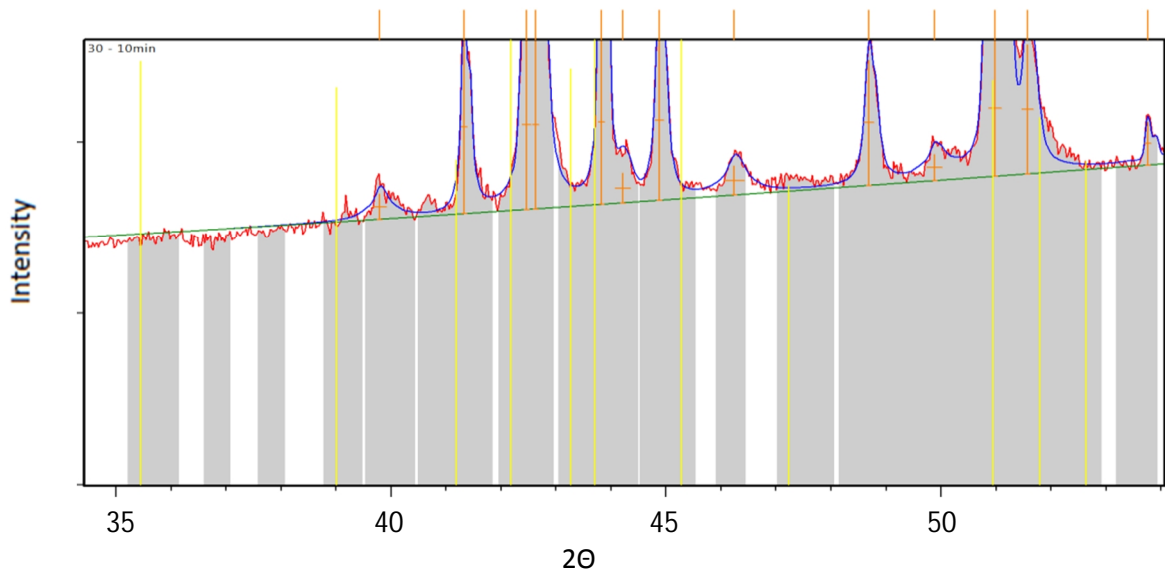

Figure 89. The Cr_3C_2 type carbide with 100 % reflection at a 43.576° angle; 54 % reflection at a 35.314° angle and 3 3% reflection at 39.189 degrees, not matching [65].

As a result of the XRD measurements of Ni-Cr-P braze – diamond composites it can be concluded that the $(Ni, Cr)_2P$ and $(Ni, Cr)_3P$ type phases are difficult to identify using XRD diffraction. This is due to the phases' crystal structures after brazing: the structures were either mostly or fully amorphous and peaks did not form despite a high proportion of the metal alloys within the phases. These results

indicate that BSE imaging is a more powerful method for analysing the phase structures of the braze materials when compared to the XRD method.

With the small proportion of carbides formed on the diamonds' surfaces meant that only a limited amount of data was available. These layers of carbide were more clearly visible and identified in the BSE images.

3.8.2 Phase structure of Ni-Cr-Si-B braze - diamond composite material

Results of the XRD measurements performed to the Ni-Cr-Si-B specimen are presented in Figures 90 to 96, below. The composite specimen with single diamond crystals was prepared on a stainless steel base material and was measured after cleaning without any grinding or polishing.

Figure 90 identifies the diffraction peaks of diamond [61]. The possible diffraction peaks for pure FCC nickel are presented in Figure 91, together with peaks for the FCC Ni-Cr alloy, which can be found on the left-hand side of each pure FCC Ni peaks, which can also be seen in Figure 84 above. Figure 92 shows the peaks for a possible Ni_2Si phase marked with light blue bars, a peak of 100 % reflection is at a 46.731° angle, 87 % reflection at a 48.696° angle and 66.1 % reflection at 49.354° angle [67]. In Figure 93 possible peaks for Ni_3Si are marked with light blue bars, a peak of 100 % reflection is at a 44.137° angle, a 42 % reflection at a 51.423° angle [68]. Figure 94 presents the diffraction peaks for Cr_2B phase, 100 % peaks at a 44.919° angle and 84 % at a 46.179° angle, here there is a possible fit with the diffraction curve [53]. Chromium carbides were not clearly identified, in keeping with the earlier measurements of the Ni-Cr-P braze - diamond composite: Figure 95 shows the Cr_7C_3 type carbide [64] and Figure 96 depicts the $Cr_{23}C_7$ type carbide [63].
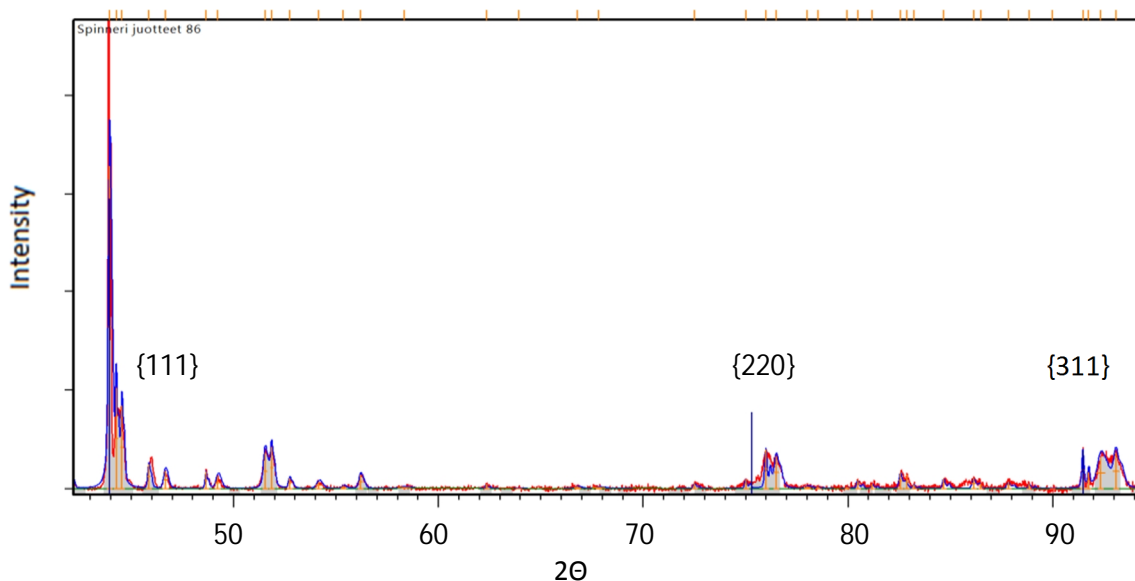

Figure 90. The Ni-Cr-Si-B type braze material with diamonds, high diffraction peaks from diamond single crystals identified and marked with blue bars [61].
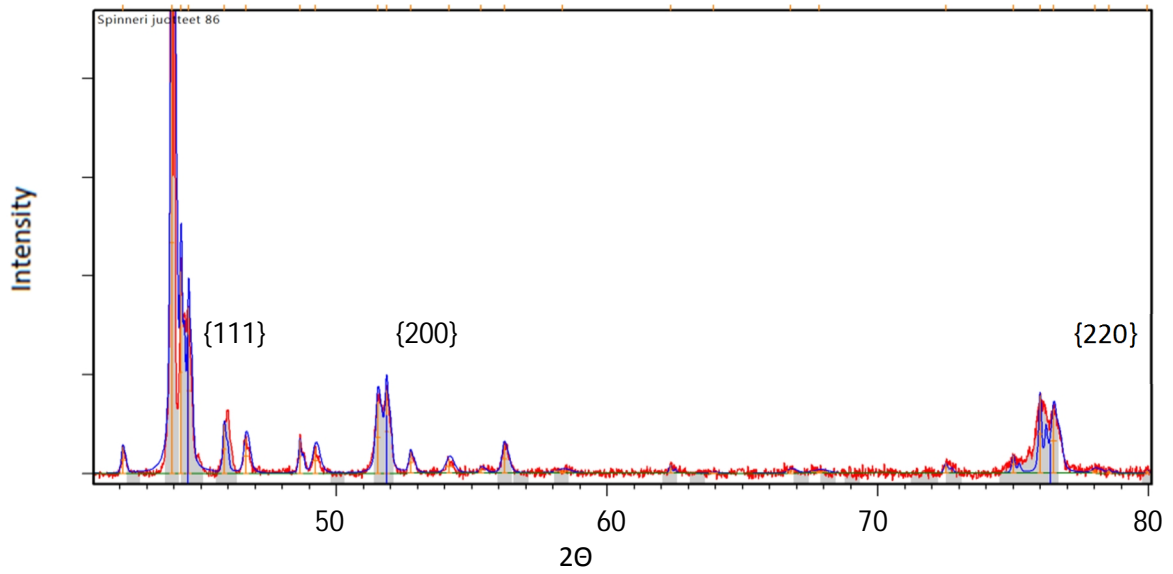
Figure 91. The marked diffraction peaks for pure FCC nickel [66], measured peaks for FCC (Cr, Ni)-alloy can be found on the left-hand side of each Ni peak marked with blue bars. This data shows there are two nickel-based FCC phases present with a slightly different basic lattice distance.
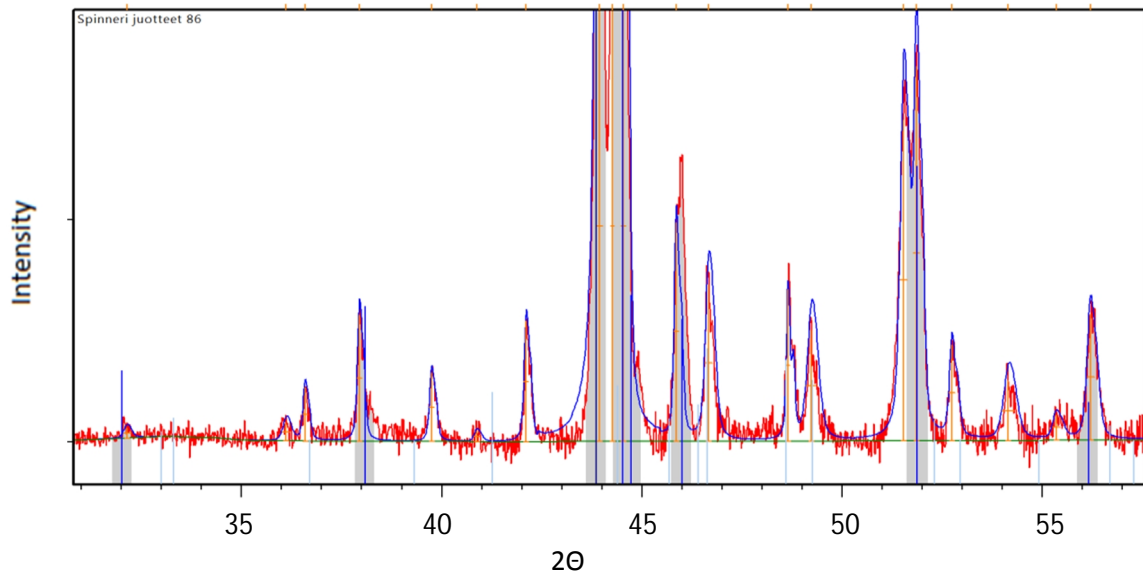

Figure 92 Diffraction peaks for the Ni_2Si marked with light blue bars [67], a peak of 100 % reflection is at a 46.731° angle, 87 % reflection at a 48.696° angle and 66.1 % reflection at a 49.354° angle [67].
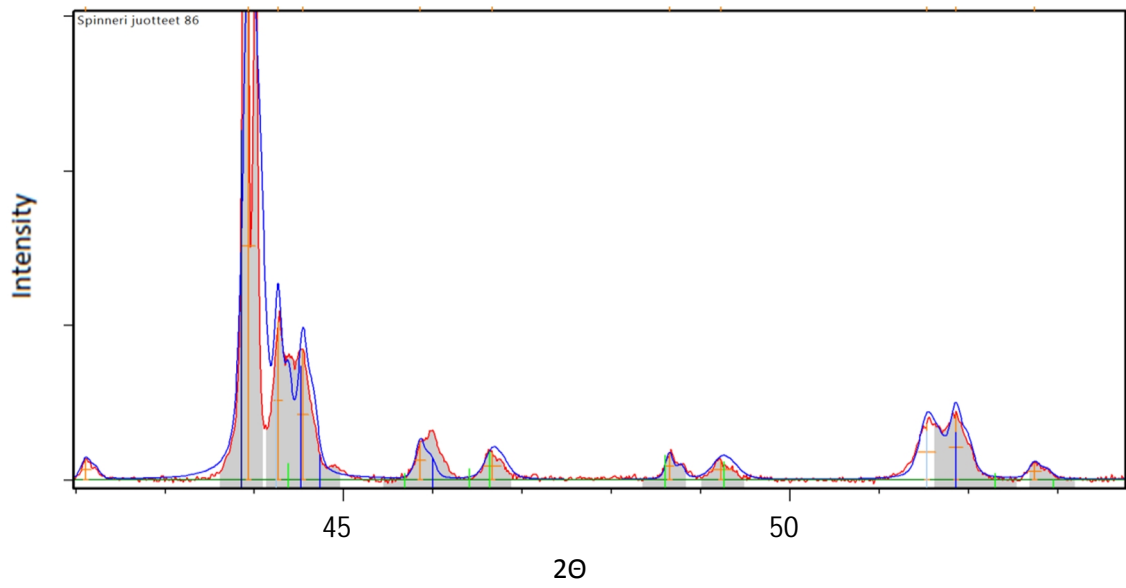
Figure 93. Diffraction peaks for Ni₃Si marked with light blue bars, a peak of 100 % reflection is at a 44.137° angle and 42 % reflection at a 51.423° angle. [68]
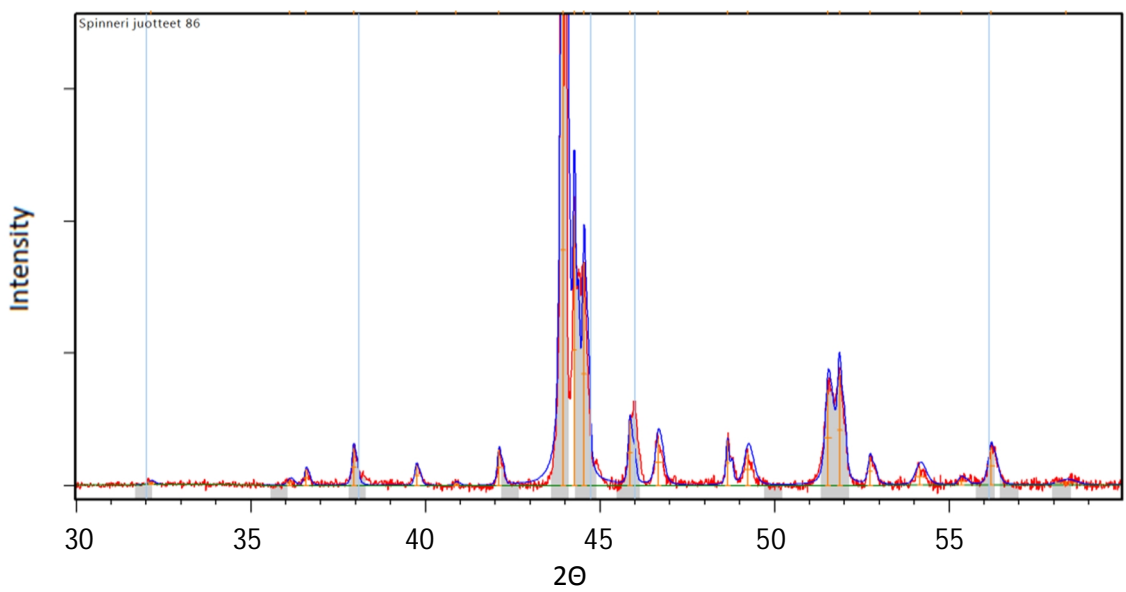

Figure 94. Diffraction peaks for chromium borides marked with light blue bars, 100 % peak at a 44.919° angle and 84 % at a 46.179° angle [69]
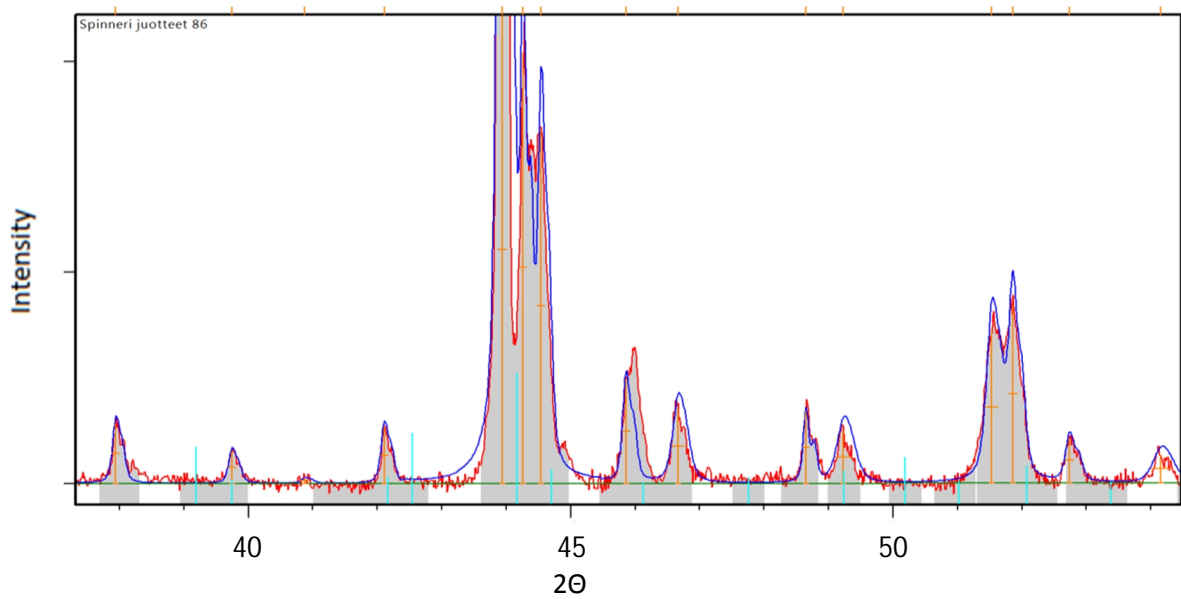
Figure 95. Possible diffraction peaks for the Cr_7C_3 type carbide marked with green bars on the image. [68].
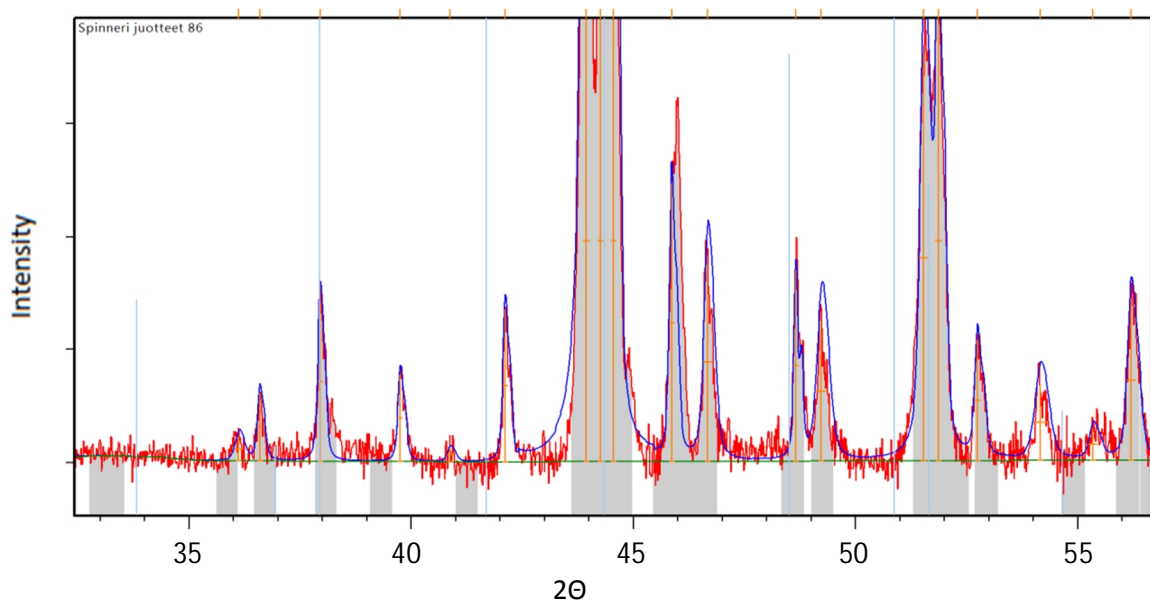

Figure 96. Possible diffraction peaks for $Cr_{23}C_7$ type carbide marked with light blue bars [63].

 3.9 Comparison of the micro-hardness values of the phases formed in the braze materials

According to analyses of the cross-sectional specimens, the brazing materials were found to have built up in several phases, even more than expected according to the binary phase diagrams presented earlier. As a consequence of this multiphase structure information on the mechanical properties of these phases could be achieved at a micro-scale. Although the dimensions of the phases were generally well under 50 µm, hardness data could be taken using a micro-hardness tester at 5 to 20g loads. Besides with the micro-hardness it was possible to get information of the toughness of the phases by analysing the formed micro-scale fractures. The values measured from different phases can

be compared with each other and perhaps after correction calculations (Eq. 3-5) made with other known materials.

Data was taken from cross-sections of the stainless steel - brazed diamond material, as well as the diamond-free graphite base material. On the left-hand side of the earlier presented Figures 72 and 73, (the Ni-Cr-P type braze cross-section near the graphite) you can find some of the hardness tester intender marks hit at the different phases.

3.9.1 Micro-hardness levels of the phases in the Ni-Cr-P braze alloy

Results of the micro-hardness tests measured from the Ni-Cr-P braze filler material's phases and the corrected hardness values are presented in Table 29. The correction equations and experimental methods were introduced in section 2.3.3 Micro-hardness measurements. Some micro-hardness test indentation marks are presented as an example in Figure 97. The single crystal diamond is seen in black on the right-hand side of the image.

According to these results presented in Table 29, the un-calibrated hardness value of the $(Ni, Cr)_2P$ type phase is high, over 900 HV0.02 while the hardness level of $(Ni, Cr)_3P$, is 14 % lover. The hardness values of the Ni-based FCC structured phase were measured both from pockets (marked with letter A in the image 97) and from protrusions (marked with letter B in the image 97) of the formed braze layer, as presented in Figure 97. There was a slight difference between these values: the hardness of the pockets was slightly elevated, and these results are collated with all others in Table 29.

Table 29. The micro--hardness values HV0.020 measured from the phases of braze filler material Ni-Cr-P presented together with the calibrated values in the last row of the table.

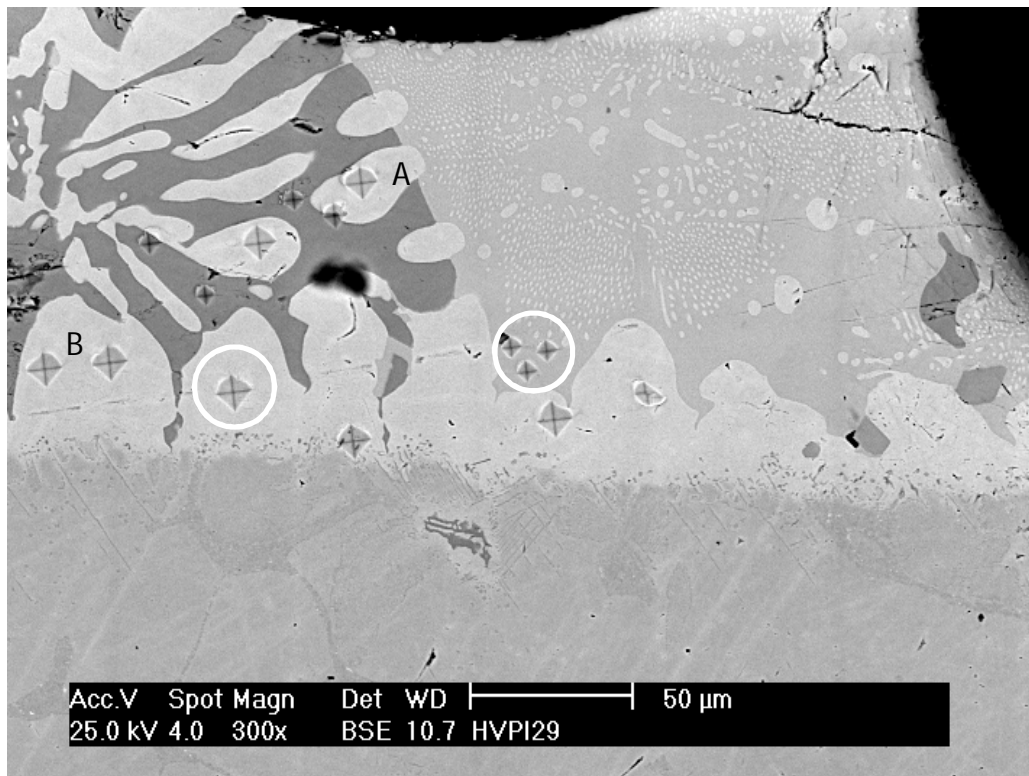|		Dark	Light	Ni based FCC	Ni based FCC
	Base	Ni2P	Ni3P	Pocket	Protrusion
Average:	217	905	776	333	284
STDEV:	13	34	21	13	9
	Values Calibrated by y = 1.59x - 161.5				
Average:	183	1277	1072	369	289

Figure 97. Some of the indentation prints (some of them marked with a ring) from the hardness indentation tip hit on the Ni-Cr-P type braze's various phases. Example of a pocket is marked with letter A and protrusion with B.

3.9.2 The micro-hardness of the Ni-Cr-P braze material phases made on the graphite base

Earlier micro-hardness data values were taken from phases away from the single diamond crystals. It was not possible to measure two carbide types and the (Cr, Ni)-P-C- type phase near the diamond single crystal because of height differences between the diamonds and the braze, that had occurred due to the mechanical specimen preparation technique. Diamond, as a harder material, cannot be ground with the same manner and speed as the relatively soft braze filler metal. The micro-hardness of the brazing Ni-Cr-P on the graphite base material was measured to learn the hardness level of the carbides formed between the graphite base and the brazing filler metal.

During the braze layer data measurements on the graphite base four different phases were established, including the carbide and the (Cr, Ni)-P-C-phase. This data, together with the corrected values, is presented in Table 30. The same calibration equations were used in these correction calculations as before.

Chromium carbide has been shown to be very hard, as has been reported in the literature. The analysis showed that the (Ni, Cr)-P-C phase formed at the same time as the carbides was also very hard phase. The hardness of the Ni-based FCC phase and the (Ni, Cr)$_3$P phase was found to be equal to hardness level measured earlier from specimen brazed with diamonds on the stainless steel base material.

103

Table 30. The results for the HV0.010 and HV0.020 micro-hardness measurements of the braze on the graphite-base material.

HV0.020	Average:	Stdev.	Corrected	Measurements
Ni based FCC	281	22	286	4
Ni_3P phase	567	24	740	3
HV0.010	Average:	Stdev.	Corrected	Measurements
Ni based FCC:	284		291	2
Cr_7C_3	1063	84	1529	4
(Cr, Ni)-P-C	796		1104	3

3.9.3 Micro-hardness levels of the phases in Ni-Cr-Si-B braze alloy

The fine-structured Ni-Cr-Si-B braze also had its micro-hardness measured. These values were taken using 10 g and 5 g loads and show the fineness of the material – it is finer than Ni-Cr-P type brazing filler material. Figure 98 shows indentation marks on the polished cross-section surface. The results of the tests are presented in Table 31, along with the corrected values calculated using the same correction equations used before.

The data shows that the hardness level of the Ni-Cr-Si-B braze material phases is considerably higher than the prior-tested Ni-Cr-P material phases. This could be due to the boron alloying of the Ni-Cr-Si-B metal. According to the measurements, there is a significant difference between the hardness levels of the braze filler materials. This kind of difference in micro-hardness is certainly affecting to the wear behaviour of braze filler material, also the finer structure of the Ni-Cr-Si-B braze filler is indicating of higher resistance for abrasive wear.

Table 31. Measured micro-hardness values and corrected values for different phases in the Ni-Cr-Si-B brazing filler material. Phases are marked with letters A, B, C, and D in Figure 98.

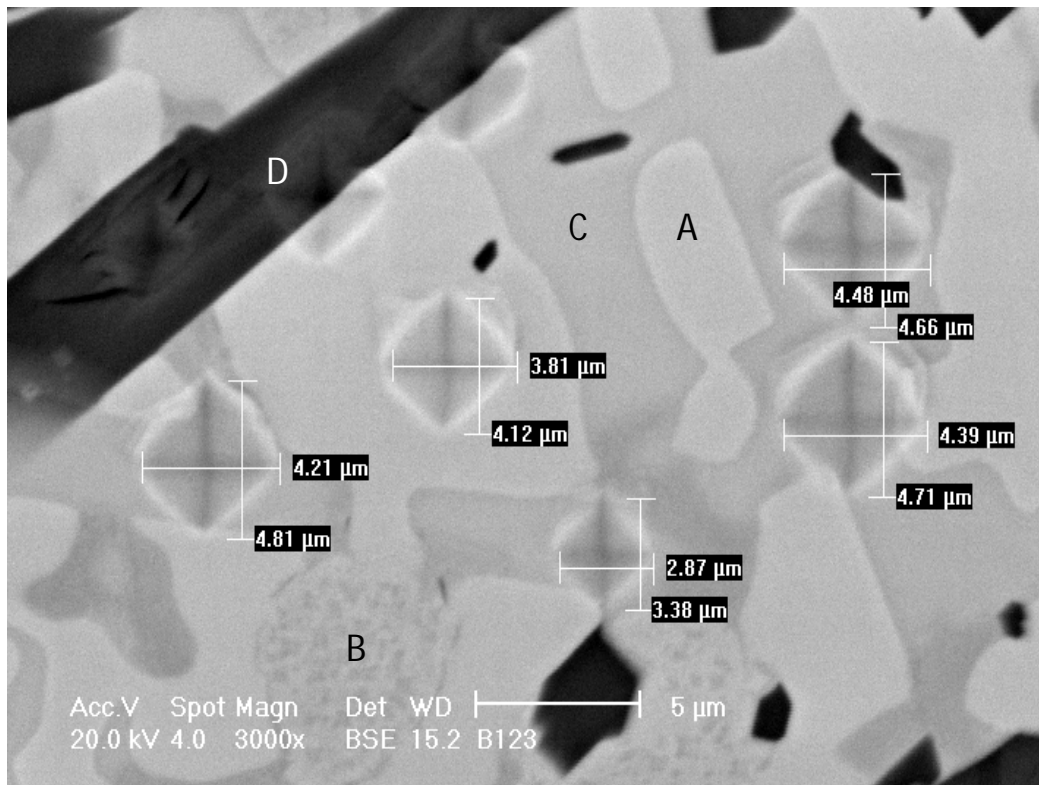| Phase:	Load/g	Points:	Average:	Stdev:	Corrected:
A: Light phase	10	7	1223	148	1735
A: Light phase	5	3	1236	82	1804
B: Spotty phase:	10	4	822	97	1093
C: Grey phase	10	5	899	52	1215
C: Grey phase:	5	3	1019	62	1231
Base material:	10	3	266	4	202
D: Boride:	5	2	1034	90	1250

Figure 98. Indentations used to measure micro-hardness from the polished Ni-Cr-Si-B brazing filler metal cross-section. Note the brittleness of the dark and hard boride (D) in the left upper corner of the image.

3.10 Residual stresses in the braze layer made on the graphite base material

During experiments analysed earlier in this study, cracks in the braze layer were found on brazed diamonds due to different coefficients of thermal expansion and their residual stresses. To get further information on these stresses, tests on how the braze material performed against graphite were completed. Graphite was chosen as a substitute for diamond in this case as no large-enough specimens of diamond were available. Carbon is diluted from graphite material in the same way as happens with diamond, to form carbides in the boundary between the graphite and brazing filler metal. What must be noted is that part of the diluted carbon did not form carbides, and could be soldered into the other brazing filler metal phases.

For these studies, braze samples were utilized on 30x50 mm graphite substrates. On the substrates carbon reacted with braze filler material creating carbide layers between the braze and the graphite base as presented earlier in Figure 76. The brazing temperature for the Ni-Cr-P braze material was 950°C and was higher for Ni-Cr-Si-B at 1032°C. Specimens were prepared within a high vacuum.

After brazing it was noticed that there were cracks on braze layers of both specimen types as is presented in Figures 99 and 100. This is because of the different coefficients of thermal expansion of the base material and braze filler metal. The number and the width of the cracks were measured with a scanning electron microscope (SEM), as presented in Figure 100. To do this a sharp line was scratched in the middle of each specimen and the width and angle of individual cracks crossing that

line were measured. Using this information the vector component of the crack width to the line direction was calculated. During the observations the accuracy of the SEM was determined using a calibration standard [56] with a consistent magnification and working distance values used to measure cracks. It was noticed that there was 1.2 % microscope error in a horizontal direction which was corrected for the final results presented in Table 32 below.

The results show that the Ni-Cr-Si-B type braze has more cracks per specimen millimetre, but that the total width of cracks per millimetre of surface is higher with the Ni-Cr-P braze material. This result is similar to earlier findings that Ni-Cr-Si-B braze filler material is harder but also a more brittle material compared to Ni-Cr-P.

Table 32. Collected results of the crack width and distribution measurements for both the Ni-Cr-Si-B and Ni-Cr-P brazing filler metals.

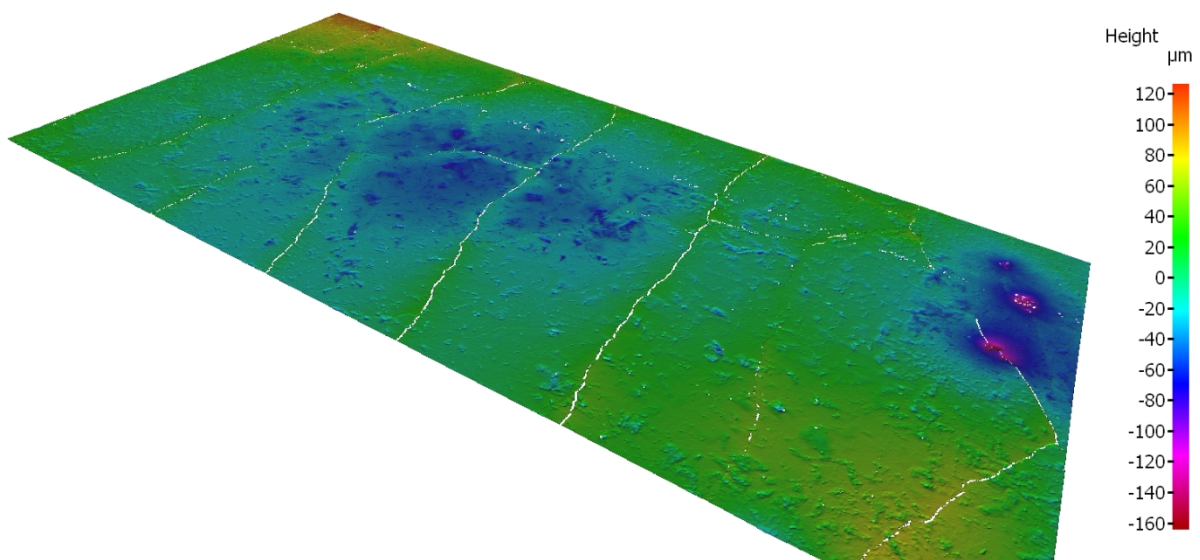| Brazing filler metal	Ni-Cr-Si-B	Ni-Cr-P
Total width of the cracks in μm	333.25	341.79
Number of cracks:	23	15
Average width of cracks in μm	20.14	27.95
Number of fractures in mm	0.49	0.35
μm of cracks/specimen mm	7.08	7.93
Coating thickness in mm	0.10	0.10

Figure 99. Fractures on the Ni-Cr-P braze filler material surface after cooling to room temperature, the image is measured using an optical profilometer.
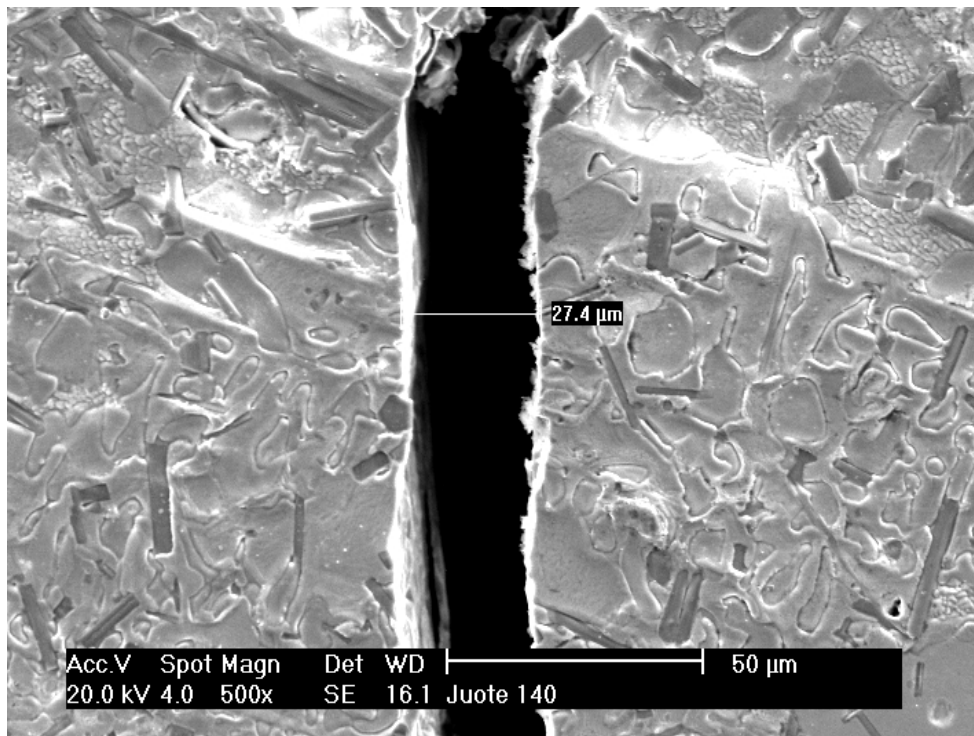
Figure 100. An example of a width measurement of one crack using SEM in the Ni-Cr-Si-B type brazing layer made on graphite base material.

What also became evident is that the brazed graphite specimens were bent after cooling to room temperature. This indicated that residual stresses remained in the structure and were not completely relaxed by fracturing.

The residual stresses remaining in the centre line of the braze layers were calculated using the Eq. 10 presented in the methodology part of this work, and according to the results the stress in the Ni-Cr-Si-B braze layer was 322 N/mm^2 and for the Ni-Cr-P braze: 213 N/mm^2. According to these results the residual stresses were more easily relaxed in the Ni-Cr-P type braze material when brazed on graphite or a carbon-filled substrate, indicating that the ductility of the braze relaxed the stresses.

3.11 Load bearing capability of brazed diamond single crystals

Brazed diamonds are used in tools or applications where they carry mechanical loads. In use, such as when grinding hard ceramics, it is important that the diamond is properly fixed on the tool surface and that it does not fracture under stress. Is it possible to measure how much stress can an individual single diamond crystals endure before breaking? And furthermore, how much can a brazed diamond tool be stressed during use?

To gain an understanding of the stress-bearing potential of the diamonds and tools, tests on the breaking loads of individual diamonds were performed. For these tests a mechanical testing method suitable for single diamond crystal testing was developed. A set of diamonds were brazed in rows on a flat stainless steel plate with nickel-based chromium alloyed braze filler material. An example of the

test sample is presented in Figure 101, where the tested specimen is presented before and after the mechanical test.

Ni-Cr-P type brazing filler material was used to braze test specimens for mechanical testing. The distance between individual diamonds was set to 1 mm and the diameter of a single crystal was between 250-300 µm. It should be noted that the tested diamonds were covered with the braze filler material and carbide layers as presented in Figure 102 a) below.
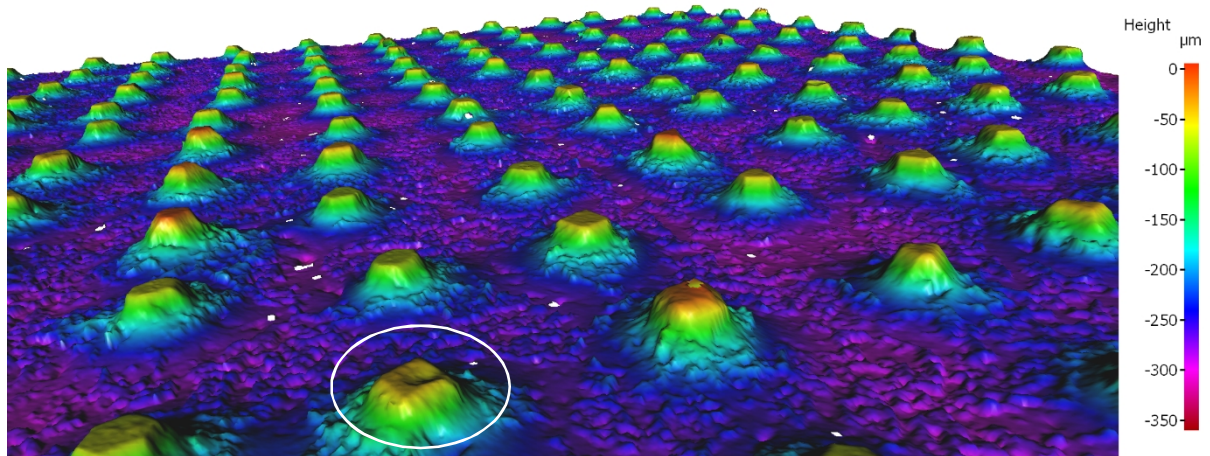

a)
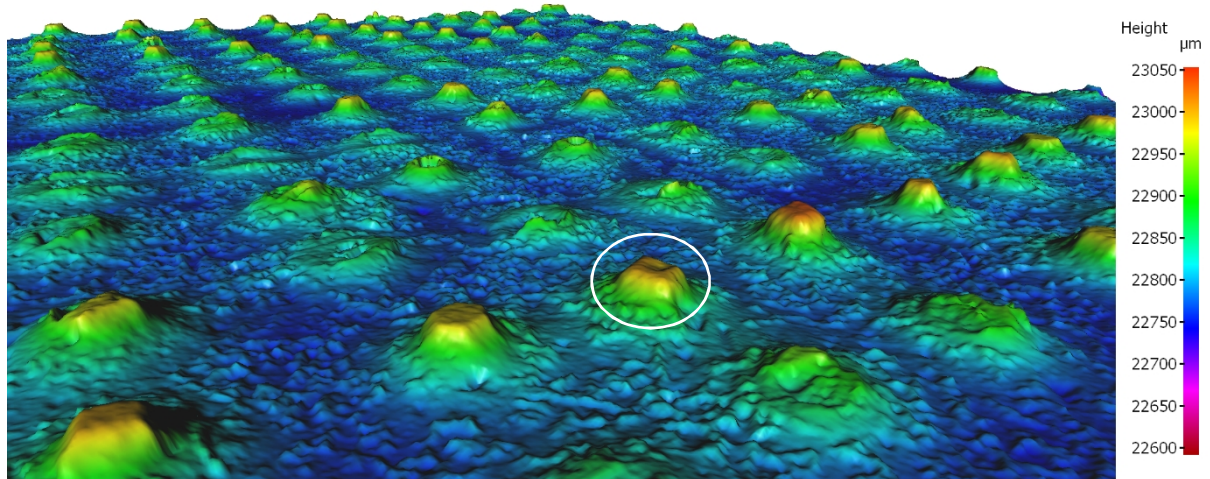
b)

Figure 101. Area of the mechanically tested specimen before (a) and after (b) the test measured using the optical profilometer. A diamond single crystal found from both images is marked with a white ring on both images.

The total thickness of the braze layer on the substrate surface was 68 µm when measured in the specimen cross-section. Figure 102 b) presents the surface fracture of the diamond after mechanical testing. Diamonds are typically fractured this way, and pull offs of the single diamond crystals were not observed. This result means that the bonding between the diamond and the braze filler material

108

is strong enough to hold the stressed diamond until the diamond breaks by fracturing. Some marks of mechanical deformation are found on the braze filler material surface near the diamond indicating that the testing tool touched the braze surface during the test.
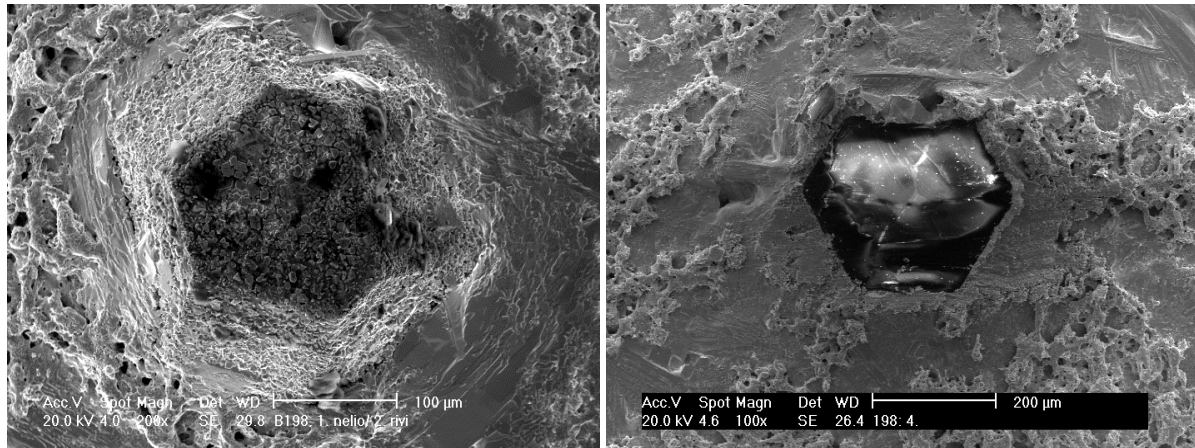
a)   b)

Figure 102. Top view of mechanically tested diamond before (a) and after (b) the test. Diamond is brazed on the stainless steel surface, the diamond is covered with braze/carbide layer. Note the different magnification of the images.

The testing speed for the tests was selected to be 2 mm per minute and the distance per test was set to 20 mm, so one test cycle would measure the breaking load of 20 diamonds, and with several test cycles altogether 296 diamonds were tested. As a matter of fact due to a slight displacement of the diamonds in rows it was not possible to hit every one, as presented in Figure 101, where the same test area is presented before and after mechanical testing. Testing destroyed only most of the diamonds in the rows.

The position of the tool and the level of the load was measured at 100 times per second. Due to noise of the measured signal, an average value of five separate measurements was calculated to reduce the noise level.

For each test the peak height (see Figure 103 below) of the force to break up the single diamond crystal was measured and the background was subtracted from the measured peak. Figure 103 presents the load peaks of one test run; the peak height gives the force needed to break up a single diamond.

As shown in Figure 103, there is some divergence in the diamonds' breaking loads. A reason for this could have been the variations in size and orientation of the single crystals, but also due to differences in the height of the braze layer. This would mean that, for some diamonds, the mechanical testing tool touches more of the braze layer than with others. This error can be minimized by subtracting the background level from the measured peak height, and this was done when analysing the test results.

Figure 104 presents a measured peak of when one diamond is tested and broken. Before hitting the diamond there is a base level of background force and when the diamond is hit the force value rapidly

increases. The distance moved by the testing tool between hitting the diamond and breaking was measured to be 0.038 mm. The slope of the curve was calculated as y = 680.65x.
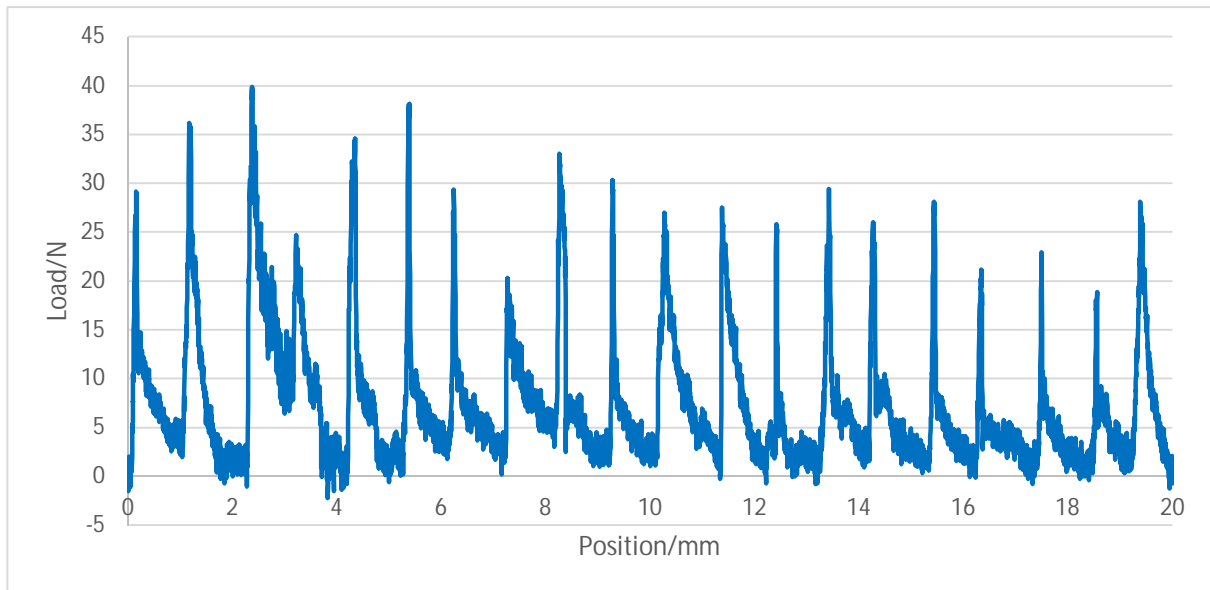
Peak	29.5	36.9	39.9	35.3	39.9	29.4	22.3	33	31.8	27	28	26.5	31	27	29.4	21.9	23.5	18.9	28.4
Background	0.5	3.8	1.2	0.4	1.8	3.6	2.8	5.4	2.7	2.8	2	3.1	1.6	2.8	1.4	1.9	1.6	1.6	2.1
Remainder	29	33.1	38.7	34.9	38.1	25.8	19.5	27.6	29.1	24.2	26	23.4	29.4	24.2	28	20	21.9	17.3	26.3

Figure 103. The results of one 20 mm test cycle with measured peaks, the background level and calculated force values needed to break up the test diamonds.
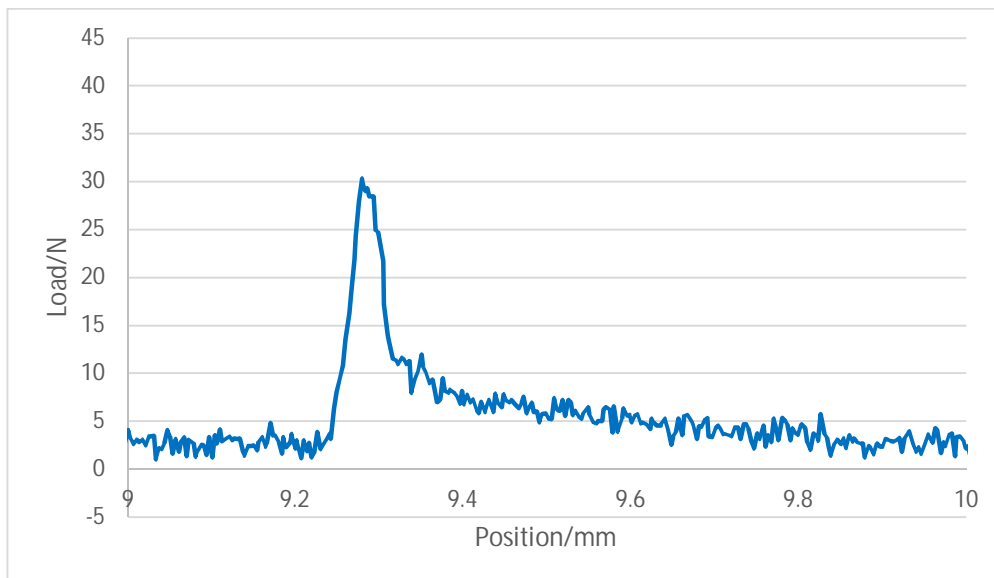

Figure 104. One of the measured load peaks to break up diamond single crystal. The slope of the linear section of the curve when breaking the diamond is calculated to be y = 680.65x

110

As stated previously, two load cells were used during the mechanical testing. Results achieved with these cells are shown in Figure 105 where the breaking load of the diamonds are presented as a function of the number of tested diamonds. In Figure 105 we can compare the results achieved with a more sensitive 5 kN load cell which shows minor differences, especially in the amount of maximum breaking loads.

All the results are collected in Figure 106 where the breaking load is presented as a function percent of all specimens tested. Figure 106 shows that 80 % of the diamonds broke at load levels between 20 N and 40 N and 50 % of the specimens broke at load levels between 24 N and 33 N. A minor portion, about 10 %, of the diamonds can hold over 40 N loads.
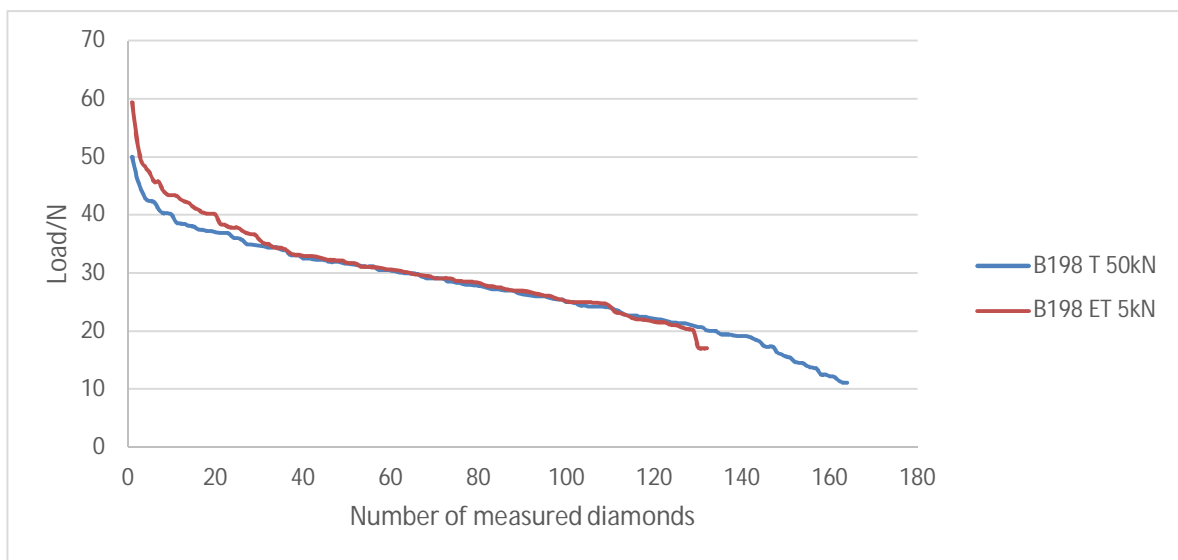

Figure 105. The breaking loads of diamonds shown as a function of the amount of measured diamonds. Results of the two load cells used are presented separately.
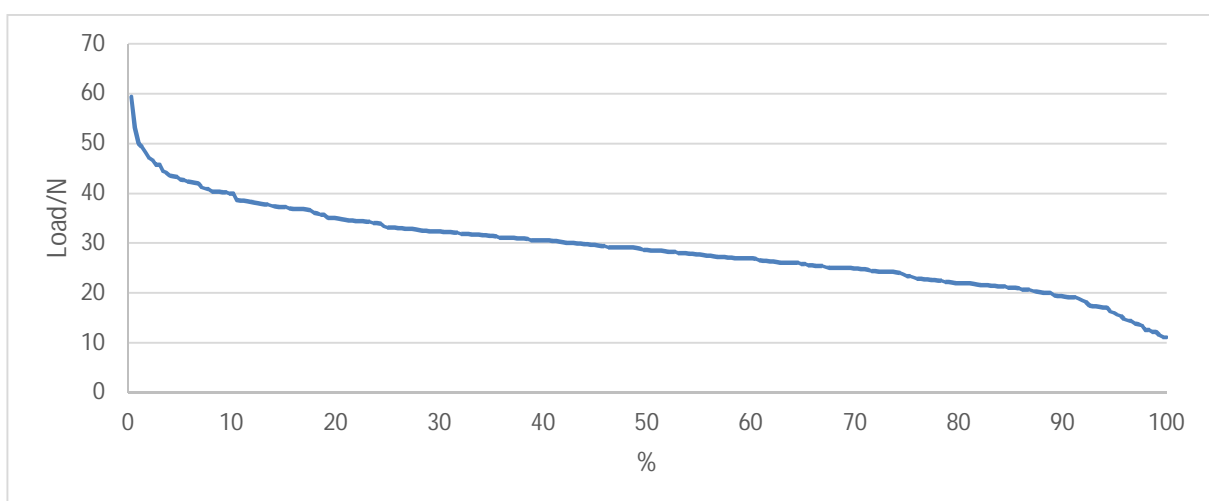

Figure 106. Mechanical testing: The load for breaking a diamond single crystal as a percentage of tested specimens.

Figure 104 showed how much force was used to break up the diamond crystal. In Figure 107, below, several of these peaks are collated. The slope of each peak after contact with the diamond is high. The level of the slope indicates the yield of the diamond, the braze fitting and the break-up of the braze with a carbide layer. The values of the slope lines presented in Figure 108 are shown in Table 33.

According to the results presented in Table 33, there is a large range of values demonstrating the difference between the thickness and structure of the carbide-braze layer compared to the tested individual single diamond crystals.
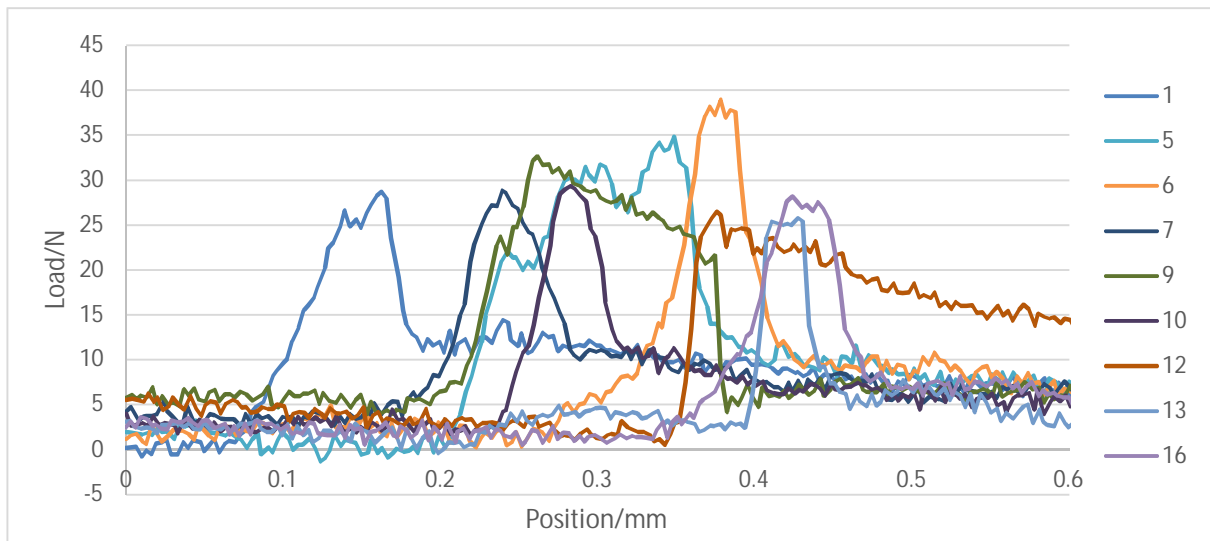

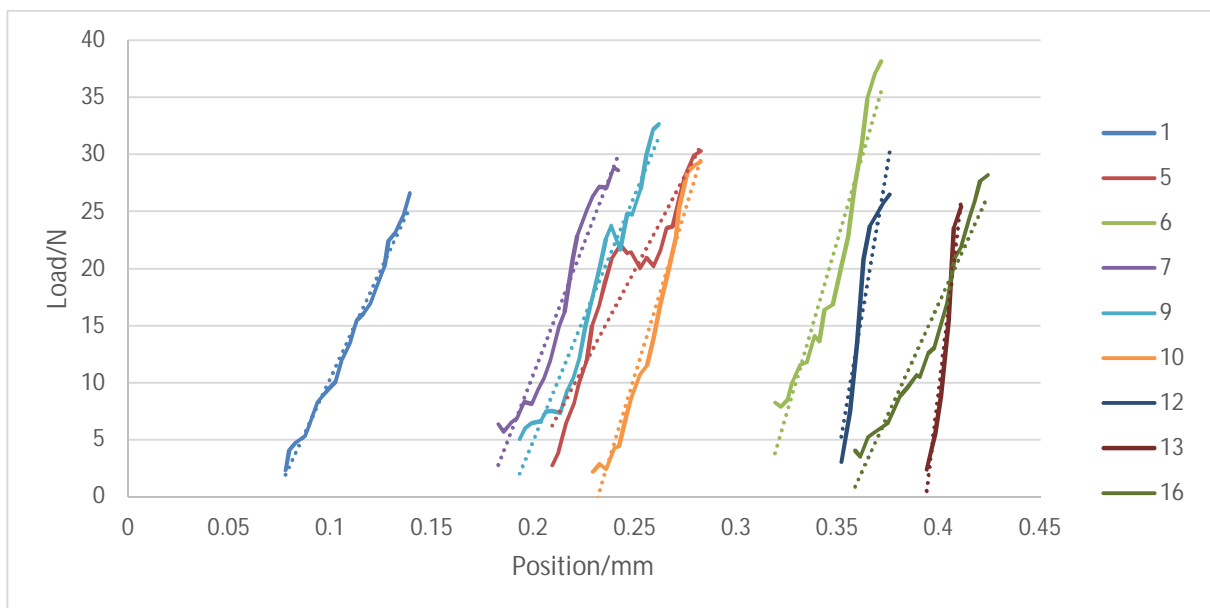Figure 107. Selected peaks presented in the same image

Figure 108. Slope lines of the selected mechanical testing curves presented according to Figure 107.

Table 33. Calculated slope values for the mechanical measurement tests presented in Figure 108

Test number	Slope
1	382x
5	334x
6	606x
7	459x
9	430x
10	582x
12	1044x
13	1496x
16	389x

3.12 Corrosion resistance of the brazed composites

As discussed in Section 1, the nickel-based brazing filler metal is used because of its strong corrosion resistance when joining single diamond crystals on the stainless steel surface. The brazing alloys studied here both have a high chromium content to improve the corrosion resistance. Because, according to the earlier studies, the microstructures the Ni-Cr-P and Ni-Cr-Si-B braze filler material are constructed of several phases with different composition of especially chromium, it is liable that there is selective corrosion found from these materials lowering the total corrosion resistance of the braze – diamond single crystal composite. To get information about the corrosion phenomena and differences of the corrosion behaviour of the studied materials simple corrosion tests were carried out.

3.12.1 Corrosion resistance of Ni-Cr-Si-B and Ni-Cr-P braze – diamond composite materials at low pH values

Altogether three Ni-Cr-Si-B type composite specimens, one Ni-Cr-P type specimen brazed with diamond crystals and reference specimens made of AISI 316 type stainless steel were tested. The specimens were scaled before and after the corrosion tests and the results are presented as weight loss during the test. The tests were carried out in a chlorine solution with a low pH value of 1.2 according to the ASTM G48-00 standard [70].

Looking at the results in Figure 109, the weight loss of the Ni-Cr-P type brazing filler metal during the corrosion test was over 2.5 times higher compared to the Ni-Cr-Si-B type brazing filler metal. The corrosion rate was also 2.5 times higher when compared to the reference material. This was a confusing result because according to Table 13 the chromium content of the Ni-Cr-P type (BNi-7) brazing filler material is considerably higher compared to the Ni-Cr-Si-B type (BNi-2) material. Weight loss of the Ni-Cr-Si-B braze–diamond composite was measured to be at the same level to the reference material, stainless steel.
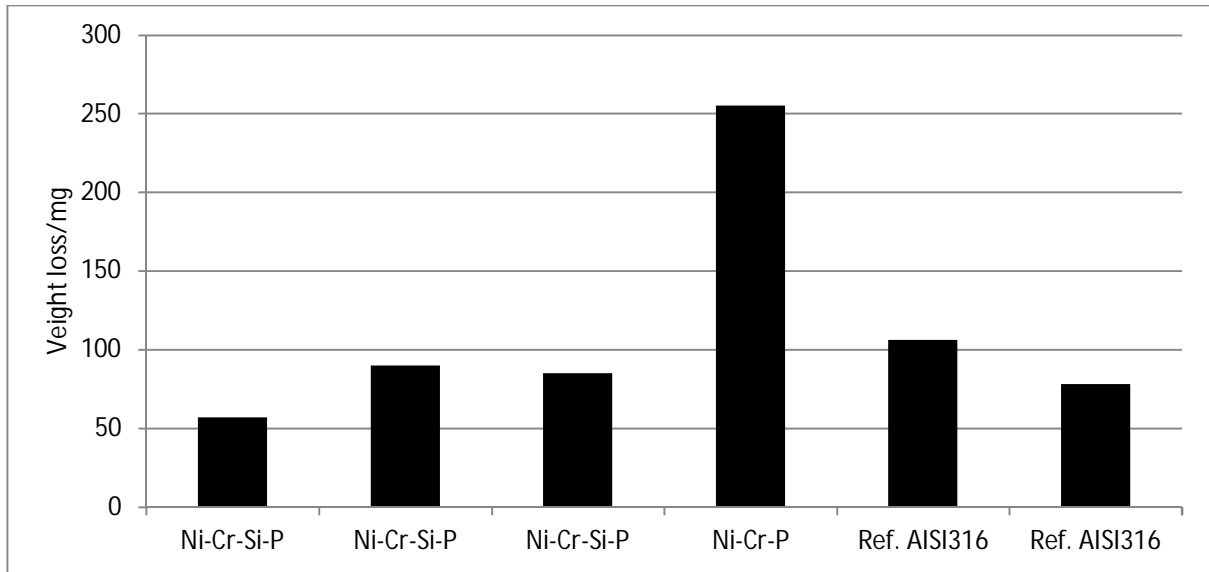
Figure 109. Weight loss of the tested materials after modified ASTM G48-00 [70] corrosion testing.

Polished cross-section specimens were prepared from these tested corrosion samples and it was noticed that the Ni-Cr-P type brazing filler metal had nearly completely disappeared from the specimen surface, which explains the high weight loss during the test. The Ni-Cr-Si-B braze only suffered corrosion in certain areas, as shown in Figures 110 a) and b), which were taken after corrosion testing. According to the images the nickel-based light phase and the spotty phase are not dissolved into the corrosive solution. The silicon, nickel and boron containing phases, no longer visible, were found to have a low chromium content of about 1-3 wt.-%.
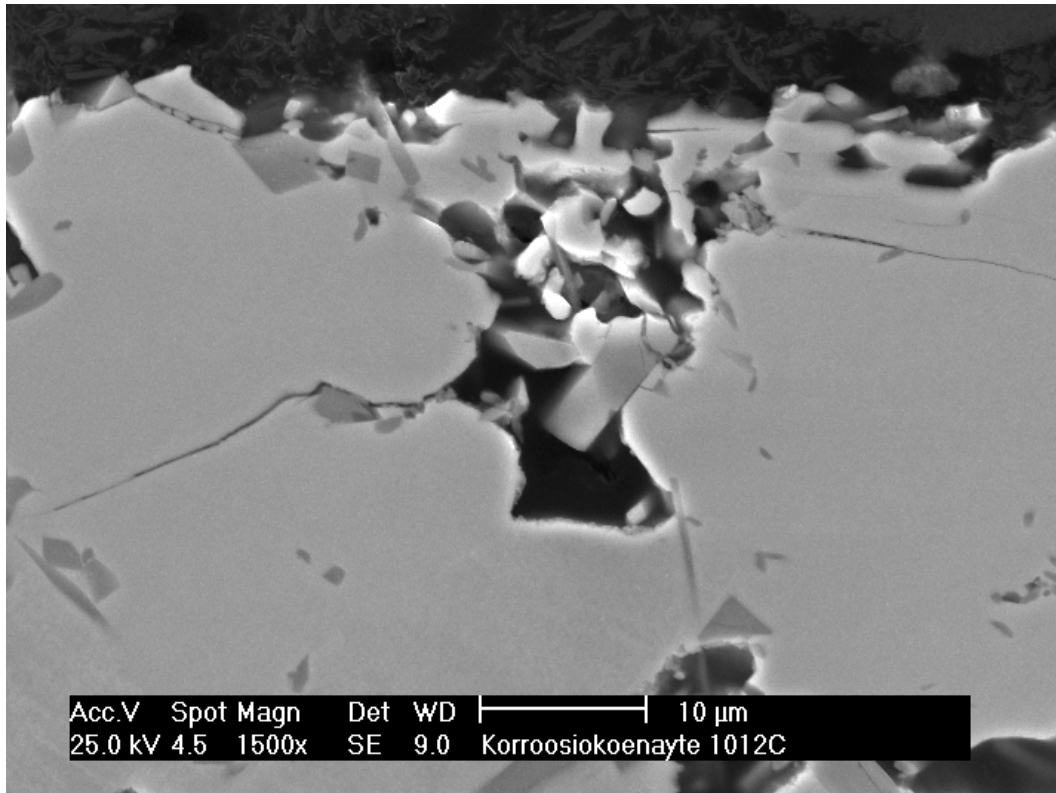
a)
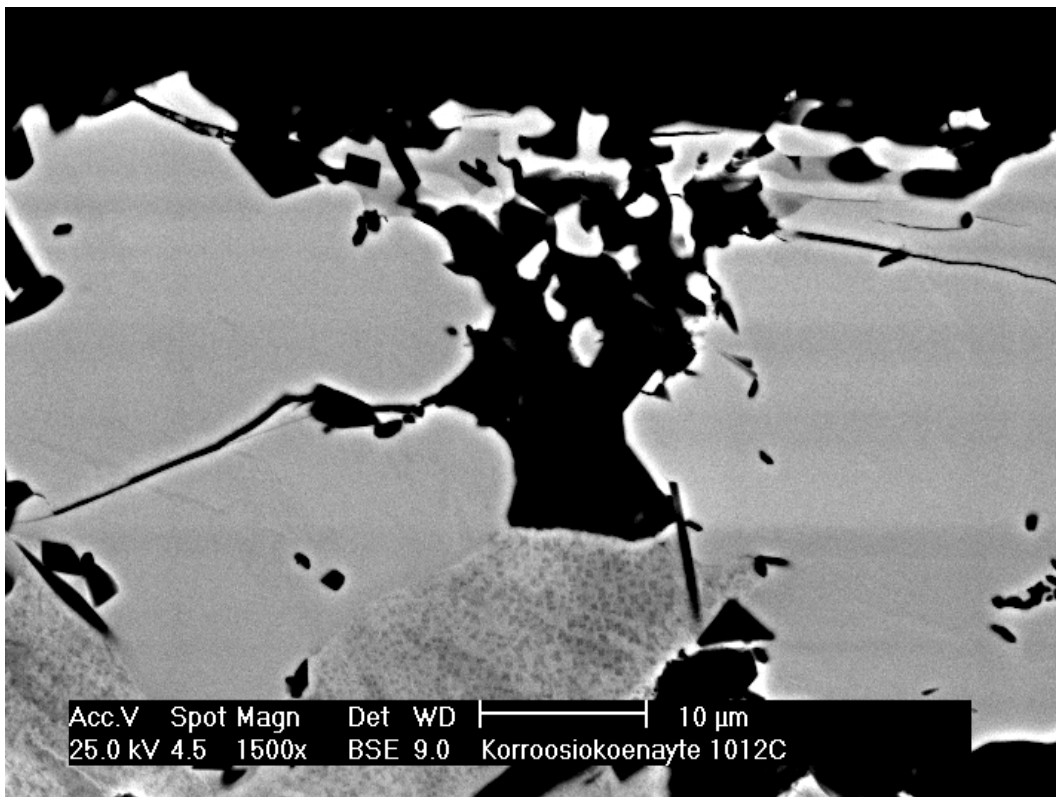
b)

Figure 110. Cross-section of the Ni-Cr-Si-B brazing material – diamond single crystal composite after the corrosion test, (a) SE-image and (b) BSE-image taken from the same area of the specimen.

Results from these simple immersion tests show that the Ni-Cr-Si-B brazing material performed better in low-pH chlorine solutions compared to the Ni-Cr-P braze, although chromium borides of the braze structure took a high faction of the chromium available in the Ni-Cr-Si-B braze material. One factor here that affected the corrosion resistance of the Ni-Cr-Si-B braze material could have been the slight difference in chromium content between the phases present, excluding the chromium boride phase. It is possible that in the specific test conditions strong corrosion pairs did not form, which reduced the corrosion rate of Ni-Cr-Si-B braze.

3.12.2 The corrosion potential and corrosion speed of the Ni-Cr-Si-B and Ni-Cr-P–diamond composite materials

The modified ASTM G48 test [70] was a simple immersion test and gave only limited information about the corrosive behaviour of the materials in one particular environment. To get more information about the corrosion behaviour of the composites, polarization curves were measured from the braze–diamond composite surfaces. For these measurements AISI 316 type stainless steel was used as a reference material to which the braze materials were compared. All of these measurements were performed at a room temperature of 22°C in 3.5 % ionized salt water, where the potential of the specimen was measured against Ag/AgCl reference electrode. Because of the height differences of the tested braze–diamond surfaces, the testing cell and the specimen was sealed with a soft rubber ring, 14 mm in diameter, making the tested area 1.54 cm^2 for each specimen. More detailed information about the test is given in the experimental methods part of this work.

The results of these studies are presented in Figures 111-105. For all the specimens three potentio-dynamic curves were measured from the same location of the specimen, refreshing the electrolytes between the measurements. These measurements were taken to see how the corrosion developed throughout the phases of the un-homogenous materials, dissolving into the electrolytes during the experiments.

From the curves, Tafel extrapolation was performed to determine the corrosion potential E_{corr} and corrosion speed I_{corr}. With the measured curve there was meant to be a linear section of two decades for complete analysis, but because of the multiphase structure of the braze materials this was not possible, giving approximate results as shown in Figures 111 - 113. [71, 72, 73]
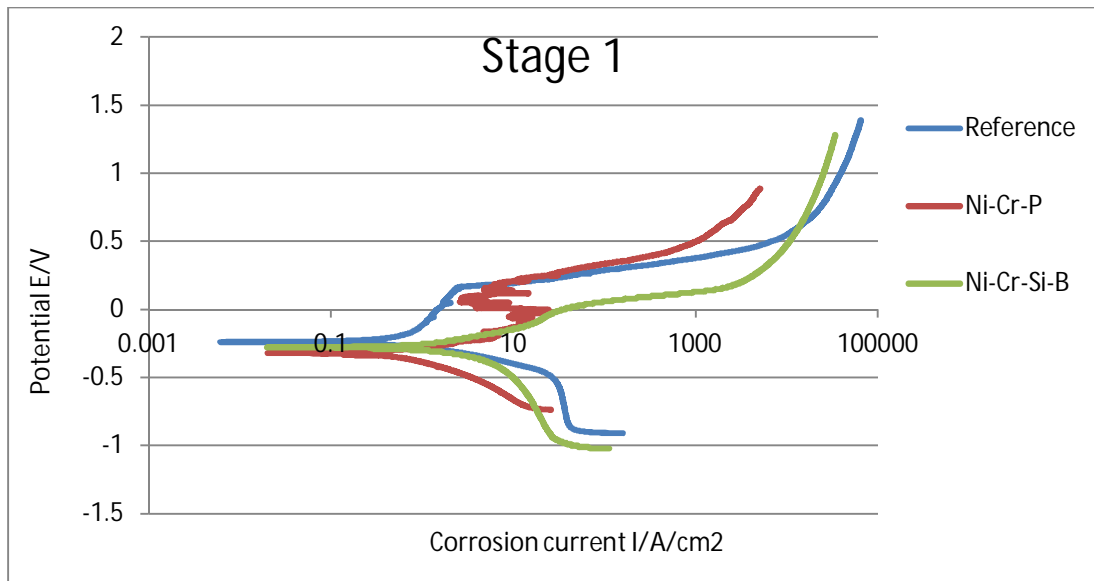
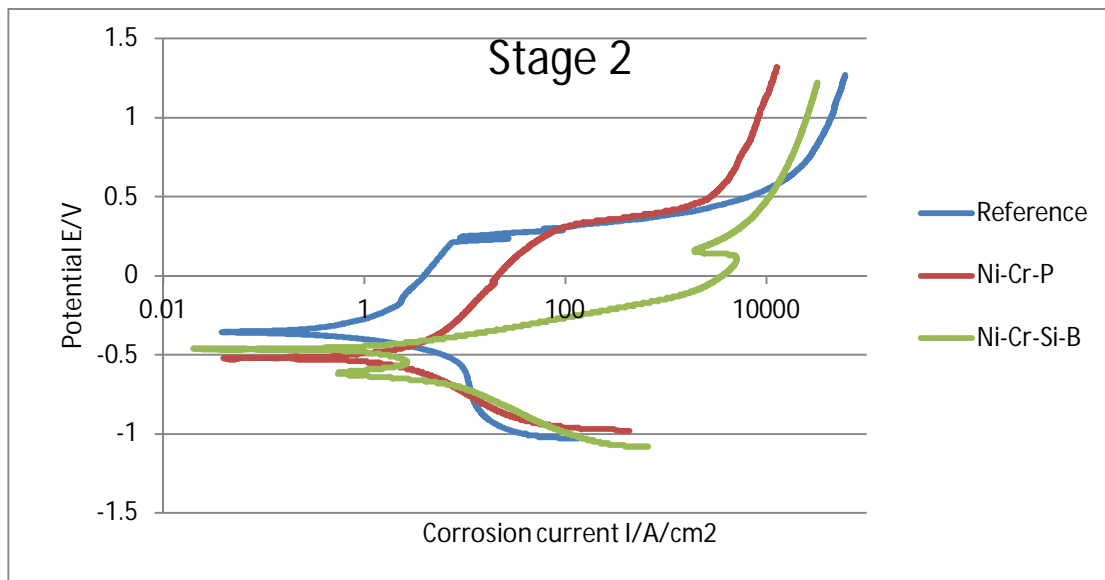Figure 111. Polarisation curves for the three tested materials after the first stage of measurements

Figure 112. Polarisation curves for the three tested materials after the second stage of measurements
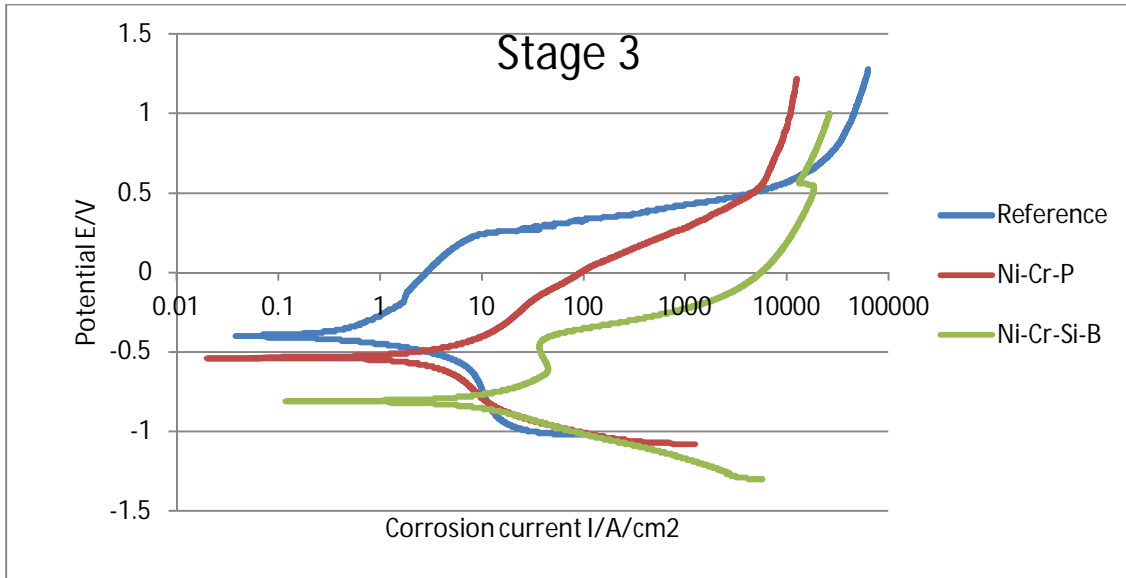
Figure 113. Polarisation curves for the three tested materials after the third stage of measurements

The results from analysis of the polarization curves, with Tafel-extrapolation, are presented in Figures 114 and 115. According to the results the corrosion potential reduced when the measurement was repeated. The development can also be seen in the corrosion current density and speed: the density increases for the braze–diamond composite specimens when the test is repeated. The surface area also increases when the measurement is repeated because of the pitting corrosion of specimen surfaces. The increase in the corrosion density presented in Figure 115 gives information about the pitting tendency of the brazed surfaces. The corrosion speed of the reference material remains constant or gets even lower when the test is repeated, indicating better corrosion resistance and pitting resistance when compared to the composite samples.
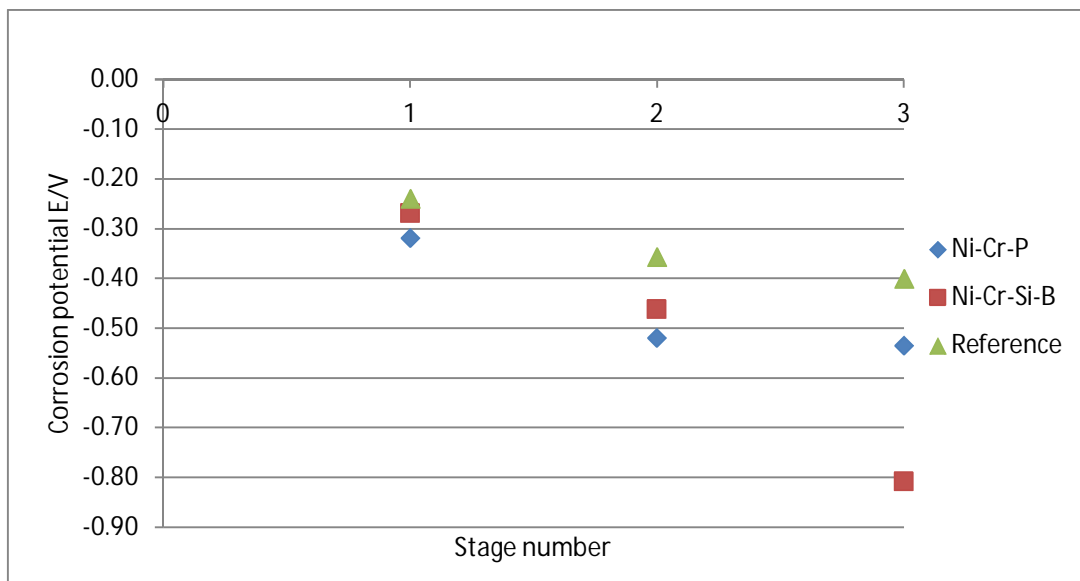

Figure 114. The development of the measured corrosion potential for the tested materials during the three-stage testing.
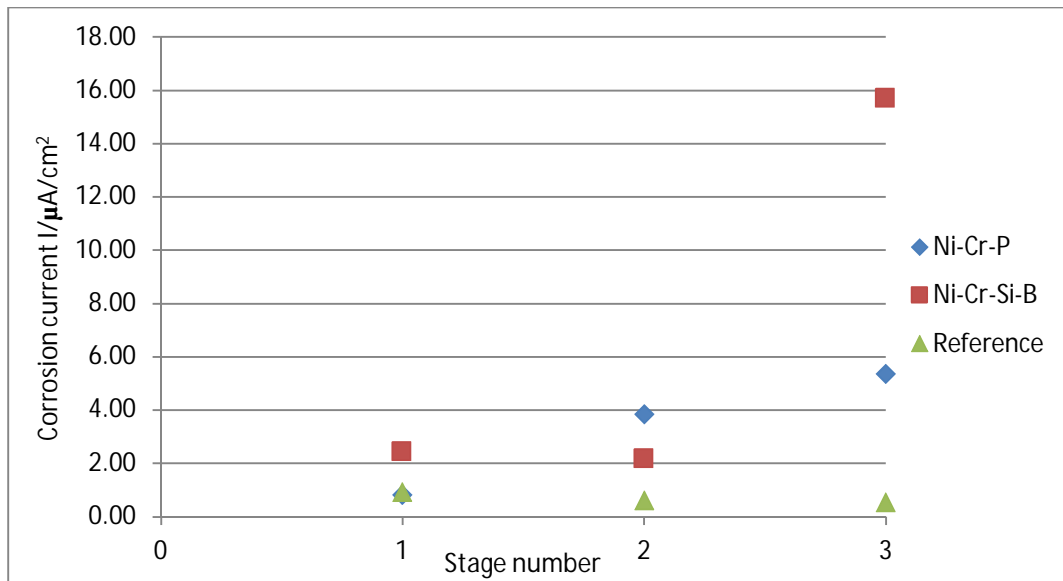
Figure 115. Development of the measured corrosion current density for the tested materials during the three-stage testing.

Figures 116 and 117 are the cross-sections of tested samples. Here it can be noted that in the case of the Ni-Cr-P brazing material corrosion is seen as pitting through the braze layer, indicating that the rather coarse and heterogeneous phase structure cannot resist corrosion and corrosion pitting is transferred into the base material. In the case of the Ni-Cr-Si-B braze–diamond composite there is selective corrosion within the braze layer. This result is in line with the others achieved from the short immersion tests. We can also, according to the cross-sectional studies, assume that the surface area of test sample Ni-Cr-Si-B is effectively increased when selective corrosion erodes the braze layer microstructure in micro scale. This can be seen in Figure 115 with the increase in current density for the Ni-Cr-Si-B–diamond composite: here the current/surface area can remain constant, because according to Figure 117, the surface area can be seen to increase. If the current density is constant after the third stage of testing (assumed to be at the same level than in the first measurement), results showed, that the surface area of the Ni-Cr-Si-B–diamond composite specimen was about 7 times larger, the area of Ni-Cr-P–diamond composite was approximately 5 times larger, while the area of the reference material remained constant.
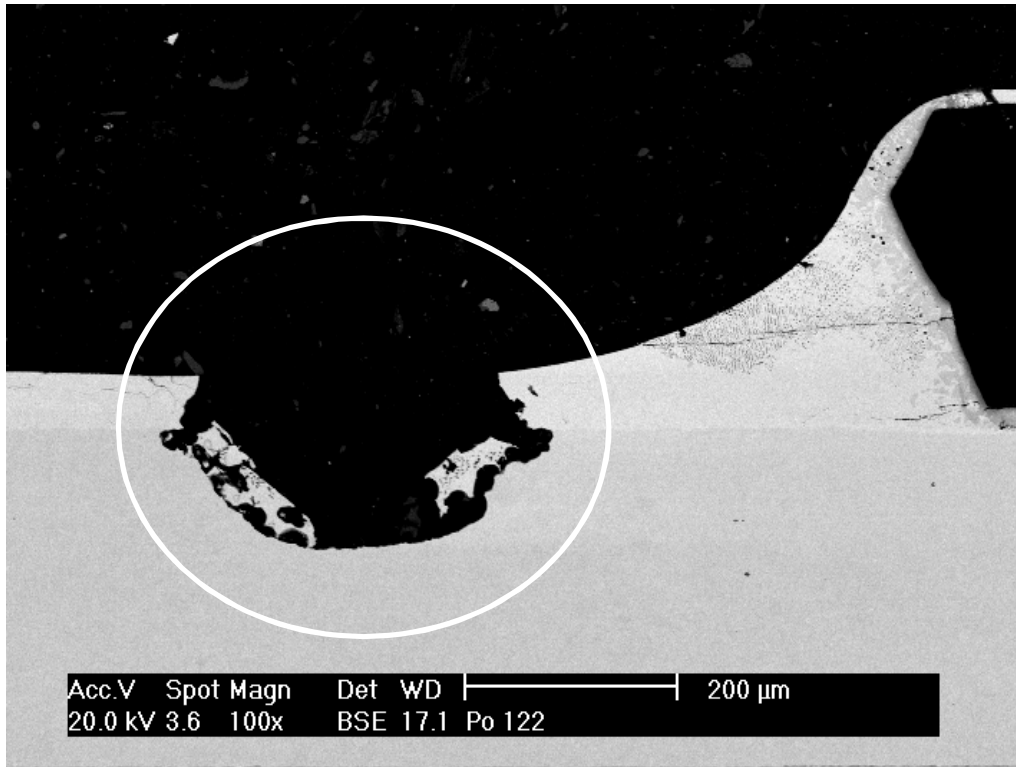
Figure 116. Cross-section of the Ni-Cr-P braze material after the three-stage potentio-dynamic testing cycle. The pitting corrosion (ring) penetrated into the base material.
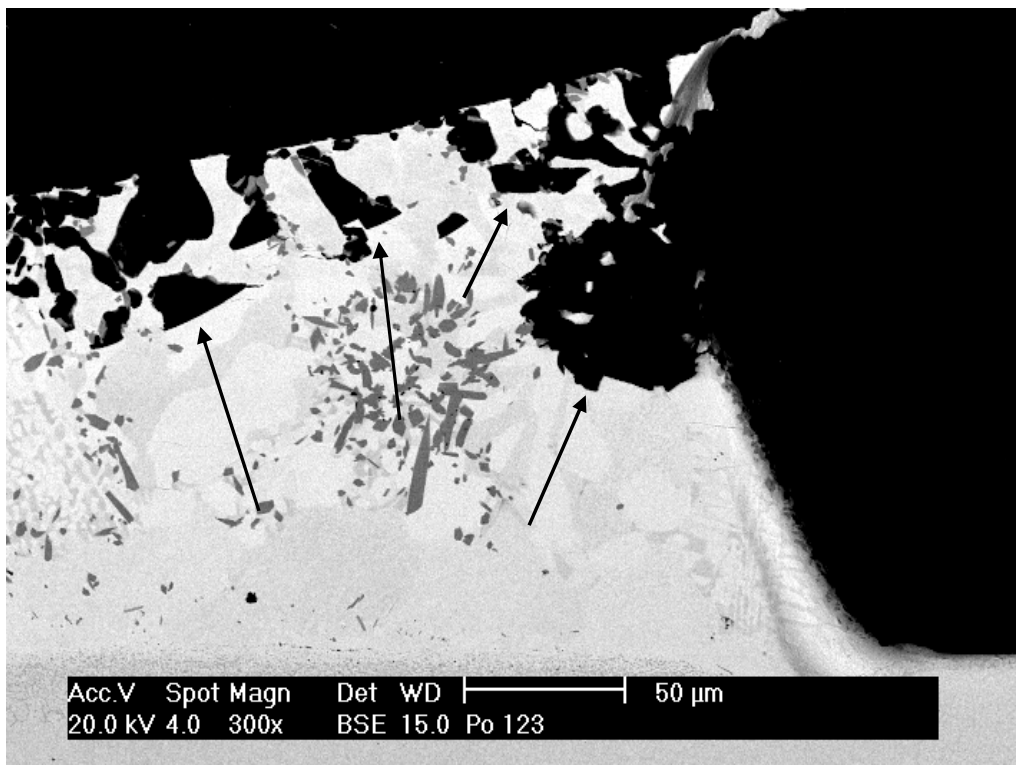

Figure 117. Cross-section of the Ni-Cr-Si-B braze material after the three-stage potentio-dynamic testing. Inside the braze layer micro scale pitting corrosion are evident, marked with arrows.

4. Concluding remarks and suggestions for future work

The diamond single crystals are jointed on to the tool surfaces using several types of braze filler materials. There are differences between the materials where the brazing temperatures vary considerably, being higher for some than others. The relatively low cost nickel-based chromium alloyed brazing filler materials are corrosion resistant with good material strength compared to other brazing filler materials, and therefore ideal for use in demanding applications such as mechanical pulping devices like Valmet's Galileo-concept.

During the high temperature brazing process carbon from the diamond is dissolved and diffused into braze filler material. Carbon forms chromium carbides between the braze material and the diamond crystals; the carbide layers help to lower the contact angle between braze and diamond, but also help to form a strong bond between the diamond and the braze. This greatly improves the mechanical bond between the braze material and the diamond and therefore improves the diamond tool's usability.

The dilution of carbon affects the microstructure and properties of the braze filler material – diamond composite. The degradation of single diamond crystals roughens the crystal facets, reduces the mechanical properties and the tooling efficiency of the diamonds as the sharp edges of the diamonds are rounded during the brazing process. Furthermore, carbide layers on the diamond surface between the braze filler material and diamond smooth out the difference in the thermal expansion coefficient between the diamond and the braze filler material, leading to a reduction in the level of residual stresses which then affects the tool performance.

Two different kinds of nickel-based braze filler materials was chosen for the studies to see what effects of composition has to the final structure and properties between the braze filler material and diamond. The Ni-Cr-Si-B braze filler material was found to have only slight carbide formation compared to the Ni-Cr-P braze, despite the higher brazing temperature of the former. The lesser amount of carbides present is because of the lower chromium content, and the formation of chromium borides in the Ni-Cr-Si-B braze matrix combines a large part of the available chromium in turn reducing the chromium carbide formation. The chromium alloying provided adequate corrosion resistance but also decreased the mechanical strength of the diamonds because of the excess carbide formation. The studied nickel based braze filler materials are originally developed mainly to join the stainless steel materials and super alloys used in corrosive applications at high temperatures and for this reason they are not necessarily the best performing alloys to join the diamonds.

Question 1 from Chapter 1.1

1. What are the reactions between the braze material and diamond crystals: the structure of the formed connecting layers and effect of the brazing process to the single diamond crystal structure and surface? Furthermore, how does the brazing process affect the diamond single crystal surface and what is the possible degradation mechanism? How can the structure be characterized and what kind of analysing techniques can be used and developed?

In answering Question 1: it was found that the degradation that occurred to the diamond facets varied, in turn affecting the mechanical strength of the individual crystals. On the {111} type diamond facets were found to form plateaus which were not found on other type of facets. These results show that

carbon atoms are removed and diffused into the braze filler material from the {111} type plains, perpendicular to the direction <111> of the {111} type diamond facet. These tests clearly show that the higher the available chromium content, the thicker the carbide layer on the diamond surface and the increase in degradation on the diamond surface.

Question 2 from Chapter 1.1

2. What is the final structure of the brazing filler material? What kind of dilution of the base material is observed? To elaborate: how does the dilution of carbon from single diamond crystals and the elemental components from the tested base material affect the final structure of the braze joint?

In answering Question 2: the cross-sections of the carbide layers between the diamond and braze were studied using Scanning Electron Microscopy (SEM) and Back Scattered Electron (BSE) analysis. BSE-imaging together with the image analysis program used to measure the grey levels of the phases proved to be a very efficient tool to characterize the phases. This imaging method is especially useful when identifying separate phases within multi-phase materials, especially where some of the components are electrically insulating like diamond or very small in size like the carbides on the diamond surface.

Using the BSE-imaging confirmed that between the diamond and braze two different layers of carbides formed, giving lighter and darker phase contrast and in turn indicating the difference in the carbon composition of these carbides. The tests and imaging showed that in the Ni-Cr-P braze filler material, a $(Ni, Cr)_3P$ type phase forms adjacent to the diamond. However, inside the braze, still further from the diamond is the $(Ni, Cr)_2P$ phase. The separation of these phases is most likely because of the carbon dilution and the formation of chromium carbides on the diamond surface, which reduces the chromium content near the diamond.

The studies also showed that the lower parts of the diamonds were round-shaped and the sharp edges had partly disappeared after brazing. The removal rate of carbon between the diamond and the base material was high, indicating the diffusion of carbon into the base material. The structure of the base material was face centred cubic austenite stainless steel, which is able to dissolve carbon inside the crystal structure at the brazing temperatures used. Rounding of the sharp edges reduces the efficiency of the tool if the edges on the top of the diamond are also rounded.

The internal structure of diamond crystals was studied with TEM and the results were confirmed with fracture surface studies. According to these results, the crystals are not degraded inside. The reactions only occur on the crystal surface, not internally weakening them. This means that although the carbon from the surface of the diamond may diffuse into the brazing material, the components of the braze filler metal cannot diffuse into the diamond at the brazing temperatures used.

The interface between diamond and braze was studied in detail. No evidence of graphite formation was observed although the braze materials contained nickel. According to the results it is possible that the deterioration of the interface's mechanical properties could in part be due to the degradation of the single diamond's crystal surfaces. Results of the mechanical testing performed also confirm this result: during the tests single diamond crystals were fractured but not pulled off the surface, which would have been the case if there was a weak graphite layer between the diamond and the braze. It

was also evident that cracks formed on the braze layers of the diamond surfaces due to differences in the thermal expansion coefficients, indicating there is no graphite between the diamond and the braze material.

Residual stresses formed on the diamond surface during brazing, as predicted. The distance between the cracks formed with the Ni-Cr-Si-B braze filler material were found to be shorter when compared to the Ni-Cr-P braze material. The latter material was found to be more flexible in its yield under tension. The bond between the braze and the diamond was adequate to carry the forming residual tension between them, and no cracks were observed in the layers there either.

Question 3 from Chapter 1.1

3. What kind of residual stresses are formed on the diamond surface during the manufacturing process and what is the mechanical strength of the single diamond crystals after the brazing process?

In answering Question 3: a special mechanical testing method was developed to measure the strength of the brazed crystals. The results of mechanical testing gave basic information on the breaking loads for the stressed individual diamond crystals when brazed on the stainless steel surface with the nickel-based braze filler material. According to the results 50 % of the diamonds are fractured between 24 N and 33 N loads. The testing method developed can later on be used to test the load-bearing ability of the crystals brazed according to different parameters and braze filler material compositions.

Question 4 from Chapter 1.1

4. How does corrosion affect the structure of the final braze layer and single diamond crystals and how does the corrosion resistance differ between the study materials?

In answering Question 4: the corrosion tests showed that the structure of the braze materials involves several phases which lead to corrosion pairs and some selective corrosion. In the Ni-Cr-Si-B braze material the phases were found to have low chromium content, with levels not high enough to refresh a protective chromium oxide layer on the braze surface. According to the EDX-measurements there were no large differences in the chromium content between phases, which is reducing the tendency to form corrosion pairs with different corrosion potentials.

The tests have revealed that the current braze materials being commonly used (because they are viewed as high strength and corrosion-resistant) are not the optimum materials when super-abrasives like diamond are brazed. These materials were originally developed for brazing stainless steels, super alloys and other similar metallic materials. The high chromium content of these alloys reacts with the carbon within the diamonds and part of the mechanical strength of the diamond singe crystals is then lost. This discovery is the basis for starting development work on new, more suitable brazing alloys: the results here give strong guidelines and form an ideal basis for further research.

It was also important to find out how the reaction between diamond and braze could be adjusted to upgrade the diamond tool performance and mechanical strength, in turn supporting further development of the braze materials. For both brazing materials the diamonds were fully covered by the braze filler metal. This process caused good wetting, which led very low contact angle values

between the braze filler material and diamond grits. The results will help form suggestions for the development of better braze material compositions. Chromium should be partly substituted for other aggressive elements to form carbides on the diamond surface and prevent excess chromium carbide formation. Suitable elements for this purpose could be titanium, molybdenum, zirconium and niobium. Copper, iron, silicon, cobalt and manganese could be used to substitute part of chromium. All of these alloys form Me_xP type compounds like Ni_xP (where x=2 or 3), a braze alloy component with phosphorus having low melting point. Some of these components can also reduce the brazing temperature reducing the dilution of the diamond. The development work of new suitable brazing filler materials was not part of present work but will be done in the future.

As a result of this work it has become clear that the mechanical properties of the crystals can be improved if the brazing materials are developed to be more suitable for brazing diamonds. More effective and durable grinding tools need to be developed and produced, focusing on optimized interface structures between the diamond particles and the braze filler material chemistry. In general, these kind of composite material tools could be used on hard materials (such as stone, concrete etc.) for cutting, drilling, finishing and in any other applications involving hard materials. This gives us the opportunity to develop and produce more durable, stable and energy-efficient grinding surfaces for a whole host of industrial applications.

As a starting point of the research in the future new mechanical testing method was developed to have statistical information about the properties of brazed diamond single crystals. Hundreds of diamond single crystals were already tested. Achieved results give basic information of the breaking load of the stressed individual diamond crystals. Development of novel method should include in the future development of testing system mechanics, testing suitability of different kinds of loading intenders and load cells and testing of sensitivity and repeatability of the method. The developed testing method can be used for testing the affect of different braze materials and brazing parameters on the load bearing ability of the diamond single crystals. For wider use the method should be better assessed for its sensitivity and repeatability, which is one topic in the future.

The studies of two different brazing filler materials gave good guidelines for the necessary material composition development work, which is now already started. Nickel based alloys should be alloyed also with other elements than chromium to lower the brazing temperature, to prevent the excess chromium carbide formation and to reduce the difference in chromium content in the formed phases to prevent the formation of corrosion pairs. As it was showed in the studies difference in composition between formed phase assists the pit formation and crevice corrosion weakening the structure in use.

The corrosion behaviour of nickel based brazing filler material – diamond composites is becoming an important issue if the tools are used in corrosive conditions. Results concerning this matter is not so much published this far and therefore the research should continue. Focus in this work should be better corrosion resistivity by tailoring the braze filler metal structure with new alloying elements.

One goal for the brazing filler metal development is to make the carbide layers formed on the surface of diamond single crystal thinner. The refinement of the layers is needing more accurate research methods and more detailed TEM studies should be done on cross-sectional specimens and more detailed surface analysis should be performed. More sensitive surface studies using techniques, such as Auger spectroscopy can be utilized.

On the basis of the achieved results and further development work tools with super hard abrasives can have better quality and can be used in more severe conditions in the future. This need the detailed development work of suitable brazing alloys together with development of good quality super-abrasive crystals.

References:

[1] S. N. Monteiro, A. L. Diegues Skury, M. Giardinieri de Azevedo, G. S. Bobrovnitchii, Cubic boron nitride competing with diamond as a superhard engineering material – an overview, J. Mater. Res. Technol., 2 (1): pp. 68-74, 2013

[2] Metals Handbook, vol. 6, ASM, asminternational.org, viewed 2016

[3] F. P. Bubdy, H. T. Hall, H. M Strong, R. H. Wentorf, Manmade diamonds, Nature, 176: pp. 51-5, 1955

[4] M. Weinstein, L. Lee, C.J. Skinner, A.M. Amanda, A. J. Battenburgh, A. M. Staines, Further Developments in Boron Free Nickel-Chromium-Phosphorus-Silicon Brazing Filler Metals, Wall Colmonoy, Detroit, MI, USA, Swansea, UK, July 2012

[5] Element Six, www.e6cvd.com, viewed 2016

[6] M. P. D'Evelyn, Industrial Diamond, Technical Information Series, GE Research & Development Center, 2001CRD026, March 2001

[7] M. A. Prelas, G. Popovici, L. K. Bigelow, Handbook of industrial diamonds and diamond films, Marcel Decker Inc., New York, 1997

[8] http://www.valmet.com/pulp/mechanical-pulping/production-consumables/segments-for-grinders/ , viewed 2017

[9] W. Tillmann, A. M. Osmanda, Production of Diamond Tools by Brazing, Materials Science Forum, Vol. 502, pp. 425-430, 2005

[10] Zhengya Xu, Hongjun Xu, Yucan Fu, Bing Xiao and Jiuhua Xu, Induction Brazing Diamond Grinding Wheel with Ni-Cr Filler Alloy, Materials Science Forum, Vols. 532-533 pp. 377-380, (2006)

[11] Zhibo Yang, Jiuhua Xu, Yucan Fu and Hongjun Xu, Laser Brazing of Diamond Grits with a Ni-based Brazing Alloy, Key Engineering Materials, Vols. 359-360, pp. 43-47, 2008

[12] Metals Handbook vol. 3, ASM, asminternational.org, viewed 2016

[13] J. Miettinen, Thermodynamic description of Cr-P and Fe-0-P systems at low phosphorus contents, Calphad, Vol. 23, No. 1, pp. 141-154, 1999

[14] E. Lugscheider and K-D. Partz, High Temperature Brazing of Stainless Steel with Nickel-Base Filler Metals BNi-2, BNi-5 and BNi-7, Welding research supplement, 1163-s, 162-s, June 1983

[15] J. Ruiz-Vargas, N. Siredey-Schwaller, P. Bocher, A. Hazotte, First melting stages during isothermal brazing of Ni/BNi-2 couples, Journal of Materials Processing Technology 213, pp. 2074–2080, 2013

[16] Advances in brazing, Science, technology and applications, Editor D. P. Sekulic, Woodhead Publishing, Oxford, 2013

[17] T. Yamazaki, A. Uzumura, T-T. Ikeshogju, T. Ishiguro, Role of valency electrons of vanadiumin metallization of diamond surface, Proc. of International Brazing and Soldering conference, Orlando, FL, USA, pp. 291-295, 2009.

[18] J. Ruiz-Vargas, N. Siredey-Schwaller , N. Gey, P. Bocher, A. Hazotte, Microstructure development during isothermal brazing of Ni/BNi-2 couples, Journal of Materials Processing Technology 213, pp. 20–29, 2013

[19] W. Tillmann, A. M. Osmanda, S. Yuechenko, M. H. Boretius, Properties of nickel based joints between diamond and steel for diamond grinding tools, Welding and Cutting, Vol. 7, No. 4, pp. 228-235, 2008

[20] Y-C. Hsien, S-T. Lin, Interfacial bonding strength between brazing alloys and CVD diamond, J. Mat. Eng. Per., Vol. 18, No. 3, pp. 312-318, 2009

[21] T. Hartmann and D. Nuetzel Nickel-chromium-based amorphous brazing foils for continuous furnace brazing of stainless steel, Proceedings of the 9th International Conference of Brazing, High Temperature Brazing and Diffusion Bonding, , (DVS-Berichte 263) June 15th to 17th 2010, Aachen, Germany, 2010

[22] Mechanical testing standard DIN EN 12797, Deutsches Institut für Normung

[23] S. Buhl, C. Leinenbach, R. Spolenak, K. Wegener, Microstructure, residual stresses and shear strength of diamond–steel joints brazed with a Cu Sn-based active filler alloy, Int. Journal of Refractory Metals and Hard Materials 30, pp. 16–24, 2012

[24] M. Koster, A. Lis, W. J. Lee, C. Kenel, C. Leinenbach, Influence of elastic–plastic base material properties on the fatigue and cyclic deformation behavior of brazed steel joints, International Journal of Fatigue, in press, 2015

[25] C. Leinenbach, R. Transchel, K. Gorgievski, F. Kuster, H. R. Elsener, and K. Wegener, Microstructure and Mechanical Performance of Cu-Sn-Ti-Based Active Braze Alloy Containing
In Situ Formed Nano-Sized TiC Particles, Journal of Materials Engineering and Performance, Vol. 24(5), May 2015

[26] S. Buhl, C. Leinenbach, R. Spolenak, K. Wegener, Influence of the brazing parameters on microstructure, residual stresses and shear strength of diamond–metal joints, J. Mater. Sci. 45: pp. 4358–4368, 2010

[27] Bojiang Ma, Guanglei Yang, Fanning Bu, Study of brazed diamond micro-powder burs fabricated using induction brazing with either an amorphous or a crystalline Ni-based filler alloy, Int. Journal of Refractory Metals and Hard Materials 62, pp. 58–63, 2017

[28] S. Anastasio, J. James, J. Fitz-Gerald, and J. R. Scully, Corrosion of Superaustenitic Stainless Steel N08367 Brazed with a Nickel-Chromium-Silicon-Phosphorous Alloy: Electrochemical Corrosion Behavior of Isolated and Combined Materials, Corrosion, Vol. 65(6), pp. 388-403, 2009

[29] J. P. James, F. Bocher, and J. R. Scully, Effect of Braze Clearance on Localized Corrosion of a Superaustenitic Stainless Steel Brazed with a Ni-Based Alloy (Ni-22Cr-6.3Si-3.8P), Corrosion, Vol. 65(8), pp. 511-526, 2009

[30] A. J. Willingham, Interfacial Corrosion in Stainless Steel Brazed Joints, Johnson Matthey Metals Ltd.

[31] M. H. Sloboda, Making corrosion resistant brazed joints in stainless steel, Platinum Metals rev., 13, (2), pp. 61-64, 1969

[32] M. Weinstein, L. Lee, C. J. Skinner, A. M. Osmanda, A. J. Battenbough, A. M. Staines, Further Developments in Boron Free Nickel-Chromium-Phosphorus-Silicon Brazing Filler Metals, Wall Colmonoy, Detroit, MI, USA, Swansea, UK Technical Article © 2012

[33] E. Lugscheider, P. Minarski (1989), Untersuchungen zur Korrosionsbeständigkeit hochtemperaturgelöteter Werkstoffe in Trinkwasser, Schweißen und Schneiden 41, Heft 11, pp. 590-595, 1989

[34] S. D. Cramer, B. S. Covino, ASM Handbook Volume 13A Corrosion: Fundamentals, Testing and Protection, S. 194, p. 420, 2003

[35] A. Rabinkin, Brazing with (NiCoCr)–B–Si amorphous brazing filler metals: alloys, processing, joint structure, properties, applications, Science and Technology of Welding and Joining, Vol. 9 No. 3, pp. 181-199, 2004

[36] T. Hartmann and D. Nuetzel, New amorphous brazing foils for exhaust gas applications, Vacuumschmelze, Hanau, Germany, 2009

[37] ChangHun Lee, JongOh Ham, MinSeok Song and ChiWang Lee, The interfacial reaction between diamond grit and Ni-based brazing filler metal, Materials Transactions, Vol. 48 No. 4 pp. 889-891, 2007

[38] B. Xiao, H. J. Xu, Y. C. Fu and J. H. Xu, Form and Distribution Characterization of Reaction Products at the Brazing Interface Between Ni-Cr Alloy and Diamond, Key Engineering Materials, Vols. 259-260 pp. 151-153, 2004

[39] Y. V. Naidich, G. A. Kolesnitchenko, A. Lavrinenko, H, Y. F. Mazak, Brazing and metallization of ultrahard tool materials, Kiev, Naukova Dumka, 1988

[40] Y. V. Naidich, V. P. Umanskii, I. A. Lavrinenko, Strength of the diamond-Metal interface and Brazing of Diamonds, Cambridge International Science Publishing Ltd, Cambridge, UK, 2007

[41] A. Rabinkin, Diamond interaction with various metals and alloys under different environmental conditions, 8th AIRAPT conference on high pressure research and industry, Uppsala, 1, pp. 361-364, 1981

[42] U. E. Klotz, C. Liu, F. A. Khalid, H-R. Elsener, Influence of brazing parameters and alloy composition on interface morphology of brazed diamond, Materials Science and Engineering, A 495, pp. 265–270, 2008

[43] Yan Chen, Yucan Fu, Honghua Su, Jiuhua Xu, Hongjun Xu, The effects of solder alloys on the morphologies and mechanical properties of brazed diamond grits, Int. Journal of Refractory Metals and Hard Materials 42, pp. 23–29, 2014

[44] D. E. Newbury, D. C. Joy, P. Echlin, C. E. Fiori, J. I. Goldstein, Advanced scanning electron microscopy and microanalysis, Plenum Press, New York, N.Y, USA, 1986

[45] W. Tillmann, M. Ferreira, A. Steffen, K. Rüster, J. Möller, S. Bieder, M. Paulus, M. Tolan, Carbon reactivity of binder metals in diamond–metal composites–characterization by scanning electron microscopy and X-ray diffraction, Diamond & Related Materials 38, pp. 118–123, 2013

[46] C. Y. Wang, Y. M. Zhou, F. L. Zhang, Z. C. Xu, Interfacial microstructure and performance of brazed diamond grits with Ni–Cr–P alloy, Journal of Alloys and Compounds, 476, pp. 884–888, 2009

[47] T. A. Hahn, Thermal expansion of copper from 20 to 800K, standard reference material 736, Journal of Applied Physics 41, pp. 5096, 1970

[48] Metals Handbook, Vol. 1, ASM Handbooks online, http://products.asminternational.org /hbk/index.jsp, 2016

[49] B. D. Cullity, Elements of X-ray diffraction, Addison-Wesley Publishing Company, Massachusetts, USA, 1967

[50] H. M. Miekk-Oja, Metallioppi, Otava, Helsinki, Finland, 1960

[51] L. A. Dobrzanski, Metaloznawstwo, Wydawnictwa Naukowo-Techncze, Warszawa, Poland, 1996

[52] http://www.turbobraze.com/fm_nickel.html, viewed 2016

[53] L. Reimer, Scanning Electron Microscopy, Springer Verlag, Berlin, Germany, 1985

[54] D. B. Williams, Practical electron microscopy in materials science, Philips electronic instruments, Inc., NJ, USA, 1983

[55] A DATABASE OF ELECTRON-SOLID INTERACTIONS, Compiled by David C. Joy EM Facility, University of Tennessee, and Oak Ridge National Laboratory Revision # 08-1, This compilation is © David C. Joy, April 2008

[56] Accessories for electron microscopy, number 1412, Polaron equipment Ltd, Warford, England, 1985

[57] D. M. Mattox, Atomistic film growth and resulting film properties: Residual film stress, Society of Vacuum Coaters SVC, Vacuum Technology & Coating, 2001

[58] R. H. Perry, C. H. Chilton, Chemical Engineers Handbook, Fifth edition, McGraw Hill, New York, N.Y., USA 1973

[59] J. Karhunen, Lujuusoppi, 4. P., Otatieto, Helsinki, Suomi, 1995

[60] JCPDS No. 04-004-4496, International Center for Diffraction Data (ICDD) database version number: 4.1605, 2016

[61] JCPDS No. 01-071-4629, International Center for Diffraction Data (ICDD) database version number: 4.1605, 2016

[62] JCPDS No. 04-016-2734, International Center for Diffraction Data (ICDD) database version number: 4.1605, 2016

[63] JCPDS No. 04-007-5437, International Center for Diffraction Data (ICDD) database version number: 4.1605, 2016

[64] JCPDS No. 00-036-1482, International Center for Diffraction Data (ICDD) database version number: 4.1605, 2016

[65] JCPDS No. 04-004-8233, International Center for Diffraction Data (ICDD) database version number: 4.1605, 2016

[66] JCPDS No. 00-004-0850, International Center for Diffraction Data (ICDD) database version number: 4.1605, 2016

[67] JCPDS No. 01-076-8259, International Center for Diffraction Data (ICDD) database version number: 4.1605, 2016

[68] JCPDS No. 04-001-3292, International Center for Diffraction Data (ICDD) database version number: 4.1605, 2016

[69] JCPDS No. 03-065-6696, International Center for Diffraction Data (ICDD) database version number: 4.1605, 2016

[70] ASTM Standard G48-00, Standard Test Methods for Pitting and Crevice Corrosion Resistance of Stainless Steels and Related Alloys by Use of Ferric Chlorine Solution, ASTM, PA, USA, 2000

[71] Korroosiokäsikirja, Suomen korroosioyhdistys, Hanko, Suomi, 1988

[72] M. G. Fontana, Corrosion Engineering, Third edition, McGraw-Hill, Singapore, 1987

[73] J. C. Scully, The Fundamentals of Corrosion, Third edition, Pergamon Press, Exeter, GB, 1990

[74] http://www-inst.eecs.berkeley.edu/~ee143/fa10/handouts/Stress_in_Thin_Films.pdf, viewed 2015